

INSTITUTUL DE FIZICĂ APLICATĂ

Cu titlu de manuscris
C.Z.U: 532.42:535.317.2(043.2)

ACHIMOVA ELENA

**OPTICA DIFRACTIVĂ PENTRU
HOLOGRAFIA OPTICĂ ȘI DIGITALĂ**

134.01 — Fizica și tehnologia materialelor

Teză de doctor habilitat în științe fizice

Consultant științific:

Culiuc Leonid, academician,
Dr. hab., prof. univ.
134.01 — Fizica și tehnologia
materialelor

Autorul:

Dr. Achimova Elena

CHIȘINĂU, 2018

INSTITUTE OF APPLIED PHYSICS

Cu titlu de manuscris
C.Z.U: 532.42:535.317.2(043.2)

ACHIMOVA ELENA

**DIFFRACTIVE OPTICS FOR
OPTICAL AND DIGITAL HOLOGRAPHY**

134.01 — Physics and technology of materials

The thesis of doctor habilitat in the physical sciences

Scientific consultant:

Culiuc Leonid, academician,
Dr. hab., prof. univ.
134.01 — Physics and technology of
materials

Author:

Dr. Achimova Elena

CHIȘINĂU, 2018

©Achimova Elena, 2018

Contents

INTRODUCTION	10
Motivation	10
The aim of the work.....	18
1. STATE-OF-THE-ART	20
1.1. Materials	20
a. Properties of chalcogenide glasses and nanostructures based on chalcogenide glasses	20
b. Azo-dyed polymers films	28
1.2. Recording methods	30
a. Optical holography	31
b. Vector or polarization holography	35
c. Digital holography.....	41
1.3. Studying methods	43
a. Raman and Optical spectroscopy	43
b. Digital holographic microscopy	49
c. Digital holographic interferometry.....	50
1.4. Application of diffractive structures based on chalcogenide glasses multilayers and azo-dyed polymers films.....	52
1.5. Objectives of the work and new contribution.....	55
2. MATERIALS: TECHNOLOGY AND STUDY METHODS	59
2.1. Thermal vacuum deposition of nanomultilayers and polymer films spin-coating	59
2.2. Carrier photoinjection at ChG-ChG interface.....	66
2.3. Optical and Raman spectroscopy measurements.....	72
a. Optical spectroscopy measurements.....	72
b. Raman Spectroscopy	86
2.4. Digital holographic measurements	94
2.5. Conclusions to Chapter 2.....	107
3. DIFFRACTIVE STRUCTURES RECORDING AND PATTERNING	110
3.1. Intensity holographic recording	111
3.2. Polarization holographic patterning.....	119
3.3. Digital holography recording.....	134
3.4. Conclusions to Chapter 3	148
4. DIFFRACTIVE STRUCTURES INVESTIGATION	150
4.1. Diffraction efficiency method.....	150

4.2. Digital holographic interferometry	155
4.3. Digital holographic microscopy.....	173
4.4. Imaging ellipsometry and AFM measurements	181
4.5. Conclusion to Chapter 4	192
5. APPLICATIONS OF DIFFRACTIVE OPTICS.....	194
5.1. Security hologram elements.....	194
5.2. Diffractive optics elements	203
5.3. Digital holography	206
5.4. Conclusion to Chapter 5	220
Main conclusions and recommendations.....	222
References	225
Annex 1	241
Annex 2	246

ADNOTARE

a tezei ”**Optica difractivă pentru holografia optică și digitală**”, Specialitatea 134.01 — *Fizica și tehnologia materialelor*, prezentată de **Elena Achimova** în vederea obținerii gradului științific de doctor habilitat în științe fizice, Institutul de Fizică Aplicată, Chișinău, 2018.

Structura tezei: Teza este scrisă în limba engleză și constă din Introducere, cinci capitole, concluzii generale și recomandări și bibliografie din 229 lucrări. Lucrarea conține 245 de pagini, inclusive 2 anexe, 187 figuri, 12 tabele și 57 formule. Rezultatele obținute au fost publicate în 63 articole științifice.

Cuvinte cheie: optică difractivă, holografie optică și digitală, sticle calcogenice (SC), azopolimer (AP), înregistrare holografică scalară și vectorială, interferometrie și microscopie holografică digitală, procesare optică și digitală a imaginilor.

Scopul cercetării constă în cercetarea și elaborarea elementelor opticii difractive, care reprezintă o combinație funcțională de componente optice, dispozitive optico-mecanice și tehnologii, precum și algoritmi lor operaționali.

Obiectivele tezei includ elaborarea elementelor optice bazate pe structuri nanomultistrat (NMS) din SC și AP drept medii de înregistrare; elaborarea tehnologiilor holografice digitale și optice pentru crearea elementelor opticii difractive (EOD) pe medii NMS din SC și filme subțiri de AP; investigarea aplicabilității acestor metode holografice drept instrument pentru studiul proprietăților optice ale materialelor de scară nanometrică; aplicarea/folosirea EOD ca componente optice în dispozitive optoelectronice, biomedicină și securitate.

Noutatea științifică și originalitatea rezultatelor obținute: a fost stabilit experimental, că, în structurile NMS din SC-Se și filmele subțiri de AP elaborate, schimbările parametrilor optici (indicele de refracție și coeficientul de absorbție) au loc sub acțiunea atât a componentei scalare, cât și a celei vectoriale a câmpului radiației optice; rețelele reliefate superficiale obținute prin înscriere directă, se formează prin imprimarea holografică optică și digitală, care sunt cauzate de răspunsul vectorial (spațial anizotrop) al mediului; (desenul) rețeaua superficială reliefată pe SC-Se NMS este guvernată de structurarea fotoindusă în nanostraturile de SC și Se, ceea ce duce la transferul de masa în SC-Se NMS; rețelele reliefate superficiale imprimate pe filmele subțiri de AP sunt formate de transformarea fotoindusă de tip *trans-cis-trans* în AP, ceea ce duce la transferul de masa în acest mediu; au fost modelate și imprimate EOD de fază pe baza NMS din SC-Se și AP, precum și studiate posibilitățile și limitele acestora din punctul de vedere al aplicațiilor practice; impactul potențial al lucrării constă în elaborarea tehnicii optice avansate pentru imprimarea/înregistrarea structurilor difracționale și investigațiile la scară nanometrică.

Problema științifică importantă soluționată constă în elaborarea aspectelor teoretice și aplicative ale proceselor induse în materialele amorfe de lumină și iradierea cu electroni, ceea ce duce la formarea în aceste medii sensibile a structurilor difracționale și aplicarea acestora în holografia optică și digitală.

Valoarea aplicativă a lucrării este determinate de faptul, că cercetările sistematice a capacității materialelor NMS de SC-Se și AP de a fi structurate prin metodele de înscriere laser, prin iradierea cu fascicol de electroni și prin imprimarea digitală a hologramelor, deschid largi oportunități pentru elaborarea și/sau optimizarea EOD din aceste materiale în optoelectronica și fotonica modernă (aplicații în optica difracțională, medicină, tehnologiile de combatere a falsificărilor, holografia imagistică ș.a.).

Implementarea rezultatelor: rezultatele obținute au fost utilizate în îndeplinirea cu succes a 15 proiecte internaționale și naționale aplicative.

АННОТАЦИЯ

диссертационной работы “Дифракционная оптика в оптической и цифровой голографии”, Специальность 134.01 — Физика и технология материалов, представленной доктором **Еленой Акимовой** на соискание учёной степени доктора хабилитат физических наук, Институт Прикладной Физики, Кишинев, 2018.

Структура работы: Диссертация состоит из введения, пяти глав, основных выводов и рекомендаций, библиографии, включающей 229 названий. Основной текст представлен на 245 страницах, включая 2 приложения, 187 рисунков, 12 таблиц и 57 формул. Полученные результаты были опубликованы в 63 научных статьях.

Ключевые слова: дифракционная оптика, оптическая и цифровая голография, халькогенидные стекла (ХС), азополимеры (АП), многослойные наноструктуры, скалярная и векторная голографическая запись, цифровая голографическая интерферометрия и микроскопия, оптическая и цифровая обработка изображений.

Цель исследования заключается в разработке элементов дифракционной оптики, которые представляют собой функциональную комбинацию оптических компонентов, оптико-механических устройств и технологий, и алгоритмов работы.

Задачи исследования включают разработку оптических элементов на основе многослойных наноструктур (МНС) из ХС и АП в качестве записывающих сред; разработку существующих цифровых и оптических голографических технологий для создания элементов дифракционной оптики (ДОЭ) на МНС из ХС и тонких пленок из АП; исследование применимости данных голографических методов как инструмента для исследования оптических свойств наноразмерных материалов; применение ДОЭ как оптических компонентов в оптоэлектронных устройствах, биомедицине и защитных технологиях.

Научная новизна и оригинальность результатов состоит в экспериментальном определении изменений оптических параметров (показатель преломления, коэффициент поглощения) в МНС ХС-Se и тонких пленках АП под воздействием как скалярных, так и векторных компонентов электрического поля оптического излучения; в том что рельефные поверхностные решетки, полученные прямой записью, формируются под воздействием оптических и цифровых голографических методов записи, которые обусловлены векторным (пространственно-анизотропным) откликом среды; в том что поверхностная рельефная решетка на МНС ХС-Se формируется фотоиндуцированным структурированием в нанослоях ХС и Se, что приводит к массопереносу в МНС ХС-Se; что поверхностная рельефная решетка, сформированная в тонких пленках АП, формируется фотоиндуцированным *транс-цис-транс*-преобразованием в АП, что приводит к массопереносу в этих средах; были смоделированы и записаны фазовые ДОЭ на МНС ХС-Se и на тонких пленках АП, изучены их возможности и ограничения для практического применения; оригинальность этой работы заключается в разработке оптических методов регистрации и исследований дифракционных структур на наноразмерных слоях ХС.

Важной научной задачей исследования является разработка теоретических и прикладных аспектов фото- и электронно-индуцированных процессов в аморфных материалах, приводящих к возможности регистрации в этих средах дифракционных структур, и применению данных структур в оптической и цифровой голографии.

Практическая значимость работы заключается в том, что систематические исследования способности МНС ХС-Se и АП структурироваться под воздействием методов лазерной и цифровой голографии, облучения электронным лучом открывают новые перспективы для разработки и/или оптимизации широкого спектра приложений ДОЭ из данных материалов в оптоэлектронике и фотонике (дифракционная оптика, медицина, защитные технологии, голографические методы неразрушающего контроля, изобразительная голография и т. д.).

Внедрение результатов: полученные экспериментальные результаты были практически использованы при успешной реализации 15 международных (ЕС, FP7, Horizon-2020, билатеральных) и национальных прикладных проектов.

ANNOTATION

of the thesis “**Diffraction optics for optical and digital holography**” Speciality 134.01 — *Physics and technology of materials*, presented by **Elena Achimova**, to obtain the title of doctor habilitat in the Physics, Institute of Applied Physics, Chisinau, 2018.

Thesis structure: The thesis contains Introduction, 5 chapters, general conclusions and recommendations, bibliography of 229 titles. The main text amounts to 245 pages, includes 2 Annexes, 187 figures, 12 tables, 57 formulas. The obtained results of the thesis were published in 63 scientific papers.

Keywords: diffractive optics, optical and digital holography, chalcogenide glasses (ChG), nanomultilayers, azopolymers (AP), scalar and vector holographic recording, digital holographic interferometry and microscopy, optical and digital image processing.

Aim of research is R&D of diffractive optics elements which are combination of optical elements, devices and technologies, and their operation algorithms.

The objectives of thesis include the development of optical elements based on nanomultilayers (NML) structures from ChG and AP as recording media; the development of digital and optical holographic technologies for creation diffractive optics elements (DOE) on NML media from ChG and AP thin films; the investigation of applicability of these holographic methods as tools for studying of materials optical properties in nanoscale; DOE application in the form of optical components in optoelectronics and photonics, biomedicine and security.

Scientific novelty and originality of the obtained results: are determined experimentally that in the ChG-Se NML and the AP thin films the complex variations of optical parameters (refractive index, absorption coefficient) take place responding to the action of both scalar and vector components of the field of optical radiation; the direct surface relief gratings are formed under optical and digital holographic recordings which are conditioned by vectoral (spatially anisotropic) response of the medium; the surface relief gratings patterned on the ChG-Se NML are governed by photoinduced structuration in nanolayers ChG and Se that leads to mass transfer in the ChG-Se NML; the surface relief gratings patterned on the AP thin films are governed by photoinduced *trans-cis-trans* transformations in the AP that leads to mass transfer in this media; it was elaborated and recorded the phase DOE on the ChG-Se NML and the AP thin films, and their potentials and limitations for practical application were studied; the potential impact of the work consists in the development of the advanced optical techniques for diffractive structures recording and investigations at nanoscale.

Important scientific problem consists in elaborating of the theoretical and applied aspects of the processes induced in amorphous materials by light and electron irradiation leading to pattern in these sensitive media the diffractive structures and the application of them in optical and digital holography.

Applicative value of the work is that the systematic studies of ability ChG NML and AP to be structured by laser writing methods, exposure with e-beam radiation, and digital hologram recording open up perspectives for development and/or optimization of wide a variety of applications in optoelectronics and photonics (diffractive optics, medicine, counterfeiting elements, holographic methods of non-distractive testing etc.).

Implementation of results: the results obtained have been applied in the successful implementation of 15 international (EC, FP7, Horizon-2020, bilateral) and national applicative projects.

ABBREVIATION LIST

DH	Digital holography
CGH	Computer-generated holography (hologram)
DOE	Diffractive optical element
MEMS, MOEMS	Micro-electro/opto-mechanical systems
ROE	Refractive optical elements
3D	Three-dimensional
CCD	Charge coupled device
CMOS	Complementary metal-oxide semiconductor
2D	Two-dimensional
PH	Polarization holography
PA	Photoinduced anisotropy
ChG	Chalcogenide glasses
PVK	Poly(N-vinylcarbazole)
CCP	Carbazole-containing polymers
SRG	Surface relief grating
AP	Azo-doped carbazole-containing polymers
NML	Nanomultilayers
NDT	Non-destructive testing
SLM	Spatial light modulator
DHI	Digital holographic interferometry
DHM	Digital holographic microscopy
FSDP	First Sharp Diffraction Peak
CRN	Continuous random network
DE	Diffraction efficiency
PST	Photoinduced structural transformations
EBL	Electron beam lithography
SPAR	Sparse Phase and Amplitude Reconstruction
ESPI	Electronic speckle pattern interferometry
DEP	Dielectrophoretic
MTF	Modulation Transfer Function
FOV	Field of view
AFM	Atom Force Microscope
QPI	Quantitative Phase Imaging

INTRODUCTION

Motivation

With diffractive (wave) optics — commonly referred to as physical optics — we take into account for important phenomena such as interference, diffraction, and polarization. The study of these phenomena lays the foundation for an understanding of such devices and concepts as holograms, interferometers, thin-film interference, gratings, polarizers, quarter-wave plates, and laser beam propagation in the near and far field.

The invention of holography by D. Gabor, followed by the works of E. Leith and J. Upatnieks, made possible to perform nearly arbitrarily wavefront transformations with the aid of optical microstructures fabricated by interference [1, 2]. The realization by A. Lohmann and co-workers in the mid-1960's that optical holograms can be simulated by digitally generated binary transparencies was another significant step forward in the path towards widespread application of diffraction in optics [3, 4]. This new approach was called digital holography (DH), or equivalently computer-generated holography (CGH). The CGH is distinguished primarily from its optical counterpart by the fact that the computer is able to design a hologram of a virtual object, and the operation of the diffractive optical element (DOE) can be optimized mathematically rather than experimentally. Since the operation of CGH is based on the diffraction of light, this field is also called diffractive optics. Its essence is the control of optical fields by microstructured media [5].

The use of refractive optical elements (ROE), such as lenses and prisms, dominates the history of optics, while the use of DOE, mainly gratings, has a relatively short history (about two centuries) and is only for specific applications (mostly in spectroscopy). However, as claimed by George R. Harrison, “No single tool has contributed more to the progress of modern physics than the diffraction grating”, the diffraction grating has been the best-established DOE and may be regarded as the equivalent of the prism in function of spectral dispersion, but is far superior to prism in many important regions of the spectrum. In recent decades, great advances in fabrication technologies, especially optical microlithography [6], and computer modeling techniques have led to an explosion of applications of diffraction in optics, which makes diffraction optics one of the most rapidly advancing areas of current research in optics.

Not only the diffraction gratings are now found to be useful in many non-spectroscopic fields such as ultrafast optics [7], optical photolithography [8], optical communications [9], but also new kinds of DOE like finite aperture and aperiodic DOE [10] are emerging and finding their places in various industrial applications [11]. It is for these reasons that so much effort has been devoted to the analysis, design and fabrication of gratings and other nonconventional DOE.

In DOE the thickness can be significantly reduced and the fabrication task for DOE can be further eased by the phase quantization of continuous phase profile. By quantization, the continuous phase profile can be replaced by a set of features of small lateral extension which is periodically replicated. Such a multi-phase level DOE profile can be fabricated by a series of same thin films or microlithography processes. Because of their ease of replication, DOE can offer significant technological and economic advantages over ROE.

Diffraction and refractive micro-optics have revolutionized the photonics industry due to their wide range of applications and their high-volume wafer-scale production potential. However, the present range of applications is severely limited by our ability to fabricate complex profiles on an optical substrate with high precision. A number of different techniques exist for the fabrication of DOE. The most spread of them which was first to apply for DOE recording is holography.

In classical holography, the wave field emitted from a real object is recorded on light-sensitive films in the form of a diffractive pattern generated by optical interference with a reference wave. The wave field of the object is optically reconstructed by diffraction with the fringe pattern. This is the three-dimensional (3D) spatial image produced by classical holography. Therefore, we need a real object to create a 3D image in classical holography.

Recently, the field has been undergoing a paradigm shift with the advent of CGH, in which the holographic interference pattern is digitally sampled by a charge coupled device (CCD) camera and the image numerically reconstructed by applying results from diffraction theory. This approach offers a number of significant advantages, including the ability to acquire images rapidly, the availability of both amplitude and the phase information, and the versatility of the processing techniques that can be applied to the complex field data acquired.

Two types of techniques are continuously being developed to advance holography. One technique commonly referred to as DH captures the interference fringe pattern using digital image sensors. Images are numerically reconstructed by digital processing of captured fields in DH. However, these are not 3D images but two-dimensional (2D) digital images displayed on a screen or printed on a piece of paper. Since the captured data contains the information of the phase of light, this technique is mainly used for microscopes or some fields of metrology such as flow measurements.

The other technique is referred to as the CGH. This technique numerically generates a fringe pattern using a computer and reconstructs wave fields of light using diffraction with the fringe pattern printed or displayed. Once the wave field is provided in the form of numerical data, CGH can reconstruct the wave field. However, it is extremely difficult, even using modern computers, to compute the high-definition wave field emitted from virtual 3D scenes.

Besides of developing digital methods of DOE recording, optical holography is advanced to optimization of recording process maintaining the advantages of optical holography — high quality of 3D holographic images such as polarization holography (PH). PH has many unique properties compared with conventional holography, such as high efficiency, achromaticity, and special polarization properties. This process was discovered by Sh. D. Kakicheshvili [12]. However, because of its complex presentation, this monograph is not easily amenable for application to practical work. PH has several unique properties [13]: 1. It is possible to achieve theoretically 100% diffraction efficiency even in thin films; 2. The diffracted beams have unique polarization properties, depending on the polarization of the recording and read-out beams; 3. It is possible to fabricate polarization-sensitive optical elements; and 4. Such polarization holograms are called vector holograms as opposed to ordinary scalar holograms. The polarization modulation is obligatory for vector holograms but the intensity modulation which is necessary for scalar hologram recording can be absent. In other words, we obtain in the material the photoinduced anisotropy (PA).

Vector DOE can perform a full transformation of light wavefronts including their polarization, by this way becoming a powerful tool for the investigation of materials. These were our motivations to study PH based on holographic and e-beam recording in chalcogenide glasses and azopolymers.

The problem of creation of DOE consists of development of optical media and recording methods which can adequate reproduce sophisticated form of DOE. The common demands for optical media are a high sensitivity, resolution, diffraction-efficiency level, signal-to-noise ratio, and ensuring temporal stability of DOE recorded. In case of polarization diffractive optics the requirement of polarization dependent transmission of DOE becomes inevitable. The appropriate recording methods are required to give the possibilities of adequate recording of DOE different kind and form. For this aim new digital recording methods are developing in addition to optical ones. But in any case, the recording method and optical media have to match each other, i.e. media does to change its parameters in according to action of the recording method.

The most important characteristics determining practical application of the media are high sensibility, high resolution and wide spectral and frequency range, stability in time, low cost, among others. Within this framework, materials were chosen to meet certain criteria for the application. These include:

1. transparency (low optical losses at working wavelengths corresponding to the characteristic optical absorption bands of molecules),
2. absorption at working wavelengths of laser illumination,

3. suitability for direct-laser writing of surface structures,
4. photoinduced changes of media's optical parameters such as refractive index (scalar and vector), absorption coefficient, structural network (for tight confinement of optical energy within the resonator structure),
5. processibility into thin film form (for compatibility with micro-based fabrication techniques),
6. chemical compatibility (for adhesion to glass substrate, for development and resistance to the chemical environment to be sensed),
7. easy mass production.

All of these criteria, except 3 and 4, are common for recording media. The third criterion means absence of the step of selective etching in technological process. It is the advantage of such media because used etchants are toxic, and during selective etching process it is necessary to control many parameters (temperature, concentration of etchant, surface quality, etc.). Thus the development of one-step methods for the fabrication of surface relief's is considered perspective for the fabrication of planar optical elements. Exclusion of chemical development allows us recording DOE with forms calculated by PC without distortions invoked by analog (chemical) treatment.

Chalcogenide glasses (ChG) are an important class of amorphous semiconductors used for development of active and passive optical elements of photonics. ChG, consisting of S, Se, and Te in the group VIb elements, meet the most of the abovementioned criteria. Applications of ChG have mainly been based on their transparency to infrared light (passive) and sensitivity to different kinds of irradiation (active). The latter produce pronounced structural changes in ChG that are the more important case, regarding the challenges of understanding their microscopic nature and applications as functional materials of photonics. Photonic applications are essentially related to the changes of optical characteristics (optical transmission, reflection or refraction), which can result in an amplitude/phase modulation together with the changes of dimensions and structure of the given element (lens, diffractive element, waveguide).

The ChG present a variety of photo-induced phenomena. The reason why the ChG exhibit many kinds of photo-induced phenomena can be ascribed to unique electronic and atomic structures. Electronically, the glass is a kind of semiconductors with the energy gap of 1–3 eV, and it can be photo-excited by visible light. In addition, excited carriers are localized in disordered and defective glass structures, and the carriers undergo strong electron-lattice interaction. Structurally, the glass has moderate atomic connectivity, which is not as rigid as in oxide glasses and not as flexible as in organic polymers. For instance, typical ChG such as $\text{As}_2\text{S}(\text{Se})_3$ are assumed to have distorted covalent-layer structures with average atomic coordination numbers of 2.4–2.67, and the glass-transition temperatures distribute at 200–400 °C. Therefore, the electron-lattice

interaction can cause some structural changes, which are stable at room temperature and may be recovered with annealing. Despite these general views, however, detailed mechanisms of each photo-induced phenomenon have not been elucidated, the main reason being the glass structure, which is difficult to determine explicitly.

ChG are known to exhibit both scalar photoinduced phenomena (photodarkening, photorefraction, photodoping) and vectorial (photoinduced anisotropy, photoinduced gyrotropy, photoinduced light-scattering) that are connected with photoinduced structural transformations, defects creation and atoms diffusion. From the general point of view, the basic effects of irradiation on ChG are similar the well-known irradiation-induced transformations that occur at both the initial level of the electron-hole excitation and further structural transformations, causing the same physical and/or chemical changes including optical (darkening and optical anisotropy), mechanical (softening), and geometrical effects (expansion or contraction). Due to amorphous structure of ChG the studying of their structural transformations require to produce structures at nanoscale which are compatible with nanoscale sizes of medium range structure of ChG.

Much research work has been focused on nanostructure formation suitable for micro/nano-electronics and photonics applications. Glasses are promising materials there for two reasons [14]. First, the control of nanostructures could give the information about a glassy structure. Unlike crystalline materials, in which we can prepare atomically controlled surfaces the amorphous structure is disordered at the atomic level. The amorphous structure is neither periodic, as that in a crystal, nor completely random, as that in an ideal gas. There are two types of order in ChG:

1. short-range order with scales ≤ 0.5 nm (three parameters: the coordination number Z of atoms, the bond length r , and the bond angle θ);
2. medium-range order with scales of 0.5–3 nm (2D sheets preserving short-range order which are connected by Van der Waals forces).

Despite the medium-range order conception is recognized, many unresolved questions concerning glass structure, and especially structure's influence on macroscopic properties are still remaining.

Multilayer structures are simplest artificial nanostructures that can be rather easily fabricated with controlled geometrical parameters and investigated as thin films. It is essential, since the changes of the optical parameters (blue shift of the fundamental absorption edge, quantum states, and luminescence) as well as of the conductivity, and melting temperature (stability), are characteristics for and usually examined in nanostructures. A few approaches are known for extending investigations of ChG layers towards the nanostructures, especially in the nanolayered,

superlattice-like multilayer structures [15–17], but the problem of photostructural transformation dependence on the artificial nano-structuring is still not solved. In addition, all of these applications of ChG are required chemical developments to form a surface relief, i.e. cannot be fabricated by one-step direct laser writing.

Thus in an effort to further enhance ultimate optical performance, this thesis work aimed to develop the nanostructures from ChG, combining the advantages of different ChG species and nanostructural properties of total nanostructure. In addition, the nanostructuring of ChG allows us exploiting not only optical, but polarization properties of nanostructures created by artificial structuring. It is much important for holographic application of ChG as it advances the field of optical holography in PH. Generally, in glasses, the smallest structural unit which can be artificially manipulated may be attained not at the atomic scale, but at the nano-scale.

The other class of materials widely used for DOE recording is photosensitive polymers. The molecular structure is the key to an understanding of the science and technology of polymers included photopolymers. The basic structure of a polymer consists of a backbone and pendant (or side) groups. Atoms that are covalently linked and stretch from one end of a polymer to the other make up the polymer backbone (which is often not only carbon, but can also contain other atoms such as N, O, or Si). All other atoms are part of the side groups (H is the simplest, methyl (CH₃) or alcohol (OH) groups are among many possibilities, making for a wide variety of structures that make up polymers).

The polymers are usually soft materials and, therefore, are likely to exhibit photoinduced atom displacements and corresponding changes in properties relatively easily. The underlying process is very similar to what happens in ChG: the light creates a photoinduced excited state in which the charge is redistributed. As a result, there is new polarization in the structure, which then induces specific atomic or molecular displacements. It may start with photo-electronic bond cessation and successive polymerization.

Among the photopolymers the poly(N-vinylcarbazole) (PVK) has been the subject of intensive investigation in the last 50 years since the discovery of its photoconductivity by Hoegl [18]. In 1957, he established that PVK sensitised with suitable electron acceptors (i.e. 2,4,7-trinitrofluorenone, TNF) showed high enough levels of photoconductivity to be useful in practical applications like electrophotography. Carbazole-containing polymers (CCP) have attracted wide interest due to their potential applications in areas such as optical data storage and information processing [19–21]. In the past decade, special attention was paid to the problem of holographic recording, mainly with the aim of protecting the documents from falsification or

counterfeiting, and reliefographic methods appeared to be a convenient answer to the problem. These requirements induce further developments of carbazole polymers.

Doped photosensitive polymers are an up-to-date way to meet these requirements since they can be tailored by chemical engineering to optimally match the practical needs. In the case of polymers functionalized with the azobenzene derivatives the cyclic photoisomerization of azobenzene-based groups can also lead to large-scale mass transport of the polymer chains which is observed as a surface relief grating (SRG) structure.

Photoinduced phenomena in azobenzene-doped polymers have attracted wide interest recently. The dyes show reversible isomerization between *cis*- and *trans*-conformation upon illumination from ultraviolet ($\lambda=365$ nm) to visible ($\lambda=570$ nm) light. When the dye is illuminated by polarized light, the transformation can produce anisotropic structures, which accompany not only optical changes as birefringence but also prominent changes in macroscopic shapes if the transformation occurs cooperatively.

There still exist a lot of similarities in photo-structural behaviours in the chalcogenide and the azodye-polymer system. For instance, in both systems, induced changes disappear at the glass transition temperatures. Photoinduced birefringence appears in ChG and in dye-polymers upon illumination of polarized and unpolarised light. Marked volume changes, anisotropic deformations, fluidity, and mechanical motions can be induced commonly.

Meanwhile a notable difference between the photoinduced changes in ChG and the azopolymer is the following: in the azodye-polymer system, it is conceivable that light excites the azodye, and its isomerization process causes successive structural changes in surrounding molecules. Accordingly, a problem in a photoinduced process is focused upon the successive structural change. On the other hand, in the ChG, the excited species cannot be identified, which may be some defective sites or disordered structures. It is plausible that the excited species change with the photon energy of excitation, light intensity, temperature, and so forth. As a result, following structural changes in ChG become largely speculative.

Having seen these many similarities, it is tempting to propose some universality in the photostructural mechanisms. Since the roles of dyes and back-bones in organic systems have been understood, the corresponding elements in the homogeneous glass should be sought, which are probably localized gap states and normal-bonding networks. The localized state can be directly photo-excited or it may trap excited carries, which will trigger successive structural changes in the disordered network. A big problem for such homogeneous systems, however, is that many kinds of defective structures can be envisaged as the gap state.

To get further insight into the photoinduced mechanisms, we take a comprehensive approach. Specifically, a comparison of photoinduced phenomena in ChG nanostructures with those in azo-doped CCP (AP) is valuable, since their photo-structural mechanisms have been understood more deeply.

The other aspects, which unite ChG and AP, are sensitivity for both laser and e-beam actions and the ability of direct surface deform under these irradiations. In this work we investigate and compare the possibilities of direct one-step surface relief formation by laser/e-irradiation on ChG nanomultilayers (NML) and AP films with the purpose of estimation of their efficiency and resolution limits.

Note that the mass transfer effect is connected with not only wavelength and dose of irradiation, but polarization state of light electrical field. Both intensity and polarization holography have been employed to direct generate surface relief in ChG NML and AP films which significantly improve and spread the features of analogue and digital holography.

There are many positive aspects to processing information using the (sometimes unwieldy and inaccurate) physical signals instead of the more accurate digital representations. These include the ability: 1) to deal with the image information in parallel, which gives dramatic improvement in the total processing speed; 2) to modify concurrently and full field an image (spatial modulation); 3) the capability to substitute space computational complexity for time computational complexity when performing certain transformations (correlation and integral Fourier transformation with coherent light); 4) the potential significant energy savings (in both creating the signal and effecting the computation); 5) the ease with which analog signals can be digitized or resampled at an arbitrary frequency for subsequent digital handling.

The problems existing in these two holographic technologies — the lack of quantitative description of optical holography and the computational complexity of the digital holography — may be resolved by applications and knowledge at the intersection of both. This work covers the investigation of the optical and digital holographic techniques considering contributions from both areas to solve application bottlenecks, and give rise to new applications and solutions.

The emerging computer technology of the last decades — increasing processing speed and memory capacity, new higher level softs, spatial light modulators (SLM), digital cameras instead of holographic films — have opened new possibilities for digital holographic applications. Such areas of DH like digital holographic interferometry (DHI) and digital holographic microscopy (DHM) provide optimal instruments for study of different objects from life and lifeless nature in nanoscale.

Optimal design of optical system is always hybrid with appropriately selected functions between analogue, and digital components of the system. The physical process determining these functions is diffraction of light. In this work, we addressed the following aspects of this problem:

- Development of the optical and digital holography methods for elaboration of high efficiency DOE;
- Development of media for DOE recording based on nanomultilayers structures from ChG and AP;
- Elaboration of digital holography methods for measuring developed DOE and testing their availability for different field of application.

The aim of the work

The main aim of the work is R&D of diffractive optics elements technologies which are combination of optical elements, devices, and their operation algorithms and practical applications:

1. The development and design of recording media based on nanomultilayers (NML) structures from chalcogenide glasses (ChG) and azo-doped carbazole-containing polymers (AP) for diffractive optics elements recording;
2. The elaboration of digital and optical holographic technologies for creation DOE on photosensitive NML media from ChG and AP thin films;
3. The simulation and one-step direct recording of DOE based on NML structures from ChG and AP as recording media;
4. The investigation of applicability of the elaborated holographic methods as tools for studying of optical properties of ChG and AP materials in nanoscale;
5. DOE application in the form of optical components in optoelectronic devices, biomedicine and protective technologies.

DOE design will be elaborated on the base of systematic studies of ability ChG NML and AP to be structured by scalar and vector laser writing methods, exposure with e-beam radiation, and digital hologram recording. Potentials and limitations of developed media and applied methods of their micro- and nanostructuring will be studied. Practical examples of optimized technology for fabrication of functional microoptical elements will be given. From the basic research point of view, this work will contribute to better understanding of phenomena within ChG NML and AP induced by their interaction with different energy/intensity laser/e-beam excitation. The other item considering in the work is the design of advanced diffractive optical systems based on hybrid optical and digital image processing.

To reach the aim the following main tasks have been determined:

- To develop the technological processes for thermal vacuum deposition of nanomultilayers from ChG glasses and spin-coating thin films preparation of new synthesized AP.

- To study optical parameters, molecular vibrations and structures of the ChG-Se NML and the AP thin films by optical and Raman spectroscopy methods.
- To determine the structures of constituents nanolayers ChG, Se, NML ChG-Se and the AP thin films, and to analyse their possibilities to one-step direct record of DOE.
- To study the photoinduced changes of optical parameters of the ChG-Se NML and the AP thin films and the appropriate photoinduced structural changes. To determine their suitability for both DOE recording methods such as optical and digital holography.
- To develop the one-step intensity and polarization holographic recording applicable to patterning process of DOE in the ChG-Se NML and the AP thin films.
- To develop the digital holographic methods for non-destructive investigation of sub-micrometres DOE surfaces in nanoscaled accuracy.
- To study the DOE properties recorded on the ChG-Se NML and the AP thin films by the digital holographic interferometry (DHI), digital holographic microscopy (DHM) and atom force microscopy (AFM).
- To study the practical applications of research findings of the diffractive optics in optical and digital holography.

1. STATE-OF-THE-ART

The necessity to save weight and size, and to improve the speed in the function of the devices, stimulated an intense research activity with the purpose to reach the nanometer size field. In the same time the worldwide interest was moved from electronic to more complex optoelectronic applications.

1.1. Materials

Any material used to record a diffraction structures must respond to exposure to light (or other excitations, e. g. electron beam) with a change in its optical properties. The absorption constant changes as a result of exposure, while in phase modulating materials thickness or refractive index changes due to the exposure. In the phase modulating materials, there is no absorption of light and the entire incident light is available for image formation, while the incident light is significantly absorbed in an amplitude modulating material. A practical recording media can be considered as a combination of these two.

In this part we give a brief review of results obtained for fundamental studies of non-crystalline chalcogenides and photopolymers, paying a special emphasis on revealed congeniality and, separately, on indicated differences in the changes of properties of photo-responsive media under the actinic light illumination. The detailed information necessary for an independent, more profound and comprehensive comparative analysis of the behavior of photosensitive amorphous chalcogenides can be found in the series of review articles [23–26]. It is expedient to assume that structurally conditioned inherent prerequisites exist, which preset the mutual likeness of the photo-responsive behavior of disordered media of amorphous ChG and other disorder functional materials like polymers.

a. Properties of chalcogenide glasses and nanostructures based on chalcogenide glasses

The great advantages of the disordered materials are: simple preparation procedures, low sensitivity to impurities, low cost, and, the last but not the least, the possibility to produce large area films of various thickness in classical systems for deposition: systems for evaporation in vacuum, magnetron systems, flash, spin-coating systems, sol-gel systems etc.

Further on we deliberately restricted the circle of consideration by well-known “classic” objects of study, as amorphous films of Se and As-S(Se) systems and the same systems with different additions Ge, Mn, Ag, Cr.

Discovered more than 40 years ago by the scientists Prof. B. T. Kolomiets and Prof. N. A. Goriunova, this class of materials became the subject of scientific research in many laboratories

throughout the world. ChG are analogs of common oxide glasses in which oxygen is replaced by one or more chalcogen atoms (S, Se, Te). Generally, chalcogens are alloyed with more electro-positive network-forming elements, such as As and Ge, with Sb, Bi, P, Sn etc. as less common alloying elements. Together they form a covalent glass network, as opposed to the ionic bonding that dominates common oxide glasses. The composition of the ChG can be selected to tailor optical and physic-chemical properties such as transmittance (T), reflectance (R), optical bandgap (E_{gopt}), refractive index (n), chemical resistance etc. for a specific application. Furthermore, ChG can be also doped with additional elements (for example metals like Ag, Cu, Zn or rare earth elements like Nd, Yb, etc.) to provide new properties and multi-functionalities [27].

In contrast to the liquid, which is thermodynamically equilibrated, the non-crystalline solid is in quasi-equilibrium, or is meta-stable. Strictly speaking, an amorphous material does not take a thermodynamically defined phase, but it takes just a spontaneous state, which necessarily changes with time. We know that a-Se films crystallize from surfaces within a few weeks when stored in humid atmospheres. In addition, a glass property depends upon preparation methods. As shown in Fig. 1.1 [28], as-evaporated and annealed As_2S_3 films give markedly different x-ray diffraction patterns.

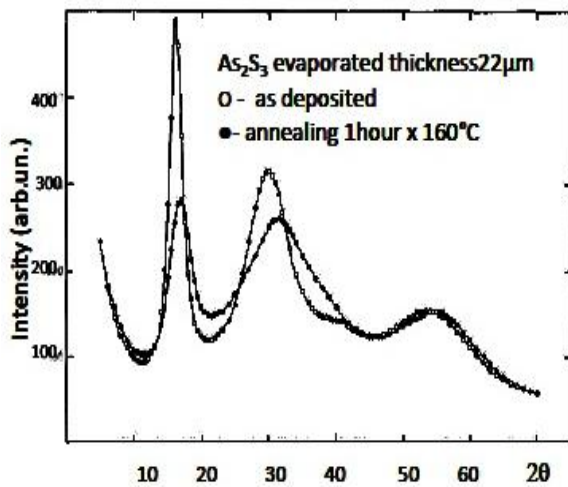


Fig. 1.1. X-ray diffraction patterns of As_2S_3 films in an as-evaporated state (\circ) and after annealing (\bullet) at 180 °C [28].

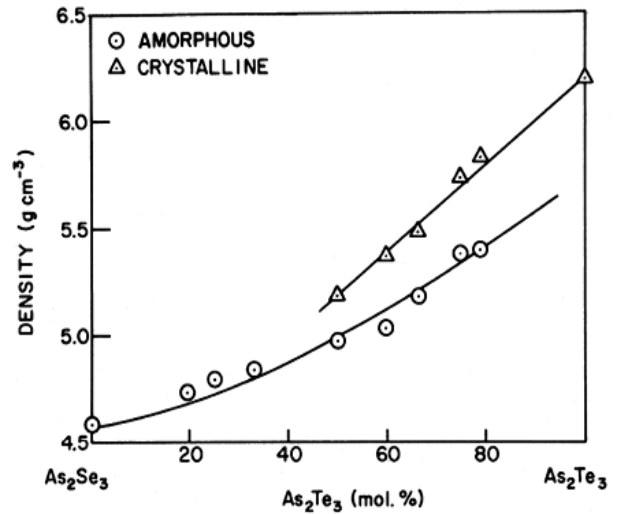


Fig. 1.2. Comparison of the densities for glassy and crystalline $As_2(Se-Te)_3$ alloys [28].

Nevertheless, meta-stability has provided an unresolved problem on the uniqueness of glassy states. For crystals, the structure can be determined in principle through analyses of Bragg peaks in x-ray diffraction patterns. However, as exemplified in Fig. 1.1, the non-crystalline solid does not provide sharp Bragg peaks but gives only broad halos.

A rough idea can be grasped from the macroscopic density (Fig. 1.2). It is known for simple glasses that the glass is less dense than the corresponding crystal by 10–20%, which varies with preparation procedures and storage after preparation. This observation suggests that atomic packing in the glass and the crystal is not very different. More generally, the densities of a glass, the corresponding crystal, and the melt can be regarded roughly as the same in comparison with that in the gas, which has nearly completely random and time-varying atomic (molecular) structures with an average separation of ~ 5 nm at 1 atm.

To analyze the amorphous structure in atomic scales, we can classify it, as shown in Fig. 1.3: structure models of one- or two-dimensional distorted layers [29].

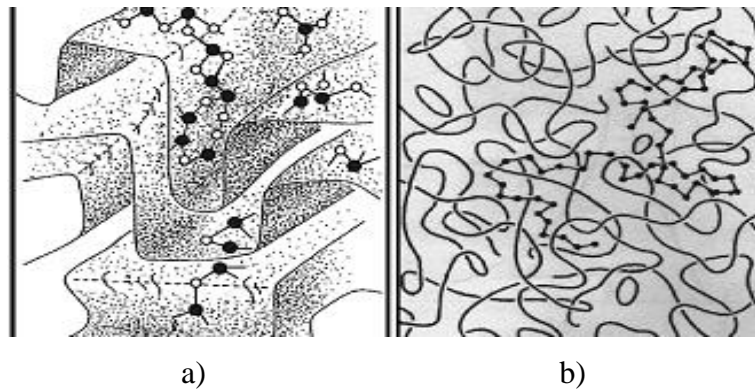


Fig. 1.3. Structure models of (a) As₂S₃ (two-dimensional distorted layers), (b) Se (one-dimensional entangled chains) [29].

In Fig. 1.3a, As and S are shown by solid and open circles with three and twofold coordination. Note that (a) contains wrong bonds (As–As and S–S), and (b) contains a few ring molecules of Se. The bond lengths are 0.23 nm in As₂S₃, and 0.24 nm in Se so that side lengths of these illustrations are 2–3 nm.

We also note that the point-like defect is spatially isolated from each other in normal bonding matrices. On the other hand, the defects tend to produce mid-gap states.

The short-range structure is determined by three parameters: the coordination number Z of atoms, the bond length r , and the bond angle θ . The short-range structure can be inferred from radial distribution function $\rho(r)$, which can be calculated from x-ray (e-beam and neutron) diffraction patterns, an example being shown in Fig. 1.4. Let us assume an elementary system such as a-Se; the diffracted intensity I at an x-ray wavenumber Q can be written as:

$$I(Q) \approx f(Q)^2 \int 4\pi r^2 [\rho(r) - \rho_0] (\sin Qr) / (Qr) \quad \text{with } Q = 4\pi \sin \theta_s / \lambda, \quad (1.1)$$

where f is the atomic scattering factor, ρ_0 an average atomic density, $2\theta_s$ the scattering angle, and λ the x-ray wavelength. Accordingly, from measured $I(Q)$, we can calculate $\rho(r)$, which provides

Z , r , and θ , respectively, from the first-peak intensity, the first-peak position r_1 , and the second-peak position r_2 with r_1 value.

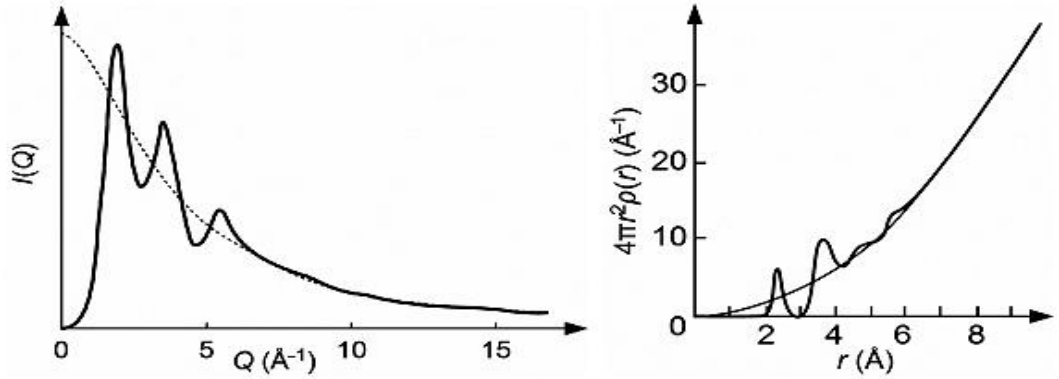


Fig. 1.4. Diffracted x-ray intensity $I(Q)$ and calculated radial distribution function $\rho(r)$ of Se [29].

However, for multi-component glasses, direct applications of the above procedures are difficult. We cannot determine the structure from only one diffraction pattern, since f changes with atom species.

Extended x-ray absorption fine structures (EXAFS) may give more direct information for the structure in multi-component systems. In EXAFS experiments, x-ray transmittance (or absorbance) of a sample of interest is measured as a function of x-ray energy $E = 2\pi\hbar/\lambda$. The oscillating EXAFS $\chi_i(k)$ can be regarded as an x-ray transmission spectrum which is modulated by the interference of x-ray excited electron waves with a wavenumber of $k = 2\pi/\lambda_e$, where λ_e is the electron wavelength (~ 0.2 nm).

Historically, the first implication of a medium-range order in glasses is believed to have been presented by Vaipolin and Porai-Koshits (1963) for glass As_2S (Se, Te)₃. Successive studies have demonstrated the existence of some medium-range structural orders with scales of 0.5–3 nm, at least, in simple glasses compositions.

De Neufville [30] was one of the first researchers who pointed towards the possible relation of the First Sharp Diffraction Peak (FSDP) in x-ray and neutron diffraction patterns with the presence of cage-like As_4S_4 molecular units in the structure of $\alpha\text{-As}_2\text{S}_3$. Since then, intensive work has been carried out on chalcogenide glasses, as didactically and comprehensively reviewed by K. Tanaka and K. Shimakawa in [29]. As a result of such intense research, the early continuous random network (CRN) paradigm is moving towards a more complete description of the glass conformation. Many electronic processes in crystals are controlled by the redistribution of charge carriers over separate discrete local levels. The chalcogenide semiconductors show a quasi-continuous

distribution of localized states, which generates peculiarities of electronic processes, in particular, in transport, in optical and photoelectric processes.

One of the main properties of ChG is their sensibility to the action of light and other electromagnetic radiations. What is the relationship between the three kinds (short range, medium range, and defect) of structural elements and structure-related (non-electronic) properties? We can neglect the defects, since its density is smaller than ~ 1 at. % and most of the structural properties, except those at low temperatures, are determined by normal bonding structures. It is natural to assume that the short-range structure governs structural properties, which are possibly modified by medium-range structures.

Early approaches to amorphous conformation were made on the basis of their crystalline counterparts. Short-range was preserved in the amorphous structure because of chemical bonding and valence rules; long-range order was absent in the amorphous structure, as expected for non-crystalline materials; and, medium-range order was needed in order to explain experimental evidence of the FSDP occurring in ChG and other amorphous materials [28, 31].

The isotropy of the structure and properties is considered to be one of the characteristic features of the amorphous materials. However, at present for the one very important and unusual class of materials, namely chalcogenides, the techniques for producing the optical anisotropy (birefringence) have been suggested. H. Fritzsche [32] has noted that initial prerequisites for anisotropic properties to be realized in amorphous chalcogenides lie in the fact that “on the molecular scale the structure of chalcogenide glasses is strongly anisotropic”. The original macroscopic isotropy originates from the random orientation of the microscopic anisotropic structural units.

Photoinduced optical anisotropy is the emergence of dichroism and/or birefringence in an initially optically isotropic chalcogenide film under the action of linearly polarized light. This effect is explained by the orientation of interatomic bonds or specific defects of the glass, leading to the appearance of some optical axis with a direction determined by the polarization vector of the exciting light. Both effects, photodarkening and photoinduced anisotropy in ChG films, are widely studied and applied in electro-optics.

Following the crystalline model proposed by Zhdanov et al. [33], Shimakawa et al. and Tanaka [30], and the phenomenological idea for photoinduced orientation by Fritzsche, the authors [34] assumed that $\text{As}_2\text{S}(\text{Se})_3$ glass illuminated with vertically (horizontally) -polarized light contains horizontal (vertical) layer structures. For Se, one may replace ‘layer’ with ‘chain’. This notion stems from the following two reasons: in $\text{As}_2\text{S}(\text{Se})_3$ and Se crystals, it is demonstrated that $n_{\parallel}^c > n_{\perp}^c$, where n_{\parallel}^c and n_{\perp}^c are the refractive indices with electric fields parallel and perpendicular to the layer plane or the chain axis. In addition, Fritzsche’s model predicts that refractive index of illumi-

nated glasses along the electric field becomes smaller since structural elements having higher refractive indices are preferentially excited by electric fields and the elements may be thermally relaxed to other orientations. Accordingly, if the layer clusters are responsible for the photoinduced anisotropy, and if the layer clusters in the glasses behave similarly to those in the crystals in refractive index, the layer planes tend to lie perpendicularly to the electric field.

Close relationship between the maximum photoinduced birefringence Δn and the natural birefringence in the corresponding crystal is shown in Fig. 1.5. That is, for Se, As_2S_3 , and As_2Se_3 , respectively, $\Delta n = -0.007$, -0.002 , and -0.0008 , and on the other hand, the crystalline birefringences are -0.8 , -0.5 , and -0.37 , respectively. The Δn is approximately proportional to the crystalline birefringence, and the former is $\sim 1/100$ of the latter. This close correlation is consistent with the crystalline model. Alternatively, it appears to be difficult to explain using atomic-scale models. Finally, the photoinduced oriented crystallization induced in Se is also in favor of the crystalline model. If linearly-polarized illumination can induce crystalline orientation in amorphous phases, the structure may work as nuclei for oriented crystals. If appropriate thermal energy is concomitantly provided, the nuclei will grow as oriented crystals. In contrast, if atomic-scale structural changes are assumed for the conventional anisotropy, what can be a motive force for the oriented-crystal formation?

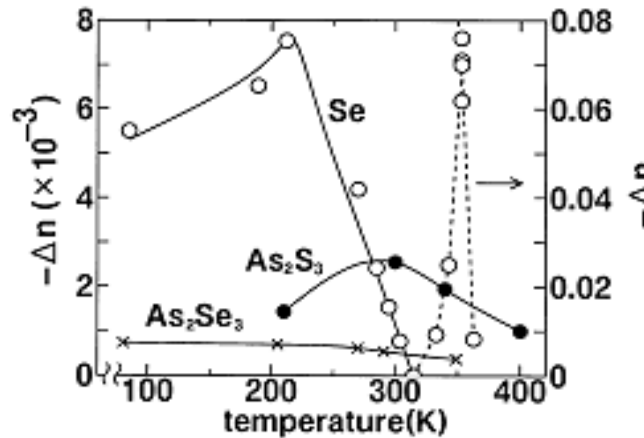


Fig. 1.5. Temperature dependence of photoinduced birefringence Δn for Se (○), As_2S_3 (●), and As_2Se_3 (x). Solid lines show the conventional photoinduced birefringence, and a dotted line for Se shows photoinduced crystalline birefringence, for which the right-hand side scale applies.

Measuring error in Δn is $\sim 10^{-4}$, and lines are eye-guides [34].

However most of the investigations have been carried out with films thicker than $0.5\text{--}1\ \mu\text{m}$. Study of photodarkening in the nanodimensional glassy chalcogenide films revealed contradictory results. Hayashi and Mitsuishi [35] observed the photodarkening disappearance at room temperature when the thickness of the glassy As_2Se_3 film was less than 50 nm. At the same

time, Eguchi et al. observed the photoinduced changes in the transparency of the nanodimensional (65–200 nm) As_2S_3 films at ~ 80 K [36]. At last, Indutnyi and Shepeljavi have shown that even very thin (0.7–2.5 nm) As_2S_3 films, which were embedded in transparent SiO_2 layers, had essential photodarkening at 80 K [37].

The multi-layer system has been the most extensively studied nano-structure from a fundamental and technological point of view. Notable studies have been reported for ChG.

Typically, for the thin films preparation, different deposition techniques are useful and of importance: vacuum thermal evaporation, sputtering, chemical vapour deposition, spin coating and pulsed laser deposition. Authors [38, 39] have reported that good quality nanostructures can be prepared by thermal evaporation and pulsed laser deposition. The aim of the work of [40] is to extend their previous results to surface patterning of amorphous chalcogenide-based nanomultilayers, formed typically by ~ 100 bilayers of materials differing in chemical composition, by laser-irradiation and electron-beam. For a comparison, authors have chosen structures of the same chemical composition (AsS/Se) prepared by different techniques and structures of different composition (AsS/Se vs. GeS/GeSe) fabricated by only pulsed laser deposition. Nanomultilayers based on AsS/Se were chosen due to their well-described properties. On the other hand, GeS/GeSe nanomultilayers were selected because of their non-toxicity and higher glass-transition temperatures that are of importance from the applications point of view.

In order to connect large thickness changes of nanomultilayers with changes of optical properties (refractive index and transmittance), light illumination experiments were performed without copper grating. Transmittance spectra were measured in-situ during light illumination. Examples of such spectra before and after light illumination are given in Fig. 1.6. Illumination times to saturation for GeS/GeSe and AsS/Se samples were 3600 and 400 s, respectively. In Fig. 1.6, the shift of the position of the short-wavelength absorption edge to shorter wavelengths is clearly observed as well as some changes in amplitudes of interference fringes which originate from the changes in refractive index n values ($\sim 4\%$ decrease in case of GeS/GeSe, $\sim 8\%$ increase in case of AsS/Se nanomultilayers) due to intermixing of the layers induced by light illumination.

Optical band gap values have the same values (in range of experimental error) for AsS/Se nanomultilayers, but for GeS/GeSe we observed 0.14 eV increase due to light illumination. The squares with dimensions of $5 \mu\text{m} \times 5 \mu\text{m}$ (wall width at half height $\sim 350\text{--}400$ nm) were patterned using e-beam with different absorbed doses ($0.15\text{--}2.7 \text{ Ccm}^{-2}$) in order to compare the thickness changes induced by e-beam and light illumination.

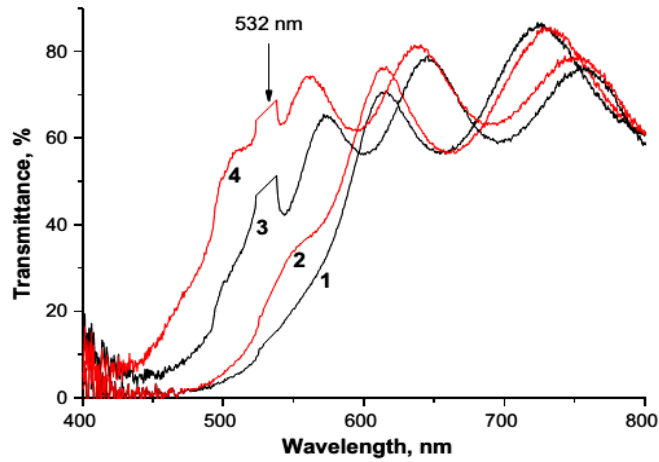


Fig. 1.6. Transmittance spectra of pulsed laser deposition nanomultilayers before and after light illumination: 1 - AsS/Se before light illumination, 2 - AsS/Se after light illumination; 3 - GeS/GeSe before light illumination, 4 - GeS/GeSe after light illumination. Laser wavelength used for light illumination is indicated in the figure. Note that the shape of the spectra for AsS/Se nanomultilayers is the same when used red laser line as well [40].

It was found that the thickness changes of the nanomultilayers took place and are of the order of 5%, thus lower when compared to light illumination induced patterns, but still large. Again, relevant differences can be only seen in the surface roughness (pulsed laser deposition vs. thermal evaporation structures). Thus the authors concluded that the e-beam patterning probably lead to similar changes, independent of chemical composition and/or nanomultilayers fabrication technique.

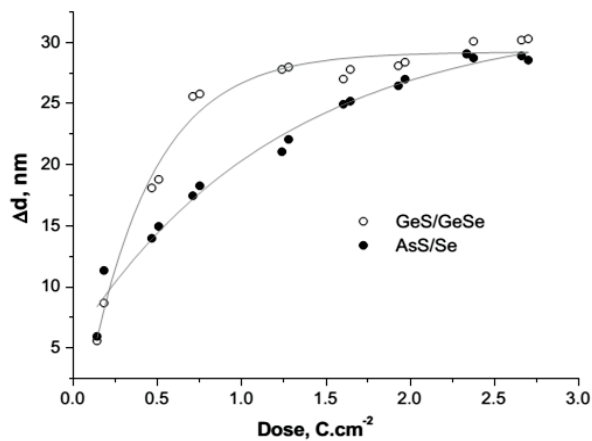


Fig. 1.7. Thickness change vs. absorbed dose for samples prepared by pulsed laser deposition technique (GeS/GeSe and AsS/Se, respectively) [40].

The magnitude of thickness change during e-beam patterning vs. absorbed dose dependence for pulsed laser deposition nanomultilayers is depicted in Fig. 1.7. The different behavior is evidenced for AsS/Se and GeS/GeSe structures, respectively. However, in saturated state, the

relative thickness changes seem to be independent of chemical composition. The absorbed dose required for the saturation of thickness changes (2.5 Ccm^{-2}) seems to be independent of chemical nature of nanomultilayers as well as of sample preparation method.

One should expect that similar behavior (thickness changes corresponding to light illumination and e-beam patterning) is accompanied by similar changes in optical properties. But, in [41] the authors wrote that it is no direct indication of refractive index and transmission spectra changes induced by e-beam patterning because of impossibility of patterning area sufficiently large for optical measurements.

With a decrease in layer thickness, a blue shift of optical absorption edges (or optical gap E_g) tends to appear, which is often interpreted as a quantum-well effect. However, the effect can appear only when the mean free path of electrons and/or holes is longer than the layer thickness. Nevertheless, the mean free path of electrons, and accordingly, the quantum-well interpretation may be misleading. The blue shift possibly appears as a result of vague layer boundaries, which are likely to govern macroscopic properties in thinner layer structures, since material diffusion becomes more evident in such systems.

b. Azo-dyed polymers films

The other class of materials widely used for diffraction optics is photosensitive polymers. The polymers are usually soft materials and, therefore, are likely to exhibit photoinduced atom displacements and corresponding changes in properties relatively easily.

The general composition of a photopolymer contains a monomer, electron donor, photosensitizing dye and, optionally, a polymer binder. Upon illumination of the photopolymer with a non-uniform light field of appropriate wavelength the sensitizing dye absorbs a photon and reacts with an electron donor to produce free radicals. This initiates polymerization where the light was absorbed. The photopolymerization process accompanies a change of absorption and refractive indices, which can be utilized for holographic recording.

Photoinduced reversible SRG have been well documented as a unique and fascinating property of azobenzene-containing polymers. This is a well known candidate for both polarization holography and optical one. Upon exposure to an interference pattern, large surface modulations can be produced on azo polymer films. The photofabricated surface structures are stable below the glass transition temperatures (T_{gs}) of the polymers and can be removed by optical erasure or by heating the samples to a temperature above their T_{gs} .

The dyes show reversible isomerization between *cis*- and *trans*-conformation upon illumination from ultraviolet ($\lambda=365 \text{ nm}$) to visible ($\lambda=570 \text{ nm}$) light. When the dye is illuminated by polarized light, the transformation can produce anisotropic structures, which accompany not only

optical changes as birefringence but also prominent changes in macroscopic shapes if the transformation occurs cooperatively. In addition, organic films can be obtained with simple coating, which may be the cheapest way for thin film preparations.

In the report [42] holographic recording of polarisation and surface relief gratings in Disperse Red 1 (DR1) doped polyurethane polymer films was studied. In this material DR1 is chemically bounded to polyurethane polymer main chain. Polarization holographic recording was performed by two orthogonal circularly polarized 532 nm laser beams. Photoinduced birefringence is a precondition for polarization holograms recording, therefore a detailed study of a photoinduced birefringence and changes of optical properties was performed. In authors's view, the structure of the synthesized polymer is follows: the DR 1 content (by weight %) is 26.6%; calculated polymerisation ratio is within 5-7; average molecular weight is 7000–10000. For photoinduced birefringence investigation plotted set-up is shown in Fig. 1.8. Verdi-6 laser with 532 nm, semiconductor lasers with 448 nm, 375 nm and He-Ne laser with 632.8 nm wavelengths were used as pumping laser (Ls1).

Laser beam was vertically linearly polarized and its transmittance changes were registered with the diode D3. As probe beam was used 634 nm diode laser with intensity $I=0.4 \text{ mJ/cm}^2$. An angle between probing and pumping laser beams was $\sim 3^\circ$. A sample (S) was placed between polarizer (P) and analyzer (A) with a polarization state -45° and $+45^\circ$, respectively.

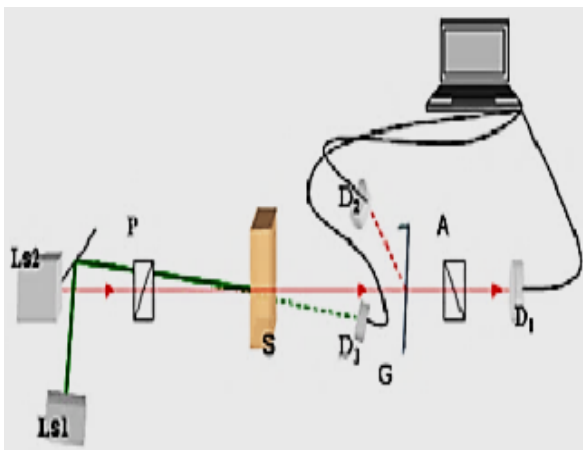


Fig. 1.8. Experimental set-up for photoinduced birefringence measuring. Ls1 - pump laser; Ls2 - probe laser; P - polarizer; S - sample; G - glass plate; A - analyzer; D1-3 - photodiodes [42].

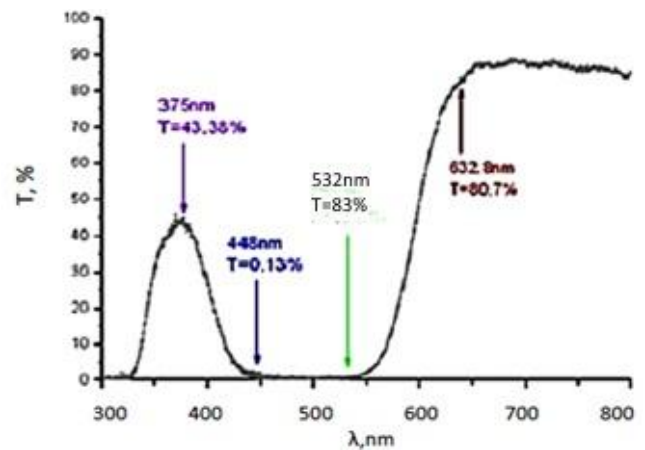


Fig. 1.9. DR1 doped polyurethane sample transmittance spectrum [42].

Behind the sample a glass plate was placed in order to control probe beam transmittance during an experiment by measuring a glass plate reflected light intensity. A diode D1 measured a signal

which characterized a photoinduced birefringence in the sample during irradiation with pumping laser. All three diodes were connected to PC. Refraction index changes Δn were calculated by formula:

$$\Delta n(t) = \frac{\lambda}{\pi d} \sin^{-1} \left(\sqrt{\frac{I(t)}{I_0}} \right), \quad (1.2)$$

where $I(t)$ is the probe intensity passing through the crossed polarizers, I_0 — probe intensity passing through the parallel polarizers before pump irradiation.

DR1 doped polyurethane polymer film's transmittance spectrum is shown in Fig. 1.9. Absorption bands of *trans* and *cis* isomers are undistinguishable. They overlap in 450–550 nm band where strong absorption has been observed.

Photoinduced birefringence phenomenon appears in material during linearly polarized light irradiation. Under pumping light radiation azo-compounds experience a photoisomerization process, which leads to dipole moment and polarizability changes. After an interaction with pumping light electrical field azo-compounds align perpendicularly to electrical field direction, thus taking the position with the lowest energy. A result of alignment is change of material optical properties. This reorientation induces anisotropy and the difference of refractive index parallel and perpendicular to the irradiating laser polarization direction.

Although many research focused on the low-molecular-weight azo-doped polymers, the stability of the induced anisotropy was low. Low-molecular-weight AP materials are superior in terms of mobility. However, it is often difficult to prepare holographic gratings with narrow fringe spacing (i.e., high resolution) and high stability because of the high mobility of azo molecules with low molecular weight. From the application point of view, azo-containing polymer materials might be one of the best choices for holograms because of their simple processability and high stability.

1.2. Recording methods

The diffraction efficiency (DE) is an important parameter in characterizing optical and digital holograms. Amplitude holograms in general possess lower DE than phase holograms. However, amplitude holograms are interesting in several respects: (1) their easy fabrication, (2) their quality of reconstruction independently of wavelength, (3) the direct correspondence of a binary hologram to the distribution of a binary phase hologram of the same signal, (4) their utility as a starting point in constructing highly efficient hybrid volume holograms.

a. Optical holography

Holography, the most significant 3D imaging technique, was first discovered by Dennis Gabor in 1948, which is before the invention of the laser. After the invention of the laser as a coherent source, Gabor's ideas became a practical reality.

The basic mechanism of holography also called coherent wave front recording and the Leith-Upatnieks hologram, the first type of hologram successfully implemented with a laser setup.

Suppose that an object (desired) wave $U(x, y)$ is expressed as

$$U(x, y) = A(x, y)e^{j\phi(x, y)}. \quad (1.3)$$

Another reference wave $R(x, y)$ is expressed as

$$R(x, y) = B(x, y)e^{j\psi(x, y)}. \quad (1.4)$$

The two waves will be incident on a recording medium that is sensitive to intensity. The intensity resulting from the sum of the two waves is given by

$$I(x, y) = |A(x, y)|^2 + |B(x, y)|^2 + 2A(x, y)B(x, y) \cos(\psi(x, y) - \phi(x, y)). \quad (1.5)$$

There are many types of holograms. Transmission holograms transmit light such that the information is viewed through the transmitted light. With reflection holograms, the information is viewed as a result of reflection from the hologram.

The optical recording in ChG is based on photoinduced structural transformations (PST), which lead to changes in optical parameters of the material. During structural transformations, as a consequence of the photo-crystallization or reversible structural alterations, besides the optical parameters (reflectivity, refractive index, absorption coefficient) the density, chemical stability (with respect to the etching) can change. It is also known that the viscosity decreases in ChG during sub band-gap illumination. This is an indication that the illumination can enhance the atomic mobility since the Stokes-Einstein relation in simple liquids linearly relates the inverse of viscosity of the media to the diffusivity of a tracer, but the atomistic mechanism responsible for the observed high diffusivity is not completely established.

Enhanced intermixing, induced by a laser beam, has been observed in amorphous Se/As₂S₃ and similar multilayers [43]. The report describes the experimental observation of the overall change of thickness due to the light-stimulated interdiffusion and presents a model of this process. This offers a new mechanism of optical recording in light sensitive chalcogenides. The recording efficiency depends on the thickness ratio of the component layers and on the modulation period of the multilayer.

In order to explore the role of mass transfer in optical recording the authors have to select a system in which chemical inhomogeneities are present. This can be achieved with a multilayered

structure. It is also important that the components must be mutually soluble in each other in the same structure. In this way the role of chemical reactions at the interface can be excluded. A number of As_xSe_{1-x}/As_yS_{1-y} -type layered structures have been fabricated.

Layers with different ratios of the Se/As_2S_3 layers have been prepared, and the change of the total thickness, d , optically after prolonged illumination leading to the total mixing of the layers being measured. The time dependence of the relative thickness change is shown in Fig. 1.10 together with experimental data for a multilayer with period of $D=9$ nm. The diffusion coefficient is 6.6×10^{-22} m^2/s , was used in the subsequent calculations. This value corresponds to 0.11 W/cm^2 illumination intensity applied in these experiments.

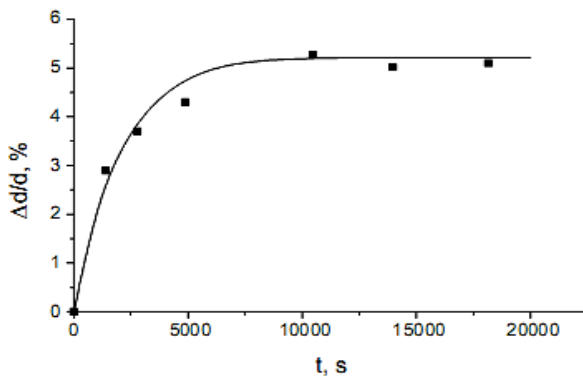


Fig. 1.10. Time dependence of the film thickness change. The dots are experimental data ($D=9$ nm and $W=0.11$ W/cm^2), the continuous line is the result of the calculation [44].

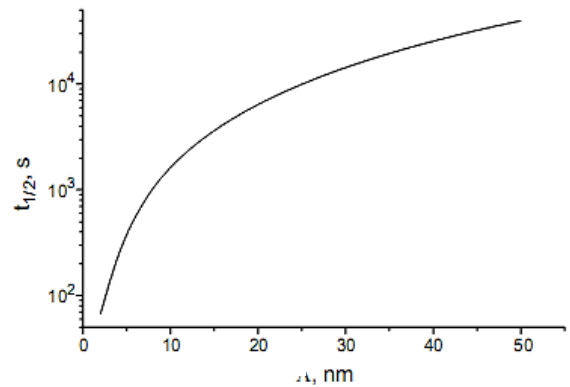


Fig. 1.11. Time for halfway completion of the thickness change vs. multilayer period [44].

The diffusion model was used to show the influence of multilayer period on the velocity of the optical recording processes: the speed of the thickness change increases with decreasing period (see Fig. 1.11) for multilayers with the same initial thickness. By convention, the recording speed is taken as the time needed for the thickness change to proceed halfway to completion.

As one can see in Fig. 1.11 for nanometer-size multilayer-periods several orders of magnitude increase of the efficiency in this type of optical recording processes may be achieved. It was found that with the thermal evaporation technique if the layer thickness is below 5 nm, the surface roughness increases considerably, which leads to a degradation of the optical recording capability. The maximum period D is limited by the maximum time, which can be used for the recording.

The layer thickness change can be used to record relief holograms without etching in these multilayers. Formation of surface relief can be described relying on above model assuming that

the interdiffusion coefficient linearly depends on light intensity I . Taking into account the light-intensity distribution along the surface in y -direction in the recorded interference pattern with period Λ we can simulate the relief formation on NML surface (Fig.1.12).

$$I(y) = I_{01} + I_0 \sin\left(\frac{2\pi}{\Lambda} y\right). \quad (1.6)$$

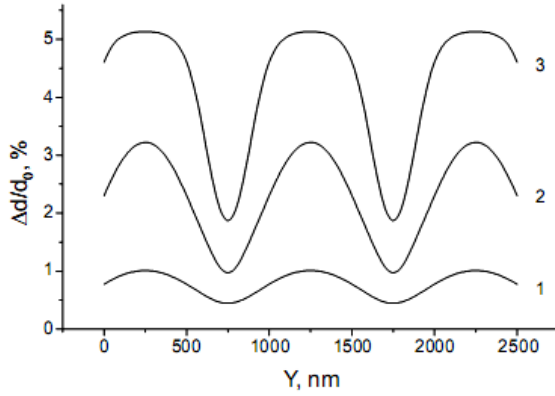


Fig. 1.12 Simulated relief profiles for hologram recording for: (1) 100 s; (2) 1000 s and (3) 4000 s [44].

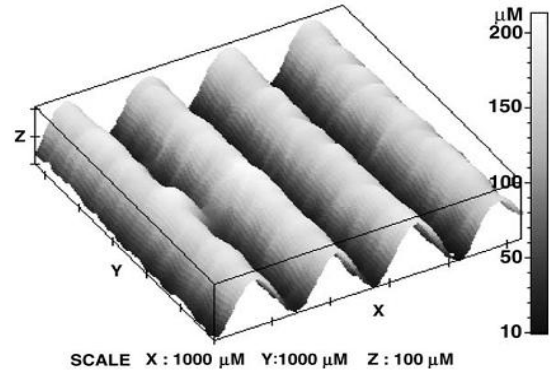


Fig. 1.13. Surface relief profile on a-Se/As₂S₃ multilayer [44].

For relief holograms, the highest diffraction efficiency is reached at 185 nm relief depth in reflection read out mode at He-Ne laser wavelengths. The holographic gratings reaching or even exceeding this modulation depth (see for example Fig. 1.13) could be recorded. The depth of the gratings is the product of the total thickness of the multilayer and the relative thickness change of a layer pair, which can be as large as 5%. Of course, the developed method and materials are not suitable for high-speed optical recording, but they are rather useful for direct one-step process of surface relief formation.

This model was developed for low-laser light intensities, when the layers are not heated during illumination and the diffusion coefficient depends linearly on light intensity. Further extension of this model takes into account the heating of the multilayer at high-intensity laser illumination and the corresponding non-linearities of the recording process.

In 1995, two groups independently reported surface-relief gratings inscribed in azo-containing polymer materials almost at the same time [45, 46]. In films of poly[4'-(2-acryloxy)ethylamino-4-nitroazobenzene] (pDR1A, Fig. 1.14a), SRG with a sinusoidal shape was recorded with an interference pattern of two light beams at 514 nm. The obtained grating structures were stable but could be erased by heating the polymer above its glass transition temperature. Multiple gratings can be simultaneously written and gratings can be overwritten. Using an epoxy-based

amorphous polymer containing azo side groups (Fig. 1.14b), SRG with relatively large amplitude was successfully inscribed with two laser beams at 488 nm. Furthermore, recording perpendicular gratings on the same film was also achieved. Such SRG in amorphous polymer films showed uniform and controllable morphologies, like the depth of relief, the grating periodicity, and so on. Moreover, more complicated topological surfaces were tailored by superimposing several surface-relief gratings.

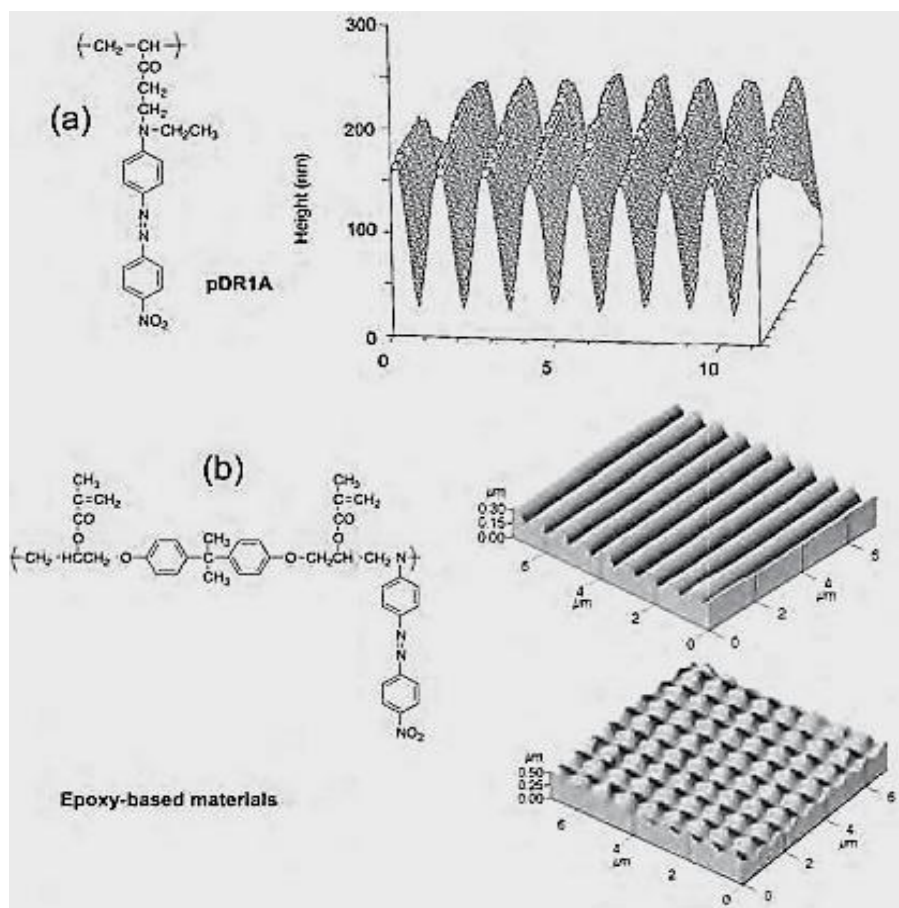


Fig. 1.14. Surface-relief gratings recorded in azo-containing amorphous polymer materials [45].

Chemically crosslinking of azo-containing polymer films with SRG could fix the obtained surface modulation, producing permanent shape change. The Raman-Nath hologram recorded in a thin film exhibited a theoretically maximum diffraction efficiency of about 34%. This was far lower than the Bragg-type hologram in a thick film with a maximum DE of 100%.

The polarization-selective multiple holographic data storage could be obtained using the photoinduced anisotropy as well as rewritable holographic recording with about 100% diffraction efficiency. These azo-dyed polymer materials prepared by a simple but balanced formulation would provide a new guideline for the construction of high-performance holographic devices.

b. Vector or polarization holography

In contrast to the conventional holographic process, in which intensity variations in an interference pattern between an object beam and a reference beam are recorded, polarization holography employs beams with two different polarizations for recording information. In this case, the polarization state of the resultant beam is recorded on a suitable medium.

Although interference is a traditional topic in physical optics, most literature in this field has only dealt with the interference of linearly polarized light. Generally, we cannot choose a common polarization for all the beams as we can for coplanar beams, where a polarization direction perpendicular to the common plane of all wave vectors may be used.

An interesting question concerns the case of the object and reference beams having different polarizations — in particular, orthogonal polarizations. Fresnel and Arago put forward a set of laws of interference of polarized light. These are the following:

1. Two linearly polarized waves in the same plane from the same coherent source can interfere; two waves that are orthogonally polarized cannot interfere.
2. Two waves that are derived from the same source and are orthogonally polarized can interfere if their polarizations are brought into the same plane.

The interference laws of Fresnel and Arago apply to the case of collinear beams. For non-collinear beams, the interference field is spatially modulated in the plane perpendicular to the bisectrix of the two beams. In the general case both the amplitude and the polarization of the resultant field are modulated.

A plane wave can be expressed as [47]

$$\mathbf{E} = E \exp[i(\mathbf{k}\mathbf{r} + \varphi_0)]\mathbf{e}, \quad (1.7)$$

where E ; \mathbf{k} ; φ_0 and \mathbf{e} are its real amplitude, wave vector, initial phase and the unit polarization vector (real for linear light or complex for circular one), respectively. In the interference of two beams with the same wavelength the intensity distribution is

$$I = E_1^2 + E_2^2 + 2E_1E_2|\mathbf{e}_1\mathbf{e}_2^*| \cos[(k_1 - k_2)r + \varphi_{10} - \varphi_{20} + \delta], \quad (1.8)$$

where

$$\delta = \arg\{\mathbf{e}_1\mathbf{e}_2^*\}. \quad (1.9)$$

The contrast of interference pattern is defined as

$$V = \frac{2E_1E_2|\mathbf{e}_1\mathbf{e}_2^*|}{E_1^2 + E_2^2}, \quad (1.10)$$

which is reduced to

$$V = |\mathbf{e}_1\mathbf{e}_2^*| \quad (1.11)$$

in the case of $E_1 = E_2$.

For a circular light propagating along z direction, if we define $kz - \omega t$ as the phase of the real wave function, and kz as that of the corresponding complex amplitude, the polarization vectors for the left and right circular lights can be written as

$$\mathbf{e}_L = \frac{1}{\sqrt{2}}(\mathbf{e}_x + i\mathbf{e}_y), \mathbf{e}_R = \frac{1}{\sqrt{2}}(\mathbf{e}_x - i\mathbf{e}_y) \quad (1.12)$$

respectively. When a circular light propagates along an arbitrary direction (α, β, γ) with $\cos \alpha$; $\cos \beta$; $\cos \gamma$ as its direction cosines in Cartesian coordinates, it is not difficult to find the expressions of the polarization vectors of the left and right circular waves,

$$\mathbf{e}_L = \frac{1}{\sqrt{2}} \begin{pmatrix} \sin \alpha \\ -\frac{1}{\sin \alpha}(\cos \alpha \cos \beta - i \cos \gamma) \\ -\frac{1}{\sin \alpha}(\cos \alpha \cos \beta + i \cos \gamma) \end{pmatrix}, \quad (1.13)$$

$$\mathbf{e}_R = \frac{1}{\sqrt{2}} \begin{pmatrix} \sin \alpha \\ -\frac{1}{\sin \alpha}(\cos \alpha \cos \beta + i \cos \gamma) \\ -\frac{1}{\sin \alpha}(\cos \alpha \cos \beta - i \cos \gamma) \end{pmatrix}. \quad (1.14)$$

Generally, we have

$$\mathbf{e}_L = \mathbf{e}_R^* \mathbf{e}_L \mathbf{e}_L^* = \mathbf{e}_R \mathbf{e}_R^* = 1 \mathbf{e}_L \mathbf{e}_R^* = \mathbf{e}_R \mathbf{e}_L^* = 0. \quad (1.15)$$

If one left circular light with direction cosines $(\cos \alpha_1; \cos \beta_1; \cos \gamma_1)$ interferes with another left circular light with $(\cos \alpha_2; \cos \beta_2; \cos \gamma_2)$, Eq. (7) leads to

$$|\mathbf{e}_{L1} \mathbf{e}_{L2}^*| = \frac{1}{2}(1 + \cos \theta), \quad (1.16)$$

where θ is the angle between k_1 and k_2 . Similarly, we can obtain

$$|\mathbf{e}_{R1} \mathbf{e}_{R2}^*| = \frac{1}{2}(1 + \cos \theta) \quad (1.17)$$

for the interference of two right circular waves, and

$$|\mathbf{e}_L \mathbf{e}_R^*| = \frac{1}{2}(1 - \cos \theta) \quad (1.18)$$

for the interference of a left circular light and a right circular light.

As a specific case, we investigate the parallel propagation of two circular beams. If the two beams travels in the same direction ($\theta = 0$), we have $|\mathbf{e}_{L1} \cdot \mathbf{e}_{L2}^*| = |\mathbf{e}_{R1} \cdot \mathbf{e}_{R2}^*| = 1$ and $|\mathbf{e}_L \cdot \mathbf{e}_R^*| = 0$; if they propagate in opposite direction ($\theta = \pi$), we have $|\mathbf{e}_{L1} \cdot \mathbf{e}_{L2}^*| = |\mathbf{e}_{R1} \cdot \mathbf{e}_{R2}^*| = 0$ and $|\mathbf{e}_L \cdot \mathbf{e}_R^*| = 1$. Consequently, we can conclude that only two circular beams with the same rotation can interfere in the former case and only two circular beams with the opposite rotation can do in the latter.

To compare the contrasts resulted from different combinations of two polarization states, we list all the results of the contrast V derived for two equal intensity beams in Table 1.1, where the combinations of s-s and s-p are also included for completeness, θ is the intersection angle of the two wave vectors.

Table 1.1. Contrast of interference pattern formed by two equal intensity beams.

Polarization combination	Contrast V
s-s	1
p-p	$ \cos \theta $
s-p	0
L-L or R-R	$(1 + \cos \theta)/2$
L-R	$(1 - \cos \theta)/2$
s-L or s-R	$1/\sqrt{2}$
p-L or p-R	$ \cos \theta /\sqrt{2}$

In Fig. 1.15 it is shown the variation of V in different cases within a range $0 < \theta < \pi$. The unique feature of the circular light interference is that its contrast depends only the intersection angle of the two beams (for the equal intensity case), whereas the contrast with two linear waves is also relative to the choice of polarization direction of each beam.

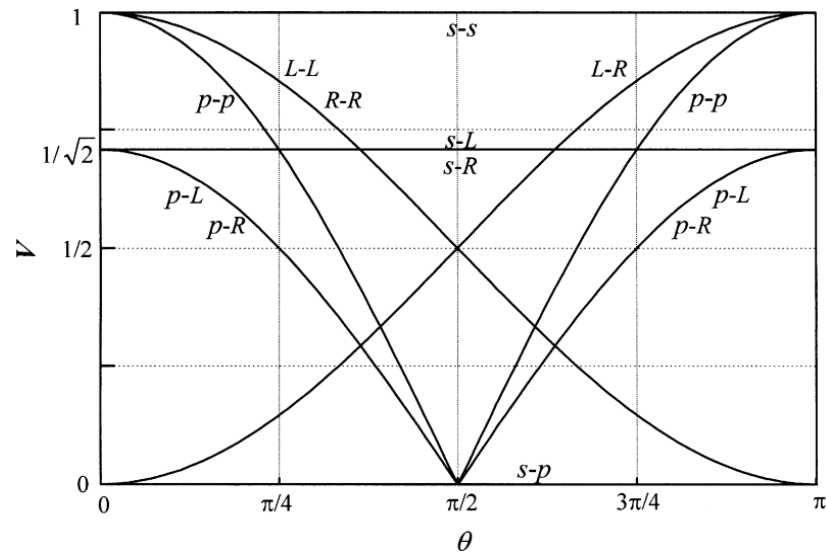


Fig. 1.15. Comparison of the contrasts resulted from different combinations of polarization states of two beams [47].

The other important conclusion consists in differences of ± 1 diffraction orders. When we use the reference beam with linear polarization the ± 1 diffraction orders are identical. But if the polarization of reference beam is circular, the states of polarizations of the ± 1 diffraction orders are different.

Conventional recording materials are sensitive only to light intensity. Exposed to such an interference pattern they would be uniformly darkened or bleached and there would be no diffraction

from them at the reconstruction stage. In order to make use of the polarization modulation it is necessary to use a recording material that has a different response when exposed to light with different polarizations and can record the information about the polarization. Such materials are called photoanisotropic materials. When exposed to polarized light they become optically anisotropic and their anisotropy is in accordance with the type and the direction of light polarization.

The main attention has been paid to the results of studying the properties of ChG with the domination of effects of photo-stimulated linear reversible birefringence [48–51], and dichroism [52–53], polarization-sensitive light-induced material transport [54–55]. We consider that usually interpreted as the scalar photoexpansion effect, it closely attaches to the above vectoral phenomena in whose dynamical changes the reversible and non-reversible components were definitely distinguished.

The main challenge in [56] is to obtain as pure as possible polarization gratings recorded with two waves of orthogonal circular polarizations (R-L) configuration. It may be easily imagined, that while there is no intensity modulation in the interference pattern of two recording beams in (s-p) configuration, it is always present in (R-L) and (45° – 135°) cases. The amplitude of this modulation increases with the increase of the cross-section angle of recording beams. In this paper [56] it is examined this problem and present the results of the experimental study of vector grating inscription in a-As₂S₃ thin films (5 and 9 μm thick) in various key recording configurations using two beams of orthogonal polarizations, i.e., (s-p), (45° – 135°) and (R-L). The main particularity of the approach is the complete photodarkening of these films to saturate all metastable scalar structural changes prior to inscription of the vector gratings.

The absorption coefficient of the films is $\alpha \sim 10^3 \text{ cm}^{-1}$ at 514.5 nm. The polarization gratings were recorded using a standard holographic setup. The Ar⁺- ion laser (operating at 514.5 nm) beam was expanded (diameter $\sim 1 \text{ cm}$) before the beam splitter to ensure a homogeneous gratings strength over the examined region. The angle between the recording beams was set to $\sim 1^\circ$, resulting in a grating period of $\sim 30 \mu\text{m}$. A He-Ne laser beam (operating at 632.8 nm) was used as a probe to characterize the inscribed gratings.

It is well known that the intensities of the ± 1 diffracted orders from a grating recorded in (R-L) configuration must always have mutual orthogonal circular polarizations (regardless of the reading beam polarization) if the grating is purely vectoral. There may be only an exchange of energy between the ± 1 orders, corresponding to the variation of the polarization state of the probe beam, their total intensity being conserved. In the case of a pure polarization grating, one of the diffraction efficiencies becomes zero (corresponding to the right or left circular polarization of the incident probe) while the other one is at its maximum (see the theoretical curve in the inset of Fig.

1.16). Accordingly, the analysis of the polarization states of the diffracted orders of a (R-L) recorded hologram reveals its degree of purity. The first indication of this phenomenon in the experiment was the noncircularity of the polarizations of ± 1 diffracted orders.

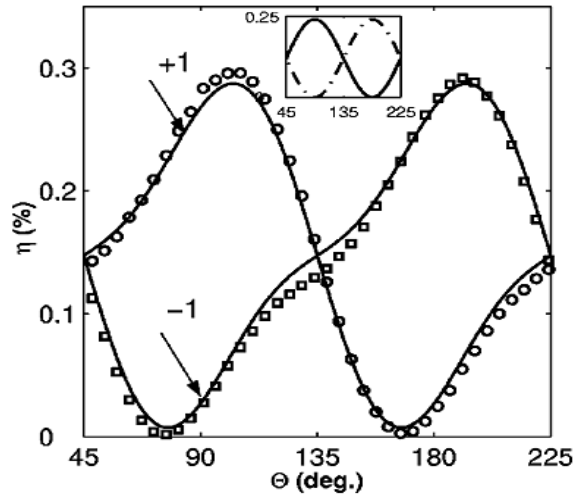


Fig. 1.16. DE of +1 and -1 diffracted orders as a function of the angle of rotation of the quarter wave plate (to change the ellipticity of the incident probe beam polarization). Film thickness $29 \mu\text{m}$, $I_{\text{total}} \sim 42 \text{ mW/cm}^2$, exposure time 20 min. The solid lines are theoretical simulation (photoinduced anisotropy $\Delta n = 1.1 \times 10^{-3}$, inherent to $\text{a-As}_2\text{S}_3$, and $\Delta d = 22 \text{ \AA}$). The inset represents the case of a pure vector grating [56].

In Fig. 1.16. the dependence of the DE of ± 1 diffraction orders on the angle of rotation of a quarter wave plate is presented, the recording beam intensity and time of exposure being 42 mW/cm^2 and 20 min, respectively. As one can see the experimental curve is deformed with respect to the theoretical one for a pure vector grating (inset in Fig. 1.16). Particularly the maxima and minima of opposed diffraction orders are shifted with respect to each other.

The non purity of the recorded the vector grating can originate from different factors such as the creation of a superimposed undesirable scalar grating, the inhomogeneity of the inscribed vector grating in the film, or some multibeam interference effects. To clarify this the authors studied the kinetics of the vector grating recording and its optical erasure with a single Ar^+ - ion laser beam, referring to the known perfect reversibility of photoinduced anisotropy in these materials. The results of this observation in the (R-L) recording configuration for $I_{\text{total}} = 350 \text{ mW/cm}^2$ are presented in Fig. 1.17a. For (45° – 135°) recording conditions it was obtained very similar results to the (R-L) case and do not present them here. As one can see, the complete erasure of the recorded gratings appears not to be achievable in these configurations. Moreover, the post-erasure residual diffraction efficiency increases after each recording — erasure cycle. The same results were obtained at

significantly smaller intensities (42 mW/cm^2) and for longer recording times (approximately for the same exposures) in the same recording configuration.

The authors [56] have also performed a grating recording in (s-p) writing condition. As one can see from Fig. 1.17b, the vector grating in this case can be erased completely with one Ar^+ -ion laser beam even after multiple recording–erasure cycles, which is consistent with previous results. These experiments clearly indicate that the main reason of the non purity of recorded vector gratings in (R-L) and (45° – 135°) configurations is their complexity, namely, the creation of an additional scalar (volume or surface) modulation, which can not be erased with uniform Ar^+ -ion laser beam.

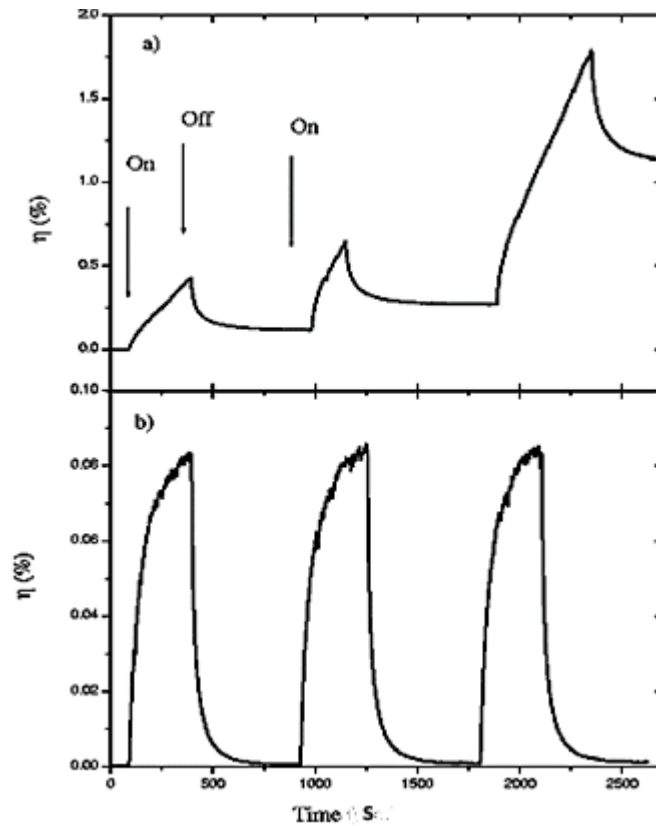


Fig. 1.17. Time dependence of the first-order diffraction efficiency ($\eta = \eta_{+1} + \eta_{-1}$) in (a) (R-L) and (b) (s-p) recording configurations during three record and erase cycles in a $5 \mu\text{m}$ -thick prephotodarkened film of a- As_2S_3 ; $I_{\text{total}} = 350 \text{ mW/cm}^2$ [57].

To check out whether the origin of the scalar modulation was linked to the residual intensity modulation in the interference pattern (due to the non ideal orthogonality of recording beams in (R-L) and (45° – 135°) cases) it is performed a holographic recording with two s-polarized beams with the same recording intensity $I_{\text{total}} = 350 \text{ mW/cm}^2$, exposure and pre-exposure (for prior photodarkening). It is observed only a negligible transient diffraction due to the transient photoinduced scalar structural changes. This confirmed that a complete photodarkening of the

films had indeed been achieved. Thus the residual intensity modulation was not responsible for the unwanted scalar modulation. A surface relief modulation at significantly higher intensities (focused recording beams) was observed in chalcogenide thin films and was attributed to the electric field gradient force [57]. The electric field gradient on the film appears to be non zero in the direction of the grating vector in the (R-L) and (45° – 135°) configurations. This electric field component is not zero in the (s-p) configuration as well, but it is not varying in the direction of the grating vector, hence the gradient of the electric field component is zero. The AFM profile analysis of the samples revealed the creation of a surface relief modulation. For example, the amplitude (peak to valley) of such modulation in the above-described experimental conditions was measured to be about 20\AA . The biasing effect of such a modulation on the efficiency curve was computed theoretically and is shown as a solid line in Fig. 1.16. The excellent coincidence of experimental and theoretical curves is good evidence that even such a small surface relief modulation of As_2S_3 films can significantly perturb the polarization selectivity of the inscribed vector gratings. It is believed that the origin of the surface relief modulation in this case also may be resulting from the same electric field gradient force as in [57].

c. Digital holography

Digital holography (DH) is an emerging technology of new paradigm in general imaging applications. By replacing the photochemical procedures of conventional holography with electronic imaging, a door opens to a wide range of new capabilities. In DH, the holographic interference pattern is optically generated by superposition of object and reference beams, which is digitally sampled by a CCD camera and transferred to a computer as an array of numbers. DH offers a number of significant advantages, such as the ability to acquire holograms rapidly, availability of complete amplitude and phase information of the optical field, and versatility of the interferometric and image processing techniques. Indeed, DH by numerical diffraction of optical fields allows imaging and image processing techniques that are difficult or not feasible in real-space holography.

The propagation of optical fields is completely and accurately described by diffraction theory, and in 1967, Goodman and Lawrence demonstrated the feasibility of numerical reconstruction of an image from a Fourier hologram detected by a vidicon camera [58]. Schnars and Jueptner, in 1994, were the first to use a CCD camera directly connected to a computer as the input, and compute the image in a Fresnel holography setup [59]. In what is now called DH, holographic interference is produced by optical processes in real space, while reconstruction is by numerical computation. In CGH the hologram can be produced by numerical computation

inside a computer, followed by printing or other outputs to real space [60]. Reconstruction is then carried out by optical means.

By direct electronic recording of holographic interference and because of the increasing speed of holographic computation, real-time holographic imaging is now possible, and more importantly, the complete and accurate representation of the optical field as an array of complex numbers allows many imaging and processing capabilities that are difficult or infeasible in real-space holography [61]. Direct access to the phase information leads to quantitative phase microscopy with nanometer sensitivity of transparent or reflective phase objects, [62] and allows further manipulations such as aberration correction [63].

DH naturally evolved from the effort to utilize electronic imaging in interferometry, such as in Electronic Speckle Pattern Interferometry (ESPI) [64]. Metrology of deformations and vibrations is a major application area of DH [65]. Optical processing, such as pattern recognition and encryption, by DH also offers new capabilities [66].

The developments of SLMs during the last three decades have boosted the technology of computerized holography. SLMs can function in different ways within holographic systems: input data displays for holographic memory storage; holographic displays of CGH, a means to synthesize CGH by iterative algorithms; a spatial phase modulator for a phase shifting process in a DH recorder.

SLM can display different kinds of DOE, what is impossible by using common ROE. In work [67] Fresnel incoherent correlation holography was implemented with two focal length diffractive lenses on a SLM. Improved image resolution over single lens systems and at wider bandwidths was observed. For a given image magnification and light source bandwidth, this holographic method with two lenses of close focal lengths yields a better hologram in comparison to a single diffractive lens used. The improved quality of the hologram results from a reduced optical path difference of the interfering beams and increased efficiency.

The other aspects, which unite ChG and AP, are sensitivity not only for laser but e-beam actions and the ability of direct surface deform under these irradiations. The phase relief may be complemented by the change of the thickness, i.e. by geometrical surface relief formation directly during the e-beam recording or afterwards by selective chemical etching. The last process is widely used nowadays for ChG photoresists, fabrication of molds, holographic gratings, and integrated optical elements. The direct relief formation without etching or ablation is possible due to the known effect of light/e-beam stimulated volume expansion or contraction, but usually the relative volume changes less than 1% and the spatial resolution is limited by the diffraction. Appreciably larger surface deformation effect is observed due to the light/e-beam stimulated mass transfer in ChG and AP films [38].

E-beam recording is a high-resolution technology to generate custom-made DOEs. It utilizes an intense and uniform electron source with a small spot size, high stability, and long life. The main attributes of e-beam technology are as follows: (1) it is capable of very high resolution; (2) it works with a variety of materials and patterns; (3) it is slow compared to optical recording; and (4) it is expensive. Combined with reactive ion etching, creation of DOEs with very fine resolution and high efficiency is possible.

A typical e-beam machine is capable of generating a beam with a spot size around 10 nm. Therefore, it is capable of exposing patterns with lines of widths less than 0.1 μm or 100 nm. For binary phase DOEs, each square aperture has a size of approximately 1 $\mu\text{m} \times 1 \mu\text{m}$. For such feature sizes around, a total pattern size of 1 $\mu\text{m} \times 1 \mu\text{m}$ can be achieved, while maintaining high resolution. Larger patterns are generated by stitching together a number of such patterns under interferometric control.

1.3. Studying methods

a. Raman and Optical spectroscopy

Raman spectroscopy permits to investigate the structure of amorphous materials through measurements of lattice vibration modes. In principle, each Raman scattering peak can be associated with a vibration of a specific structural unit. This intrinsic nano-probing makes Raman spectroscopy very sensitive to short and medium-range structures — including in glassy materials, and offers a “bottom-up” approach to nanostructured materials that comes as a good complement to methods like the transmission electron microscopy or x-ray diffraction. However, studies on nano-chalcogenides are still at an early stage and need to be further extended to cover more ChGs, which is due to the primary remarkable results obtained in their nanostructure forms.

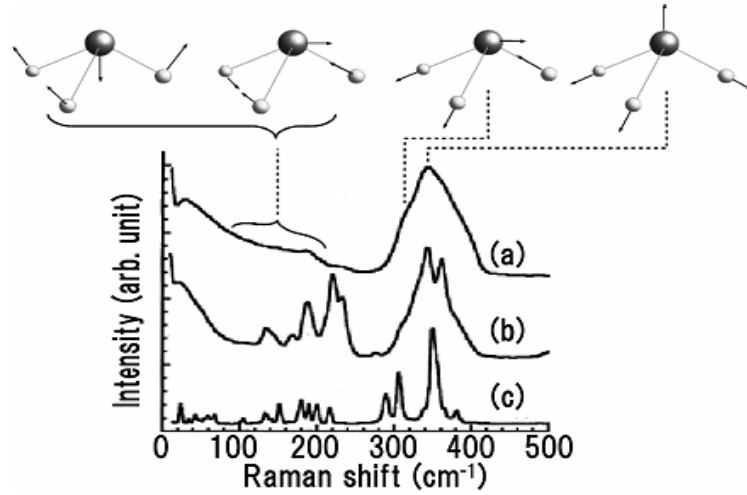


Fig. 1.18. Raman scattering spectra of (a) glassy, (b) as-evaporated, and (c) crystalline As_2S_3 . Responsible vibrational modes are shown for (a) [30].

Raman scattering spectroscopy becomes experimentally more useful, due to the recent progress of lasers and imaging detectors at visible to near-infrared wavelengths. We can obtain not only the conventional Raman scattering spectra in short exposure times for small probe areas ($\sim 1 \mu\text{m}$), but also resonant and nonlinear Raman scattering spectra.

Infrared and Raman spectroscopy measure the intensity and frequency (wavenumber) of vibrational modes. As known, the frequency is written as $\omega \sim (\kappa/M)^{1/2}$, where κ is the force constant of a spring connecting a pair of atoms (or atomic units) and M is the atomic mass. Accordingly, the peak frequency gives insight into the vibrational mode, which is an optical phonon in crystals or a molecular vibration in disordered materials, e.g., vibrations of $\text{AsS}_{3/2}$ in As_2S_3 , as shown in Fig. 1.18 [30].

As an example, Fig. 1.18 shows Raman scattering spectra of glassy, as-evaporated, and crystalline As_2S_3 . The broad and relatively sharp spectra of the glass and the as-evaporated film suggest that these are cross-linked and molecular, respectively [68].

Direct and indirect experimental studies suggest that the short-range ($\leq 0.5 \text{ nm}$) structure of a glass is similar to that in the corresponding crystal [29]. An example for Se is summarized in Table 1.2, where Z is the atomic coordination number, r the bond length, θ the bond angle, Φ the dihedral angle, ρ the density. The coordination number Z seems to satisfy the so-called 8-N rule [70], where N is the atomic group number in the previous crystal form, with an accuracy of $\sim 10\%$, which may reflect experimental uncertainty and effects of dangling bonds. The bond distance r is fixed with an accuracy of $\Delta r/r \approx 1\%$. The bond angle also shows a similar result in Se.

Table 1.2. Comparison of atomic parameters in c-Se (hexagonal) and g-Se (glass).

	Z	r (nm)	θ	Φ	ρ (g/cm ³)
Hex Se	2.0	0.23	105°	102°	4.80
g-Se	2.0 ± 0.04	0.23 ± 0.002	105±0.5°	70–110°	4.25

For alloys (Table 1.3), it seems difficult to accurately determine the bond angle, which distributes roughly at $\Delta\theta/\theta \approx 5 - 10\%$, where θ is the angle for a group VIb atom. Note that the angle is not uniquely fixed even in the crystal, which contains different kinds of atomic units. On the other hand, experiments show that the cation angle, such as S-As-S, is more tightly fixed due to steric (the spatial arrangement of atoms in a molecule) restrictions. In short, there exists the short-range structural order in glasses. This result suggests that an energetic equilibrium is satisfied in the short-range scale.

In more detail, there exist some variations in the short-range structures. First, the coordination number, which is a direct consequence of the electron configuration s^2p^4 of the group VIb atoms, is modified when ionic and metallic characters are added. The metallic effect is appreciable in tellurides. Second, the bond length r increases in proportion to the period (2–5) in the periodic table, e.g., from 0.12 to 0.29 nm in the elements (Table 1.3), in accordance with the atomic size. Third, and which should be underlined, the bond angles are appreciably different between the oxide and the chalcogenide. As listed in Table 1.3, it is $\sim 130^\circ$ in As_2O_3 and $\sim 100^\circ$ in $\text{As}_2\text{S}(\text{Se}, \text{Te})_3$, which may be approximated very roughly to 180° (ionic) and 90° (covalent). These characteristic angles are favorable to produce the so-called corner-shared and edge-shared configurations, which will be connected to the medium-range structure. The short-range structure is determined by the chemical bonding, and accordingly, the existence of structural orders is plausible.

Table 1.3. Bond lengths (in nm) and bond angles around the VIb atoms (in parentheses) in the VIb elemental materials (O, S, Se, and Te) and amorphous $\text{As}_2\text{O}(\text{S}, \text{Se}, \text{Te})_3$ and $\text{GeO}(\text{S}, \text{Se}, \text{Te})_2$ compositions. The bond angle in a- GeTe_2 is unclear.

	O	S	Se	Te
Elemental	0.12 in O_2	0.21 (106°)	0.23 (105°)	0.29 (103°)
As-	0.18 ($\sim 130^\circ$)	0.23 ($\sim 100^\circ$)	0.24 ($\sim 105^\circ$)	0.27 ($\sim 90^\circ$)
Ge-	0.18 ($\sim 105^\circ$)	0.22 (80–110°)	0.24 (80–100°)	0.26 (?)

The more and more emerging evidences about this non-random scenario of the creation of complex networks are moving the view of the amorphous state far from the traditional continuous random network approach [71]. Novel experimental techniques, as modulated differential scanning calorimetry, and also novel theoretical approaches [72], are currently being applied to glass research, and they are throwing light on intriguing features occurring in the glass and liquid state. The current view points to size increasing cluster approximations to explain the origin of the glass transition temperature of glass alloys [73], as well as the appearance of first-order transitions in its compositional dependence, which, to some extent, could remind the rich-club ordering phenomenon happening in complex networks.

Photoinduced metastabilities occurring in recording media are strongly affected by thermal relaxation processes (the so-called aging), and this reduces the working life of any functional structure recorded in them [73, 74]. Such a drawback is deeply related to the sequential nature of the traditional sequential approaches followed in optical recording applications, as recording is performed in an already conformed, and in turn constrained, material medium. In addition, these traditional approaches find limitations to exploit volume holographic functionalities, as the attenuation of the light intensity along the recording medium thickness, according to the Beer-Lambert law: $I(z)=I_0\exp(-\alpha z)$; $I(z)$ being the light intensity at depth z , I_0 the incident intensity and α the absorption coefficient, which seriously reduces the effective thickness of any structure optically recorded in the material [73]. The above introduced drawbacks for recording media to efficiently exploit volume holography performances could be overlaid by concurrent material exposure to external potentials (light) during its conformation.

Transmission optical spectrum of $\text{As}_{12.6}\text{Ge}_{23.8}\text{S}_{63.6}$ film is presented in Fig. 1.19 along with computer drawn envelopes. There is broad transparency region at long wavelengths and significant drop of transparency in the region of 400–600 nm due to the increase of absorption.

Spectral dependence of refractive index calculated together with films thickness by Swanepoel method [76] is given in the Fig. 1.20. Solid line corresponds to the least squares fitting of this dependence to the function

$$n(\lambda) = a/\lambda^2 + c \tag{1.19}$$

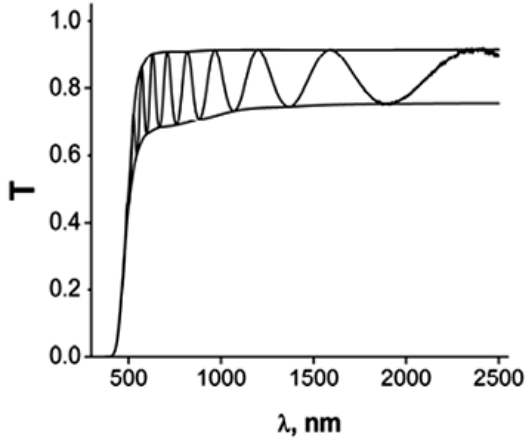


Fig. 1.19. Transmission spectrum of $\text{As}_{12.6}\text{Ge}_{23.8}\text{S}_{63.6}$ thin film provided with computer drawn envelopes [77].

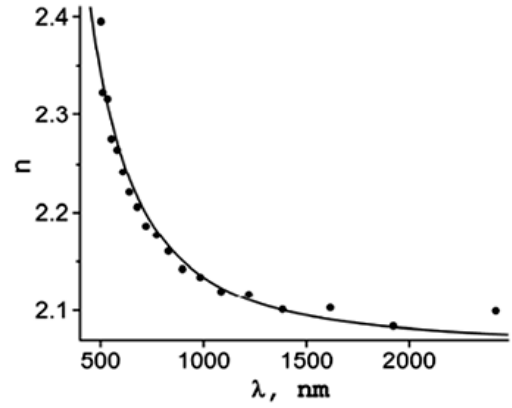


Fig. 1.20. Spectral dependence of the refractive index of $\text{As}_{12.6}\text{Ge}_{23.8}\text{S}_{63.6}$ thin film determined by Swanepoel method [77].

Spectral dependence of refractive index can be well described by single oscillator model [77]. According to this model refractive index is related to energy of incident photon by equation

$$n^2 - 1 = \frac{E_d E_0}{E_0^2 - E^2} \quad (1.20)$$

where E_0 is single oscillator energy, E_d is dispersion energy. In this expression E_0 determines the position of effective oscillator connected with average energy gap; E_d is the dispersion energy characterizing the strength of inter band transitions.

To obtain E_0 and E_d we plotted dependence

$$(n^2 - 1)^{-1} = f(E^2) \quad (1.21)$$

at the points corresponding to the extremes on the transmission spectrum and then performed least squares fitting to the straight line (see Fig. 1.19). It can be seen that points corresponding to maximum photon energy were dropped out from the straight linear dependence, therefore they were excluded from consideration during evaluation E_d and E_0 parameters.

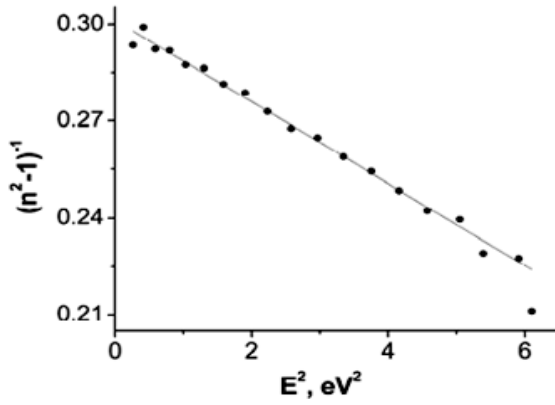


Fig. 1.21. Transmission spectrum of $\text{As}_{12.6}\text{Ge}_{23.8}\text{S}_{63.6}$ thin film provided with computer drawn envelopes [77].

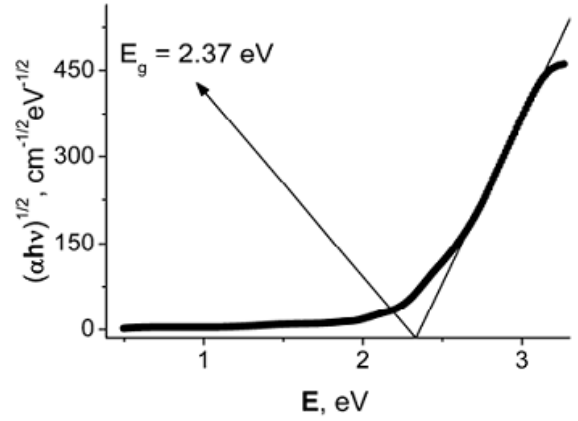


Fig. 1.22. Determination of optical band gap, E_g , of $\text{As}_{12.6}\text{Ge}_{23.8}\text{S}_{63.6}$ thin film from Tauc plot [78].

Optical band gap E_g was also determined. It can be obtained either from Tauc law, $(\alpha\hbar\omega)^{1/2} = f(E)$, or using dependence $\alpha = f(E)$. In paper [78] it was stated that difference in value E_g would be up to 10–20% from one method to another. For the present type of materials one should prefer Tauc law [78]. In Fig. 1.22 the energy dependence of $(\alpha E)^{1/2}$ parameter is plotted. Linear range in the region of high photon energies corresponds to the Tauc law. Energy band gap is the point where this line intersects with abscissa (see Fig. 1.23).

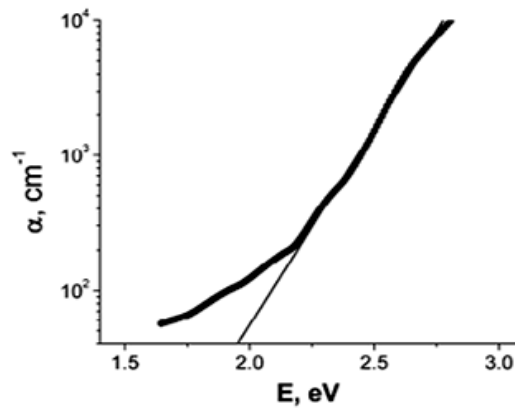


Fig. 1.23. Urbach absorption tail of $\text{As}_{12.6}\text{Ge}_{23.8}\text{S}_{63.6}$ thin film [78].

In Fig. 1.23 the absorption coefficient (in logarithmic scale) versus incident photon energy is plotted. Almost linear region where absorption coefficient ranges from $2 \cdot 10^2$ to $5 \cdot 10^3 \text{ cm}^{-1}$ obeys Urbach's law:

$$\alpha(E) = \alpha_0 \exp\left(\frac{E}{E_c}\right) \quad (1.22)$$

Exponential absorption edge of chalcogenide glassy alloys with sulphur in the region of topological transition is studied in [79]. It is shown that the slope of the tail depends on mean

coordination number and stoichiometry of ChG materials. Results are presented of absorption edge investigations of $\text{AsS}_{1.5}\text{Ge}_x$ amorphous films ($0 \leq x \leq 2$) at temperatures of 110, 300, 370, and 420 °C. An effect of low-temperature annealing on the optical parameters of the films has been observed. The annealing causes a shift of the absorption edge to the higher energy region and an increase of the optical gap of the samples. Electron diffraction examining indicated that the films were in the amorphous state both before annealing and after it. The functional dependence of the absorption edge on photon energy has been found. In the range of the photon energy $h\nu < E_g$ the absorption edge can be described by an exponential function and in the range of $h\nu > E_g$ by a quadratic function of the photon energy. When the temperature varies the slope of the exponential absorption edge does not change, but the edge is shifted with temperature to the lower energy region. The values of the temperature coefficient of the absorption edge shift are $(-4 \text{ to } 8) \times 10^{-4}$ eV/deg. The gap E_g of $\text{AsS}_{1.5}\text{Ge}_x$ amorphous films ($0 \leq x \leq 2$) determined at room temperature by optical methods lies in the range 2.4 to 1.5 eV. The shape of the absorption edge of the films under investigation and its temperature dependence are in accordance with the data obtained on glasses with a simpler chemical composition.

b. Digital holographic microscopy

A basic DHM setup consists of an illumination source, an interferometer, a digitizing camera, and a computer with necessary programs. Most often, a laser is used for illumination with the necessary coherence to produce interference. There are also low-coherence techniques for the purpose of reducing speckle and spurious interference noise, or generating contour or homographic images.

Increasing the optical resolution is still a declared goal in microscopy. According to Abbe's famous theory the limiting factors for the maximally achievable resolution, and thus the largest meaningful magnification, are directly related to the wave properties of light.

Apart from resolution, image contrast represents another frontier, where efforts are being made to advance optical imaging. Many biological samples typically do not contain a substantial amount of natural pigments, which makes them phase objects rather than amplitude objects.

A variety of techniques has been developed in the imaging internal layers of specimens, like optical sectioning techniques such as confocal microscopy. In parallel, scan-free methods like DHM have been introduced to extract the object wave-front leading to a multilayer image of a specimen via digital refocusing and quantitative phase (topographic) image [80]. One of the major issues in imaging the internal structures of nonorganic and biological specimens is the absorption and scattering that distort the information coming from the object. However, in the ma-

jority of cases, neither the specimen satisfies the weak scattering approximation nor is the prediction of the scatterer distribution possible to create the corresponding model.

In many applications staining the sample might not be feasible. Hence, label-free 3D microscopy methods have been also developed based on auto-fluorescence or scattering properties, like optical projection tomography [81] and methods based on Raman scattering [82]. Dark-field technique has been shown to be promising in improving the image contrast for internal layers in combination with digital holographic refocusing [83].

Being a wide-field scan-free method, DHM showed to be promising in monitoring live biological processes [84] and in 3D tracking of particles with video rates [85]. Despite all these developments, label-free wide-field microscopy is still suffering from unwanted scattering and absorption from the out-of-focus structures, which are inhomogeneously distributed inside an object, especially in sub-millimeter sized biological organisms.

The off-axis DHM allows the extraction of both amplitude and phase information for a wave diffracted by a specimen from a single hologram [86]. The phase information provides 3D quantitative mapping of the phase shift induced by microscopic specimens with a resolution along the optical axis (axial resolution) better than 1° . Thanks to the performance of PC and progress in digital image acquisition, DHM currently provides cost-effective and easy-to-use instruments with high acquisition rates (camera limited) for real-time measurements and quality control in production facilities.

In a general context, DHM technology has been successfully applied for numerous operating modes, for instance, tomography on a biological sample performed with wavelength scanning [87], investigation of the polarization state of an object by use of two orthogonally polarized wavefronts [88] and multiple-wavelength interferometry of dynamic systems [89].

c. Digital holographic interferometry

Choosing DOE studying methods, we focus on computational optical methods, by which we mean the creation of digital information from electromagnetic radiation with optical wavelengths ranging. This computational sensing is revolutionizing the design and utility of optical imagers.

The main opportunities of digital imaging include the following:

Image metrics. It can improve depth of field, field of view, spatial resolution, spectral resolution, signal fidelity, sensitivity, and dynamic range. Digital systems to the time of this writing often compromised image quality to obtain the utility of digital signals, but over time digital images will increasingly exceed analog performance on all metrics.

Multidimensional imaging. The goal of multidimensional imaging system is to reconstruct a digital model of object in their native embedding spaces. Conventional 2D images of 3D objects

originate in the capacity of lens and mirror systems to form physical isomorphism between the fields on two planes. With the development of digital processing, tomographic algorithms have been developed to transform arrays of 2D images into digital 3D object models.

Object analysis and feature detection. The aim of object analysis is to abstract nonimage data from a scene. Sensors enable completely automated tasks, such as robotic positioning and control, biometric recognition, and human-computer interface management. Current systems emphasize heuristic analysis of images. Integrated design allows direct measurement of low-level physical primitives, such as basic object size, shape, position, polarization, and spectral radiance.

Image compression and analysis. The aim of image compression is to represent the digital model of an object as compactly as possible. As with multidimensional imaging and object analysis, current compression algorithms assume a 2D focal model for objects. Current technology seeks a compressed linear basis or a nonlinear feature map capable of efficiently representing a picture. Integrated analog and digital design implements generalized bases and adaptive maps directly in the optical layer.

Sensor array data fusion and analysis. Multiaperture imaging is common in biological systems but was alien to artificial imaging prior to the computational age. Modern computational systems will dramatically surpass the multiaperture capabilities of biology by fusing data from many subapertures spanning broad spectral ranges.

In the former optical holographic interferometry, the interference patterns have been generated by double exposure, realtime, or stroboscopic methods. Now in the digital case we have direct access to the phase distribution of e. g. a diffusely reflecting surface without going over the intensity. If we have the two numerically reconstructed wave fields $b_1(n,m)$ and $b_2(n,m)$ of a surface before and after deformation, the phase difference is calculated pointwisely by

$$\Delta\varphi(n,m) = \arctan \frac{\text{Im}\{b_2(n,m)b_1^*(n,m)\}}{\text{Re}\{b_2(n,m)b_1^*(n,m)\}} \quad (1.23)$$

with values between $-\pi$ and $+\pi$. Since it is generally known which field belongs to the state before, and which one to the state after the deformation, there is no sign ambiguity in $\Delta\varphi$ as would be the case when evaluating an intensity distribution. In this way the three interference phase distributions of 0 are generated [90]. They belong to an aluminum plate clamped at all four sides and which Fig. 1.24(a) was pressed from behind, Fig. 1.24(b) was shifted laterally, and Fig. 1.24(c) was simultaneously pressed and shifted.

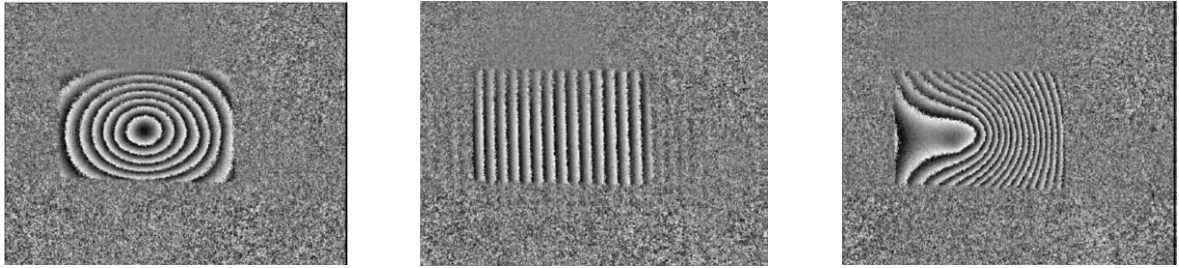


Fig. 1.24. Interference phase distributions of aluminum plate a) pressed from back side, b) shifted laterally, c) pressed and shifted [90].

Digital holographic interferometry not only is used for deformation measurement in experimental stress analysis or nondestructive testing, but also for form determination, vibration analysis, or measurement of refractive index variations and has found numerous applications in metrology [91].

1.4. Application of diffractive structures based on chalcogenide glasses multilayers and azo-dyed polymers films

A fundamental research of all-optical or direct recording techniques provides a wide range of possible applications, such as the nano-/micropatterning of surfaces, as well as applications for the production of various-purpose optical elements. The demand for lower cost surface relief based optical instruments such as grating-based resonators or filters for waveguides, diffractometers, spectrometers, and so forth is one of the main driving forces for the investigation of a direct light induced relief formation. The obtained micro- and nanosurface patterns have already been demonstrated as optical polarizers, angular or spectral filters, optical transmission devices, data storage devices, and even photonic crystals. They are also used in the production of tunable lasers, where the wavelength can be varied and depends on the geometrical parameters of gratings. Additionally, this processing technique will continue to improve the performance of materials in existing applications and will open the door to new materials and novel applications that would not be easily achievable through other means.

DOE can be approximated as holograms of point sources or collimated beams of light, such that light from one source is imaged onto the other. Optical elements such as lenses, beam splitters, diffraction gratings and filters can be produced by holographic imaging, digital and analog. These DOE have the advantage of being low cost (due to their simple design, small size and light weight) and are easily reproducible by embossing polymer materials. DOE can duplicate most of the functions provided by glass optics if optical system operates over narrow spectral bandwidth or requires chromatic dispersion. Some of the unique functions of DOE are multiple

function optics, independent of substrate shape, large optical apertures, lightweight and narrow spectral response. DOE have realized certain optics that could not be produced with previous optical technologies. Areas such as optical sensors, optical interconnect, optical information processing, fiber optics, optical scanners, optical disc pick up heads and solar concentrators have benefited from the use of DOE [92].

Security holograms offer a unique solution to product and document counterfeit providing unambiguous visual authentication that requires no external device or reader for verification. To be successful, security features for the public need to be easily recognisable and authenticated, yet be extremely difficult to copy by commonly available technologies. They need to be leading-edge yet user friendly. The use of small holograms in credit cards, which are made to prevent falsification, has made holograms a well known concept. Holograms show up more and more often on tickets and original covers. Important areas of application are bar-code readers in shops, warehouses, libraries and so on, which is based on holographic components like optical gratings.

In the aircraft industry head-up displays are an important example of holographic technology. It helps the pilots so they do not need to look down onto the instrument panels, because the instruments are projected onto the windscreen with the help of holographic technology, and thus make flying easier.

The unique advantage of holographic interferometry arises from the fact that holography permits storing a wavefront for reconstruction at a later time. Wavefronts which were originally separated in time or space, or even wavefronts of different wavelengths, can be compared by holographic interferometry. As a result, changes in shape of quite rough surfaces can be studied by interferometric precision.

One of the most important applications of holographic interferometry is non-destructive testing. It visually reveals structural faults without damaging the specimen. Holographic interferometry has also proved its utility in aerodynamics, heat transfer, and plasma diagnostics etc.

Diffraction optics finds its application in medicine also. Doctors use three-dimensional holographic scans to make measurements without invasive surgery. This technique is also used in medical education. Holographic interferometric techniques have been widely applied with success for the study of different parts of human body including cornea, tooth mobility, tympanic membrane, basilar membrane, joint, chest, and bones. Endoscopic holography is a powerful tool for non contact high resolution imaging and nondestructive measurements inside the natural cavities of human internal organs. This technique can be used for cellular structure analysis and may even substitute biopsy in tumor diagnosis.

Today there are hundreds of potential real world applications for diffractive optics and it has far surpassed being limited only to the realm of art, although it is hard to deny that indeed art is an excellent application. DOE has been used to make archival recordings of valuable and/or fragile museum artifacts. Holography has been used by artists to create pulsed holographic portraits as well as other works of art.

Polarization diffraction gratings were shown to be useful elements for the fabrication of polarization-discrimination systems. Indeed, from theoretical considerations it follows that pure polarization gratings can be used for the measurement of Stokes parameters and can serve as an essential constituent of a spectropolarimeter. Such holographic elements are less sensitive to angular change of the incident beam and more compact compared with the conventional polarizing systems based, for example, on the natural crystal birefringence.

Nanostructures (for instance multilayer structure chalcogenide films) with sub 15 nm dimensions have attracted significant interest due to their potential applications in nanofabrication for the next generation of electronic devices, photoluminescence, bio-light emission devices, and solar cells. Also, another interesting application could be the development of all-optical memory using photo-induced optical transmission that occurs in films of semiconductor chalcogenide glasses after the irradiation with polarized light [93]. Low loss planar waveguides can be realized using a multilayer structure of As_xS_{1-x} chalcogenide films with different compositions [94].

Possibilities of application in microelectronics of ChG as inorganic high-resolution photoresists were demonstrated in [95]. A brief consideration of three main effects: photostructural transformations, photo-doping and electrostimulated interaction of ChG with some metals for lithography was given. The emphasis was put on the third effect which appears to be original and less known as well as on the technical features of lithography processes with ChG.

A new kind of gas sensor based on ChG for the detection of nitrogen dioxide has been investigated in [96]. It contains a sandwich metal-semiconductor (Ge-As-Te ternary alloys)-metal structure which is used as chemical sensor for the detection of NO_2 to concentrations in the ppm and sub-ppm ranges. The detection principle is based on the measurement of the conductivity of the sensitive film. The dependence of the sensitivity to the gas concentration has been studied. The NO_2 response was found to be high and reversible. The response time was fast and the reproducibility satisfactory. The cross-sensitivity to interfering gases has been investigated. The chalcogenide-oxide-silicon field effect transistor based sensor is presented as an application example of these layers. All measurements were performed at room temperature.

1.5. Objectives of the work and new contribution

There still exist a lot of similarities in photo-structural behaviors in the chalcogenide and the azodye-polymer system. Meanwhile a notable difference between the photoinduced changes in ChG and the azo-polymer is the following: in the azodye-polymer system, it is conceivable that light excites the azodye, and its isomerization process causes successive structural changes in surrounding molecules. A problem in a photoinduced process is focused upon the successive structural change. On the other hand, in the ChG, the excited species cannot be identified, which may be some defective sites or disordered structures. It is plausible that the excited species change with the photon energy of excitation, light intensity, temperature, and so forth. As a result, following structural changes in ChG become largely speculative.

Having seen these many similarities, it is tempting to propose some universality in the photostructural mechanisms. Since the roles of dyes and back-bones in organic systems have been understood, the corresponding elements in the homogeneous glass should be sought, which are probably localized gap states and normal-bonding networks. The localized state can be directly photo-excited or it may trap excited carries, which will trigger successive structural changes in the disordered network. A big problem for such homogeneous systems, however, is that many kinds of defective structures can be envisaged as the gap state.

To get further insight into the photoinduced mechanisms, we take a comprehensive approach. Specifically, a comparison of photoinduced phenomena in ChG nanostructures with those in AP is valuable, since their photo-structural mechanisms have been understood more deeply.

Scientific novelty of the research results:

- The PC based technology of nanomultilayers vacuum deposition from a number of ChG-Se compositions for one step direct holographic and e-beam recordings was elaborated for the first time.
- The chemical synthesis technology and spin coating thin films preparation of new AP to make used for one step direct holographic and e-beam recordings was elaborated for the first time.
- The one step direct surface relief recordings of DOE on ChG-Se NML and AP films by application of the polarization holography method were done for the first time. It must be emphasized that the method excludes to be use any wet and/or other selective etching step, and, as a consequence, no amplitude distortion of DOE surface.
- It was firstly experimentally determined the complex variations of optical parameters (refractive index, absorption coefficient) of the ChG-Se NML and the AP thin films take place responding to the action of both scalar and vector components of the electrical field of light.
- The one step direct surface relief gratings on the ChG-Se NML patterned by virtue of low dose of laser illumination ($\sim 1 \text{ W/cm}^2$ unless otherwise specified) was obtained and studied

experimentally for the first time. Process of patterning is governed by photoinduced structuration of material which starts the surface mass transfer.

- For the first time the Gradient Magnetic Force Microscopy diagnostics has shown that obtained by the one step direct holographic recording the small periodical relief thickness changes leads to the essential fluctuations of magnetic field value over the relief surface in the $\text{As}_{40}\text{S}_{60}:\text{Mn}-\text{Se}$ NML.
- It was firstly experimentally determined that the surface relief gratings in the ChG-Se NML and the AP thin films formed under optical and digital holographic recording methods are conditioned by vectoral (spatially anisotropic) response of the medium.
- During carry out experiments it was established for the first time that the surface relief gratings in the AP thin films formed by one step direct laser and e-beam illumination are induced by the *trans-cis-trans* transformations which lead to the mass transfer process.
- It was established the first time that the usage of the one step direct holographic recording significantly improves the optical quality of the surface relief of the DOE at nanometre scale (~by a factor of 10) in comparison with film surface.

The practical value of the work.

- The systematic studies of the ability of ChG NML and AP to be structured by laser writing methods, exposure with e-beam radiation, and digital hologram recording open up perspectives for development and/or optimization of wide a variety of applications in different technical fields (diffractive optics, medicine, anti-counterfeiting elements, image holography etc.).
- Elaborated the new PC based technology of nanomultilayers vacuum deposition can be applied for obtaining nanomultilayers structure from different compositions of ChG. A number of new structural and optical properties of nanomultilayers have been revealed which are suitable for new practical applications.
- The developed digital holographic technology for direct laser marking of gold items has been successfully applied in two contracts with the Ministry of Finance of Moldova, the State Assay Chamber. It consists in the developing PC digital holograms, designing the optical system for laser marker set-up and the devices for hologram verification. The technology can be applied to other authentic products for protect internal market of Moldova from counterfeits.
- Application of polarization holography method excludes any wet or other etching during DOE production. It leads to faster processes for holograms embossing and raise a quality of DOE (the DOE's surfaces are smoother relief structures in nanometric level).
- It was elaborated and recorded the phase DOE on the ChG-Se NML and the AP thin films with a variety of grating periods determine the spectrum of practical application of these DOE.

- The portable fiber-optics Electronic Speckle Pattern Interferometer elaborated has been tested for the wood masterwork investigations, and it can yield practical help for restorers.
- The results of the work were practically applied in the successful implementation of the following projects, among them 7 EC projects, transfer technology projects and 2 Vouchers projects.

Scientific concept: The theoretical and applied aspects of the processes induced in amorphous materials by light and electron irradiation leading to pattern in these sensitive media the diffractive structures and the application them in optical and digital holography.

Statements supported:

- The new elaborated technology of PC controlled successive multilayers thermal vacuum deposition on a glass substrate with cyclic motion of substrate permits to obtain amorphous nanomultilayers ChG–Se (the thicknesses from 5 nm to 3000 nm) with preserving the composition of constituent nanolayers.
- New azo-doped photopolymer Poly-n-Epoxypropyl Carbazole and Dispers Orange (poly-PEPC-co-DO) was synthesized by free radical polymerization method with the conjunction of azo group in synthesized copolymer. It is proved that illumination results in *trans-cis-trans* transformation.
- The ChG-Se NML's spectral transmission range is dominated by the stack of Se nanomultilayers, what is proved by coincidence of absorption edges. The optical parameters of the ChG-Se NML are conditioned by the structurization of constituent nanolayers. The short-range order of constituent materials is kept in NML, but the optimal thicknesses of constituents nanolayers for preserving of medium-range were determined. The photoinduced processes in the ChG-Se NML are governed by carrier photoexcitation in volume of nanomultilayers and the effective injection of holes at interfaces Se/ChG.
- For the first time the polarization (vectorial) holographic recording at states of polarizations P-P, S-S, S-P, LCP-RCP, $\pm 45^\circ$ for the grating surface relief formation in the ChG-Se NML and the AP thin films were carried out. It was established that the diffraction efficiency values increase in 8-10 times at circular right-left and orthogonally oriented $\pm 45^\circ$ polarization states of recording beams. The diffraction efficiency values in transmission mode for ChG-Se NML gratings have a maximal value 45%.
- One-step direct grating surface relief formation in the ChG-Se NML and the AP thin films by the optical and the digital holographic methods are realized. Surface relief is resulted under mass transfer induced by vector character of the polarization (vectorial) holography, and the depths of surface relief have a values in the range of 100-400 nm. No any additional treatments of films are needed for relief formation.

- At the first time the direct one-step magnetic relief formation during surface relief gratings recording on $\text{As}_{40}\text{S}_{60}:\text{Mn}-\text{Se}$ NML caused by periodical relief thickness changes was shown.
- The engineering approach with application of ZEMAX optical code for the DHI system design and analysis, the determination of DHM performance and quality of final image has been demonstrated. The quantitative criteria for determining the weak points of the DHM system performance, their role in limiting the image quality, and the ways to overcome them were elaborated.
- The high resolution off-axis configuration of the DHM setup applicable for quantitative measurements of surface topography and refraction index of diffraction structures, formed in the ChG-Se NML and the AP thin films was elaborated. The novel variational algorithm for the digital off-axis holographic setup (SPAR) capable to produce holographic images from noisy data with increased signal-noise ratio was developed and applied.
- The practical application of developed ChG-Se NML and the AP thin films as diffractive optical components has been demonstrated: phase masks for optical processing in DHM, security elements with increased security level and protective signs for different kind of products.

2. MATERIALS: TECHNOLOGY AND STUDY METHODS

2.1. Thermal vacuum deposition of nanomultilayers and polymer films spin-coating

The main method for chalcogenide glasses application is thermal evaporation in vacuum. Thermal vacuum deposition describes the family of processes used to deposit layers of material atom-by-atom or molecule-by-molecule on a solid surface. These processes operate at pressures well below atmospheric pressure i.e., vacuum. It is known that the layer properties (stability, compositions) depend not only on the composition of chalcogenide, but also on the conditions of deposition (substrate temperature and deposition rate of chalcogenide film on it). In order to reproduce the properties and characteristics of deposited layers the layers are apply under the following conditions:

- The chalcogenide is evaporated at a residual pressure in the vacuum chamber of at least 10^{-3} Pa;
- The substrate temperature during the deposition of chalcogenide layer is equal to the ambient temperature;
- The deposition rate ranges within 1–2 nm/s.

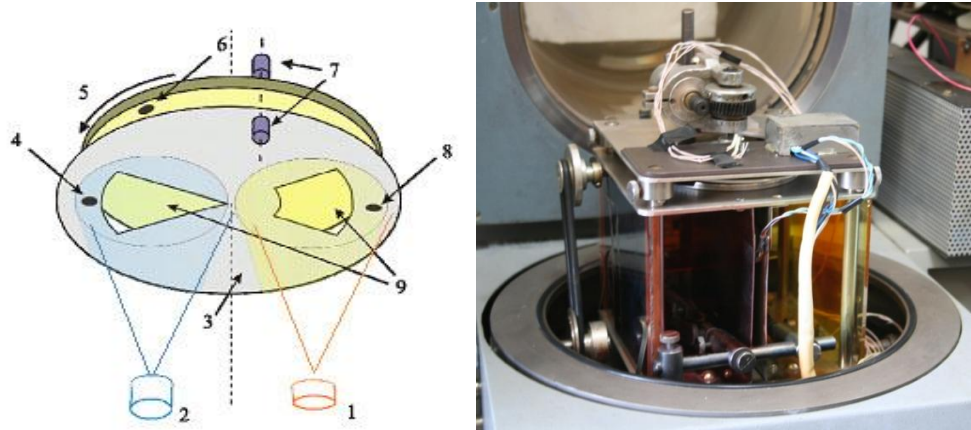


Fig. 2.1. The vacuum chamber arrangement for the deposition of multilayer nanocomposites on the base of ChG: (1) evaporator of ChG, (2) evaporator of Se, (3) stationary mask, (4), (8) quartz thickness sensors fixed on mask, (5) rotating samples holder, (6) quartz thickness sensor fixed on rotating samples holder, (7) optical fibers of spectrophotometer, (9) windows in mask.

The bulk ChG was synthesized by common melt-quenching technique from high purity components. After synthesis ampoules were quenched in cold water. Amorphous ChG-Se nanomultilayers were prepared by computer driven cyclic thermal vacuum deposition from two isolated boats with ChG and Se on constantly rotated substrate at room temperature in one vacuum deposition cycle (Fig. 2.1). The technology allows depositing thin films with thicknesses

from 0.005 up to 3.0 μm . The control of the thickness was carried out in-situ during the thermal evaporation by interference thickness sensor at $\lambda = 0.95 \mu\text{m}$.

Cross-section of sample structure is shown in Fig. 2.2. Overlapping part of samples (3- in Fig. 2.2) contains alternating nanolayers of ChG with thickness of 10–30 nm and Se with thickness of 5–15 nm. The total numbers of nanolayers were 100–200. Outside and internal rings of layers on the substrate contain pure compositions of ChG and Se (2 and 4 in Fig. 2.2, consequently).

Control layers of Se and ChG were deposited at the same time onto the same substrate, consequently, through masks and used to check the composition and calculate the ratio of the sublayer thicknesses in one modulation period.

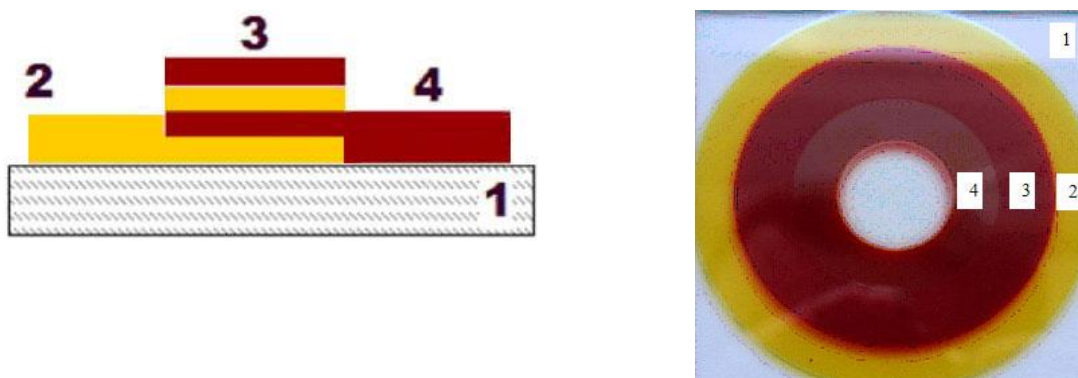


Fig. 2.2. Cross-section and top view photo of sample ($75 \times 75 \text{ mm}^2$): 1 — glass substrate; 2 — ChG layer by layer; 3 — ChG-Se nanomultilayers structure; 4 — Se layer by layer.

Although stimulated structural transformations were observed in a wide range of chalcogenide glass compositions, we selected for first experiments As_2S_3 -Se nanolayered films as well as Se and As_2S_3 layers because of their known parameters and well-known technology. Important criteria were low softening temperatures and low crystallization abilities of As_2S_3 , small effects of the direct photostimulated scalar surface relief formation within the amorphous phase. Slow fabrication processes seem to produce large agglomerates, while ultra-fast processes seem to inhibit it, leading to more homogeneous/sensitive materials, in similar fashion as reported for complex dynamical systems. Then we applied the developed thermal deposition methods for other ChG compositions, namely $\text{Ge}_5\text{As}_{37}\text{S}_{58}$, $\text{As}_2\text{S}_3\text{Mn}_{2\%}$, $\text{As}_2\text{S}_3\text{Cr}_{4\%}$. Doping of Ge to As_2S_3 increases intensity of the process of structural relaxation in regions with local disordering in the vicinity of atoms with unsaturated (dangling) bonds. Introduction of Mn dopant changes magnetic properties of chalcogenide glasses which are diamagnetics, in particular glass of As_2S_3 composition (see Fig. 2.3) [97]. In constant magnetic field dependence of mass magnetization $M=M(T)$ on temperature was observed for doped by Mn in glasses (Fig. 2.4) which is character-

istic for paramagnetics and ferromagnetics in paramagnetic region of temperature and described by Curie-Weiss law [98].

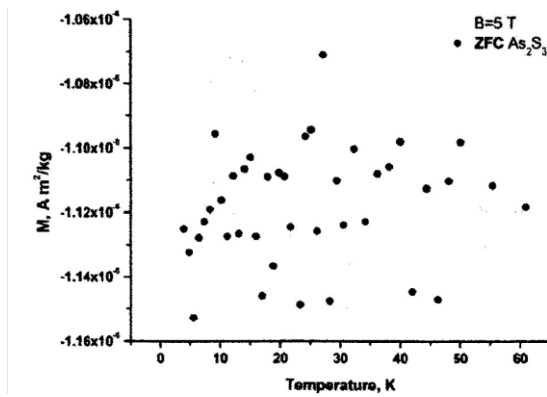


Fig. 2.3. Dependence of mass magnetization M on temperature for As_2S_3 [97].

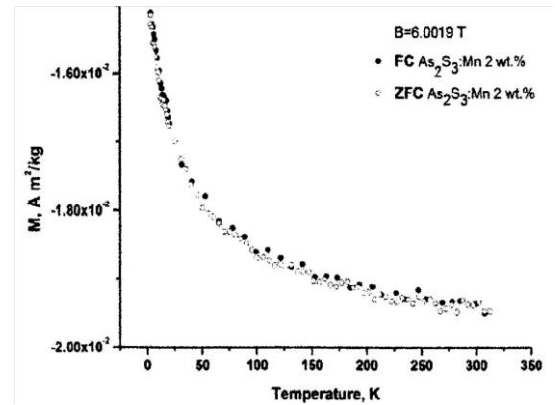


Fig. 2.4. Dependence of mass magnetization M on temperature for $\text{As}_2\text{S}_3:\text{Mn}$ [97].

Resulting sample was ChG-Se multilayer structure with total thickness from 1500 nm to 3500 nm with the composition modulation period (common thickness of one ChG nanolayer and one Se nanolayer) varied 17–50 nm. In order to prevent crystallization of Se layers (see Fig. 2.5) which are structurally unstable under heating and/or exposure by light, e-beams, etc., heating of layers was minimized by substrate rotation and lowered evaporator temperature. Crystalline phase of Se was found in open nanolayers, but not inside NML as x-ray analys shown.

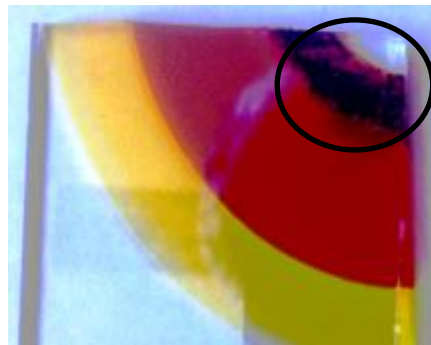


Fig. 2.5. Crystalline phase of Se layer is visible as indicated by the circle.

Optical transmission was measured in 200–900 nm optical range in order to determine the refractive index, thickness and optical band-gap energy of pure ChG and Se layers and ChG-Se multilayers.

Polymer synthesis and films spin-coating.

Before preparing the azo-dyed carbazol polymer, we tested the pure carbazol based polymers. In this study, a series of carbazole-containing compounds, namely poly-

epoxypropylcarbazole (PEPC), poly-epithiopropylcarbazole (PETPC), and copolymers of PETPC: glycidyl butyrate (PETPC:GB) were synthesized.

PEPC and PETPC were prepared by polymerization of epoxypropylcarbazole and epithiopropylcarbazole at the presence of 1–3% potassium methylate on the anionic mechanism at temperature 80–120°C within 2–6 h. For the full drying they were stored in a vacuum drying chamber at 50°C up to constant mass. Molecular weight was from 2000 to 3000. In Fig. 2.6 the chemical structure of polymers PEPC and PETPC after polymerization are presented.

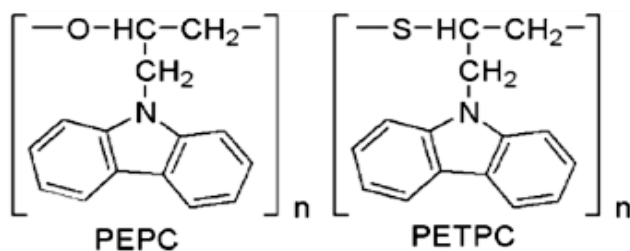


Fig. 2.6. Chemical structure of polymers after polymerization.

For the improving of plastification properties copolymer PETPC:GB in proportion 90:10 was prepared by a method of radical polymerization in a toluene solution at the presence of 1–3% potassium methylate at a temperature of 80°C. Prepared polymers and copolymers PEPC, PETPC, and PETPC:GB were re-precipitated from hexane. The chemical formula of PETPC:GB copolymer is given in Fig. 2.7.

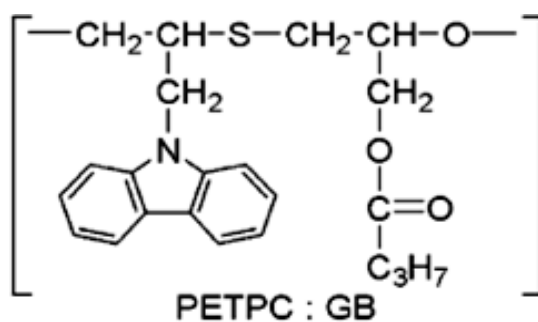


Fig. 2.7. Chemical structure of copolymer PETPC:GB.

The PEPC, PETPC, and PETPC:GB layers were applied by casting from solutions on a flexible poly(ethylene terephthalate) substrate with the use of a special meniscus device. The layer thickness d was varied from 2 to 10 μm . To prepare thicker layers, solutions with a concentration higher than 15% were taken. After the storage of the samples in air, the layers were additionally dried in a vacuum drying oven at ambient temperature. The thickness of the layers was monitored with an MII-4 interference microscope.

The photosensitive azopolymer based on carbazole-containing oligomer and purchased azo dye Disperse Orange 3 (poly(PEPC-co-DO)) was synthesized. All used solvents and reagents were of reagent quality and used without additional purification. 4-[(4'-Nitrophenyl)azo] aniline, Disperse Orange 3 (DO 3) with dye 90% purchased from Sigma-Aldrich. Analytical TLC plates were Silufol[®] UV-254 (Silpearl on aluminum foil). IR spectra were recorded on a Spectrum 100 FT-IR spectrophotometer (Perkin-Elmer) using the universal ATR sampling accessory. UV spectra were recorded on a Spectrophotometer PerkinElmer LAMBDA 25 UV/Vis. DO 3 is a nonlinear optical azo dye which is well known for its trans \leftrightarrow cis photoisomerization and for its ability to undergo efficient orientation and trigger important polymer movement when it is excited by polarized light [99]. Carbazole-containing polymers were employed as effective recording media for holographic and e-beam recording [100]. In our study using modified procedure [101] azobenzene polymer has been obtained by reaction of 340 mg poly-*n*-epoxypropyl carbazole (PEPC) with 34 mg of DO in boiling toluene (2 ml) during 3 hours. The resultant solution of carbazole-based 4-[(4'-nitrophenyl)azo]aniline-labeled azopolymer called as poly(PEPC-co-DO) was filtered, determined by UV-Vis absorption and used for thin film deposition. The reaction scheme is shown in Fig. 2.8.

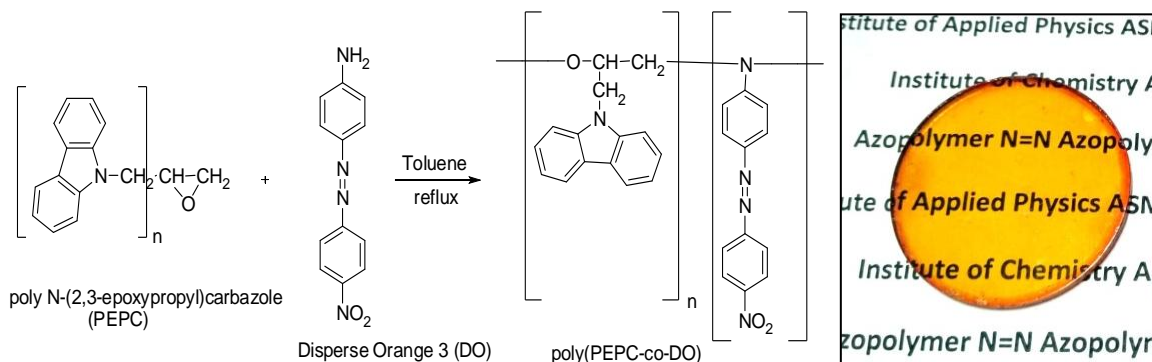


Fig. 2.8. Synthetic scheme of poly(PEPC-co-DO) and obtained thin film on glass substrate.

The synthesis of poly(PEPC-co-DO) with 20–60 weight% of azo dye were carried out as the same method as for described above. The reaction scheme is shown in Fig. 2.8.

In order to obtain films with different thickness resultant solution was diluted with different amounts of toluene. Thin azopolymer films were obtained in equal conditions by spin-coating of initial and diluted solution under 500 rpm for 30 s and dried at room temperature for a day. The photo of spin-coated poly(PEPC-co-DO) film is shown in Fig. 2.8.

The thickness of dried films was measured by high-precision interference microscopy [102]. A groove was made on the surface of each sample, inside which the azopolymer film was removed up to glass substrate and the distance between the “plateau” and the bottom of the

groove corresponded to the layer's thickness. A number of films with thicknesses 250, 300, 400, 800 and 1600 nm were obtained.

Fourier Transform Infrared Spectroscopy (FTIR) was applied for copolymer structure characterizing and identifying organic molecules. The chemical composition and the bonding arrangement of constituents of the monomer, the azodye, and the azopolymer were investigated by FTIR spectroscopy. Position of absorption peaks correspond to the frequencies of vibrations between the bonds of the atoms and the size of the peaks is a direct indication of the amount of constituents. Before infrared analysis, powdered samples were dried in exsiccator up to constant mass. Infrared spectra of the samples were recorded with a PerkinElmer Spectrum 100 FT-IR spectrometer. Data collection covers a total spectral range from 7800 cm^{-1} to 400 cm^{-1} with the resolution 4 cm^{-1} .

The constituents of synthesizing copolymer (monomer EPC, azo-dye DO) and copolymer EPC:DO obtained were characterized by FTIR spectroscopy with attribution of infrared absorption bands to main functional groups. On the Fig. 2.9 we present IR spectrum of the monomer EPC and the copolymer EPC:DO. The conjunction of azo group in synthesized copolymer EPC:DO was confirmed by the appearance of the peak at 1389 cm^{-1} in the IR spectrum (Fig. 2.9) corresponding to the N = N stretching frequency.

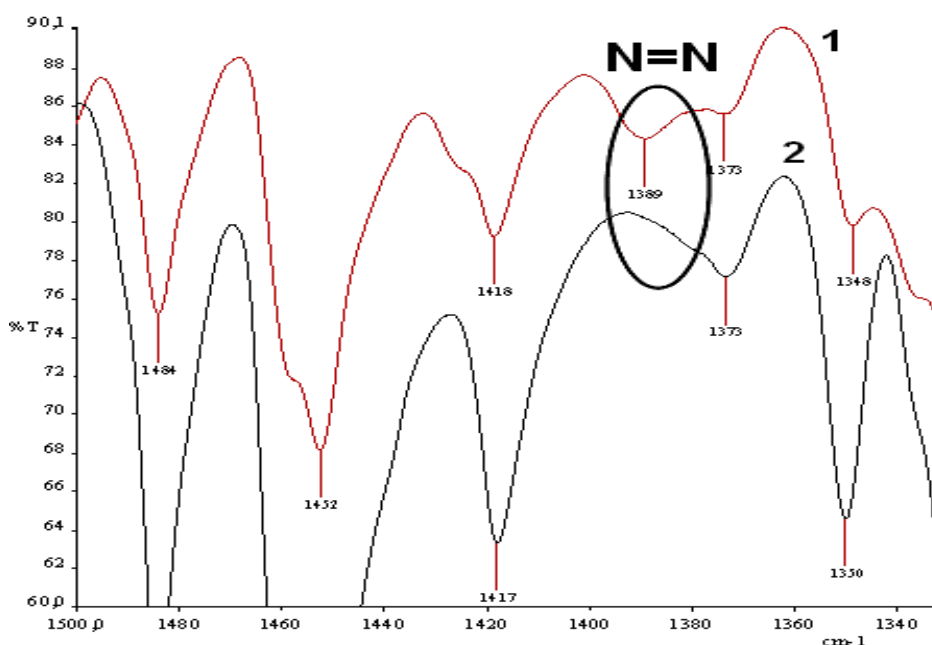


Fig. 2.9. Fragments of IR spectrum: 1 — copolymer EPC:DO (90:10); 2 — EPC.

A widely used technique to produce thin layers is spin-coating. In spin-coating, a solution drops of the coating material dissolved in an appropriate solvent is dispensed onto the substrate surface, which is made to rotate at large velocity (typically around 600–3000 rpm). Programma-

ble spin-coater (Fig. 2.10) has the capacity to store and execute up to 30 programs, with up to 20 steps each. Spin profiles adjustable in 1.0 rpm rotation increments, 0.1 s timing increments, and 1.0 s increments for dwell time, with precise repeatability from cycle to cycle and speed of 0–10000 rpm. The spinning motion spreads out the solution and, as the solvent evaporates away, a thin film of coating is left on the surface.



Fig. 2.10. Photo of programmable spin-coater “SGS Spincoat G3P-8”.

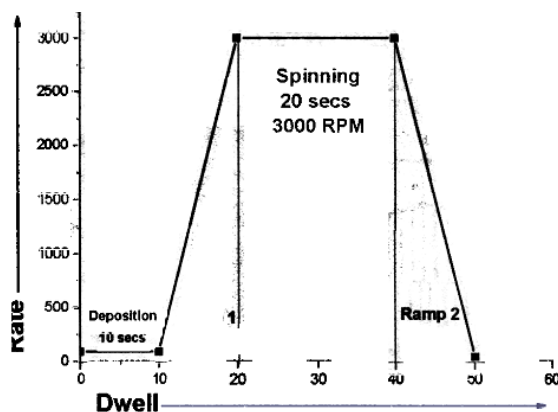


Fig. 2.11. Rate/time schedule of spin-coating for polymer films.

There are several major factors affecting the coating process. Among these are spin speed, acceleration, spin time and exhaust volatility. It was shown that spin coating of thin and thick polymer films, examined in several solvents of varying volatility over a broad range of polymer solution concentrations and spin speeds, could give film thicknesses from 10 nm to 33 nm.

In our study, the thin polymer films were prepared from the 10 wt. % homogeneous polymer solution in toluene onto glass substrate using programmable spin-coater “SGS Spincoat G3P-8”. Operation conditions for polymer solution deposited on 5 cm diameter optical glass substrate (BK7) were as follows: 1 cm³ of liquid dispensed on the disk at rest, subsequently accelerated in about 3 s to 800 rpm and spun for 60 s. Obtained films were dried in an oven at 60 °C for 6 hours. The broad range of thicknesses can be covered by using polymer solution with increasing solids content or for a given solution by changing the final spin speed (Fig. 2.11).

Determination of film thickness by optical techniques is widely used. Measurements are nondestructive, relatively inexpensive. Interferometry relies on the interference of two or more beams of light, e.g. from the air/film surface and the film/substrate interfaces, where the optical path difference is related to film thickness.

For the determination of film thickness the modified digital MII-4 interference microscope with CCD-camera was applied [103]. True optical resolution (snapshots) is 1920×1080pxs of

Logitech HD webcam. A magnification of $490\times$ was used. The horizontal field of view, from which a data analysis is performed, was 0.3 mm diameter circle.

It was shown that by raising the polymer concentration from 2.5 to 15.0 wt%, the final film thickness increase from 160 to 960 nm at a spin speed of 3000 rpm during 20 s. Applied method of thickness measurements has shown a quasi-linear thickness dependence on polymer concentration. (Fig. 2.12).

Working with computerized MII-4 interference microscope and elaborated software has shown that precise determination of layer thickness of thin films can be user-friendly. Software can process the interferograms in the case of interference fringe tilt respect to pixels row angles deviation.

In contrast to conventional layer thickness measuring devices such as profilometers or atomic force microscopes (AFM), this technique provides the full field analyzing specimens, is more rapid, noncontact, and does not require complicated specimen preparation. Thanks to these advantages, the modernized MII-4 interference microscope has great potential as a combined analysis system (optical microscope and layer thickness measurement device), particularly in thin-film engineering [103, 103]. Moreover, the cheaper USB webcam with more than 2mln pxs is a good alternative to CCD camera and framegrabber. Webcam uses the low power USB interface for data transfer and provides the plug-and-play functionality.

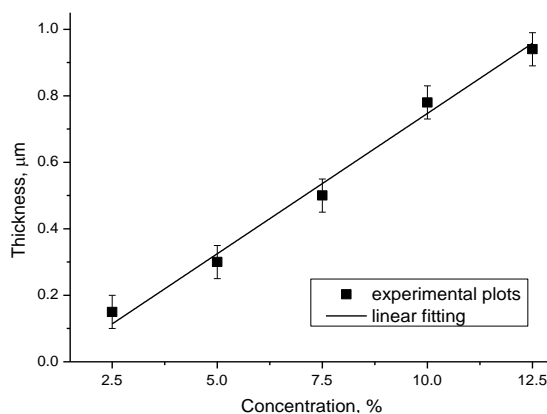


Fig. 2.12. Film thickness as a function of concentration of PEPC solution in chloroform.

2.2. Carrier photoinjection at ChG-ChG interface

The possibility to increase photosensitivity of ChG heterostructures (HS) by means of injection sensibilization of As_2S_3 (As_2Se_3) by holes from Sb_2S_3 (Se) in two-layer structures was investigated in work [104].

The two-layer structures were obtained on a glass substrate covered with lower electrode (Al, Au, Bi, SnO_2) by subsequent thermal deposition in vacuum of ChG layers and top electrode Al.

I-V characteristics, photoconductivity spectra, transient injection photocurrents as well as discharge characteristics in xerographic regime without top electrode were measured.

It is difficult to make an analysis of the examined ChG, consisted of elements with different field dependence of conductivity, but the following relations may be qualitatively observed.

Electric current transport in the fields up to $4 \cdot 10^4$ V/cm and temperatures to 313 K in the structure Me- Sb_2S_3 - As_2S_3 -Me does not depend on bias voltage polarity, the structure's conductivity is governed by the volume conductivity of the layers. But with rising temperature, as well as increasing the electric field the current under negative potential on As_2S_3 exceeds the current magnitude under opposite bias, which may be considered as an indication of the hole injection from Sb_2S_3 to As_2S_3 layer [107].

This effect can be more clearly seen by investigation of the I-V characteristics under illumination. The current strongly increases in the case of injection's polarity (Fig. 2.13, curve 1') in contrast to the opposite polarity, when the structure conductivity does not change greatly (Fig. 2.13, curve 2').

Feature marked above also takes place for the structure Me-Se- As_2Se_3 -Me, when the sample conductivity changes more strongly under the negative potential on the As_2Se_3 , than under opposite polarity (Fig. 2.13, curve 3', 4').

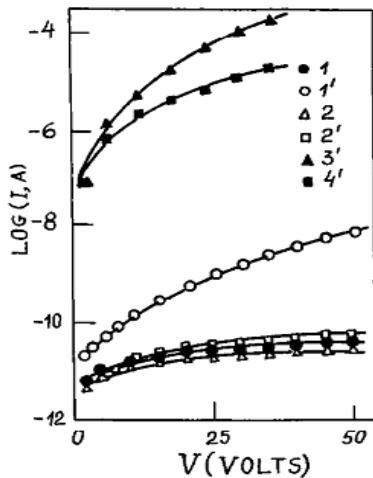


Fig. 2.13. I-V characteristics in dark (1, 2) and under illumination (1', 2', 3', 4') at injection (1', 3') and opposite (2', 4') bias polarity for the HS:

Au- Sb_2S_3 - As_2S_3 -Al (1, 1', 2, 2'); SnO_2 -Se- As_2Se_3 -Al (3', 4').

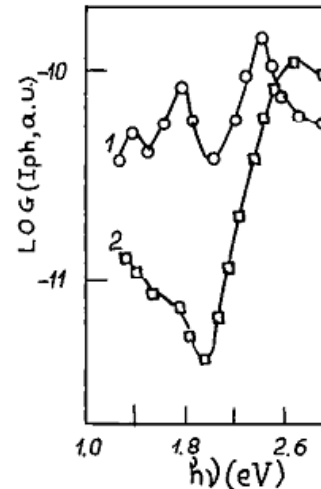


Fig. 2.14. The photocurrent spectra of the HS Au- Sb_2S_3 - As_2S_3 -Al at injection (1) and opposite (2) bias polarity.

Measurement of the photogenerated hole drift in the field regions up to 10^5 V/cm and temperature up to 400 K showed, that the carriers quickly pass the Sb_2S_3 layer and accumulate, due

to great difference of drift mobilities, at ChG-ChG interface, creating after that current in As_2S_3 under the field action (Fig. 2.14). Transport of a charge packet takes place consequently in the layers of the $\text{Sb}_2\text{S}_3\text{-As}_2\text{S}_3$ and shows dispersive character in contrast with the $\text{Se-As}_2\text{Se}_3$, in which charge transport injected from Se into As_2Se_3 in the field region from 10^3 to 10^5 V/cm and temperature range 300–330 K has normal character.

Under illumination of the structure $\text{Au-Sb}_2\text{S}_3\text{-As}_2\text{S}_3\text{-Al}$ from the side of the wide gap ChG (As_2S_3) the photocurrent spectra (Fig. 2.14) are significantly different for positive and negative bias of the top electrode. The main difference corresponds to Sb_2S_3 photogeneration region (1.4–2.1 eV) indicating the injection nature of holes photogenerated in Sb_2S_3 and passing through the As_2S_3 layer.

The injection sensibilization is confirmed by strong correlation of the spectrum behaviour with variation of the layer thickness. The photocurrent spectra slightly depended on bias polarity in the structures with thick As_2S_3 layer.

The photocurrent spectra of the structure $\text{SnO}_2\text{-Se-As}_2\text{Se}_3\text{-Al}$ are shown in Fig. 2.15. As the total structure resistance is mainly determined by the As_2S_3 layer resistance, the injection of holes photogenerated in Se into As_2S_3 reduces its resistance, increasing the photocurrent (Fig. 2.15, curve 1). At opposite bias polarity the holes photogenerated in Se, under action of the electrical field, are extracted in the contact without lowering the structure resistance because of the absence of injection (Fig. 2.15, curve 2).

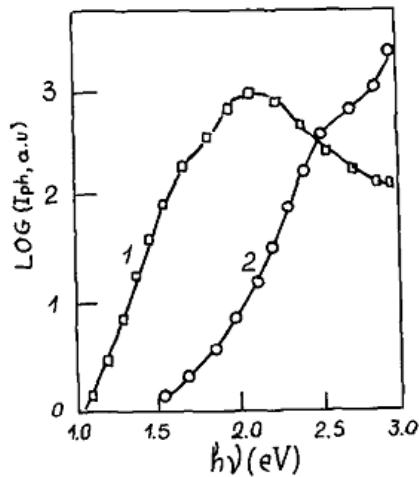


Fig. 2.15. The photocurrent spectra of the HS $\text{SnO}_2\text{-Se-As}_2\text{Se}_3\text{-Al}$ at injection (1) and opposite (2) bias polarity.

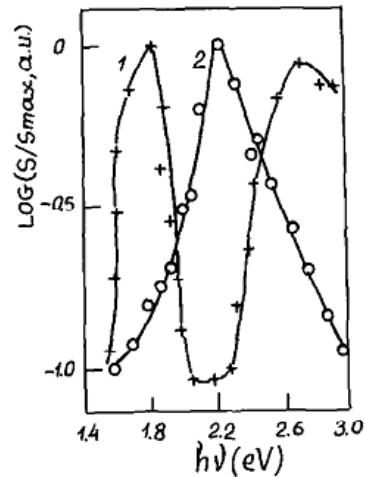


Fig. 2.16. The spectrum of xerographic sensitivity of the HS $\text{Al-Sb}_2\text{S}_3\text{-As}_2\text{S}_3$ under positive (1) and negative (2) electrization.

Sensibilization of As_2S_3 (As_2Se_3) by photogenerated holes from Sb_2S_3 (Se) is proved by tests in xerographic regime. For example, the spectrum of xerographic sensitivity is shown in Fig. 2.16 for the structure $\text{Al-Sb}_2\text{S}_3\text{-As}_2\text{S}_3$. The choice of layer thicknesses provided the equal

contribution to photosensitivity spectrum of this structure, when the top layer of As_2S_3 is positively charged, there are no conditions for injection and the spectrum consists of two maxima corresponding to the contribution of each layer (Fig. 2.16, curve 1). In the case of negative charging the injection maximum dominates in the spectrum at intermediate region of excitation energies (Fig. 2.16, curve 2). The sensitivity of this maximum is 4–5 times higher than the volume sensitivity of the individual layers.

Thus the analysis of the experimental results of the light and dark I-V characteristics, spectral sensitivity distribution in resistive and xerographic regimes, as well as transient injection photocurrent indicates the presence of the injection sensibilization effect. This permits to extend the spectral sensitivity region and increase photoconversion efficiency in the studied ChG structures [108].

The charge carrier transport through interface of two ChG in conditions of photoexcited carrier's injection was investigated in heterostructure Se- As_2Se_3 . In this case the transport of holes injected from Se to As_2Se_3 has been considered.

The samples of heterostructures have been obtained by abovementioned method. To restrict a dark current injection, the barrier layer from high-resistance dielectric transparent in UV region has been deposited between lower electrode and Se layer. The constituent layers of Se and As_2Se_3 have been obtained in one technological cycle with heterostructure to compare their characteristics. Nonequilibrium carriers were generated in Se by pulse of high absorbed light ($\lambda=0.34 \mu m$) of N_2 -laser LGI-21. At positive polarity on illuminated electrode (SnO_2) the transport of holes photoexcited in Se takes place through As_2Se_3 . The photocurrent at opposite polarity corresponding to electron transport is negligible in comparison with hole transport.

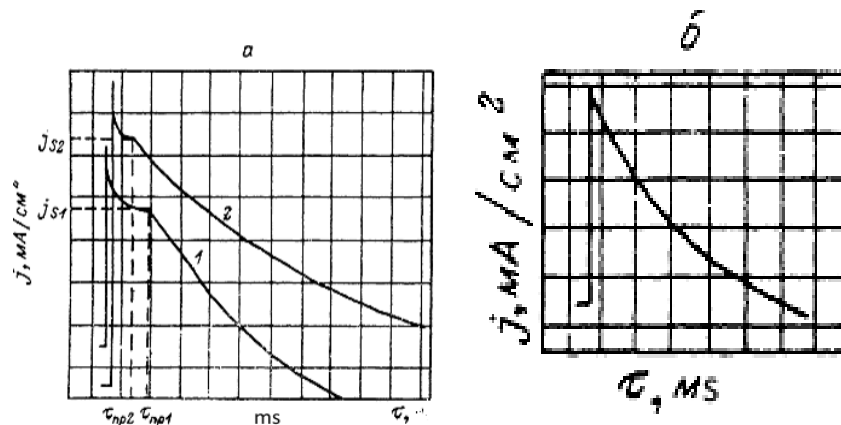


Fig. 2.17. The oscillograms of transfer photocurrent in SnO_2 -Se- As_2Se_3 -Al (a) and SnO_2 - As_2Se_3 -Al (b). a) U, V : 1 — 2.5, 2 — 5; $j, A/cm^2 \cdot div$: 1 — $1 \cdot 10^{-6}$, 2 — $2 \cdot 10^{-6}$; $\tau_{pul}=1 \text{ ms/div}$. b) $U=5 \text{ V}$; $j=2 \cdot 10^{-8} \text{ A/cm}^2 \cdot div$; $\tau_{pul}=5 \text{ ms/div}$.

Typical oscillograms of the transient photocurrent in heterostructure Se-As₂Se₃ and As₂Se₃ are shown in Fig. 2.17. From comparison of these oscillograms it is seen that current density in heterostructure is two order high than in As₂Se₃ which proves the existence of effective hole injection from Se into As₂Se₃.

One can separate two parts in the oscillograms of nonstationary photocurrents in heterostructure Se-As₂Se₃: 1. rapid decay matching hole transfer in Se, and 2. the plateau and consequent slow decay matching hole transport in As₂Se₃. Time of flight of hole “packet” center of gravity τ_{pul} in As₂Se₃ is defined in part 2 at the point of inflection separated the plateau and consequent decay. The density of quasi stationary current j_s is determined at the same point of inflection (Fig. 2.18). The plateau on the iscullograms of quasi stationary currents is the evidence of the carriers’ packet transport with constant rate, i.e. the evidence of normal (Gaussian) transfer in As₂Se₃. For similar oscillogram for layer of As₂Se₃ it is seen the absence of the plateau, and the transport is dispersive one. The dispersive hole transfer in As₂Se₃ was observed by many researchers such as [109], whereas the normal transport was discovered only at certain conditions like for example [107]. In our experiment the hole injection from Se it seems influences on the transfer mechanism in As₂Se₃ which becomes normal.

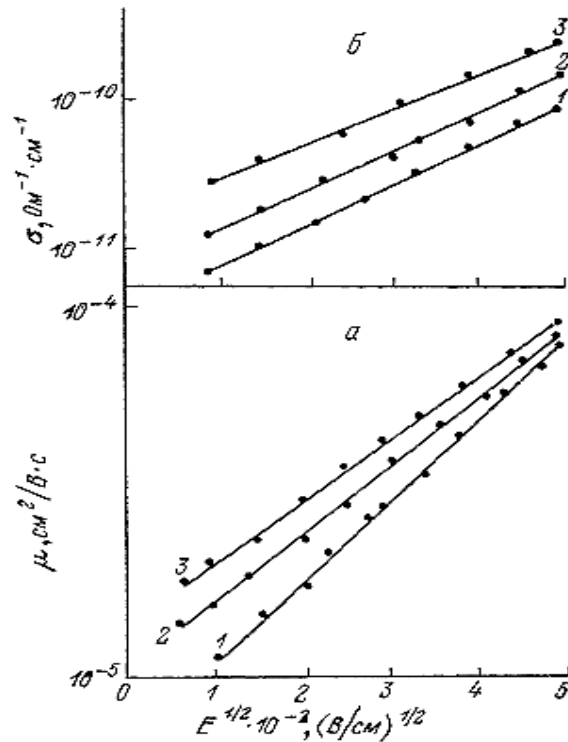


Fig. 2.18. The field dependences of holes drift mobility μ (a) and conductivity σ (b) of As₂Se₃ layer in heterostructure SnO₂-Se-As₂Se₃-Al. 1 — 25°C, 2 — 35°C, 3 — 50°C.

In Fig. 2.19 the electrical field dependences of holes drift mobility μ and conductivity $\sigma = j_s/E$ in As_2Se_3 at different temperatures are shown where $\mu = L/\tau_{pul} E$ (L — thickness of As_2Se_3 layer, E — intensity of electrical fields, j_s and τ_{pul} are pointed in 0). As one can see from Fig. 2.18 the dependences of $\lg \sigma(E^{1/2})$ and $\lg \mu(E^{1/2})$ are linear.

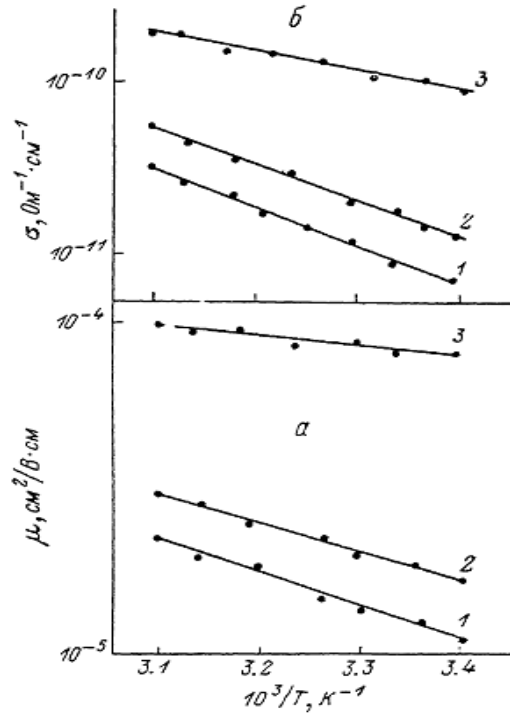


Fig. 2.19. The temperature dependences of holes drift mobility μ (a) and conductivity σ (b) of As_2Se_3 layer in heterostructure $\text{SnO}_2\text{-Se-As}_2\text{Se}_3\text{-Al}$. E , V/cm: 1 — 10^4 , 2 — 10^5 , 3 — $2.5 \cdot 10^5$.

The drift mobility of holes in As_2Se_3 measured at conditions of holes' injection from Se is $10^{-5} \text{ cm}^2/\text{V}\cdot\text{s}$ at field $\sim 10^3 \text{ V/cm}$. The activation energy amounts 0.22 eV. For As_2Se_3 layers the value of the hole drift mobility determined by the same technique is about $10^{-6} \text{ cm}^2/\text{V}\cdot\text{s}$ with the activation energy 0.52 eV. The fact, that the activation energy of holes' drift mobility decreases more than twice whereas the drift mobility increases by only one order, may be connected in the differences of preexponential factor of drift mobility which is dependent of trapping center concentration at 0.52 and 0.22 eV energy levels.

If we consider that the dependencies of $\mu(E, T)$ and $\sigma(E, T)$ are similar, i.e. the root dependence of field and activation dependence of temperature, and $\sigma = ep_{in} \mu$ (p_{in} — concentration of injected carriers) we can assume the similar field and temperature characteristic for the concentration of holes injected from Se into As_2Se_3 :

$$p_{in} = p_0 \exp \left[-\frac{\varepsilon_p - \beta_p \sqrt{E}}{kT} \right], \quad (2.1)$$

where p_0 — concentration of holes generated in Se by illumination. The magnitude of $\Delta\varepsilon_p = (\varepsilon_p - \beta_p\sqrt{E})$ is characteristic of the potential barrier of holes at interface of Se-As₂Se₃, ε_p and β_p — barrier parameters which may be expressed as $\varepsilon_p = \varepsilon_\sigma - \varepsilon_\mu$, $\beta_p = \beta_\sigma - \beta_\mu$. Theoretical magnitude is $2\beta_p = [e/\varepsilon_0\varepsilon_1(\varepsilon_1 + \varepsilon_2)(\varepsilon_2 - \varepsilon_1)]^{1/2} = 0.67 \cdot 10^{-4} \text{ eV(cm/V)}^{1/2}$ where $\varepsilon_1 = 6$ and $\varepsilon_2 = 9$ - dielectric susceptibilities of Se and As₂Se₃ respectively, and experimental value of $2\beta_p$ is $0.8 \cdot 10^{-4} \text{ eV(cm/V)}^{1/2}$. It is evident in favor of Richardson-Schottky mechanism. From experimental results the following estimations of injection barrier $\Delta\varepsilon_p$ and coefficient of injection $\eta = p_{in}/p_0$ have been obtained: $\Delta\varepsilon_p = 0.16 \text{ eV}$, $\eta = 2.1 \cdot 10^{-3}$ at $E = 10^4 \text{ V/cm}$ and $\Delta\varepsilon_p = 0.05 \text{ eV}$, $\eta = 1.5 \cdot 10^{-1}$ at $E = 2.5 \cdot 10^5 \text{ V/cm}$. The formation of potential barrier for holes at interface Se-As₂Se₃ is conditioned by bending down of Se valence band which is in agreement in field dependence of barrier's value: with field increasing (positive potential at Se) the barrier's magnitude decreases.

Comparison of injection features of the heterostructure Se-As₂Se₃ with corresponding features of other structures Se-PVC, AsSeTe-Se where $\eta = 10^{-4}$ [107] says about high efficiency of holes injection through barrier at interface Se-As₂Se₃ ($\eta = 10^{-1}$). If we take instead of As₂Se₃ the wider band gap ChG like As₂S₃ the hole injection from Se into As₂S₃ increases due to lowering the barrier value at interface Se-As₂S₃.

2.3. Optical and Raman spectroscopy measurements

a. Optical spectroscopy measurements

The changes of the optical parameters (blue or red shift of the fundamental absorption edge- bleaching or darkening, quantum states, luminescence) as well as of the conductivity and melting temperature (stability), are characteristic for and usually examined in nanostructures. A few approaches are known for extending investigations of ChG layers towards the nanostructures, especially in the nanolayered, superlattice-like multilayer structures, but the problem of photostructural transformation dependence on the artificial nanostructuring is still not solved. In addition, in most cases, the ChG applications require step of selective etching to form a surface relief, i.e. it cannot be fabricated by one-step direct laser writing. The etching process significantly complicates the DOE creation.

Optical transmission spectra were studied in the region 200–900 nm with the use of spectrophotometer Specord M40, and in the region 200–3000 nm with Shimadzu UV 3600. These spectra were measured in order to define the refractive index, the absorption coefficient, the thickness and the optical band-gap energy of constituent layers and NML. The darkening effect

and especially photodarkening effect have been studied extensively in As-chalcogenide glasses for the past three decades, bleaching has been observed rarely.

The typical optical transmission spectra of studied films are presented in Fig. 2.20 on the example of As₂S₃-Se NML structure with the thickness of one As₂S₃ nanolayer $d_{\text{As}_2\text{S}_3}=13$ nm and one Se nanolayer $d_{\text{Se}}=7$ nm. The total number of nanolayers is 200, so thicknesses of As₂S₃ — 1300 nm, and Se — about 700 nm, and the total thickness of NML is 2100 nm. There is a broad transparency region at long wavelengths side and significant drop of transparency in the region of 650–450 nm due to absorption increase. The samples have good optical quality. The interference maxima of transmissions are near the transmission of glass substrate which is evidence of optical quality of the films surface. The absorption edge of the NML composite structure As₂S₃-Se is close to the absorption edge of Se multilayers which is says about 1. the absorption of NML is determined by Se, and 2. good quality of the interfaces between nanolayers, i.e. no interdiffusion of the materials during evaporation [108]. These features of the absorption edge of NML are preserved for all investigated nanostructures.

The thicknesses of constituent As₂S₃-Se nanolayers lie in region 7–15 nm, and are sufficiently smaller than the wavelength of irradiation. Thus, in the analysis of optical transmission spectra of NML structure it was possible to use the “effective optical medium” model: the layers with small optical band gap E_g value determine the optical absorption at the average absorption edge E_g , and the “barrier” layers with larger E_g are transparent. For ChG, the optical absorption coefficient, α , changes rapidly for photon energies comparable to that of the band gap, E_g , giving rise to an absorption edge with three regions — for the largest electron energies, in the region of the edge itself ($10 < \alpha < 10^4 \text{ cm}^{-1}$), and at the lowest photon energies. The first one is for the highest values of the absorption coefficient ($\alpha \geq 10^4 \text{ cm}^{-1}$) which corresponds to transitions between extended states in both valence and conduction bands where the power law of Tauc is valid.

$$\alpha(h\nu) = B(h\nu - E_g)^2/h\nu. \quad (2.2)$$

Constanta B is the slope of the Tauc edge which reflects some disorder of the samples. Usually, this constant depends on the width of the localized states in the band gap, a fact explained with the homopolar bonds' presence in the chalcogenide glasses. Thus, Tauc plots of $(\alpha h\nu)^{1/2}$ versus $(h\nu)$ should be linear and extrapolate to value of the optical gap, E_g .

The edge absorption is determined by the relation $\alpha \cdot h\nu = \text{const}(h\nu - E_g)^2$, where $h\nu$ is the energy of light quantum, α is the absorption coefficient.

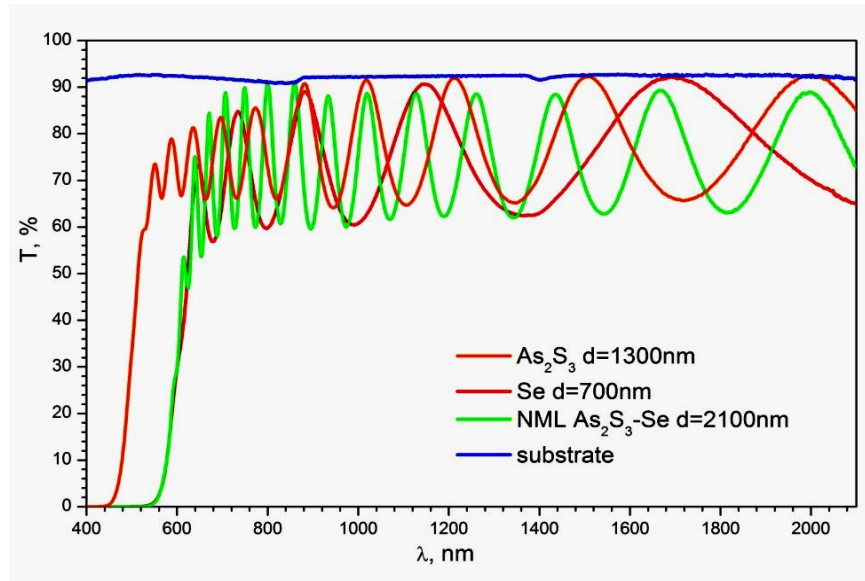


Fig. 2.20. The optical transmission spectra T of films vs. wavelength λ .

The optical transmission spectra of $\text{Ge}_5\text{As}_{37}\text{S}_{58}$ -Se studied films are presented in Fig. 2.21.

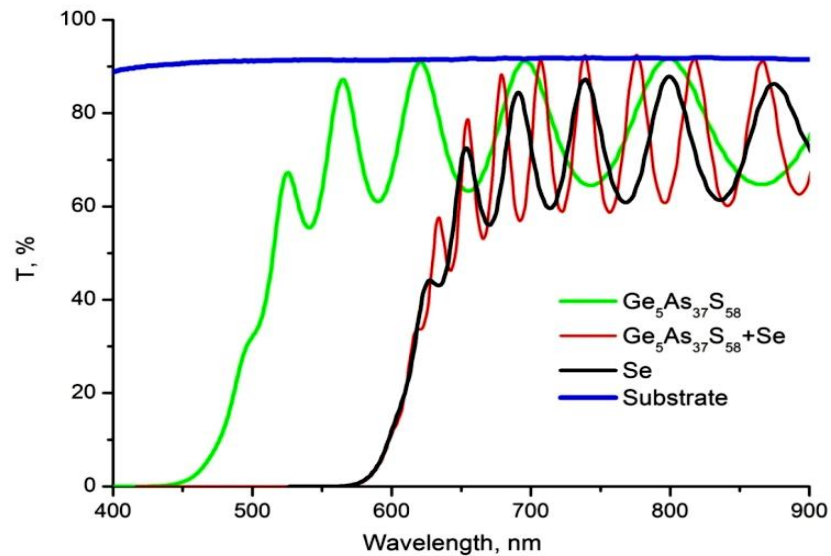


Fig. 2.21. Optical transmission spectra of $\text{Ge}_5\text{As}_{37}\text{S}_{58}$, Se layers and $\text{Ge}_5\text{As}_{37}\text{S}_{58}$ -Se NML.

As can be seen from comparison of Fig. 2.20 and Fig. 2.21 the optical transmission spectra for As_2S_3 -Se and $\text{Ge}_5\text{As}_{37}\text{S}_{58}$ -Se NML are similar. The absorption edge of $\text{Ge}_5\text{As}_{37}\text{S}_{58}$ -Se NML practically coincides with the absorption edge of Se. It is necessary to note the high optical quality of NML (in sites of interference maxima films transmission coincides with the substrate transmission) and presence of scattering in Se layer (transmission values of interference maxima for Se layers are smaller than values of substrate transmission).

Transmission spectra of $\text{Ge}_5\text{As}_{37}\text{S}_{58}$, Se layers and $\text{Ge}_5\text{As}_{37}\text{S}_{58}$ -Se NML (Fig. 2.21) show a broad transparency region at long wavelengths side and significant drop of transparency in the region of 400–650 nm due to the increase of absorption.

The optical transmission spectra of $\text{As}_2\text{S}_3:\text{Mn}$ 2 wt% –Se NML are shown in Fig. 2.22. E_g values were: Se — 1.9 eV, $\text{As}_2\text{S}_3:\text{Mn}$ 2 wt% and $\text{As}_2\text{S}_3:\text{Mn}$ 2 wt% –Se NML — 1.93 eV. Absorption edge of the $\text{As}_2\text{S}_3:\text{Mn}$ 2 wt% –Se NML is close to the absorption edge of Se multilayers (Fig. 2.22).

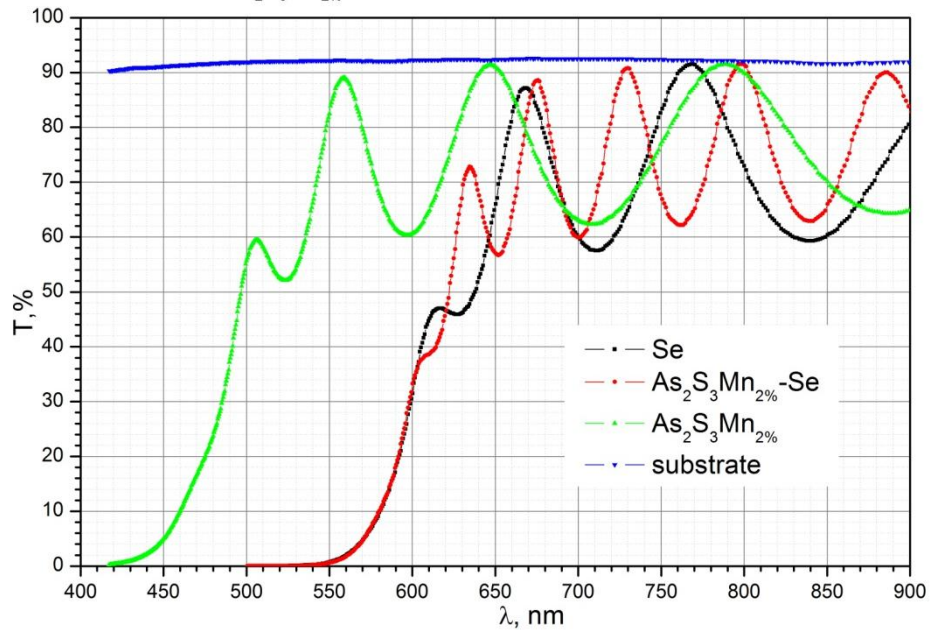


Fig. 2.22. The optical transmission spectra of $\text{As}_2\text{S}_3:\text{Mn}$ 2 wt% –Se NML.

The spectral dependence of the refractive index $n(\lambda)$ calculated together with the film thicknesses were obtained by the Swanepoel method [106].

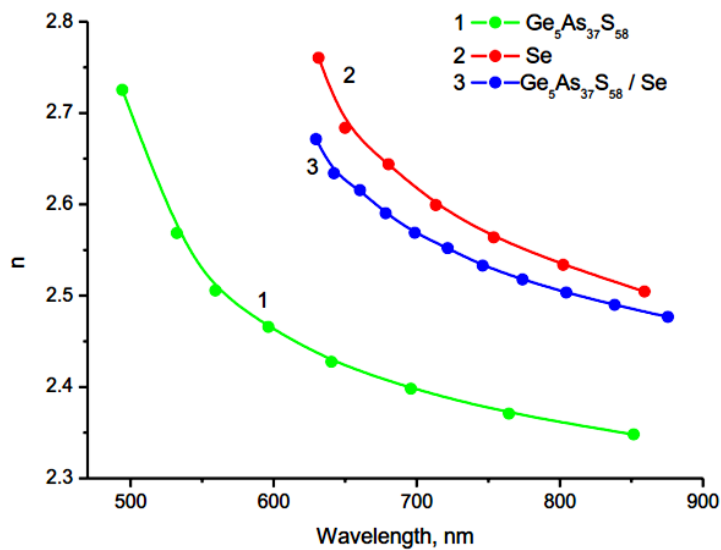


Fig.2.23. Spectral dependencies of refractive index n of $\text{Ge}_5\text{As}_{37}\text{S}_{58}\text{-Se}$ NML.

The refractive index n as a function of wavelength was analyzed on the basis of the Wemple-DiDomenico dispersion model [71], which is based on the single-oscillator approach. According to this model the refractive index n is related to energy of incident photon E by equation $n^2 - 1 = E_d \cdot E_0 / (E_0^2 - E^2)$, where E_0 is single oscillator energy, E_d is dispersion energy. In this expression E_0 determines the position of effective oscillator connected with average energy gap. E_d is the dispersion energy characterizing the strength of interband transitions.

To obtain E_0 and E_d we plotted dependences $(n^2 - 1)^{-1} = f(E^2)$ and then performed least squares fitting method to the straight line (see Fig. 2.24). Optical band gap E_g was determined from Tauc law, using the construction in the coordinates $(\alpha \cdot hv)^{1/2} = f(E)$.

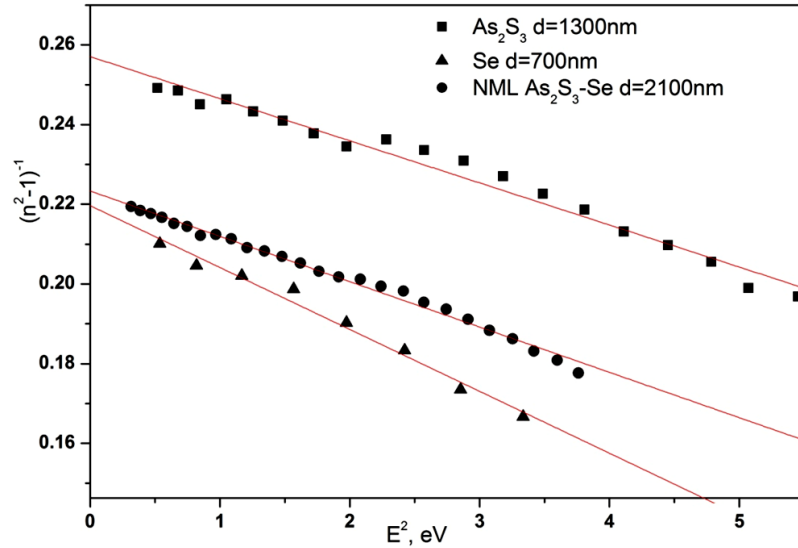


Fig. 2.24. Plot of $(n^2 - 1)^{-1}$ on E^2 for the E_0 , E_d parameters determination by single oscillator model.

The material of interest in this experiment was to compare the optical parameters of the NML $\text{As}_2\text{S}_3\text{-Se}$ with different thickness modulation periods D (the total thickness of one As_2S_3 and one Se nanolayers). Single-oscillator model parameters and E_g obtained for Se , As_2S_3 and NML $\text{As}_2\text{S}_3\text{-Se}$ for three modulation periods are presented in Table 2.1.

Table 2.1. Single oscillator model parameters for NML $\text{As}_2\text{S}_3\text{-Se}$.

D, nm	d, nm	n (0)	E_d , eV	E_0 , eV	E_g , eV
41	2080	2.30	18.34	4.29	1.95
20	2100	2.34	19.84	4.43	1.95

13	1370	2.38	19.46	4.18	1.95
----	------	------	-------	------	------

From the data in Table 2.1 it is seen that refraction index increases with decreases of the thickness modulation period. Larger refractive index is caused by more polarizability of media. However, the dispersion parameter E_d does not follow for the refraction index and has maximum value 19.84 eV at $D=20$ nm. The oscillator energy E_0 behavior is the same although the optical band gap E_g , which according the model $E_g \approx 2E_0$, maintains constant value 1.95 eV.

To check the influence of ChG conformity on the optical parameters we calculated them for NML $As_{37}S_{58}Ge_5$ -Se with total thickness ~ 3000 nm. Thicknesses of constituent $As_{37}S_{58}Ge_5$ and Se layers were 16 and 14 nm, respectively. The parameter calculation was the same as we described above. The results are presented in Table 2.2

Table 2.2. Single oscillator model parameters for NML $As_{37}S_{58}Ge_5$ -Se.

Composition	$n(0)$	E_d , eV	E_0 , eV	E_g , eV
Se	2.28	19.09	3.74	1.92
$As_{37}S_{58}Ge_5$	2.24	18.29	4.57	2.27
$As_{37}S_{58}Ge_5$ -Se	2.37	17.67	3.84	1.92

It can be seen from the data given in this Table 2.2 that E_0 scales well with the optical band gap ($E_0 \approx 2E_g$) for $As_{37}S_{58}Ge_5$ layers and for NML $As_{37}S_{58}Ge_5$ -Se. E_0 for Se layers exhibits $\sim 3\%$ less than value of $2E_g$.

According the Wemple-DiDomenico model the dispersion energy, E_d , relates to other physical parameters of the material through the following empirical relationship: $E_d(\text{eV}) = \beta \cdot N_c \cdot Z_a \cdot N_e$, where N_c is the effective coordination number of the cation nearest-neighbor to the anion, Z_a is the formal chemical valency of the anion, N_e is the effective number of valence electrons per anion and β is a two-valued constant with either an ionic or a covalent value. Based on the assumptions of glass stoichiometry, any difference in E_d derived by the Wemple-DiDomenico model will be likely due to the difference in N_c , which indicates the structure of the glass network [111]. The explanation suggested in the case of Se, the amorphous form the chain-chain bonding increases the effective coordination number above the nearest-neighbor value, and these interactions are effectively lost, or at least greatly reduced. The following optical effect is a reduction in oscillator strength of lone-pair to conduction band transitions.

In conclusion, the optical parameters for NML integrally and constituent nanolayers are calculated on the base of single-oscillator model. It was found that constituent nanolayers are well described by this model independent on composition. Optical parameters of NML are declined from single-oscillator model which manifest nanostructuring of the samples.

To study the influence of the temperature and illumination on the optical constant of $\text{As}_2\text{S}_3\text{-Se}$ NML and constituents nanolayers, the samples with different thicknesses were heated at 70 and 90°C, and illuminated at $\lambda=525$ nm during 20 min. These experimental parameters were chosen to prevent the development of recording process on the samples under study.

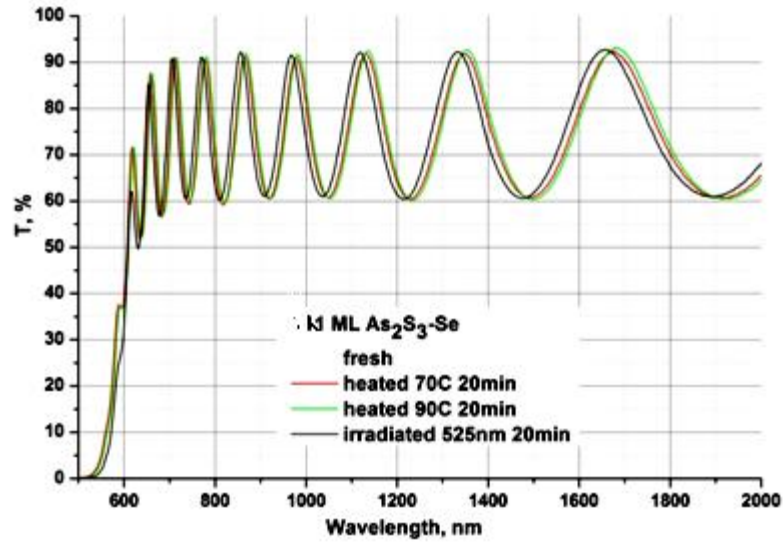


Fig 2.25. The transmission spectra of $\text{As}_2\text{S}_3\text{-Se}$ NML with total thickness 1370 nm.

In Fig. 2.25 and 2.26 the transmission spectra for two types of samples are presented. From these figures one can see that the heating and irradiation shift the edge of spectra to shorter wavelengths. Other words, the NML is bleached under there kinds of excitation.

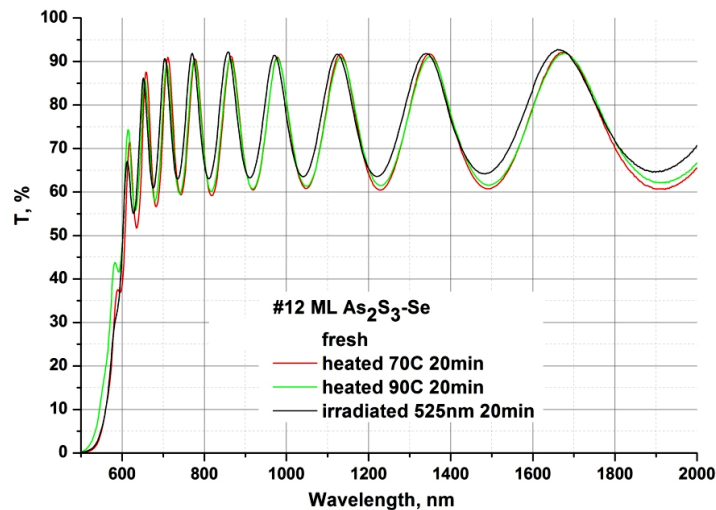


Fig. 2.26. The transmission spectra of $\text{As}_2\text{S}_3\text{-Se}$ NML with total thickness 1420 nm.

From the transmission spectra of the nanolayers of Se, As_2S_3 and NML $\text{As}_2\text{S}_3\text{-Se}$, the refractive index and thickness were calculated according to the Swanepoel method, the optical band gap E_g - by the Tauc method. Calculated parameters are presented in Table 2.3.

Table 2.3 Parameters calculated from the transmission spectra.

		d, nm	n ($\lambda=1000$ nm)	$E_{g\ opt}$, eV
NML As ₂ S ₃ -Se Fig 2.25.	Fresh As ₂ S ₃	740±6	2.32±0.02	2.35
	Fresh Se	630±9	2.50±0.02	1.92
	Fresh ML As ₂ S ₃ -Se	1370±20	2.46±0.013	1.95
	heated 70 ⁰ C 20 min	1357±15	2.49±0.02	
	heated 90 ⁰ C 20 min	1365±8	2.495±0.02	
	irradiated 525 nm 20 min	1369±15	2.50±0.02	
NML As ₂ S ₃ -Se Fig 2.26.	Fresh As ₂ S ₃	960±9	2.28±0.02	2.35
	Fresh Se	445±10	2.48±0.01	1.90
	Fresh ML As ₂ S ₃ -Se	1420±15	2.37±0.02	1.95
	heated 70 ⁰ C 20 min	1395±12	2.43±0.02	
	heated 90 ⁰ C 20 min	1405±12	2.42±0.02	
	irradiated 525 nm 20 min	1390±12	2.45±0.02	

The spectra of refractive index of the As₂S₃-Se NML are arranged between the spectra of refractive index of the As₂S₃ (lower curve on Fig. 2.27a) and Se (upper curve on Fig.2.27a).

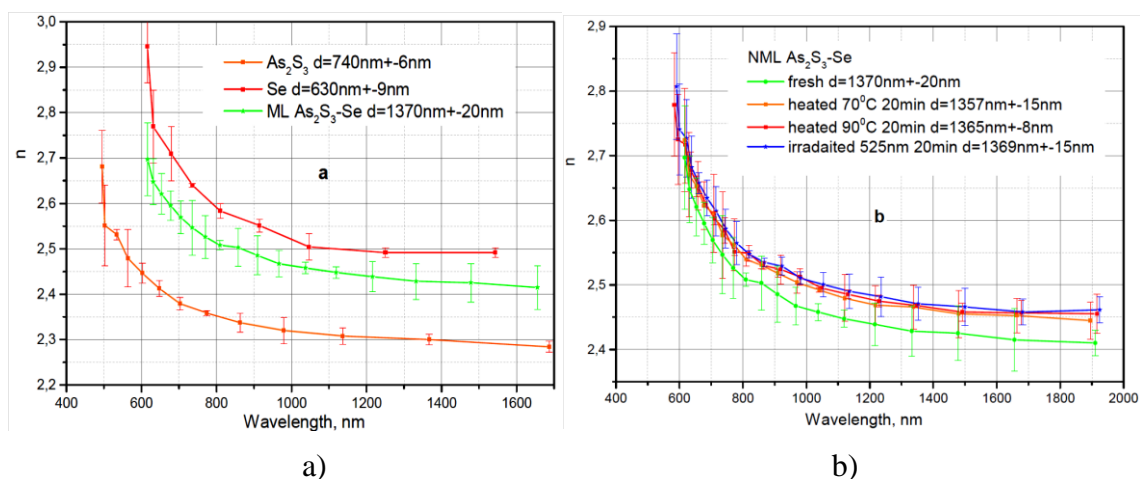


Fig. 2.27. a). The spectral dependence of the refractive index of the As₂S₃-Se NML; b) The spectral dependence of the refractive index of the As₂S₃-Se NML at different kind of excitations.

The absorption spectrum of PEPC -10% CHI₃ (Fig. 2.28) exhibits in the visible range an increase in absorbance (A) at $\lambda = 400$ nm and, which is more important, a new band at 640–650 nm associated with the formation of a charge-transfer complex between carbazole cycles and triiodomethane CHI₃ [112, 167], whose degradation gives colored products. This results in the

networking of the irradiated portions of the photoresist layer. As found by instrumental analysis techniques, an increase in A at $\lambda = 640$ nm is proportional to the network density of the polymeric layer (Fig. 2.28).

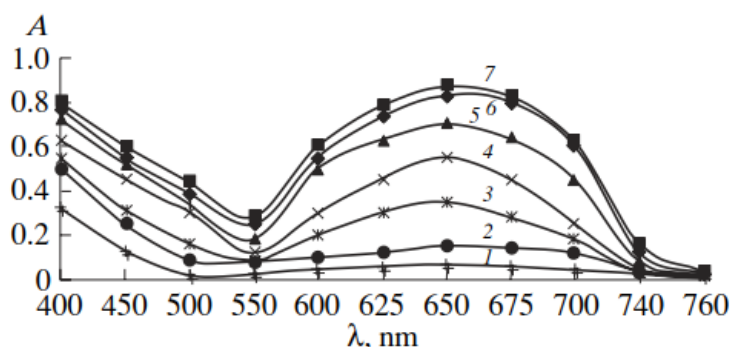


Fig. 2.28. Absorption spectra of a photopolymer layer from PEPC containing 10% CHI_3 upon irradiation by the PRK-4 (220W, 0.2-0.4 μm) mercury lamp. Irradiation time, min:
(1) 0, (2) 3, (3) 6, (4) 10, (5) 15, (6) 20, and (7) 30.

It has also been shown that the rate of photoinduced networking depends on the polymeric layer thickness and temperature. For example, photopolymers of a given thickness based on PEPC or CAM are crosslinked during 10–15 min at $T = 30^\circ\text{C}$ or 1–3 min at $T = 60^\circ\text{C}$.

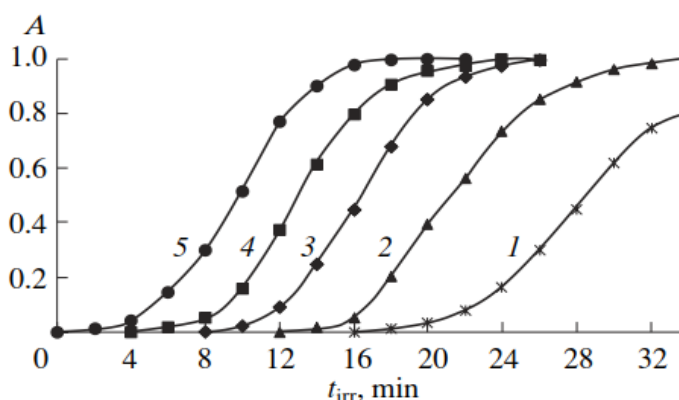


Fig. 2.29. Absorbance $A_{640\text{ nm}}$ as a function of irradiation time for PEPC photopolymer layers of different thickness, μm : (1) 1, (2) 3, (3) 5, (4) 8, and (5) 10; $E_{\text{irr}} = 15.5\text{ mW cm}^{-2}$, $\text{CHI}_3 = 10\text{ wt \%}$.

An increase the thickness accelerates the crosslinking of polymer. As follows from Fig. 2.29 an increase in the polymer layer thickness from 1.0 to 10.0 μm decreases the crosslinking time from 30–35 to 10–12 min. The photocrosslinking time was taken as the time when the $A = f(t_{\text{irr}})$ curve begins to flatten out.

In general, the photosensitivity (S) of recording media was determined as the reciprocal of the exposure [110]:

$$S = \frac{1}{H} \text{ or } S = \frac{1}{E\tau}, \quad (2.3)$$

where H is the exposure in Ws cm^{-2} , E is the intensity of illumination in mW cm^{-2} , and τ is the illumination time, in S , required for crosslinking more than 90% of the photopolymer.

Like the crosslinking time, the layer sensitivity depends on the photopolymer thickness, as well as on the illuminance E and the spectral composition of the band at which the material is exposed. As the photopolymer thickness increases from 1.0 to 10.0 μm , the photosensitivity increases more than tenfold reaching a saturation value at the thickness greater than 5–6 μm . The contrast index C was determined by the expression [110]:

$$C = \frac{A_{\max} - A_{\min}}{\log H_{\max} - \log H_{\min}} \quad (2.4)$$

where A_{\max} and A_{\min} are the absorbance after and before UV irradiation, respectively, and H_{\max} and H_{\min} are the corresponding values of exposure.

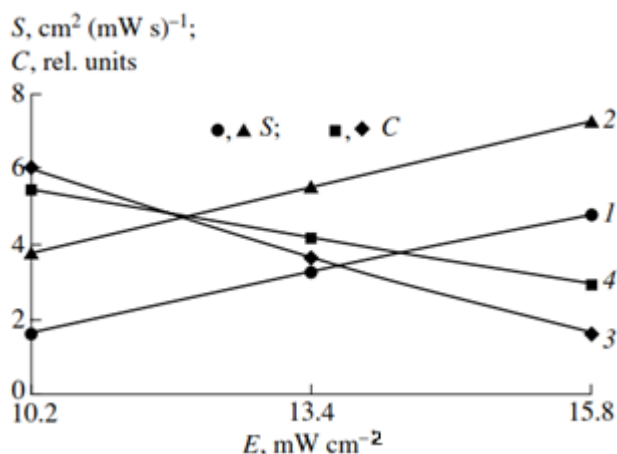


Fig. 2.30. Dependence of the photosensitivity S (1) and (2) and the contrast index C (3) and (4) on illuminance: (2) and (3) PEPC and (1) and (4) CAM: OMA.

The study of the dependence of the photosensitivity and the contrast index on the illuminance showed that an increase in E from 10.2 to 15.5 mW cm^{-2} increased the photosensitivity of the media more than twofold for both PEPC and CAM: OMA (Fig. 2.30). The reverse was observed for the contrast. An increase in the illuminance E from 10.2 to 15.8 mW cm^{-2} decreased the contrast index by a factor of 2.3–3.0 (Fig. 2.30), a result that is consistent to the behavior observed in silver halide photography.

It was of interest to examine the dependence of the photosensitivity on the iodoform concentration c in photopolymer. As follows from Fig. 2.31 the photosensitivity increases more than threefold with an increase in the CHI_3 concentration in the range from 5 to 10–12 wt % and de-

creases noticeably with a further increase in the CHI_3 concentration. It should be noted that the photopolymer optical properties deteriorate at CHI_3 concentrations higher than 12% owing to CHI_3 crystallization.

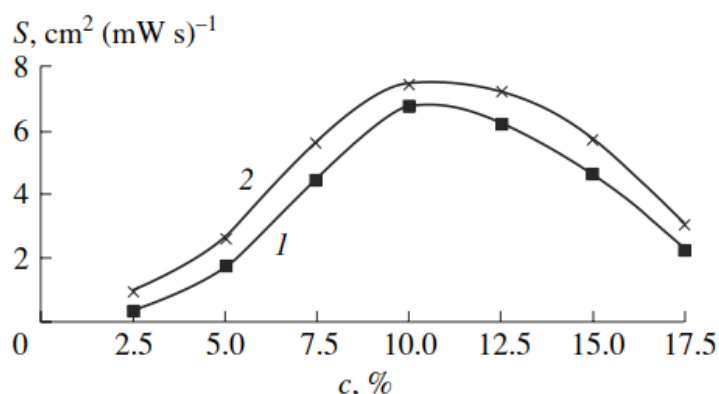


Fig. 2.31. Dependence of the photosensitivity of (1) CAM: OMA and (2) PEPC photopolymer layers on the CHI_3 concentration, $E_{\text{irr}} = 15.5 \text{ mW cm}^{-2}$.

To analyze photoinduced variations of optical properties the poly-epoxypropylcarbazole (PEPC), poly-epithiopropylcarbazole (PETPC) films were exposed to UV-irradiation of the ultraviolet quartz lamp DRT-230 ($E = 3.3 \text{ mW/cm}^2$) and Ar^+ ion laser ($H = 54 \text{ J/cm}^2$).

Examinations of transmission spectra of polymer films on the basis of PEPC and PEPC:PETPC showed that the films are transparent in the whole visible band ($T = 82\%$ in the range of wavelengths 450–900 nm) (Fig. 2.30).

To investigate the influence of irradiation on optical properties of the deposited films, dependences of the kinetics of photoinduced absorption peak on the irradiation time were measured. After irradiation by Ar^+ -laser as well as by UV light the films became colored in the green color with the appearance of an absorption band with the peak at 652 nm and the simultaneous shift of the absorption edge to the long-wave field. The transmission spectra of PEPC and PEPC:PETPC (1:1) films (the thickness $1.6 \mu\text{m}$) before and after irradiation by Ar^+ ion laser are shown in Fig. 2.32a. The transmission spectra of PEPC films before and after UV-irradiation are presented in Fig. 2.32b.

As it is seen from Fig. 2.32, after irradiation the absorption edge shifts to the long-wave field and a new absorption band appears at wavelength 652 nm. The nature of this band is related to the charge-transfer complex formation between carbazole nuclei and iodoform CHI_3 . These copolymers form intramolecular charge transfer complexes which are deeply colored and extend the spectral response of these materials into the visible region.

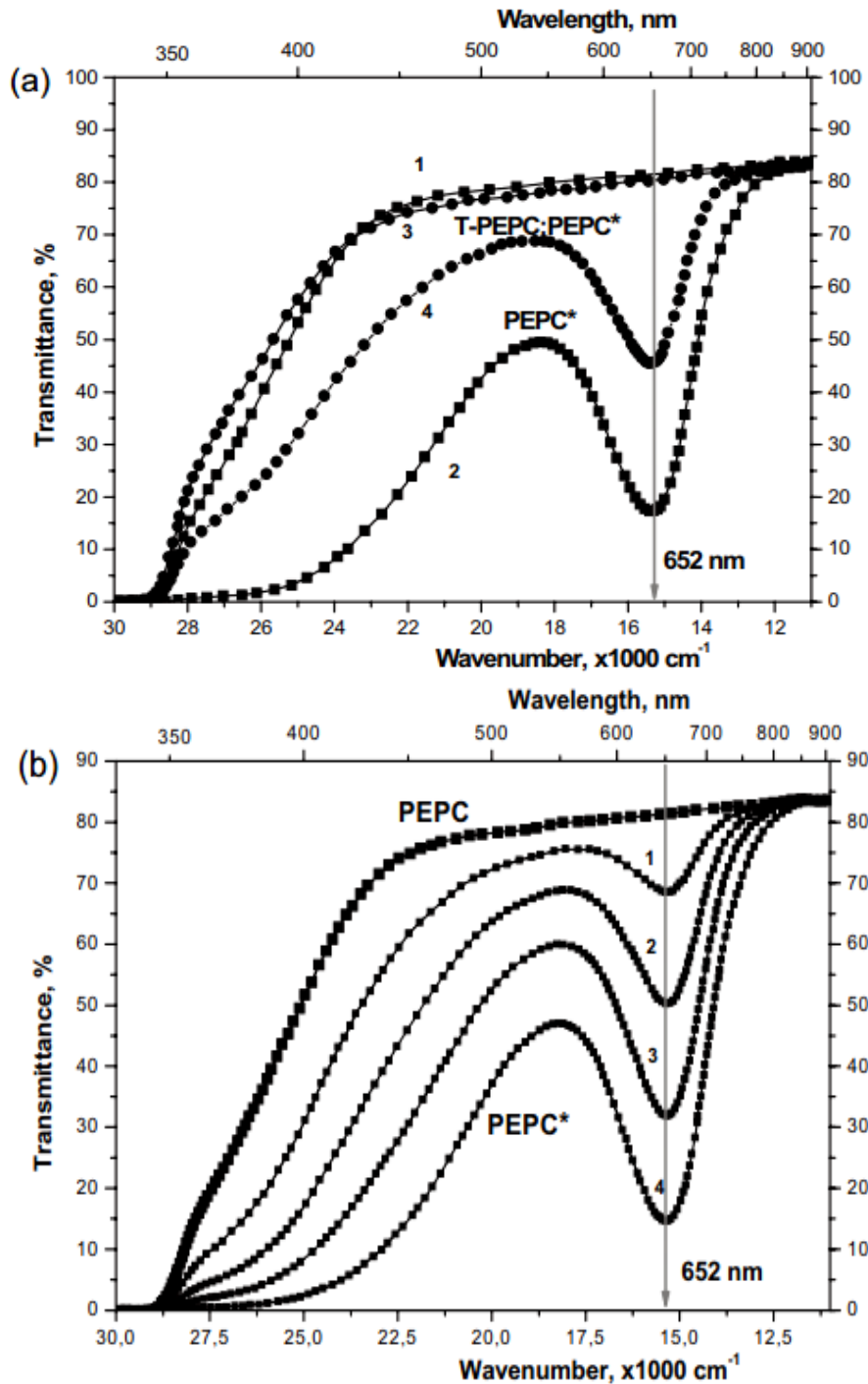


Fig. 2.32. The transmission spectra (a) of PEPC (1) and PEPC:PETPC (3) films before and after ($*$) irradiation by Ar^+ ion laser (2, 4, respectively); (b) PEPC films before and after ($*$) UV irradiation during: (1) 3, (2) 10, (3) 25, and (4) 60 min.

Decomposition of CHI_3 leads to the formation of the colored products. Then the latter leads to the structuring of the irradiated sections of a photosensitive layer. Growth of absorption value at $\lambda = 652 \text{ nm}$ is proportional to the degree of structuring of polymer layer. After the storage in darkness of the samples of PEPC and PEPC:PETPC films, the “after-effect” of the fur-

ther self-amplification of the absorption peak was observed. The spectra of unexposed area of the films remained unchanged at the darkness storage.

The UV-Vis transmission spectra of obtained poly(PEPC-co-DO) azopolymer films with different DO content (from 10 to 60 wt%) and equal thickness $d=1600$ nm are presented in Fig. 2.33. In Fig. 2.34 the transmission spectra of obtained poly(PEPC-co-DO) azopolymer films with different film thickness (from 250 to 2160 nm) and equal DO content 30 wt% are presented.

The maximum of the absorption peak for this azopolymer lies at wavelength of 450 nm, which is characteristic for DO azo dye classified as pseudo-stilbene [113]. It confirms azo coupling reaction of PEPC with DO. In Fig. 2.33 the wavelength used for recording (473 nm) and reading (650 nm) of phase grating are shown the same. The absorbance at wavelength of 473 nm is close to maximum, so this wavelength can be used for recording, whereas red laser at wavelength of 650 nm is in transparent region of spectra. The azopolymer film formation was carried out in the dark to obtain the film in its *trans* state of isomer.

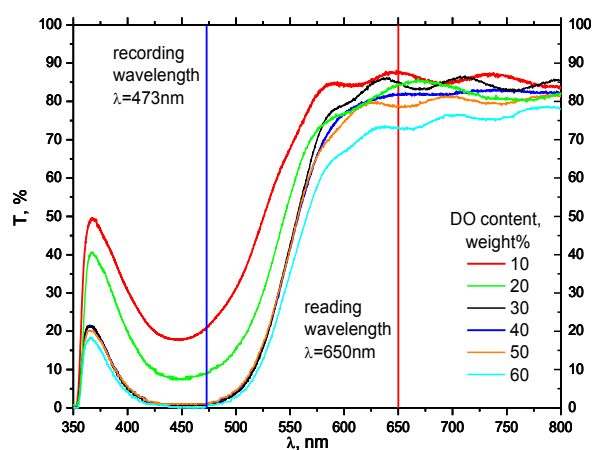


Fig. 2.33. UV-Vis transmission spectra of poly(PEPC-co-DO) films (the film thickness $d=1600$ nm) with different DO content. The blue (473 nm) and red (650 nm) lines mark the wavelength used for recording and reading of phase grating, respectively.

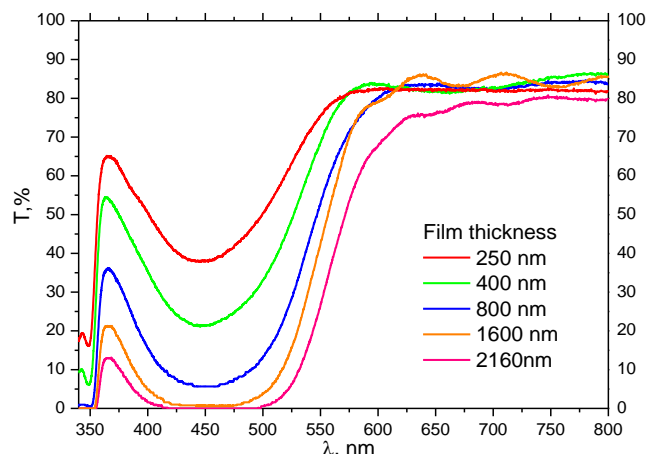


Fig. 2.34. UV-Vis transmission spectra of poly(PEPC-co-DO) films with different film thickness. DO content is 30 wt%.

The optically induced changes in the azopolymer film transmittance were studied by comparison of non-exposed and exposed films.

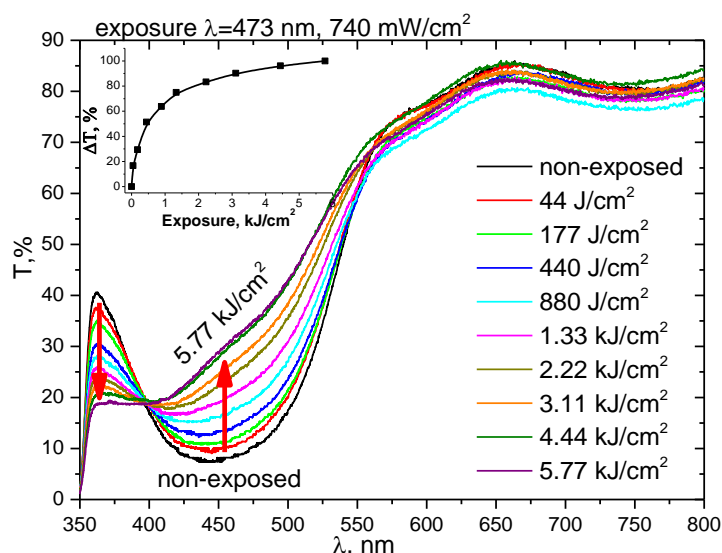


Fig. 2.35. Photoinduced spectra changing of poly(PEPC-co-DO) film with DO content 20 wt% and film thickness $d=1600$ nm.

An initial transmittance measurement of as-deposited films was made, and then the film was exposed to an expanded 473 nm single laser beam (diameter 3.4 mm, intensity 740 mW/cm^2) from a 100 mW DPSS single mode laser with linear polarization. This was immediately followed by a transmittance measurement. *Trans-cis* isomerization can occur by optical excitation into the trans-isomer absorption band. This *trans-cis* isomerization process is well-known in a number of photochromic dyes including the azobenzene dyes [114, 175].

Fig. 2.35 shows the evolution of the transmittance spectrum upon irradiation with 473 nm laser light, which demonstrates the photo-induced isomerisation of poly(PEPC-co-DO) film with DO content 20 wt% and film thickness $d=1600$ nm after exposure 4.44 kJ/cm^2 (c. 100 minutes). The *cis*-isomer can thermally relax back to the *trans*-isomer or this process can occur via optical excitation.

The peak at about 450 nm corresponds to the *trans* form of isomer, which increase upon irradiation. The series of spectra presented correspond to the 473 nm laser light photoisomerization of the *trans* isomer into the *cis*. The inset shows the change of transmittance at wavelength 450 nm (in %) vs exposure. The appearance of a second peak at ~ 360 nm (indicated by arrow) can be attributed to the *cis*-isomer absorption [115]. As it can be seen, the used $\lambda=473$ nm is close to the *trans*-isomer peak absorption coefficient; hence, photo-induced changes from *trans-cis* isomerization are expected to be faster than those that could occur if a longer wavelength was used. We show in the Fig. 2.35 that the absorption change increases with exposure and it saturates at exposure 4.44 kJ/cm^2 . The saturation is likely to appear due to equilibrium between opti-

cally induced *trans-to-cis*-isomerization by exciting into the trans-isomer band peaked at wavelength of 450 nm and thermal relaxation from the *cis-to-trans*-isomer.

b. Raman Spectroscopy

The aim of this part is to extend the research of nanostructuring properties of the As_2S_3 -Se NML on the dimensions of constituent layers by measuring the Raman spectra. The purpose of this research is to investigate the structural changes in the As_2S_3 -Se MN and, in particular, to examine the relative contribution of As_2S_3 and Se to nanostructuring. We have selected Se and As_2S_3 nanolayers as components for the As_2S_3 -Se MN because of their known Raman spectra. In addition, while chalcogens are good glass formers over a wide range of composition, a large majority of studies have focused on the stoichiometric chalcogenide As_2S_3 due to its good stability. Nevertheless, the formation of a nano-structure such as As_2S_3 -Se is of much interest as the addition of Se nanolayer allows us to tune and change the optical transparency and to improve the recording properties.

FT-Raman spectra were measured on a Bruker IFS 55 with a Bruker FRA 106 Raman module [116]. Near-IR Nd: YAG laser with a wavelength of 1064 nm ($E = 1.17$ eV) was used as excitation source. All measurements were performed at room temperature in back-scattering geometry.

Table 2.4. Multilayers nanostructure As_2S_3 -Se thicknesses.

	Test 1	Test 2	Test 3
Total thickness	2.5 μm	2.5 μm	1.5 μm
Number of nanolayers	50	100	100
D	50 nm	25 nm	15 nm
$d_{\text{As}_2\text{S}_3}$	30 nm	15 nm	8 nm
d_{Se}	20 nm	10 nm	7 nm
$d_{\text{As}_2\text{S}_3}$	1.5 μm	1.5 μm	0.8 μm
d_{Se}	1.0 μm	1.0 μm	0.7 μm

The Raman spectra of three different As_2S_3 films corresponding to three thickness modulation periods ($D = 15; 25; 50$ nm) of the NML are shown in Fig. 2.36. Each Raman spectrum was fitted using a series of Gaussian peaks with a width appropriate for glasses. Table 2.5 provides a list of frequency as assignments of the known structural units in the As_2S_3 glass. These assignments were used to perform the peak-fitting analyses and to compare the relative contribution of each structural unit of As_2S_3 . The material of interest is the As_2S_3 -Se NML with three thickness modulation periods D pointed in Table 2.4.

Table 2.5. Vibrational mode frequencies.

Peaks As ₂ S ₃ from [215]	Peak assignments from [117]
135.4	As-As units
145.0	145.7, $\alpha(\beta)$ -As ₄ S ₄
169.1	171.4, <i>p</i> - As ₄ S ₄
189.4	182.6, $\alpha(\beta)$ -As ₄ S ₄
223.1	221.0, $\alpha(\beta)$ -As ₄ S ₄
233.7	238.4, <i>p</i> - As ₄ S ₄
274.2	271.0, $\alpha(\beta)$ -As ₄ S ₄
344.6	341.5, $\alpha(\beta)$ -As ₄ S ₄
362.0	363.0, As-As units; $\alpha(\beta)$ -As ₄ S ₄
495.0	495.0, S-S chains

The Raman spectra reveal two main vibration bands located at 130–250 and 310–390 cm⁻¹ (Fig. 2.36) which can be assigned to the vibration of the As-As containing units, such as As₄S₄, together with an additional band with maxima at 495 cm⁻¹ [117]. These two bands indicate that S-S containing structural units such as -S-S-chains are present and connect individual S-S chains (495 cm⁻¹). Appearance of these structural units containing homopolar bonds in the structure of the evaporated As₂S₃ can be explained by the thermal dissociation reaction during evaporation, where a non-stoichiometric As₄S₄ unit contains a homopolar As-As bond. A weak band near 495 cm⁻¹ indicates small numbers of S-S bonds. Due to fast condensation of vapours on the cold (at room temperature) substrate these structural units are frozen and thus responsible for the photo-sensitivity of these films.

From Fig. 2.36 it is clear that the peak positions coincide for three different As₂S₃ parts of the samples and correspond to results of other authors [118]. The intensities of all peaks are maxima for the maximal thickness of As₂S₃ $d_{As_2S_3} = 1.5 \mu\text{m}$. In test 2 and test 3, the curves of Raman spectra are very close, but the plot of the sample with $d_{As_2S_3} = 1 \mu\text{m}$ (test 2) lies lower than that for the sample with $d_{As_2S_3} = 0.8 \mu\text{m}$ (test 3).

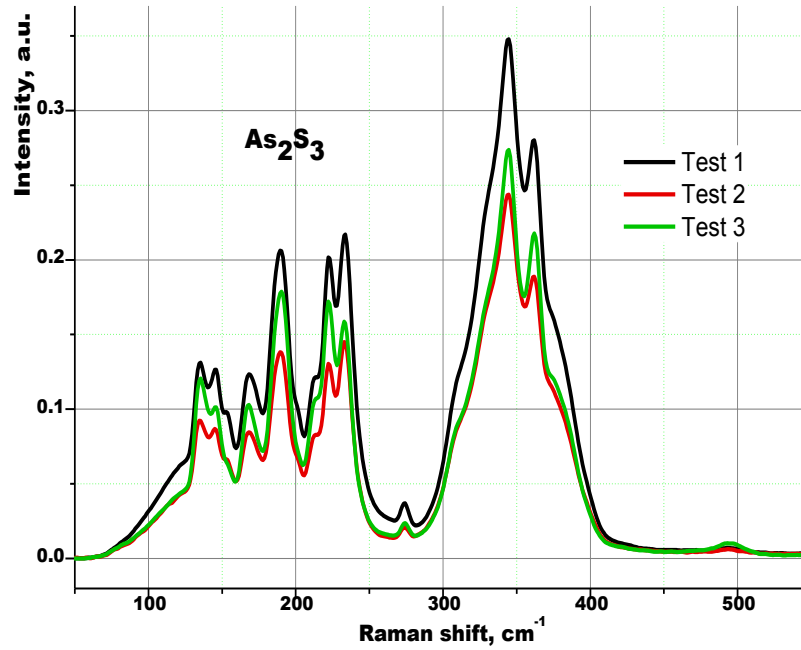


Fig. 2.36. Raman spectra of As_2S_3 from three NMLs.

Raman spectra of the fresh evaporated $\text{Ge}_5\text{As}_{37}\text{S}_{58}$ films are presented in Fig. 2.37. The Raman spectrum of $\text{Ge}_5\text{As}_{37}\text{S}_{58}$ glass is almost similar to the spectrum of binary As_2S_3 glass. The main broad band in the spectra of As_2S_3 and $\text{Ge}_5\text{As}_{37}\text{S}_{58}$ glasses at 342 cm^{-1} corresponds to the band characteristic for $\text{As}_x\text{S}_{100-x}$ glasses of different compositions. The bands at 321 , 343 and 361 cm^{-1} that are present in the decomposition of main band are typical to the $\text{As}_{42}\text{S}_{58}$ glass enriched by arsenic as compared to the stoichiometric As_2S_3 glass. The 342 cm^{-1} band, as generally accepted, corresponds to the symmetric vibrations of pyramidal $\text{As}(\text{S}_{1/2})_3$ units. The band at 361 cm^{-1} corresponds to the intensive mode of crystalline As_4S_4 [119–121].

The most intensive peak at 342 cm^{-1} observed either in $\text{Ge}_5\text{As}_{37}\text{S}_{58}$ thin film spectra or in bulk glass spectra consisted of two overlapped parts originated from pyramidal $\text{AsS}_{3/2}$ and tetrahedral $\text{GeS}_{4/2}$ units which constitute structural backbone of the glass. The shape of this peak in the film spectrum is more diffuse which points on higher degree of chemical disorder in evaporated films compared to initial glasses. A certain amount of As_4S_4 monomers is present in the film as indicated by the presence of low-frequency modes (bands 361 , 152 , 167 , 188 and 213 cm^{-1}) in the film spectrum (Fig. 2.37).

The bulk glass and thin film spectra also contain mode (band 275 cm^{-1}) which is characteristic mode of As_4S_3 monomers. Peak at 377 cm^{-1} in the bulk glass spectrum and thin film can be ascribed to the oscillations of edge-shared (ES) tetrahedra or medium range order structures consisted of AsS pyramids along with corner shared (CS) or ES tetrahedra GeS [122–124]. A broad band

near 245 cm^{-1} was observed earlier in Raman spectra of $\text{Ge}_x\text{As}_{40-x}\text{S}_{60}$ glasses for x values higher than 24 [121]. As pointed by authors of [122] the emerging and ascending of 245 cm^{-1} band with raising x number was a result of increasing the ratio of Ge-Ge vs. As-As bond concentration. The Ge-Ge bonds were stated to be found either in $\text{Ge}_2\text{S}_{6/2}$ ethan-like units or in $\text{Ge-S}_{4-n}\text{-Ge}_n$ tetrahedra.

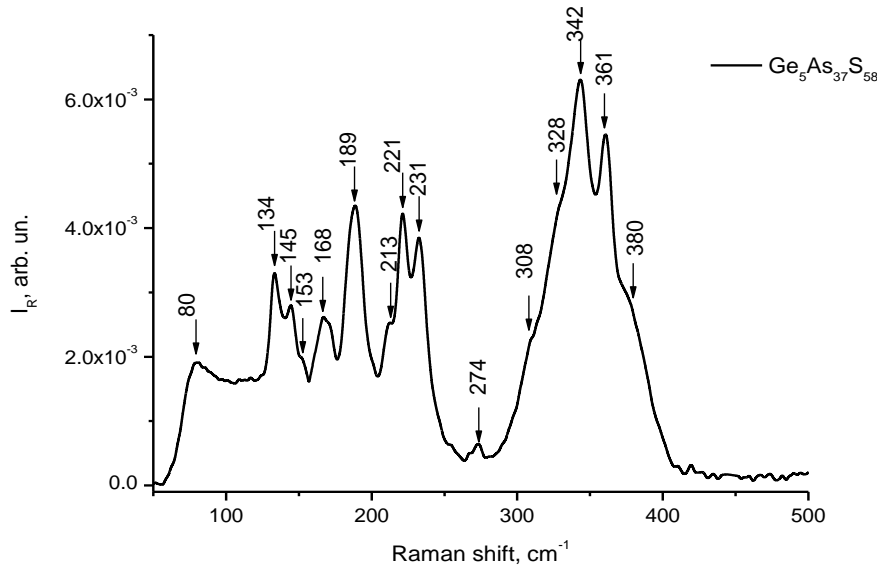


Fig. 2.37. Raman spectra $\text{Ge}_5\text{As}_{37}\text{S}_{58}$ layer.

The two overlapped peaks at 237 and 256 cm^{-1} was also observed in Raman spectra of glassy GeS_2 obtained under certain technological conditions [123]. Numerical calculations provided by authors [123] showed that although line at 256 cm^{-1} can be ascribed to oscillations in the ethan-like nanophase whereas the 237 cm^{-1} peak only present in vibration modes of three-fold coordinated GeS structures. Therefore, modes at 237 and 256 cm^{-1} were ascribed to oscillations in three-fold coordinated GeS structures. As pointed by authors [123], these structures may exist in the glass matrix in the form of crystalline GeS_2 nanophase of about $7\text{--}12\text{ \AA}$ in size. Modes at $70, 84, 494\text{ cm}^{-1}$ are related to vibrations of covalent S-S bonds. Weak traces of S_8 rings can be found in bulk glass as well as in evaporated film. They have vibrational modes at $150, 220$ and 474 cm^{-1} . Whereas line observed at 220 cm^{-1} can be ascribed to different structural units, the 475 cm^{-1} mode is characteristic of S_8 rings.

Fig. 2.38 shows the Raman spectra of separated Se parts of films constituents in NML (tests 1, 2, and 3). For all NML the Raman spectra of pure Se films exhibit a strong band at 251.1 cm^{-1} and weaker bands at 110 cm^{-1} and 131.5 cm^{-1} , which are specific for Se_8 rings and fragments of Se_8 rings containing 5 and 6 Se atoms [125]. The shoulder near 233 cm^{-1} corresponds to Se chains and is clearly seen for the thinnest NML test 3. It is known that Se is a not stable mate-

rial, but for the crystallization to occur, the size of Se films (clusters) should be greater than that of crystallites, which is probably 5–20 nm [126]. This requirement may be satisfied in the spatially-restricted test 1 and test 2, unlike test 3.

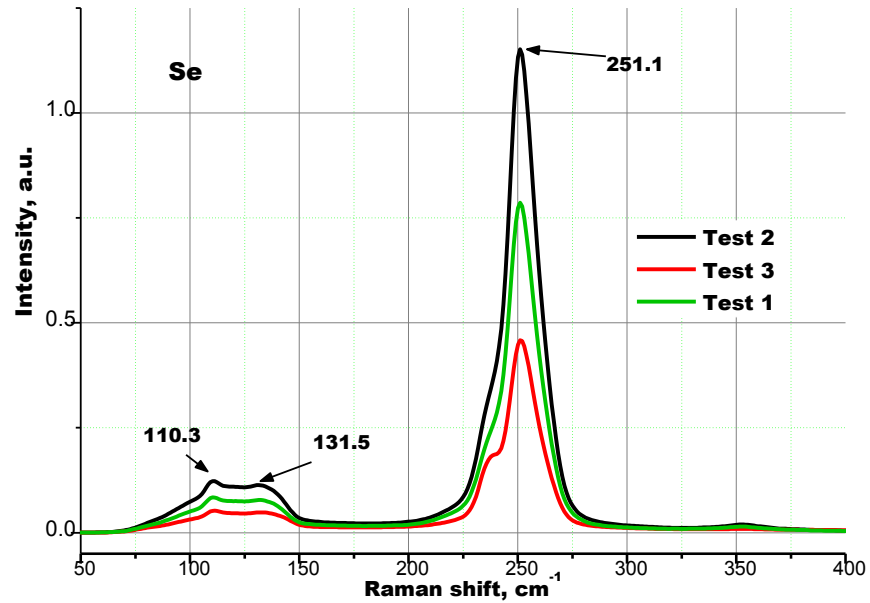


Fig. 2.38. Raman spectra of Se nanolayers from three As_2S_3 -Se NML.

The band at 251 cm^{-1} can be assigned to bond stretching vibrations and the band at 109 cm^{-1} to bond bending vibrations in the meandering chain. The shoulder that appears at 235 cm^{-1} can be associated with a small fraction of "pure" helical chains.

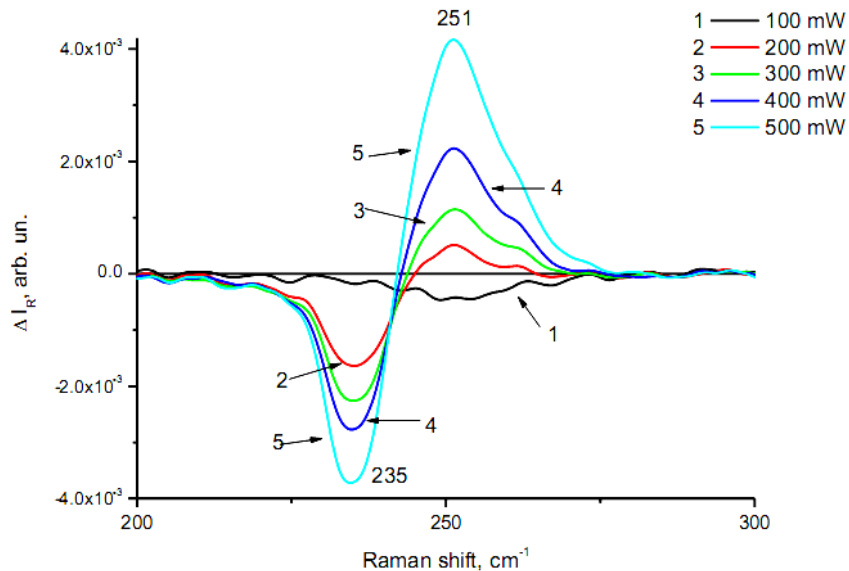


Fig. 2.39. Differential Raman spectra of Se layer in dependence on exposure (for different values of laser power, exposure time is 132 s) as compared to that at 50 mW laser power exposure.

From differential Raman spectra shown in Fig. 2.39 it can be seen that structure of Se films is changing under the action of light. With the exposure increase the intensity of the 235 cm^{-1} band is increasing and intensity of the 251 cm^{-1} band is decreasing and as is also for 80 and 109 cm^{-1} bands (not shown in Fig. 2.39). Changing of Se film structure under exposure (Fig. 2.39) shows that processes in Se (T_g value for Se is $\sim 35^\circ\text{C}$) trigger processes of mass transfer in $\text{Ge}_5\text{As}_{37}\text{S}_{58}$ -Se NML due to arising structural non-uniformity according to intensity distribution during grating recording. In our experiment, the S-S polarizations of recording beams do not create the conditions for vectorial mass transfer, for which the polarization along the grating vector is needed. Therefore, we can suppose that 6% depth of grating recorded in $\text{Ge}_5\text{As}_{37}\text{S}_{58}$ -Se is mainly the result of scalar deformations. Here it is necessary to note that mentioned features of light-sensitive chalcogenide-based nanomultilayers depend on composition of combined layers and on the nano-periodicity.

Fig. 2.40 gives the Raman spectra of the As_2S_3 -Se NML for three types of the samples under test. As is seen, the Raman spectrum for the NML incorporates of Raman spectra of separated films constituent of the As_2S_3 and Se NML. The position and shape of the peaks and their number says in favour of this.

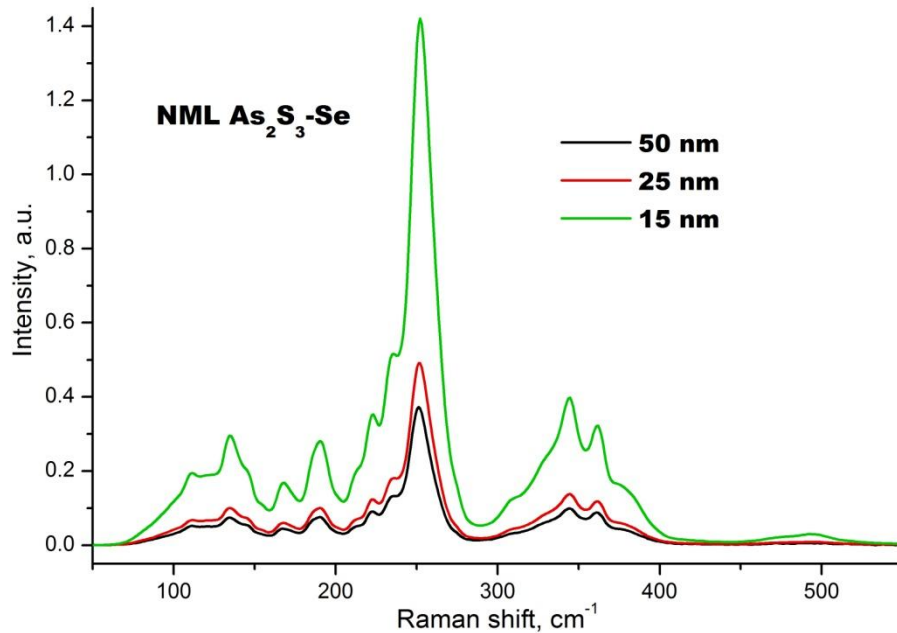


Fig. 2.40. Raman spectra of As_2S_3 -Se NML with modulation period $D = 50\text{ nm}$ (test 1), $D = 25\text{ nm}$ (test 2), $D = 15\text{ nm}$ (test 3).

From the comparison of the Raman spectra for the NML with different modulation periods, it is clear that the MNL with $D = 15\text{ nm}$ (test 3) has sharp and high-intensity peaks. These parameters of spectra (the peak sharpness and the arbitrary intensity) decrease with the thickness modula-

tion period increasing. This feature may be explained by the ordering of the NML structure. Lower the layer thickness leads to higher the degree of order of each constituent of the NML layers.

The Raman spectra of the $\text{As}_2\text{S}_3\text{-Se}$ NML measured after illumination by 525 nm during 20 min are shown in Fig. 2.41. The behaviour of Raman spectra after illumination is opposite the one before illumination in sense of the ordering of constituent layers. The peaks of the NML with larger modulation periods are of higher intensities and sharper. Note that no new peaks appear so no new structural units are formed.

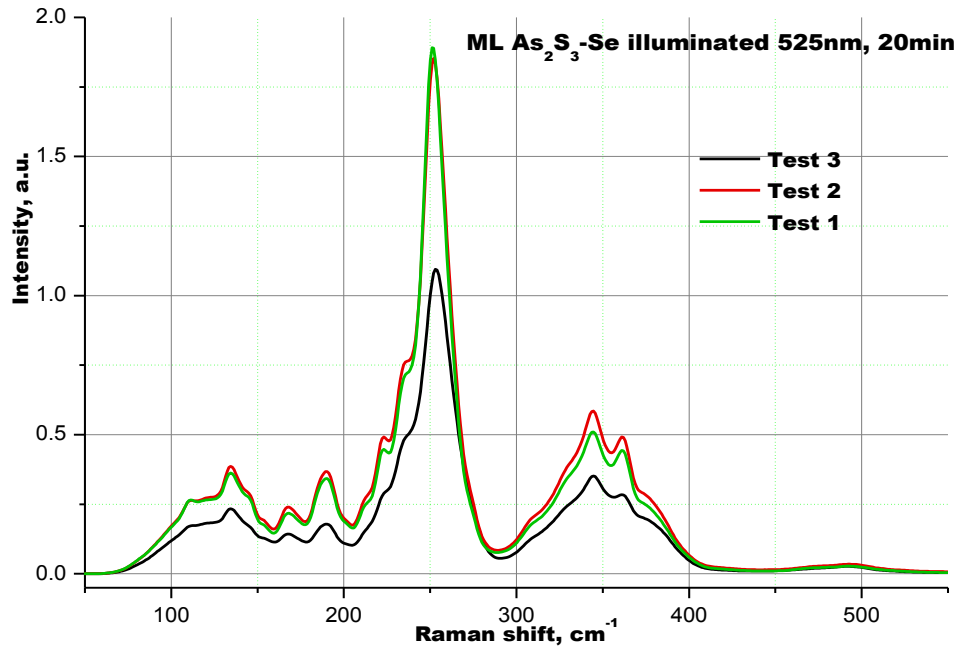


Fig. 2.41. Raman spectra of $\text{As}_2\text{S}_3\text{-Se}$ NML with modulation period $D = 50$ nm (test 1), $D = 25$ nm (test 2), $D = 15$ nm (test 3) after illumination with wavelength 525 nm.

To demonstrate clearer the Raman spectra modifications under light, we plotted the subtraction of the Raman spectra before and after illumination (Fig. 2.42). Each Raman spectrum was normalized by the area under the curve, and differential spectra for each NML were obtained by subtracting the appropriate spectra for the exposed and as-deposited sample (Fig. 2.42).

As can be seen from Raman subtracted spectra, the largest changes appeared in the spectra of sample 3 mainly due to the decrease of intensity of the Se main band at 252 cm^{-1} . Also in the exposed sample the bands get narrower in $120\text{--}240\text{ cm}^{-1}$ range and the band at 360 cm^{-1} , connected mainly with a “wrong” As-As bond in the As_4S_4 cages, and at the same time in the subtracted spectra a new band appeared at $228, 240$ and 270 cm^{-1} , which is very close to a band for the AsSe_3 pyramidal units in the As_2Se_3 glass [118]. There is no measurable change discovered for a broad band at 495 cm^{-1} connected with the S-S bonds.

Changes in the Raman spectra for the exposed NML allow us assuming that photostructural changes under exposition occur mainly due to a decrease in the amount of the Se rings, which means the inter-diffusion on the interface As_2S_3 -Se of the NML and creation of new As-Se bonds. Decreasing the amount of “wrong” As-As bonds and appearing of new 228, 240 and 270 cm^{-1} bonds confirm this process and also could be connected with photo-polymerization of the As_2S_3 sublayers. From this point of view, the efficiency of photostructural changes in the NML should depend on the amount of the As_2S_3 -Se interfaces, that is why the observed photoinduced changes are larger for the NML with a smaller periodicity. In addition, these photostructural changes are favoured in chalcogenides because of a rapid localization of photo-excited carriers, a low energy of the valence alternation of pair defects and the freedom of low-coordination atoms to change their positions and bond configurations [127].

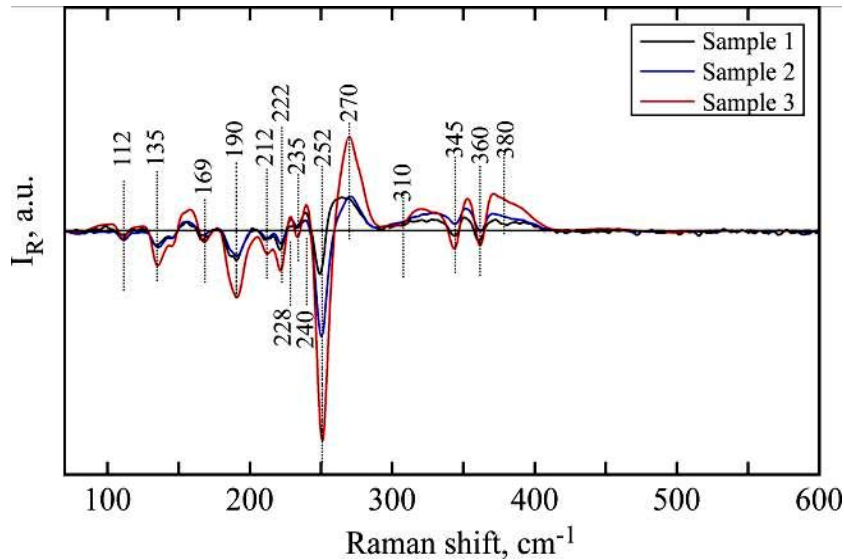


Fig. 2.42. The results of subtraction spectra for NML As_2S_3 -Se from data Fig. 2.41.

Raman spectra of $\text{Ge}_5\text{As}_{37}\text{S}_{58}$ -Se multilayer structure is presented in Fig. 2.43. It can be seen that spectra contain all bands characteristic to Se and $\text{Ge}_5\text{As}_{37}\text{S}_{58}$ films. Here it is necessary to note, that similar to Raman spectra of Se, for differential Raman spectra in dependence on exposure the intensity of the 235 cm^{-1} band is increasing with the exposure increase and intensity of the 251 cm^{-1} band is decreasing, respectively. But evolution of other weak bands is difficult to separate in differential spectra because many bands characteristic for different molecular structures are present.

In conclusion, we have established that the Raman spectra of the separated As_2S_3 and Se films are similar to those reported in literature. For the as-deposited samples, the interfaces, which are the great fraction of the total volume of a sample, do not affect peak positions for both materials. It indicates that no new bonds are formed in comparison with the films prepared by

conventional vacuum deposition methods. The changing of the peaks intensity, more pronounced in the Se film, is caused by a higher ordering of structure.

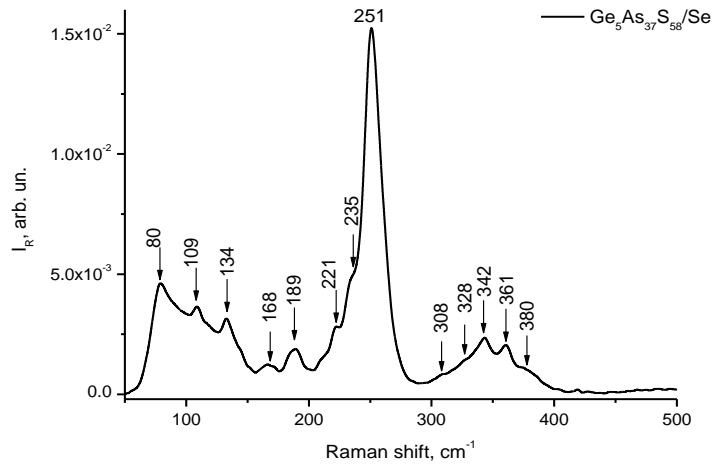


Fig. 2.43. Raman spectra $\text{Ge}_5\text{As}_{37}\text{S}_{58}\text{-Se}$ NML.

Raman spectra vs laser power shown that the following structural changes in Se nanolayers take place by laser illumination: a) band at 251 cm^{-1} decreases which points on decreasing of Se_8 rings quantity, b) band 235 cm^{-1} increases which is associated with increasing a small fraction of "pure" helical chains.

Raman spectra of $\text{Ge}_5\text{As}_{37}\text{S}_{58}\text{-Se}$ NML contain all bands characteristic of Se and $\text{Ge}_5\text{As}_{37}\text{S}_{58}$ films. Similar to Raman spectra of pure Se films, for differential Raman spectra in dependence on exposure the intensity of the 235 cm^{-1} band is increasing with the exposure increase and intensity of the 251 cm^{-1} band is decreasing, respectively.

2.4. Digital holographic measurements

The optical properties of chalcogenide glasses, especially the refractive index value and its changes under different kind of excitations, are currently a subject of systematic research due to their manifest strong photo- and thermally-induced properties that offer the possibility of using amorphous chalcogenide for high-density information storage, fabrication of diffractive optics such as phase and Bragg gratings elements, inorganic photo-resists, and different holographic patterns.

There are two main problems of optical parameters measurement: the precise definition of the refractive index, and independent assessment of refractive index and thickness of the samples. The formed gratings represent microscopic phase/amplitude objects with a photoinduced parameters modulation at nanometres scale. The modulation of refractive index and thickness

causes phase variations. For the investigation of above mentioned phase objects quantitative phase imaging has been applied.

The principal problem solved by quantitative phase imaging (QPI) is the study of objects that do not absorb or scattering light significantly i.e., they are transparent, or phase objects. In the 1930s Zernike developed phase contrast microscopy, in which the contrast of the interferogram generated by the scattered and unscattered light, i.e., the image contrast, is enhanced by shifting their relative phase by a quarter wavelength and further matching their relative power. It represents a major advance in intrinsic contrast imaging, as it reveals inner details of transparent structures without staining or tagging. However, the resulting phase contrast image is an intensity distribution, in which the phase information is coupled nonlinearly and cannot be retrieved quantitatively.

Among different microscopic QPI techniques, the off-axis digital holography is regarded as a method that allows optical thickness measurements with nanometers accuracy in a single-shot wide-field acquisition [128]. In DH the object wavefront from a single frame observation is reconstructed [129]. Digitalization of optical holograms plays a major role in the improvement of reconstruction quality [130] and retrieval of information about the phase of the recording wave [131–133]. The quantitative phase and amplitude information of the object wavefront can be digitally obtained along the depth of the object from the recorded hologram, which makes it possible to digitally focus on different layers of the specimen and reconstruct a 3D profile of the optical thickness of the sample [129]. Therefore, the off-axis DHM is the suitable QPI technique for the investigation of physical parameter changes (refractive index and thickness) that are at the origin of ChG properties. The measured image in QPI is a map of path-length shifts associated with the specimen. This image contains quantitative information about both the local thickness and refractive index of the structure. Recent work shows that QPI provides a powerful means to study dynamics associated with both thickness and refractive index fluctuations.

It is important to understand the meaning of the measured phase. After all, photodetectors respond to power and not the phase of the fields (the actual phase of the field varies extremely fast, at the scale of the optical period, or femtoseconds for visible light). Therefore, experimentally we can only access the phase difference between fields via interferometric experiments, that is, we measure the phase of crosscorrelations and not of the field itself. This phase is well defined over a limited spatiotemporal domain, that is, coherence time and area.

Three main types of diffraction gratings can be distinguished according to the changes that occur during holographic recording [134]:

- RIG, due to the refractive index changes Δn .

- SRG, resulting from the changes of thickness Δd .
- Amplitude gratings, resulting from the absorption coefficient changes $\Delta\alpha$.

First two types of gratings represent phase gratings. The DE of holographic gratings is the main parameter determining the quality of grating important for practical applications. Since the DE of phase gratings is defined both by refractive index and thickness modulations it is very important to determine accurately the map of these changes. Topography map of SRG is conventionally measured by AFM, but it is amplitude measurements technique with does not take in consideration the volume parameters of materials, like refractive index. AFM is scanning technique with restricted field of view. Moreover, revealing refractive index map of RIG is still a problem. For refractive index mapping optical techniques such as refracted near-field measurements [135], imaging ellipsometry [136, 137], and lateral shearing interferometer [138] are used. The drawback of these methods is complicated mechanical arrangement required. To overcome this drawback, the DHM with optical fibers for laser beams delivery can be applied. The goal of this work is defined as QPI calculation of refractive index modulation and surface topography by using DHM.

DHM has several advantages over AFM. One primary advantage consists on amplitude and phase information registered by DHM whereas only amplitude measurements by AFM. Other advantages of DHM are the full-field image acquisition and the obtained image size. In one acquisition, the DHM can image an area of square millimeters with a depth of field of millimeters (these sizes generally depend on the chosen microscope objective and its parameters) whereas the maximum scanning area of AFM is in the micrometer ranges. Furthermore, DHM allows scanless and label-free imaging in real-time, and even if adding hologram reconstruction time, it will be faster than AFM scanning. The only disadvantage of DHM compared to AFM would be a lower resolution. However, if used with appropriate reconstruction algorithm, it gives almost similar accuracies.

The investigation of holograms by DHM.

The interpretation of the phase delay, φ , associated with a monochromatic plane wave is straightforward,

$$U(\mathbf{r}, t) = Ae^{-i(\omega t - \mathbf{k} \cdot \mathbf{r})} \quad (2.5)$$

$$\varphi(\mathbf{r}, t) = -\omega t + \mathbf{k} \cdot \mathbf{r}, \quad (2.6)$$

where A is the amplitude, ω is the angular temporal frequency, and \mathbf{k} is the wavevector. Thus, for such an idealized wave, the phase changes in time at a rate of ω rad/s and in space at a rate \mathbf{k} rad/m along a direction parallel to wavevector \mathbf{k} (i.e., when $\mathbf{k} \parallel \mathbf{r}$).

Starting with the wave equation for a deterministic scalar field U , we have

$$\nabla^2 U(\mathbf{r}, t) - \mu\varepsilon \frac{\partial^2}{\partial t^2} U(\mathbf{r}, t) = 0 \quad (2.7)$$

where ε is the dielectric permittivity and μ is the magnetic permittivity in the medium (assumed to be homogeneous). Taking the Fourier transform with respect to both \mathbf{r} and t , we obtain the wave equation in the (\mathbf{k}, ω) representation,

$$(\omega^2 \mu\varepsilon - \mathbf{k}^2) \tilde{U}(\mathbf{k}, \omega) = 0 \quad (2.8)$$

where \tilde{U} is the Fourier transform of U , \mathbf{k} is the conjugate variable to \mathbf{r} , and ω is the conjugate to t . The non-trivial solution of Eq. (2.7), i.e., $U \neq 0$, requires that

$$k^2 = \omega^2 \mu\varepsilon \quad (2.9)$$

known as the dispersion relation, relates the modulus of the wavevector or wavenumber, $k = |\mathbf{k}|$, to the temporal frequency ω via material properties, $\mu\varepsilon$. In a dielectric of refractive index n , the wavenumber is $k = n\beta_0$, with $\beta_0 = \omega/c$ the vacuum wavenumber. This dispersion relation establishes a hard limit on the maximum spatial frequency that a propagating field can carry and, thus, the maximum resolution with which one can image a structure using far-field measurements.

Fig. 2.44 defines the off-axis DHM bright-field configuration in transmission mode that was used to extract the 3D information of recorded diffraction gratings. The light emitted by a laser was coupled into a monomode fiber and splitted into two beams by a Y splitter. One beam is directed towards the surface of the grating; the other one is the reference beam that is coming at the registration plane at a small angle to produce phase tilt. The diameter of the light spot on the sample was adjusted by the fiber/sample distance. In order to enhance the hologram quality, maximum contrast of interference fringes was obtained by adjustment of object and reference beams intensities. An oil immersion objective with magnification 100x and NA=1.25 has been used. Cedarwood oil drop was introduced between cover slip and the first objective lens.

The CCD sensor was located at the distance of 190 mm from microscope objective (MO) for minimum aberrations in the image. The angle between the object and the reference beams is equal of 4.5° and the period of the interference fringes is 3.5 pixel or $\sim 8 \mu\text{m}$. The light source has wavelength $\lambda = 633 \text{ nm}$ thus considering Abbe formula $\lambda/2\text{NA}$, the resolution of microscope objective is about 253 nm (smallest resolvable object detail). The CCD camera resolution is 2592 pixel \times 1944 pixel with pixel size $2.2 \mu\text{m} \times 2.2 \mu\text{m}$. The period of diffraction gratings under investigation are $\Lambda = 1 \mu\text{m}$, thus it is 4 times larger than the resolution limit.

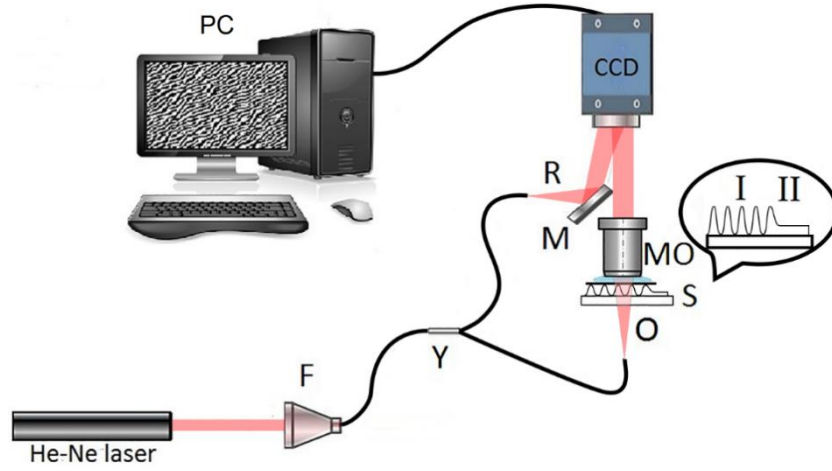


Fig. 2.44. Setup of the DHM: He-Ne laser ($\lambda = 633 \mu\text{m}$, power = 10 mW), F — single-mode fiber launch device, Y — 1×2 single-mode fiber optic coupler, O — object beam, R — reference beam, S — sample with diffraction grating and coverslip on top with immersion liquid ($n=1.51$), MO — immersion microscope objective, M — mirror, CCD — CCD camera, PC — computer, I, II show two illumination beams positions on the sample, namely I — through the grating and II — outside of the grating.

The complex-valued wavefront at the sensor plane is given as

$$u_s = B_0 \exp(j\varphi_0) + A_r \exp(j\varphi_r), \quad (2.10)$$

where $u_0 = B_0 \exp(j\varphi_0)$ and $u_r = A_r \exp(j\varphi_r)$ are the object and reference wavefronts, respectively. Here B_0, A_0 are their amplitudes and φ_0, φ_r are phases.

The spherical reference wavefront is used in our experiments because the reference beam is delivered by single mode optical fiber.

The recorded intensity is:

$$I = |B_0 \exp(j\varphi_0) + A_r \exp(j\varphi_r)|^2 = B_0^2 + A_r^2 + B_0 A_r (\exp(j(\varphi_0 - \varphi_r)) + (-j \exp(\varphi_0 - \varphi_r))). \quad (2.11)$$

The observed data are noisy, i.e. can be presented in the form

$$Y = I + \sigma \varepsilon, \quad (2.12)$$

where I is the true intensity, σ is the noisy standard deviation and ε a random noise. It is assumed in this paper that the noise is zero-mean i.i.d. standard Gaussian, $\varepsilon \sim N(0,1)$.

The phase and amplitude values obtained from the observation Y are used for the reconstruction of the surface relief and refractive index phase of gratings. The phase map $\Delta\varphi(x, y)$ of gratings was determined through the difference between the phase φ_{01} obtained from the reconstructed

object hologram of the exposed grating and the phase φ_{02} obtained from the reconstructed reference hologram of the unexposed area respectively $\Delta\varphi(x, y) = \varphi_{01}(x, y) - \varphi_{02}(x, y)$.

SPAR algorithm for phase reconstruction from digital holograms.

The main off-axis reconstruction approaches include Fourier transform, adjustable magnification methods, Fresnelet transform (Fresnel-Bluestein transform [139], Fresnelet decomposition [140]), convolution based methods (digital quadratic lens method) [141, 142], iterative local least square methods [143]. The choice of the reconstruction method is driven by the hologram recording conditions [144]. For instance, when dealing with far and extended objects, the single-FFT algorithm will be the most appropriate, whereas convolution approaches will be suited for the reconstruction of small objects located near the sensor array.

For our purposes, we use the iterative Sparse Phase and Amplitude Reconstruction (SPAR) technique recently developed for wavefront reconstruction with efficient noise suppression [145].

This new algorithm is based on the sparse modeling of the object amplitude and phase as functions of the coordinates (x, y) . The sparsity hypothesis assumes that there are functions (atoms) such that both the phase and amplitude can be well approximated by series of small number of these functions. Conceptually, the sparsity is a consequence of the self-similarity of images, what means that it is quite possible to find in them many similar patches in different locations. For sparse modeling of phase and amplitude the non-local block-matching technique is implemented in SPAR. It includes the grouping of similar patches, their joint analysis, synthesis, and filtering. These procedures are produced in parallel for the phase and amplitude images.

The SPAR algorithm combines two different ideas: the local least square solution for Gaussian noise in observations [145], and the sparse modelling of phase and amplitude. The SPAR algorithm is derived from the variational formulation of the phase/amplitude reconstruction and in this way provides the optimal phase/amplitude estimates for the noisy observation. The noise suppression of this algorithm is essentially based on the used sparsification of the phase and amplitude representations furthermore.

The algorithm is quite efficient for the phase and amplitude reconstruction of off-axis holograms. A strong robustness of this algorithm with respect to noise is important for the problem considered in this paper because the standard Fourier transform based techniques give very noisy results.

Series of holographic gratings with different DE were obtained by varying the exposure time and exposure of illumination. Table 2.6 shows the exposure time and DE of gratings recorded on As_2S_3 thin films and As_2S_3 -Se NML.

DE of gratings on As_2S_3 thin films reaches maximum at time ~ 2 min, and then decreases. To present the progress of DE with time we plotted the data of Table 2.6 in the DE vs. time coordinates supplemented by the data from other samples. In Fig. 2.45 the evolution of DE in dependence to exposure time is illustrated.

Table 2.6. The exposure time and DE of gratings recorded on As_2S_3 thin films and As_2S_3 -Se NML.

Grating №	NML, As_2S_3 -Se		As_2S_3	
	Time, min	Diffraction efficiency, %	Time, min	Diffraction efficiency, %
1	28	8	0.95	8
2	35	10	1.6	10
3	45	12	1.9	10.4
4	60	13.4	-	-

In Fig. 2.45 the gratings with close values of DE and recorded on As_2S_3 thin films and As_2S_3 -Se NML are pointed as 1-1*, 2-2*, 3-3*, respectively. These gratings were studied to compare the recording parameters of two materials. The grating 4* on As_2S_3 -Se NML has maximum DE (13.4%) achieved during the time recording, and is needed to measure the contribution of refractive index Δn and thickness Δd modulation in DE.

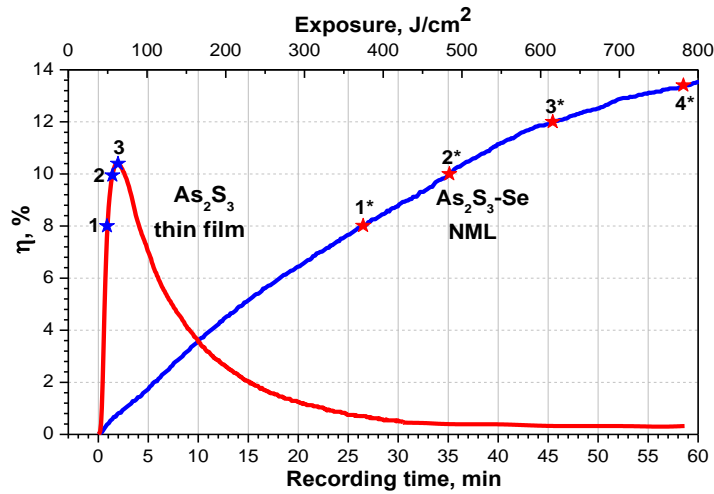


Fig. 2.45. Evolution of the diffraction efficiency versus the exposure time.

The phase map $\Delta\varphi(x, y)$ can be expressed as

$$\Delta\varphi(x, y) = \frac{2\pi}{\lambda} [d_0\Delta n(x, y) + (n_0 - 1)\Delta d(x, y)], \quad (2.13)$$

where d_0 is the thickness of the film, Δd represents the change in thickness, n_0 is the refractive index of the film, Δn is the photoinduced change in refractive index, and λ is the wavelength.

The phase map consists of two components: first $\frac{2\pi}{\lambda} d_0 \Delta n(x, y)$ responding for refractive index modulation and second $\frac{2\pi}{\lambda} (n_0 - 1) \Delta d(x, y)$ for the thickness modulation.

Let us consider the next parameters $\Delta\varphi$, Δn and Δd as average range of corresponding maps $\Delta\varphi(x, y)$, $\Delta n(x, y)$ and $\Delta d(x, y)$.

$$\Delta\varphi = \frac{2\pi}{\lambda} [d_0 \Delta n + (n_0 - 1) \Delta d]. \quad (2.14)$$

It should be noted that the fluctuations in the phase map of digital holograms are due to both modulations in thickness and refractive index. From the phase map $\Delta\varphi(x, y)$ rendered by DHM we can extract the grating phase profile and the average range of the phase $\Delta\varphi$. On condition that the thickness change $\Delta d(x, y)$ of grating is measured by AFM, it is possible based on (2.14) to extract the average refractive index modulation Δn by subtraction the AFM thickness change Δd from the thickness corresponding the total DHM phase $\Delta\varphi$. In the next figure (Fig. 2.46) the AFM data for the As_2S_3 -Se NML (the grating 4*) are presented which have been used for DHM calculations. The grating 4* has the maximum DE therefore it may be the better illustration for comparison of the contribution of refractive index grating and surface modulation in total DE of NML.

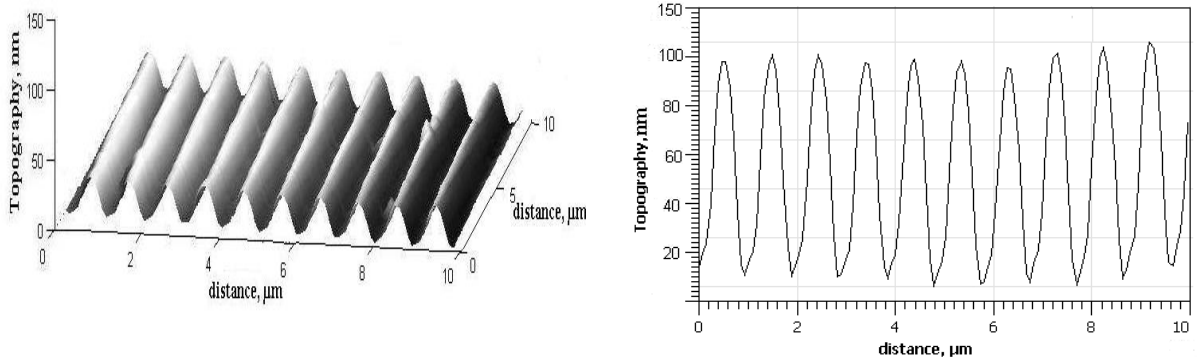


Fig. 2.46. The AFM topography map (left) and cross-section (right) of grating 4* formed on NML As_2S_3 -Se.

Fig. 2.47 shows DHM topography map and cross-section of RIG for holographic grating 4* recorded on As_2S_3 -Se NML.

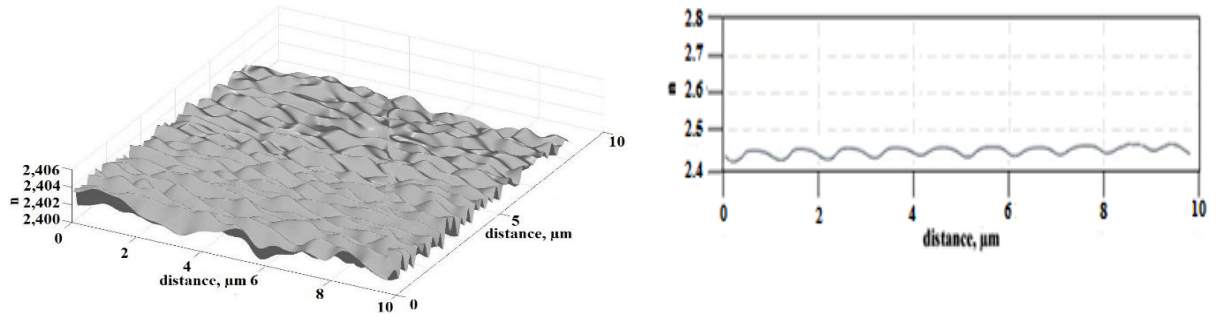


Fig. 2.47. DHM topography map (left) and cross-section (right) of RIG for holographic grating 4* recorded on As₂S₃-Se NML.

From the AFM measurements the mean value of Δd for holographic grating 4* is about 90 nm, therefore a refractive index modulation is 0.004 (Fig. 2.47). Hence according to Eq. (2.14), the influence ratio of the refractive index Δn and thickness Δd on the average range of the phase $\Delta\varphi$ is about 1:10. It is also proved in the refractive index map (Fig. 2.47) that the modulation of refractive index is comparable to the noise of DHM. Thus, we consider that the holographic grating recorded on As₂S₃-Se is determined mostly by the relief thickness modulation.

Therefore, the topography of the grating was obtained from $\Delta\varphi(x, y)$ by using the relation deduced from (4), taking into account that the impact of refractive index is negligible:

$$\Delta d(x, y) = \frac{\Delta\varphi(x, y)}{2\pi(n_0 - 1)} \lambda, \quad (2.15)$$

where $\lambda = 632.8$ nm is the wavelength and $n_0 = 2.46$ the refractive index at $\lambda = 750$ nm (see ch. 2.2). The topography and cross-section of grating 4* with the DE of 13.4% (Fig. 2.45) obtained by DHM with SPAR technique (Fig. 2.48, left) were compared with a measurements done by AFM shown in Fig. 2.48, right.

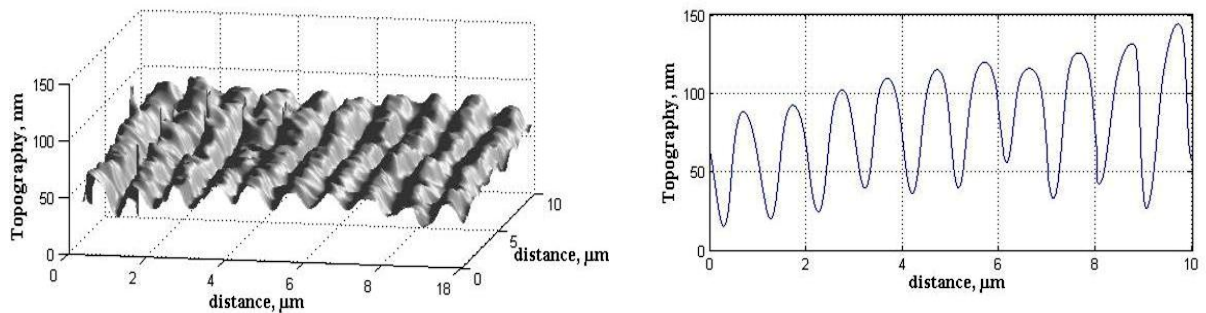


Fig. 2.48. The topography map (left) and cross-section (right) of grating 4* formed on NML As₂S₃-Se and obtained by DHM with SPAR technique.

From Fig. 2.47 and Fig. 2.48 we can conclude that the DHM with SPAR reconstruction algorithm can be successfully used as an alternative for the phase reconstruction of SRG and it shows

only small differences from the AFM cross-sections. According to the measurements by AFM and DHM the depth of SRG of grating 4* with DE 13.4% is about 90 nm. For gratings nr. 1*-3*, with DE's from 8–12% the depth of SRG increases from 75 to 85 nm.

Investigation of ChG films optical parameters during the grating formation is necessary for a better understanding of the photoinduced phenomena that take place at the microscopic level [146]. A preference of the DHM with SPAR is that it can be used for the study of small variation of the refractive index mapping. Before reconstructing the refractive index map $\Delta n(x, y)$, we determined the thickness changes Δd from AFM.

AFM measurements (Fig. 2.49) showed that investigated grating formed on As_2S_3 thin film had small value of thickness modulation (2–3 nm). Thus, the formula for refractive index map (2.14) is converted into (2.16). Real refractive index map after grating recording consists of refractive index of the thin film before recording n_0 and modulation of refractive index: $n(x, y) = n_0 + \Delta n(x, y)$. Thus, the relation between the phase $\Delta\varphi(x, y)$ obtained by DHM and the refractive index map $n(x, y)$ is:

$$n(x, y) = \frac{\Delta\varphi(x, y)}{2\pi \cdot d_0} \lambda + n_0. \quad (2.16)$$

Since the measured phase map can be a combination of both the refractive index and the thickness modulation of the film, this formula should be used in conjunction with a known surface relief depth.

The cross-section and the refractive index profile of patterned holographic gratings obtained prove the feasibility of DHM indirect measurements. From Fig. 2.47 we can see the refractive index modulation of holographic gratings 3 with DE 10.4% (Fig. 2.45, As_2S_3) is about 0.1. The refractive index modulation from 0.08 to 0.1 of holographic gratings (1–3) with the DE (8–10.4%) recorded on As_2S_3 increases in dependence on the exposure time. The obtained results match with the photoinduced changes in refractive index measured by lateral shearing interferometer in [142].

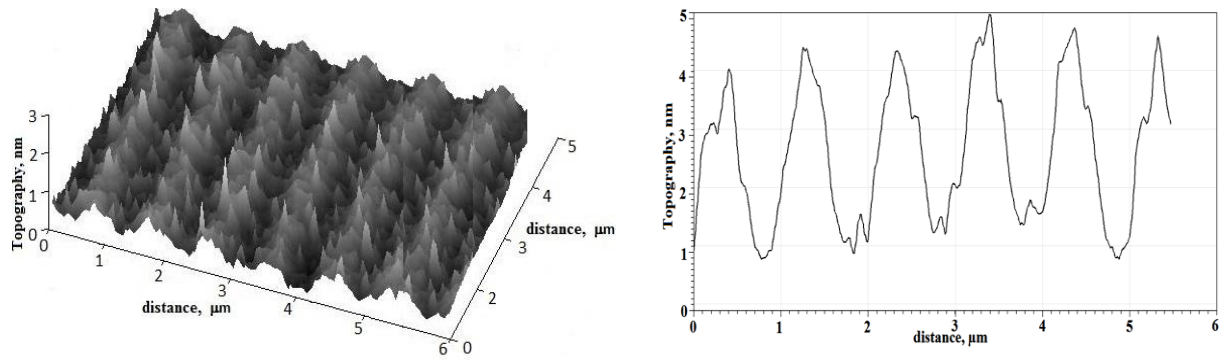


Fig. 2.49. The topography map (left) and cross-section (right) of holographic grating 3 recorded on As_2S_3 film and measured by AFM.

The holographic fiber-optic electron speckle pattern interferometry (ESPI) as a method of small displacement measurements was formed in 80-th years [147], but to study the optical parameters have learned recently. This method combines merits of optical method, noncontact and full-field, and digital one, high precision and digital processing possibilities, for measuring the optical properties changes. Data from speckle interference patterns for further determining of optical properties of the samples under study is processing by holographic and programming methods.

Our main aim of this work is to design holographic fiber-optic ESPI and to study the refractive index of ChG, its variations in dependence of thicknesses (thin films and bulk materials) by elaborated holographic fiber-optic ESPI. Especially this method can be very useful for full-field measurements of the index of refraction after recording process on chalcogenide glasses [145].

It should be noted, that during the planned research is expected to establish that the application of digital speckle correlation interferometry technique can be extend the number of experimental data and expand the range of tasks due to flexibility of LabVIEW program, portable set-up, immunity to the environment influences (temperature, vibration).

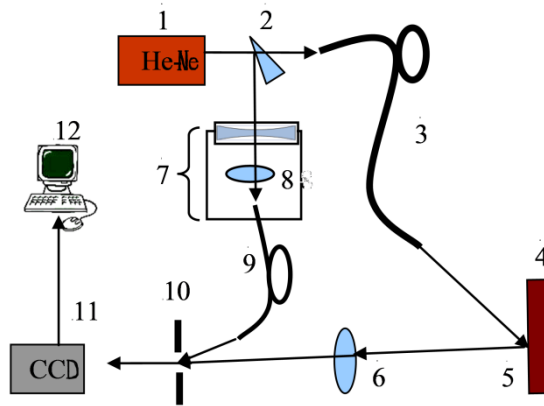


Fig. 2.50. Optical set-up of holographic fiber-optic ESPI.

Breadboard with tapped holes as a stable platform for mount interferometer and optical experiments for various test configurations was used. Fiber-optical design of ESPI was chosen to sustain vibration immunity (Fig. 2.50, 2.51). There are 10 mW monomode He-Ne laser (1), wedge prism as beamsplitters (2), multimode optical fiber as object arm (3), sample (bulk or thin films of the chalcogenide glasses) (4), object arm (5), camera objective (6), optical lever composed from negative lens and positive lens (7) as microobjective (8) ($60\times$ and $NA_{\text{objective}} = 0.5$) and monomode optical fiber as reference arm (9), rectangular diaphragm (10), CCD Smart Camera (11), PC (12).

There are 3 conditions for effective coupling laser beam energy and monomode fiber:

1. Coincidence of the aperture of the objective and fiber core respect to condition $NA_{\text{objective}} \geq NA_{\text{fiber}}$;
2. Diameters coincidence of microobjective focal spot and monomode fiber core;
3. Adjustment of the modes and wavelength transmission of the laser and monomode fiber.

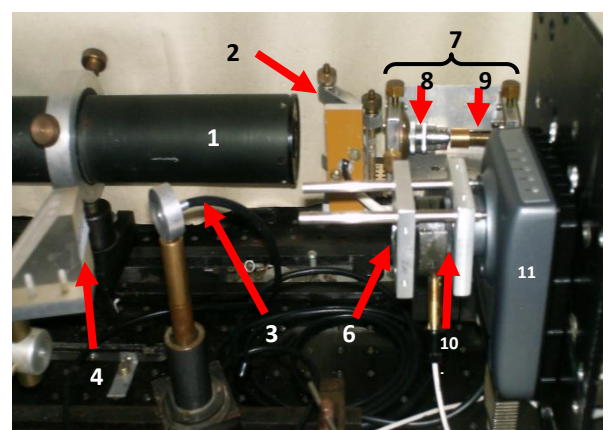
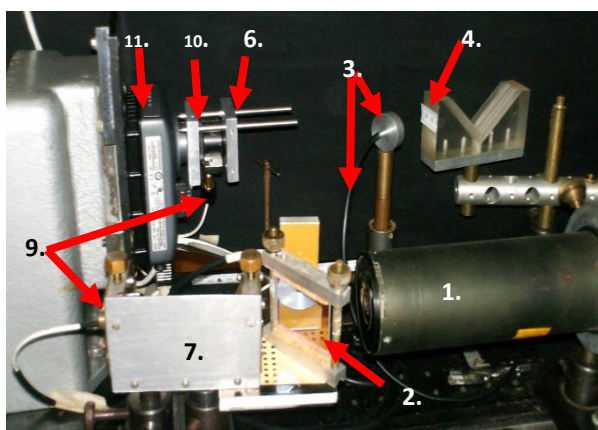


Fig.2.51. Two side photos of the holographic fiber-optic ESPI set-up.

This advantageous interferometric arrangement allows obtaining the speckle pattern fast enough (due to recording rate of CCD Smart Camera) and with high precision (less than $\lambda/4$).

A digital holographic speckle pattern interferometer relies on the correlation between two speckle patterns. Each one created by the interference between a reference beam and the image of an object illuminated by laser [149–151]. Typically, the two images are of an object before and after some changes (in-plane or out-of-plane displacements). Acquired by CCD camera's image is converted into a corresponding video signal. This video signal is electronically processed by PC through Gigabit Ethernet, so that texture variations of the speckle pattern are converted into brightness variations. A speckle interferogram is generated arithmetically by subtracting two digitized speckle patterns. The similar operation of subtraction of two stored on PC interferogram can be made using our program elaborated on LabVIEW platform [152]. In this case, the distribution intensity of the resulting speckle pattern depends on the relative phase shift of superimposed fields. Deformation of the object leads to the change in the phase of the object speckle field and, consequently, to the changes in the intensity of the speckle pattern. Obtained the digital speckle patterns are also subjected to PC processing in order to increase the contrast fringe and smoothing of optical noise — the speckle modulation. In practice, the intensity distribution in the camera detector plane is stored with the object in its reference state. The object is then deformed and a second frame is stored. The two frames are then subtracted and correlation live fringes are displayed on a monitor (Fig. 2.52). Images subtraction makes the interferogram easy to form, view, and record in time. Recording rate of Smart Camera is about 60 fps. NI 1722 Smart Camera simplify machine vision by analyzing images directly on the camera with a powerful, embedded processor capable of running NI Smart Camera digital I/O lines, which are opto isolated for direct connectivity with industrial devices such as triggers and actuators. All smart camera models incorporate an image sensor, processor, and digital I/O in a compact, rugged housing. The Smart Camera also includes LEDs for communicating system status, four DIP switches to specify startup options, isolated inputs, and isolated outputs for connecting to external devices.

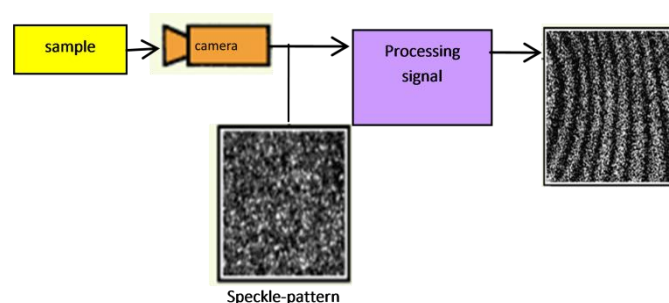


Fig. 2.52. Schematic presentation of ESPI measurement processing.

Developing applications with the NI Smart Camera requires one of the following software options: Vision Builder for Automated Inspection (Vision Builder AI), which is configurable machine vision software using to configure the NI Smart Camera and prototype, benchmark, and deploy machine vision applications. Creating applications in Vision Builder AI does not require programming. It allows us to easily configure and benchmark a sequence of visual inspection steps, as well as deploy the visual inspection system for automated inspection.

LabVIEW is a graphical programming environment for developing flexible and scalable applications. The NI Smart Camera provides control of the image sensor exposure time through software.

If a squared difference is performed between two digitized speckle patterns and recorded at different states of the object, the result will be:

$$I(x,y) = 8I_o(x,y) I_r(x,y) \sin^2[v(x,y)+\Delta v(x,y)/2] \{1-\cos[\Delta v(x,y)]\} \quad (2.17)$$

where $I_o(x,y)$ and $I_r(x,y)$ are the object and reference beam intensities, and $v(x,y)$ is the speckles random phase. The $\Delta v(x,y)$ term contains the phase variation between the two subtracted patterns. This equation represents ESPI interferogram description obtained by subtraction technique. The details of developed ESPI programme one can read in Annex 2 and [153, 154].

2.5. Conclusions to Chapter 2

1. Amorphous nanomultilayers of Se, As₂S₃, As₃₇S₅₈Ge₅, As₂S₃Mn_{2%}, As₂S₃Cr_{4%} (ChG) and ChG-Se composition were developed by the alternate deposition of two materials in one vacuum deposition cycle. The technology allows depositing thin films with a nanometric monolayer thickness from 0.005 μm up to the total NML sample thickness of 3.0 μm. The absorption edge of the NML ChG-Se is close to the absorption edge of Se multilayers obtained in the same deposition process, thereby Se multilayers dominate NML As₂S₃-Se transmission.
2. The solution of carbazole-based 4-[(4'-nitrophenyl)azo]aniline-labeled azopolymer called as poly(PEPC-co-DO) was used for thin film deposition. The spin-coating method was applied for thin layers deposition. A series of carbazole-containing compounds, namely poly-epoxypropylcarbazole (PEPC), poly-epithiopropylcarbazole (PETPC), and copolymers of PETPC:glycidyl butyrate (PETPC:GB) were synthesized.
3. The analysis of the experimental results of the light and dark I-V characteristics, spectral sensitivity distribution in resistive and xerographic regimes, as well as transient injection photocurrent in two-layers ChG-ChG structures indicates the presence of the injection sensibilization effect through interface between two ChG. The hole injection from the narrower band ChG in the wider band ChG changes the carrier transport from dispersive type

to Gaussian, and increase photoconversion efficiency. In case of the interface Se-ChG the efficiency of holes injection through barrier is 10^{-1} . This permits to extend the spectral sensitivity region and increase photoconversion efficiency in the studied ChG-ChG structures.

4. The spectral dependence on the refractive index n calculated together with films thicknesses obtained by the Swanepoel method was studied. Three kinds of the NML As_2S_3 -Se specimens have been prepared with three thickness modulation periods, covering one, two and three molecular and cluster dimensions for As_2S_3 and Se, which are characteristic of the medium-range order in glasses.
5. Optical parameters for NML integrally and constituent nanolayers are calculated on the base of single-oscillator model. Optical band gap E_g was determined from Tauc law, $(ahv)^{1/2} = f(E)$. The refractive index n as a function of wavelength is analyzed on the basis of the Wemple-DiDomenico dispersion model, which is based on the single-oscillator approach. Optical parameters of NML are declined from single-oscillator model, which manifest nanostructuring of the samples. In the case of Se in the amorphous form the chain-chain bonding increase the effective coordination number above the nearest-neighbor value, and these interactions are effectively lost, or at least greatly reduced. The following optical effect is a reduction in oscillator strength of lone-pair to conduction band transitions. It was found that constituent nanolayers are well described by this model independent on composition.
6. The action of UV and visible light (80000 lx) on the photopolymer layers made from PEPC or CAM copolymers with triiodomethane induces photocrosslinking, which is characterized by the appearance of a new absorption band at $\lambda = 640\text{--}650$ nm in the electronic spectra. The intensity of the band at $\lambda = 640$ nm correlates with the photoinduced structural changes in the photopolymer layer.
7. Irradiation of the poly(PEPC-co-DO) films by single beam at 473 nm with the *trans*-isomer band centered ~ 450 nm leads to a structural transition to the *cis*-isomer and a concomitant reduction in the *trans*-isomer band absorption coefficient.
8. The Raman spectra of the separated ChG and Se films are similar to those reported in literature. For the as-deposited samples, the interfaces do not affect the peak positions for both materials. It indicates that no new bonds are formed in comparison with the films prepared by conventional vacuum deposition methods. The changing of the peaks intensity, more pronounced in the Se film, is caused by a higher ordering of the structure.

9. The off-axis DHM is applied for the investigation of the photoinduced phase gratings. The separated contribution of topography and refractive index maps of recorded gratings in DE is estimated. We performed the quantitative phase imaging diagnostics via DHM data for calculation of diffraction grating parameters.
10. The applicability of DHM combined with SPAR reconstruction algorithm to phase gratings study is proved. The developed variational algorithm is able to produce high-quality phase imaging from quite noisy data of DHM. On As_2S_3 -Se NML the surface relief grating is determined mostly by surface thickness modulation. For As_2S_3 thin films the refractive index grating is determined mostly by refractive index modulation. Comparisons of the topography maps recovered by DHM with SPAR and AFM data show that our results qualitatively and quantitatively match with AFM data.
11. The optical set-up design of fiber-optic ESPI and the elaboration program based on LabVIEW code were performed. The process of measuring by our installation is reduced to receiving two speckle snapshots of unloading and loading object. Farther with image processing of speckle patterns and data processing with LabVIEW we extract phase map, and finally calculate the required optical parameters by elaborated method.

3. DIFFRACTIVE STRUCTURES RECORDING AND PATTERNING

Hologram is a three-dimensional image that allows seeing the depth of an image; when it is viewed from different angles, different image is observed, so that three-dimensional perception is achieved.

In all conventional imaging techniques, such as photography, we record the intensity distribution in the original scene. As a result, all information of relative optical paths to different parts of the scene is lost. In holography, the intensity at any point in the pattern depends on the phase as well as the amplitude of the original object wave. Accordingly, the processed photographic film, which is called a hologram, contains information on both the phase and the amplitude of the object wave. When the resulting hologram is subsequently illuminated with the reference wave, it contains enough information about the phase and amplitude to permit their reconstruction.

In general, holography is an interference method of recording the light waves diffracted by an object, illuminated with coherent light. Two major types of holography are called analogue and digital holography. Analog holography deals with continuous-space waves. Digital holography results when the wave fields are sampled, and the information carried in amplitude and/or phase of the wave is coded with special algorithms. Digital holography is more commonly known as diffractive optics. Some other terminologies used for diffractive optics are computer-generated holography (CGH), DOE, and binary optics.

ChG and photopolymers are known to exhibit several photoinduced phenomena not only scalar (photodarkening, photorefraction, photodoping), but and vectorial (photoinduced anisotropy, photoinduced gyrotropy, photoinduced light-scattering) which are connected with photoinduced structural transformations, defects creation and atoms diffusion. The basic effects of irradiation on these materials are similar the well-known irradiation-induced transformations occur at the initial level of electron-hole excitation and further structural transformations, causing the same physical and/or chemical changes including optical (darkening and optical anisotropy), mechanical (softening), geometrical effects (expansion or contraction) and so on. Both intensity and polarization holography have been employed to generate diffraction structures in ChG and photopolymer materials.

Briefly description of the intensity (scalar) and polarization (vector) effects in amorphous materials may be like followed. In a simplified two-dimensional model, all transition dipoles are randomly distributed after the exposure to unpolarized light (z -axis incidence), although isotropic photodarkening and photoexpansion occur (scalar effects). Subsequent exposure to linearly polarized light along the y axis causes selective conversion of the transition dipoles directed along the y axis

into the x axis, producing optical and mechanical anisotropy (vector effects): directional change in optical absorption (dichroism) and refractive index (birefringence). At the same time, directional compressive stress induces nanocontraction and nanodilatation along the y and x axes, respectively.

3.1. Intensity holographic recording

Our approach to the sample layer configuration is aimed at an effort to answer the research questions, namely, size restriction of the constituent ChG layers of the samples. Our purpose is to investigate the recording properties of the As_2S_3 -Se NML and, in particular, to examine the relative contribution of As_2S_3 and Se to nanostructuring. We have begun from Se and As_2S_3 nanolayers as components for the ChG-Se NML because of their known parameters and well-developed deposition technology. In addition, while chalcogens are good glass formers over a wide range of composition, a large majority of studies have focused on the stoichiometric chalcogenide As_2S_3 due to its good stability. Nevertheless, the formation of a nanostructure such as As_2S_3 -Se is of much interest as the addition of Se nanolayer allows us to tune and change the optical transparency and to improve the recording properties. The interplay between a microstructure and desirable properties of DOE may be illustrated in photoinduced changes of nanostructures. These require a broad transmittance optical window and light switching capabilities that must be compatible with the current system configurations, have both broadband linear and nonlinear indices of refraction, as well as low volume losses. The As_2S_3 -Se NML is considered promising as it exhibits properties compatible with the mentioned above. The wide band-gap material As_2S_3 ($E_g = 2.4$ eV) was an optically transparent barrier and the active material Se had a narrower band-gap ($E = 1.8$ eV).

The interferometric holographic recording was used to expose linear grating on the film sample. The period of the grating $\Lambda = \lambda/(2\sin\alpha)$, where λ is the wavelength of laser beam, α is the angle between the incidence laser beams. A CW DPSS single mode laser operated at 532 nm with output power 50 mW was applied. A spot power density on the sample 350 mW/cm^2 was used for recording. The holographic gratings with a period of $\Lambda = 1 \mu\text{m}$ were recorded by two symmetrical angled laser beams with respect to the sample surface normal. The intensity ratio of the recording beams 1:1 was used in order to achieve the maximum visibility of interference fringes. Interfering beams with S:S polarization of recording laser beams keeping intensity hologram recording was used for gratings formation. The experimental set up is sketched in Fig. 3.1.

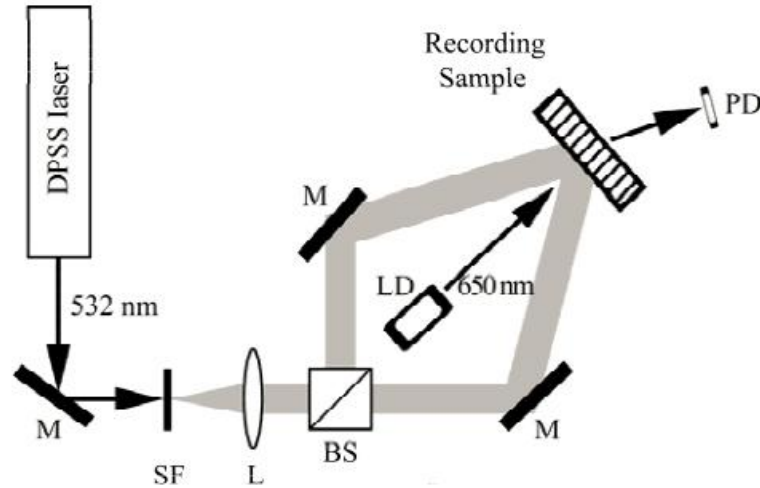


Fig. 3.1. The optical arrangement for holographic grating recording with real-time measurement of diffraction efficiency by photodetector. DPSS laser (532 nm, 50 mW), M — mirror; SF — spatial filter; L — collimating lens; BS — beam splitter; LD — laser diode ($\lambda_{\text{red}} = 650$ nm) for monitoring recording process; PD — photodetector.

The material of interest in this experiment was to compare the optical parameters of the NML ChG-Se with different thickness modulation periods D (the total thickness of one ChG and one Se nanolayers).

So observing the intensity holograms we can see the influence of nanolayers thicknesses on recording properties of NML. In Fig. 3.2 the DE η of gratings *vs.* dose value of illumination for NML As_2S_3 -Se for different thickness modulation period are presented.

It is seen that only for NML with $D=15$ nm the saturation of the DE value takes place. For other NML and pure As_2S_3 we observed a constant rise of η , but at a different η rate. From the comparison of these dependences for different samples we can conclude that NML with $D=25$ nm has optimal recording properties meaning the maximum of both the value and the rate of the diffraction efficiency. The optical and Raman spectra measurements (see ch. 2.3) support this statement. For pure Se we did not observe the gratings record because the energy at recording wavelength $\lambda_{\text{rec}} = 532$ nm is absorbed in a thin (less than 10 nm) Se layer. Note the absorption coefficient of Se $\alpha > 10^5 \text{ cm}^{-1}$ for a wavelength of 525 nm, i.e. it is the region of high absorption for Se. The suppression of this irradiation takes place in a thin $d < 10$ nm selenium layer. It is important to distinguish that recording properties of multilayers and monolayer of the same ChG composition and thickness are differ.

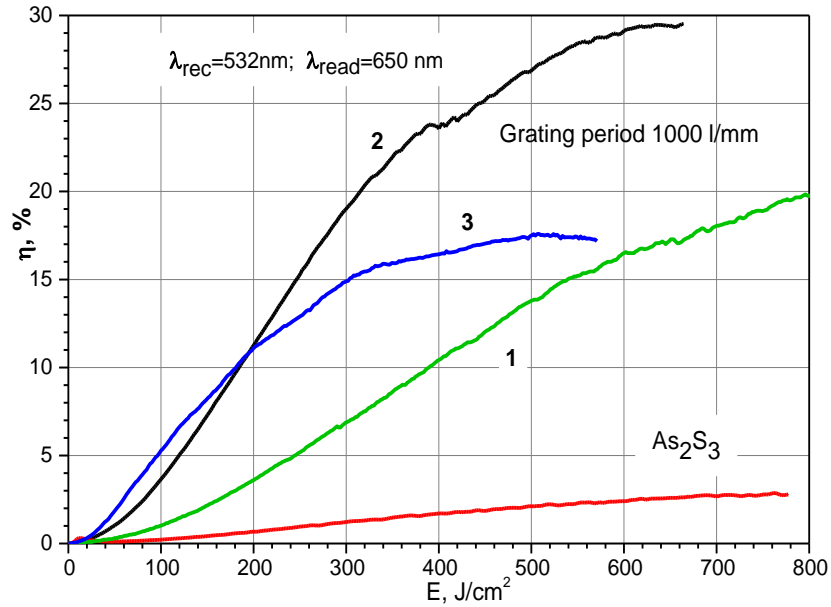


Fig. 3.2. The diffraction efficiencies η of gratings vs. illumination dose for NML As₂S₃-Se for thickness modulation periods: D=41 nm (1), D=25 nm (2), D=13 nm (3), and for As₂S₃.

Changing of Se film structure under exposure shown in [155] can trigger processes of mass transfer in chalcogenide multilayer structure due to arising structural non-uniformity according to intensity distribution during grating recording.

To raise the photosensitivity of NML we doped As₂S₃ by Ge with concentration of 5 at. %. In addition, at shift of photosensitivity region to more long wavelengths, the light with wavelength of 525 nm will absorb not only in Se nanolayers but in As-S-Ge nanolayers too.

Diffraction gratings with 1 μm period were recorded by two laser beams with polarization with synchronous DE η measurement by red laser ($\lambda = 650\text{ nm}$) in the first diffraction order on NML As₃₇S₅₈Ge₅-Se. We have shown that diffraction efficiency η of recorded grating is much more in NML As₃₇S₅₈Ge₅-Se (ten times as much) than in pure As₃₇S₅₈Ge₅ due to relief grating formation [156].

The application of NML As₃₇S₅₈Ge₅-Se leads to increase of holographic sensitivity by two times in comparison with NML As₂S₃-Se under similar conditions of holographic recording. The gratings obtained on the base of NML are stable (dependence of diffraction efficiency η on exposure saturates, while for “pure” As₃₇S₅₈Ge₅ layers such dependence has maximum with further decrease of η while dose increases). Note that the grating frequency in this case is 1600 l/mm.

Special interest for applications is related with glassy As₂S₃ doped with optically active transition metal ions because they alter magnetic and optical properties of the host material due to structural and electronic changes of the glass network [157]. It was shown that doping affects

the interlayer distance leads to creation of additional localized states in the forbidden gap of the chalcogenide glass. These effects are manifested by changes in electrical and photoelectrical characteristics of glass, while doping stabilizes the glassy matrix with respect to light exposure and thermal treatment. For As_2S_3 the diamagnetic effect is characteristic, but introduction of the manganese impurity of different concentration facilitates the transition from the diamagnetic state into the paramagnetic one [158]. This can be used for the creation of nanocomposites on the base of ChG with new properties, optimization of sensitivity, stability improving of recording media on their base. As can be seen from the data obtained in [159, 160] with the increase of Mn doping level of As_2S_3 the glass transition temperature is decreased and activation energy of glass transition is decreased. That can be associated with structural changes due to interaction of Mn with As_2S_3 glass matrix [161].

AFM data presented in Fig. 3.3 manifest that SRG is formed under laser illumination on the NML $\text{As}_2\text{S}_3\text{Mn}_{2\%}\text{-Se}$ despite the fact that contribution of amplitude (bulk) recording is significant for this NML. The bulk properties of As_2S_3 glasses are changed by Mn dopant, which may be attributed to the increase in the average amplitude of the internal electric fields produced by the introduction of additional charged centers. Mn ions are effective in producing optically active centers in As_2S_3 . Thus, the stronger contribution of $\text{As}_2\text{S}_3\text{Mn}_{2\%}$ in recording properties of NML than As_2S_3 may be explained by abovementioned Mn impurity.

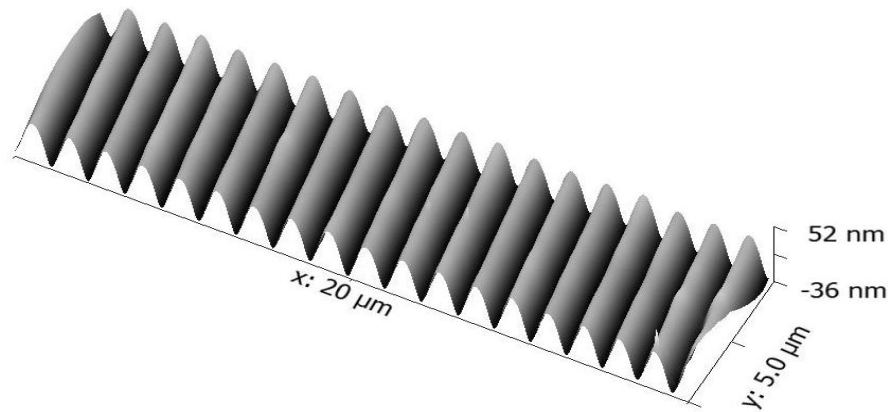


Fig. 3.3. 3D image (AFM) of holographic grating direct recorded on NML $\text{As}_2\text{S}_3\text{Mn}_{2\%}\text{-Se}$, $\Lambda=1 \mu\text{m}$, S:S linear polarizations.

Local magnetic properties of SRG of NML $\text{As}_2\text{S}_3\text{Mn}_{2\%}\text{-Se}$ were studied using Gradient Magnetic Force Microscopy NanoScope IIIa Dimension 3000 (MFM) with the use of two-scan method. MFM diagnostics has shown that small periodical relief thickness changes lead to the essential fluctuations of magnetic field value over the relief surface. AFM and MFM images show that distribution and value of magnetic field (Fig. 3.4b) correlates with gratings relief in

counter phase (Fig. 3.4a and Fig. 3.4c). If magnetization direction of tip is changed grating relief profile and profile of MFM signal are in phase. It was shown that direct one-step magnetic relief formation is possible during gratings recording on NML $\text{As}_2\text{S}_3\text{Mn}_{2\%}\text{-Se}$ structures. Note that before recording we observed the magnetic uniformity of samples.

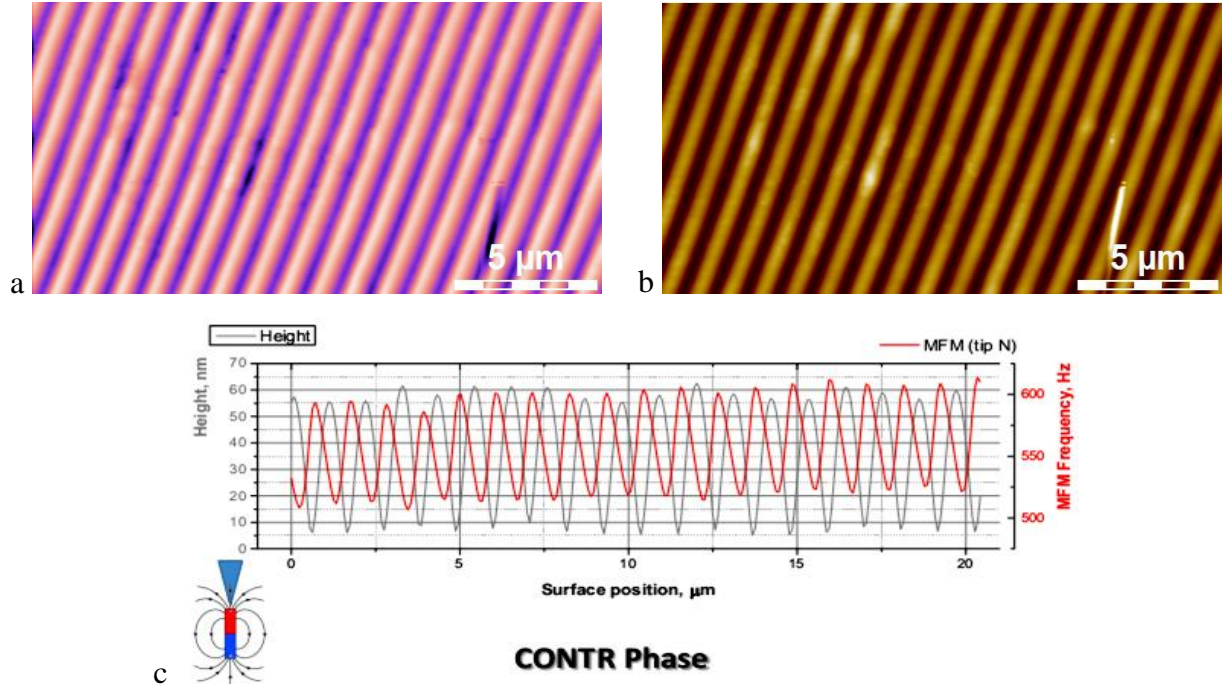


Fig. 3.4. AFM (a), MFM (b) images and profile of SRG (blue curve) and MFM signal (red curve) (c) of NML $\text{As}_2\text{S}_3\text{Mn}_{2\%}\text{-Se}$. Magnetic field direction is perpendicular to sample surface.

MFM diagnostics has shown that small periodical relief thickness changes lead to the essential fluctuations of magnetic field value over the relief surface.

The investigation of azo-dyed carbazol polymers we began from pure carbazol. A lot of interest in CCP was caused by the discovery of photoconductivity in them. Due to the unique properties of carbazole and its derivatives, they have been widely employed as effective charge-transport components in photorefractive and photoconductive materials [162] in electrophotography, xerography, electro-luminescent, and photovoltaic devices [163].

In this study, a series of carbazole-containing compounds, namely poly-epoxypropylcarbazole (PEPC), poly-epithiopyrrolcarbazole (PETPC), and copolymers of PETPC:glycidyl butyrate (PETPC:GB) were synthesized and investigated applying such methods as modification of CCP structure by different chemical processes, by copolymerization, sensitization, plastification, and also by selectivity of etching of the recorded patterns. Synthesis of these polymers and layers deposition were described in Ch. 2.

Holographic properties of PEPC, PETPC, and PETPC:GB layers were investigated by the recording of the diffraction gratings using the classical scheme (see Fig. 3.1) in converging beams of Ar⁺ ion laser at $\lambda=488$ nm [160]. The recording control was carried out by He-Ne laser at $\lambda=633$ nm. For the purpose of comparison of the recording properties of materials, the diffraction gratings were holographically recorded in all samples at the equal conditions: the spatial frequency 1000 l/mm, the power irradiation is 41 mW/cm², the exposure is 147 J/cm².

After recording the DE η of all samples without etching was less than 0.1%. It was established that the investigating polymer films demonstrate the etching selectivity of the recorded diffraction gratings [165]. Etching treatment was controlled by measuring of η in transmission mode at $\lambda=633$ nm within the equal etching interval. A special organic solution was chosen as etching agent. It was shown that the achieved η (after etching) of PETPC:GB films is three times higher than η of PEPC films, which is due to the increased etching selectivity of the selected composition. Achieved DE of etching polymer films with the recorded gratings are shown in Table 3.1.

Table 3.1. Diffraction efficiency (%) of etching polymer films (thickness 1.6 mm).

sample composition	etching time (s)		
	5	10	15
PEPC	2	2.7	9.8
PETPC	11	24	26
PETPC:GB	20	35	41

The possibility to use CCP layers for both optical and electron-beam writing spreads the area of their application [166]. It was shown that the selectivity of etching of the recorded patterns allows improving and, in any case, revealing the characteristics of recorded relief phase structures [167]. The sensitization process of CCP also was used for improving of parameters of holographic recording materials [166].

For e-beam recording the PETPC:GB (90:10 mol%) layers of 1 mm thickness were deposited onto poly(ethylene terephthalate) substrates covered with a semitransparent electrode for electric charge leakage. Diffraction gratings with period $\Lambda=1$ μ m were recorded in fresh polymer layers by the scanning electron microscope SEM BS 300. Current of beam, determining dose of electron irradiation, was ranged from 0.5 to 10 nA; η was measured in the first diffraction order at normal incidence of He-Ne laser beam ($\lambda = 633$ nm) in transmission mode. Value η was calculated as ratio of intensities of diffracted and incident laser beams. Electron irradiation did not

result in induced photodarkening of copolymer layers for beam current values up to 4 nA. No absorption gratings were formed at such recording conditions. Note, that it concerns only the photodarkening process which is visible in transmission changes of polymer layers. Dependence of η on beam current for as-recorded gratings is shown in Fig. 3.5a. For low I values no diffracted beam was registered. A sharp rising of η with current followed the exceeding some threshold beam current value I_{th} . Etching of gratings led to forming of the relief diffraction gratings (Fig. 3.5b). It is seen that after etching the patterns, recorded at low beam current (Fig. 3.5a), have measurable diffraction efficiency (Fig. 3.5b). The maximum η of relief gratings was about 20%. Value of η about 33% was estimated taking into account light absorption by semi-transparent electrode.

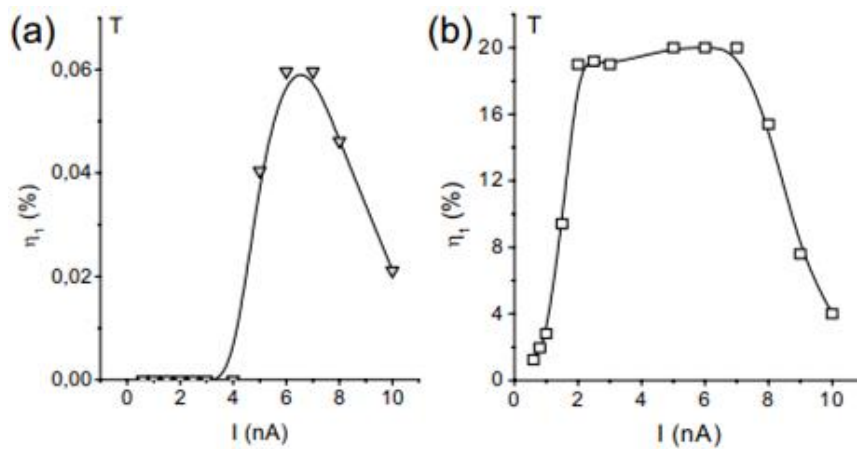


Fig. 3.5. DE (η_R) versus beam current for as-recorded gratings (a); η_T relief gratings, formed by etching in organic solution (b).

The new feature which was observed on PETPC:GB films was the formation of hidden gratings: after both methods of recording by laser and e-beam expose no image of gratings were observed. The gratings presence appeared only after the etching. We consider that at least two processes take place in the polymer layers during recording processes: 1) the absorption coefficient alteration that results the transmission change, 2) the index of refraction alteration that results the DE growth up. The value of DE after etching was close to 40%. Note that the theoretical maximum of DE for a grating with ideal sinusoidal surface profile is about 33%. The DE more than 40% may be caused by non-sinusoidal grating profile.

Diffraction gratings were recorded on samples of the PEPC-CHI3 and CAM: OMA-CHI3 systems with the use of the He-Cd laser and on the PEPC-CHI3-BNSP samples with the use of the CW Ar^+ ion laser (the emission wavelength of $\lambda = 0.42 \mu\text{m}$, a radiation power of 7 mW). Experimental recording of reflection holograms showed that the resolution of the holographic monolayer

based on PEPC and CAM: OMA polymeric layers were at least 2000 l/mm. The maximum DE of the holograms can be as high as 1.5% at a layer thickness of 5–6 μm . The subsequent chemical treatment allowed the DE to be increased up to 20%. For CCP that are capable of photocrosslinking and have been synthesized from carbazole-containing copolymers with an admixture of 4–10% binding agents, we studied the dependence of the DE during writing on the thickness and the exposure time t_{exp} . All samples used for transmittance measurements were chemical treated during t_{treat} after recording. The diffraction gratings were written at a spatial frequency of 1500 l/mm. The results of measurements of DE for different thicknesses in μm are presented in the Table 3.2.

Table 3.2. Experimental data on hologram recording.

Sample no.	μm	η_R	η_T	t_{exp}	t_{treat}
		%		min	
1	3–4	0.63	0.81	5	0.5
2	3–4	1.8	8.1	10	0.5
3	8–9	0.78	2.6	7	0.5
4	8–9	2.1	18.3	15	0.5
5	5–6	4.5	2.0	5	0.5
6	5–6	20.0	10.0	7.5	0.5
7	5–6	7.7	1.0	10	0.5
8	5–6	1.9	18.6	5	0.33

Note: The samples were prepared on the basis of (1–4) PEPC–CHI₃ (5–7) CAM : OMA–CHI₃, and (8) PEPC–CHI₃–BMSP systems.

From the data given in the table, one can see that the transmission diffraction efficiency (η_T) of the layers based on the PEPC–CHI₃ increases to 18.3% with an increase in the layer thickness to 9 μm and in the exposure time to 15 min.

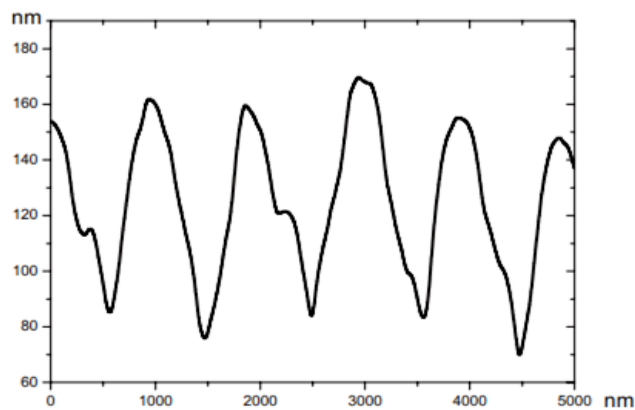


Fig. 3.6. The AFM surface profile for the grating with $\Lambda=1 \mu\text{m}$ recorded in PETPC:GB.

The reflection diffraction efficiency (η_R) of the layers based on the CAM: OMA–CHI₃ system increases to 20% with an increase in the layer thickness to 6 μm and in the exposure time to 7.5 min.

The introduction of the photochromic component BNSP allows quality holograms with the transmission DE to 18.6% to be recorded with the use of wavelength 490 nm from an Ar⁺ ion laser.

The measurements of surface profile by AFM NANO Station II have proved the non-sinusoidal form of gratings recorded (Fig. 3.6). The depth of surface profile after etching in organic solution was as much as 50–100 nm. The excess value of DE can be explained by the fact that laser or e-beam action does not change the visible transmittance of the film during the recording time. So no changes in absorption/transmission of “strata” in depth of layer on recording wavelength were observed. It leads to formation after etching of not sinusoidal, but near triangular profile of surface.

3.2. Polarization holographic patterning

In contrast to the scalar holographic process described above, in which intensity variations in an interference pattern between an object beam and a reference beam are recorded, polarization holography employs beams with two different states of polarizations for recording information. In this case, the polarization state of the resultant beam is recorded on a suitable medium.

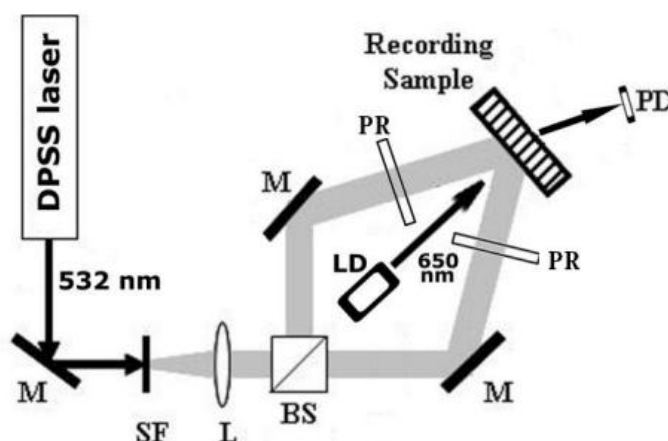


Fig. 3.7. Optical arrangement for polarization holographic grating recording with real-time measurement of diffraction efficiency by photodetector. CW DPSS monomode laser ($\lambda=532$ nm, power =100 mW), M — mirror; SF — spatial filter; L — collimating lens; BS — beam splitter; LD — laser diode ($\lambda=650$ nm) for monitoring of the recording process; PR — polarization retarder; PD — photodetector.

An interferometric holographic recording was used to record a grating on the NML As₂S₃-Se like described in previous. The average spot power density from 150 up to 350 mW/cm² on the sample was used for recording. Angular turning the quarter wave plates in each optical path performed the phase shift experiments, therefore, we can change the state of polarization of both

recording beams. The two interfering beams independently pass through phase turning quarter wave plates to provide a control over the polarization state of the writing beams. Interfering beams with P:P, S:S, LCP:RCP or $\pm 45^\circ$ polarization combinations were used for SRG recording. The experimental set up is sketched in Fig. 3.7. During holographic recording all the changes in NML volume and surface (like those in absorption and refractive index) were controlled by measuring the transmission DE. Thus, the cumulative changes in DE η of NML As₂S₃-Se structure were measured.

The polarization states of the two writing beams were individually controlled by half-and/or quarter wave plates. The holographic gratings were written using parallel and orthogonal polarizations of recording laser beams leading to intensity and polarization modulation in interference pattern. In order to evaluate intensity modulation of the two-beam interference pattern for different polarization configurations, we used interference contrast V given by $V = \left| \frac{I_{max} - I_{min}}{I_{max} + I_{min}} \right| * 100\%$, where I_{max} and I_{min} are the maximum and minimum of the light intensity in the interference pattern. The interference contrast V was calculated for grating period $\Lambda = 1.25 \mu\text{m}$ corresponding to angle between incident beams $\theta = 21.8^\circ$ at $\lambda = 473 \text{ nm}$.

Diffraction gratings in our experiments were recorded in five different polarization configurations:

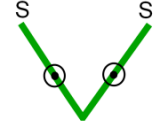
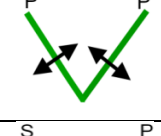
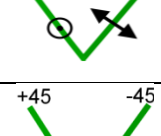
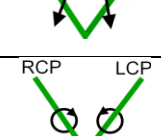
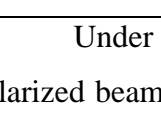
- S:S, two beams are linearly polarized with electric field vectors perpendicular to the incidence plane;
- P:P, two beams are linearly polarized with electric field vectors parallel to the incidence plane;
- S:P, two beams are orthogonally polarized with respect to each other, one is S and the other is P (horizontally polarized);
- $\pm 45^\circ$, two beams are orthogonally linearly polarized at $\pm 45^\circ$ with respect to the grating vector;
- RCP:LCP, when two beams were circular orthogonally polarized with respect to each other, one is right-circular polarization (RCP) and the other is left-circular polarization (LCP).

The interference pattern of two coherent waves with parallel linear polarizations has a periodically modulated intensity, but a polarization state is constant. In case of orthogonal linear polarizations S:P the interference pattern has a constant intensity, but a polarization state that is periodically modulated. In case of orthogonal linear $\pm 45^\circ$ and circular RCP:LCP polarizations the interference pattern has a small modulated intensity (4% for $1.25 \mu\text{m}$ period grating) and periodically modulated polarization states. The theoretical calculation of polarization distribution and interference contrast of the two-beam interference pattern with $\Lambda = 1.25 \mu\text{m}$ for all studied polarization configurations are presented in Table 3.3.

Therefore, the interference pattern with S:S polarization configuration with 100% of interference contrast ensures best intensity modulation contrast used for standard optical holography. Contrary to it, S:P polarization configuration has no intensity modulation but interference resulted polarization varies periodically between linear, elliptical and circular forms. For the case of $\pm 45^\circ$ and RCP:LCP polarization configuration, the resultant polarization becomes a linear polarization where the polarization direction changes periodically, and there is 4% of interference pattern contrast.

Fig. 3.8 shows the typical DE η changes vs. dose value of illumination at different states of the recording beams polarizations. The results presented on the Fig. 3.8 describe the DE vs. exposure for NML $\text{As}_2\text{S}_3\text{-Se}$ with following nanostructuring parameters: $d_{\text{As}_2\text{S}_3\text{-Se}} = 2500$ nm, number of layers 100+100, thickness modulation period $D=25$ nm. We have chosen the NML $\text{As}_2\text{S}_3\text{-Se}$ with this thickness modulation period because it demonstrates more clearly the response of NML to the polarization states of laser beams, but the main course of the dependences is typical for majority of thickness modulation periods of investigated NML.

Table 3.3. Resulting polarization modulation in one fringe period Λ and interference contrast (corresponds to intensity modulation) of the two recording beams for each polarization configuration.

Polarization of writing beams	Polarization configuration	0	$\Lambda/8$	$\Lambda/4$	$3\Lambda/8$	$\Lambda/2$	$5\Lambda/8$	$3\Lambda/4$	$7\Lambda/8$	Λ	V, %
	S:S	•	↑	↕	↕	↕	↕	↕	↑	•	100
	P:P	•	↔	↔	↔	↔	↔	↔	↔	•	93
	S:P	↗	↻	↻	↻	↖	↻	↻	↻	↗	0
	$\pm 45^\circ$	↔	↻	↻	↻	↕	↻	↻	↻	↔	4
	RCP:LCP	↔	↗	↗	↗	↕	↘	↘	↘	↔	4

Under the polarization modulated holographic recording, the two linear (P:P and S:S) polarized beams produce the similar surface relief deformations but with a different profile depth.

The two linear polarized beams falling on the sample surface under angles of polarization $\pm 45^\circ$ produce the largest variation in the surface relief according to our measurements.

From Fig. 3.8 it is seen that not only the maximal shown η , but the kinetics of grating recording process depends on the state of polarization of the recording beams. For S:S and P:P polarizations the recording process begins just after turning on the laser illumination. It was found out that at doze of 700 J/cm^2 the DE reaches the saturation for pointed polarizations. For LCP:RCP and $\pm 45^\circ$ polarizations we observed the constant rise of η but with a different rate. The recording was stopped at exposure doze 1200 J/cm^2 .

For the purpose of comparison of the recording properties of NML $\text{As}_2\text{S}_3\text{-Se}$ with As_2S_3 multilayers sample part at different polarization states of the recording beams, the diffraction gratings were recorded in the As_2S_3 samples obtained at the one technological cycle and at the equal recording conditions.

Dependences of η on exposure doze at different polarizations for As_2S_3 multilayers sample part are presented in the Fig. 3.9. From this figure it is clear noticed that the behavior of As_2S_3 multilayers at holographic recording strongly differs from NML $\text{As}_2\text{S}_3\text{-Se}$. But the dependence of the SRG recording efficiency on the polarization state combinations of recording beams has been observed for As_2S_3 sample part too.

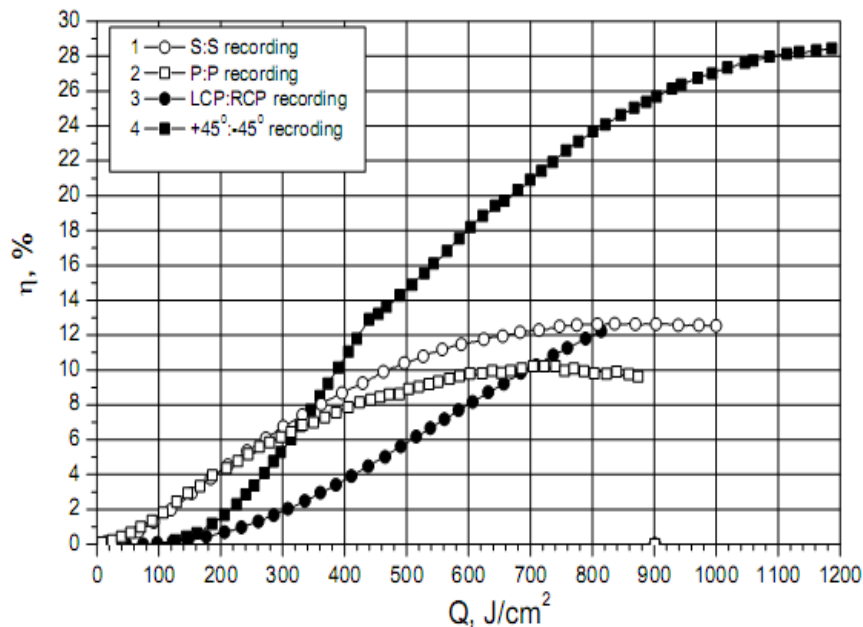


Fig. 3.8. Kinetics of holographic grating recording (grating period $\Lambda=1 \mu\text{m}$) on NML $\text{As}_2\text{S}_3\text{-Se}$ ($D=2500 \text{ nm}$) for different light beam polarization: 1 — S:S, total light intensity $I=270 \text{ mW/cm}^2$; 2 — P:P, $I=160 \text{ mW/cm}^2$; 3 — LCP:RCP, $I=220 \text{ mW/cm}^2$; 4 — $\pm 45^\circ$, $I=160 \text{ mW/cm}^2$.

As photoinduced changes of absorption and refractive index in the As_2S_3 material are comparatively fast, the transmission DE at S:S and P:P polarization (curve 1, 2 in Fig. 3.9) reaches the maximum ($\sim 12\%$ DE) very quickly. Due to the overexposure the contrast of the volume grating decreases; transmission DE starts to decrease. From the literature and our experience, we know that such direct recording process is reversible for the amorphous chalcogenide monolayer [134, 168]. The reversibility factor is a vital stage, because the further work is based on the research of mass transfer processes in amorphous chalcogenides. The calculation of optical absorption coefficient at a recording wavelength 532 nm for the As_2S_3 film in a photodarkened state produced a value of $\alpha \approx 10^4 \text{ cm}^{-1}$ (see Ch. 2). It means that the penetration depth of recording light in the film is about 1 μm ; that is, each one-micron thick layer will absorb the light Euler's number times in according of Lambert-Beer's law.

Under the intensity modulated holographic recording conditions, the two parallel linear (S:S, P:P) and $\pm 45^\circ$ and circular LCP:RCP polarized beams produce the light intensity modulation. However, there are no spatial modulation dependences on the direction of the resultant electric vector of light. These polarization configurations produce a very low η and small surface relief modulation. The curves for S:S and P:P polarization are similar, the maximum value $\eta=12\%$ which is almost two times less than the maximum value $\eta=28\%$ for NML. The process of grating recording begins right after switch on the laser illumination. A rapid increase of DE of the grating is observed at the beginning of the recording process. After reaching the maximum, a decrease η of gratings follows.

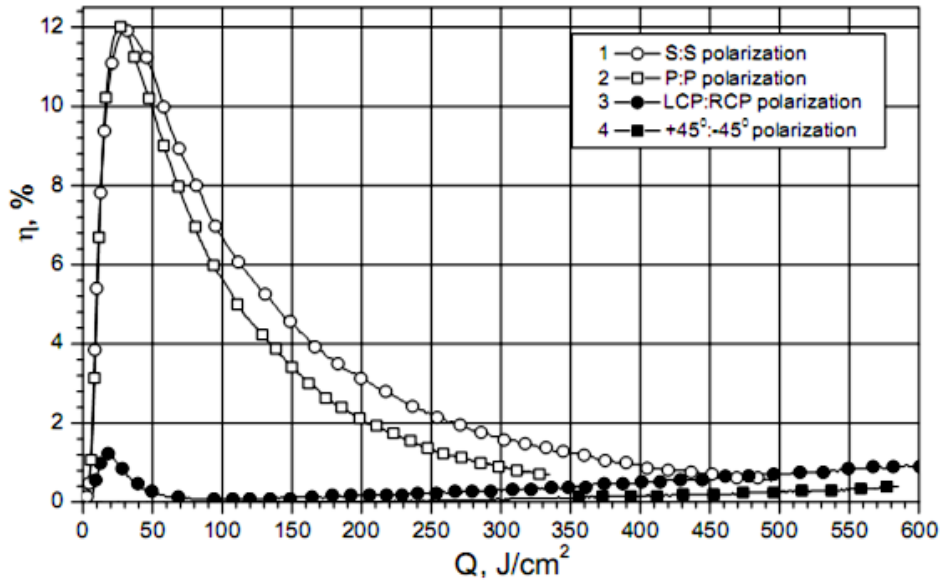


Fig. 3.9. Kinetics of holographic grating recording (grating period 1 μm) on As_2S_3 layer ($d=1240$ nm) for different light beam polarization: 1 - S:S, $I=270$ mW/cm^2 ; 2 - P:P, $I=160$ mW/cm^2 ; 3 - LCP:RCP, $I=220$ mW/cm^2 ; 4 - $\pm 45^\circ$, $I=160$ mW/cm^2 .

For the circular polarization LCP:RCP, 3 segments on the curve (Fig. 3.9) are observed: 1) the fast recording up to $\eta=1.2\%$; 2) the delay; 3) the slowly recording begins at exposure dose about 100 J/cm^2 and the slowly η increasing up to the dose 800 J/cm^2 . As it is seen from these results, the main input in diffraction grating recording in As_2S_3 sample part is the photoinduced scalar recording at least at the exposure dose up to 1000 J/cm^2 (not shown). This recording process may consist of photoinduced refractive index changes, darkening, volume expansion/shrinkage and mass transfer [169]. In NML As_2S_3 -Se the grating formation is distinguished from this one in As_2S_3 sample part. We observe in NML As_2S_3 -Se the rise of DE η with higher rate and without saturation in contrast to As_2S_3 multilayers. In addition, the time delay of η taking place in the beginning of the grating recording in NML points to more inertial process. The features of SGR in NML As_2S_3 -Se may be explained by different molecular structures of NML constituents. According to [29] the structure of As_2S_3 glass is two-dimensional distorted layers, whereas the structure of Se glass films consists of one-dimensional entangled chains. By this way one-dimensional Se multilayers can support the vectorial SRG formation in As_2S_3 multilayers. The surface relief formation leads to the vectorial SRG formation. The recording quantum energy with $\lambda=532$ nm is the bandgap light only for As_2S_3 compound and more than the value of bandgap energy for Se. But due to the fact that the thickness of each Se nanolayer is within 10 nm, the light ($\lambda=532$ nm) penetrates sufficiently deeply in NML As_2S_3 -Se.

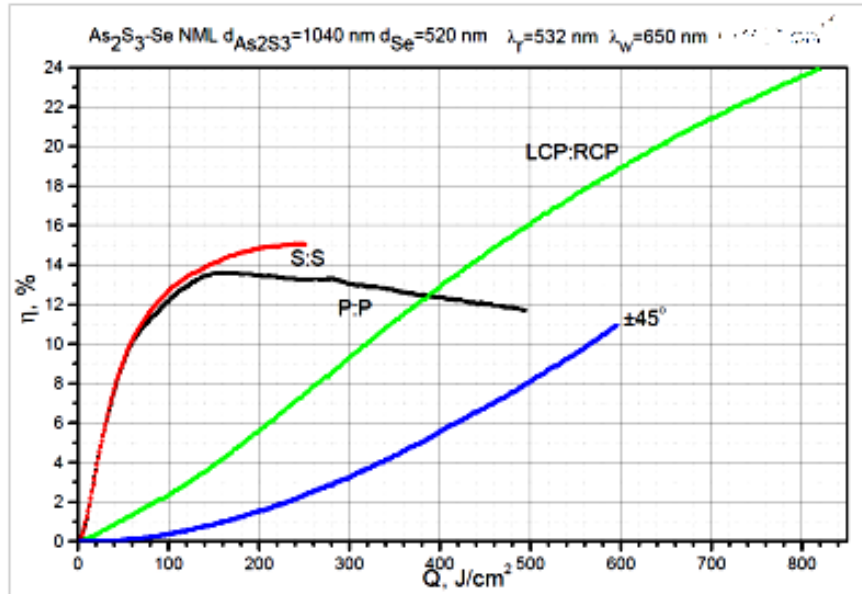


Fig. 3.10. Kinetics of holographic grating recording (grating period $\Lambda=1 \mu\text{m}$) on NML $\text{As}_2\text{S}_3\text{-Se}$ ($d=1560 \text{ nm}$) for different light beam polarization: S:S, total light intensity 270 mW/cm^2 ; P:P, total light intensity 160 mW/cm^2 ; LCP:RCP, total light intensity 220 mW/cm^2 ; $\pm 45^\circ$, total light intensity 160 mW/cm^2 .

The optical investigations are often made and analyzed to determine the mechanism of the stimulated structural transformations in NML [38, 170-172]. The photoinduced diffusion in amorphous nanomultilayers is proposed as the main mechanism influencing their optical features. According to [155], the interdiffusion is the main effect taking place in NML with the modulation period below 10 nm or of the thickness of the “well” layers (in our case Se) below 5 nm. When the thickness modulation period is more than 10 nm ($D=25 \text{ nm}$) and the thickness of Se nanomonomolayer is about 13 nm, we can suppose that besides the interdiffusion, photostimulated structural transformations in the nanomonomolayers occur. As a rule, the photodarkening in amorphous nanolayered As_2S_3 and Se follows photoinduced diffusion [29]. We observed the photobleaching in our NML $\text{As}_2\text{S}_3\text{-Se}$, and we suppose that interdiffusion is not a single process terminating the SGR properties of these NML.

In the Fig. 3.10 we present the kinetic of holographic grating recording at different light beam polarization for the NML with thicknesses of constituents nanolayers for As_2S_3 $d=1040 \text{ nm}$ and Se $d=520 \text{ nm}$, i.e. thickness modulation period $D=10.4 \text{ nm}$. From this figure one can see that the As_2S_3 predominant influences on behaviour of NML. Though nanostructuring takes place because the DE at LCP:RCP and $\pm 45^\circ$ polarizations reaches higher value than at S:S and P:P polarizations.

Kinetics of holographic grating recording (grating period $\Lambda=1 \mu\text{m}$) on NML $\text{As}_2\text{S}_3\text{-Se}$ and As_2S_3 for LCP:RCP polarization is shown in Fig. 3.11.

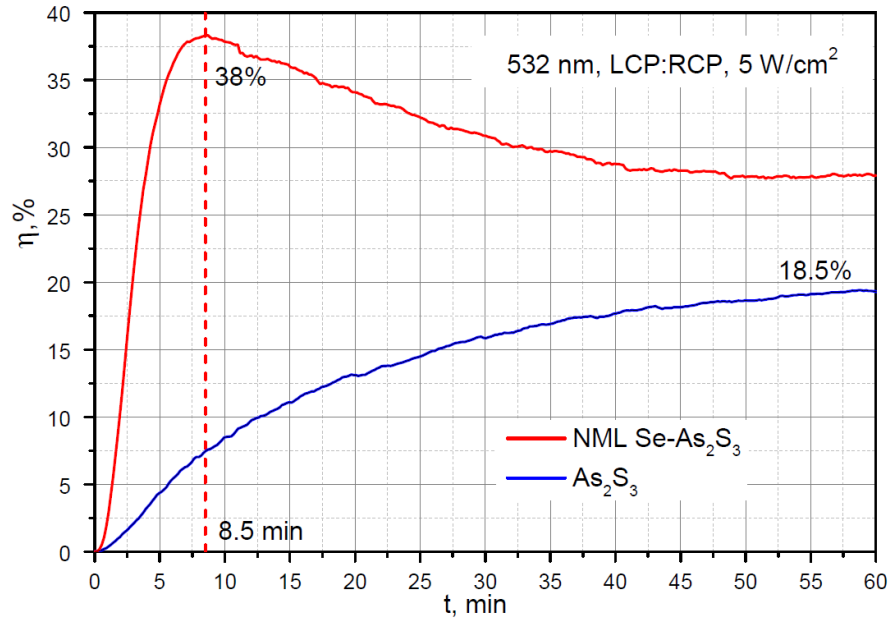


Fig. 3.11. Kinetics of DE growth (grating period $1 \mu\text{m}$) on NML $\text{As}_2\text{S}_3\text{-Se}$ and nanolayers As_2S_3 at LCP:RCP polarization.

The thickness of the NML $\text{As}_2\text{S}_3\text{-Se}$ was $1.7 \mu\text{m}$ and As_2S_3 - $1.0 \mu\text{m}$. Total number of nanolayers in NML is 220, which corresponds to the thickness of each alternating nanolayer As_2S_3 $d=9 \text{ nm}$ и Se $d=6 \text{ nm}$. Also, from the transmission spectra of the layers, calculated refractive indices at the wavelength $\lambda=650 \text{ nm}$, are $n=2.45\pm 0.01$ for NML $\text{As}_2\text{S}_3\text{-Se}$ and $n=2.35\pm 0.01$ for As_2S_3 .

In the next figure (Fig. 3.12), we present the analogue data as Fig. 3.11, but at S:S polarizations.

From comparison these figures we can see the different behaviour of NML and nanolayers at circular and linear polarizations. The S:S polarization giving intensity holographic recording forms holographic grating with constantly rise of the DE on NML and with maximum and decay of the DE on As_2S_3 nanolayers.

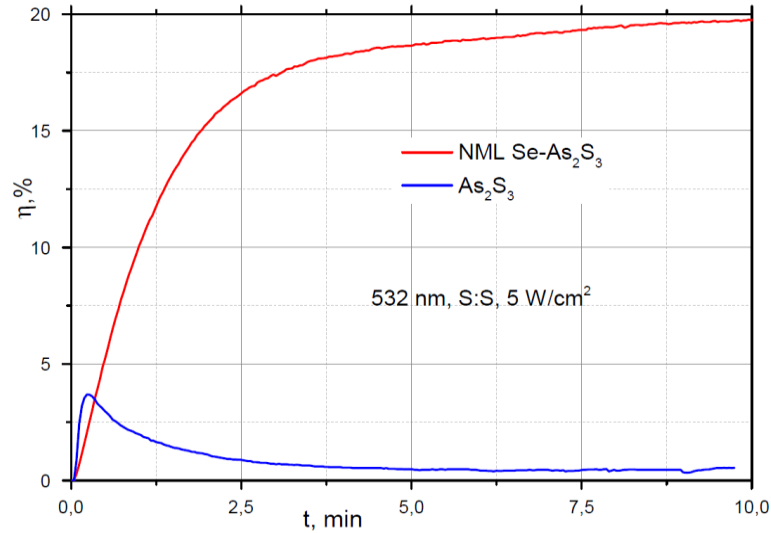


Fig. 3.12. Kinetics of DE evolution (grating period 1 μm) on NML $\text{As}_2\text{S}_3\text{-Se}$ and nanolayers As_2S_3 at S:S polarization.

Kinetics of grating recording at different state of polarizations of recording beams has been measured for NML $\text{As}_{37}\text{S}_{58}\text{Ge}_5\text{-Se}$. Fig. 3.13 shows the time dependence of DE η of NML $\text{As}_{37}\text{S}_{58}\text{Ge}_5\text{-Se}$ at three combinations of beams polarization and $\text{As}_{37}\text{S}_{58}\text{Ge}_5$ multilayers at S:S polarization. As we can see that LCP:RCP orthogonally circularly polarization creates better recording condition meaning rate of rise of DE and its value. The $\pm 45^\circ$ orthogonally linear polarization providing “pure” vector recording gives slow rise of DE. Scalar recording on NML at S:S polarization has maximum value $\sim 6.5\%$ which is three times more than for $\text{As}_{37}\text{S}_{58}\text{Ge}_5$. We can suggest that as scalar as vector recording take place in this NML composition. The scalar recording is similar to $\text{As}_{37}\text{S}_{58}\text{Ge}_5$ nanolayers, but Se nanolayers support mass transfer in $\text{As}_{37}\text{S}_{58}\text{Ge}_5$ nanolayers. In comparison with NML $\text{As}_2\text{S}_3\text{-Se}$ more rigid network of $\text{As}_{37}\text{S}_{58}\text{Ge}_5$ interferes with molecules movement.

Note, that the grating frequency in this NML composition reached to 1600 l/mm. So NML $\text{As}_{37}\text{S}_{58}\text{Ge}_5\text{-Se}$ may be used for effective high-frequency amplitude-phase optical information recording.

Special interest for applications is related with glassy As_2S_3 doped with optically active transition metal ions, because they alter magnetic and optical properties of the host material due to structural and electronic changes of the glass network [173]. It was shown that doping affects the interlayer distance and leads to creation of additional localized states in the forbidden gap of the ChG. These effects are manifested by changes in electrical and photoelectrical characteristics of glass, while doping stabilizes the glassy matrix with respect to light exposure and thermal treat-

ment. For As_2S_3 the diamagnetic feature is characteristic but introduction of the manganese impurity of different concentration facilitates the transition from the diamagnetic state into the paramagnetic one. This can be used for the creation of nanocomposites on the base of ChG with new properties, optimization of sensitivity, stability improving of recording media on their base. As can be seen from the data obtained in [174] with the increase of Mn doping level of As_2S_3 the glass transition temperature is decreased and activation energy of glass transition is decreased. That can be associated with structural changes due to interaction of Mn with As_2S_3 glass matrix.

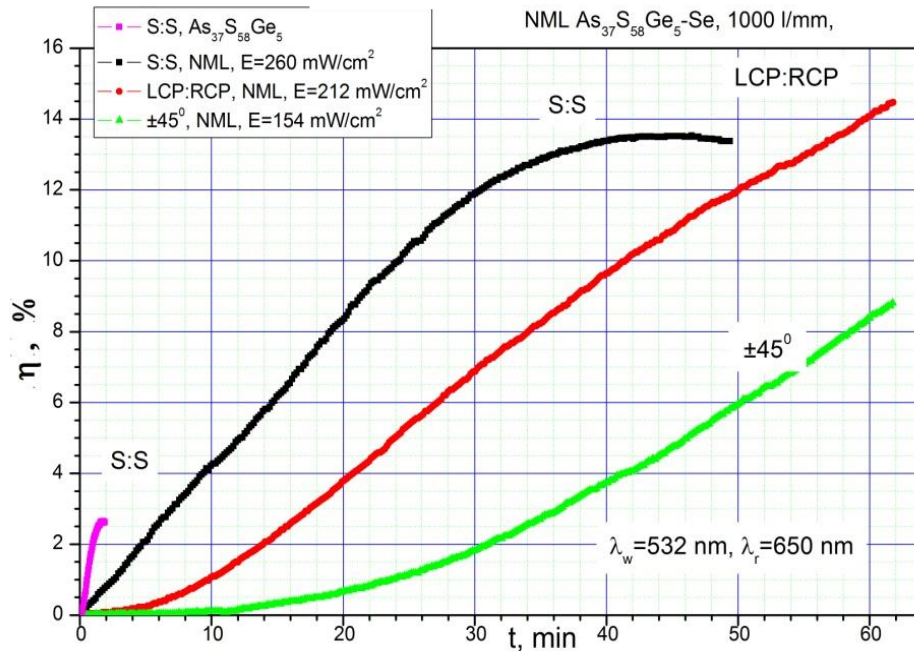


Fig. 3.13. Kinetics of diffraction efficiency of NML $\text{As}_{37}\text{S}_{58}\text{Ge}_5\text{-Se}$ at different state of polarizations of recording beams. Grating frequency 1000 l/mm.

The measured time dependence of DE for NML $\text{As}_2\text{S}_3\text{Mn}_{2\%}\text{-Se}$ is presented in Fig. 3.14. As in the case of NML $\text{As}_2\text{S}_3\text{-Se}$ and $\text{As}_{37}\text{S}_{58}\text{Ge}_5\text{-Se}$ we observe the strong dependence of η on state of recording beam polarization. Behavior of NML $\text{As}_2\text{S}_3\text{Mn}_{2\%}\text{-Se}$ is similar to NML $\text{As}_{37}\text{S}_{58}\text{Ge}_5\text{-Se}$, namely the LCP:RCP polarized beams produce the better recording conditions considering the rate of rise and the value of DE. In contrary, the NML $\text{As}_2\text{S}_3\text{-Se}$ exhibits optimal recording properties under $\pm 45^\circ$ polarization. This may be attributed to bigger contribution of vector type of recording because $\pm 45^\circ$ orthogonally linear polarization supports phase recording not intensity one. The maximum value of $\eta \approx 6\%$ for NML $\text{As}_2\text{S}_3\text{Mn}_{2\%}\text{-Se}$ is lower than $\eta \approx 8\%$ for NML $\text{As}_{37}\text{S}_{58}\text{Ge}_5\text{-Se}$ like maximum values for $\text{As}_2\text{S}_3\text{Mn}_{2\%}$ ($\eta \approx 0.6\%$) and $\text{As}_{37}\text{S}_{58}\text{Ge}_5$ ($\eta \approx 2.2\%$).

Bulk properties of As_2S_3 glasses are changed by Mn dopant which may be attributed to the increase in the average amplitude of the internal electric fields produced by the introduction of

additional charged centers. Mn ions are effective in producing optically active centers in As_2S_3 . Thus, the stronger contribution of $\text{As}_2\text{S}_3\text{Mn}_{2\%}$ in recording properties of NML than As_2S_3 may be explained by abovementioned Mn impurity.

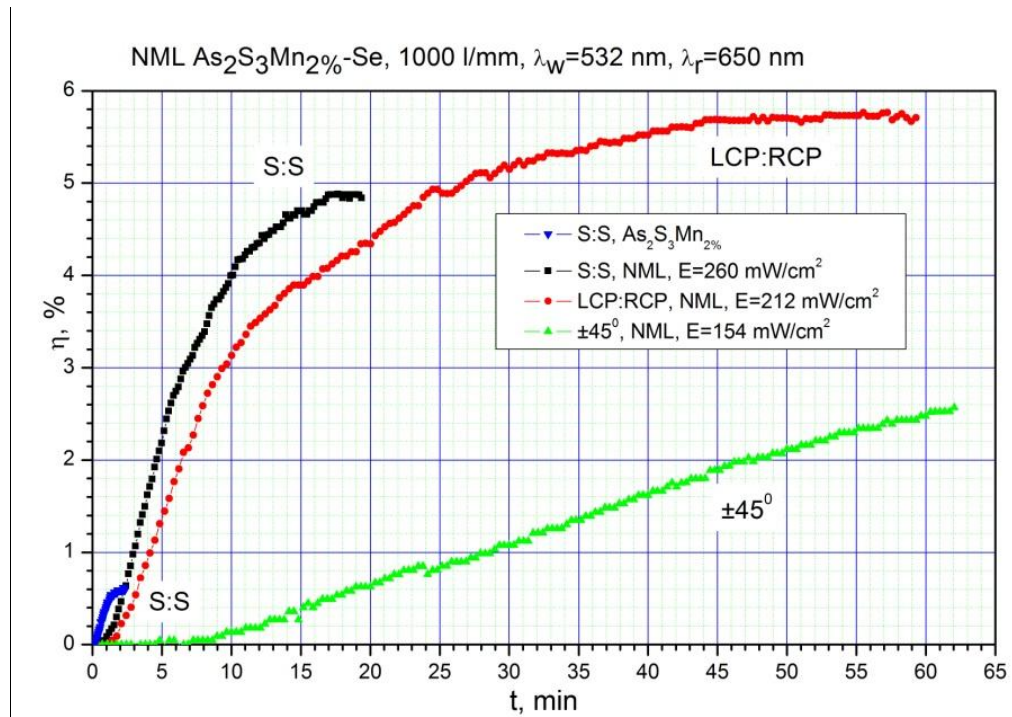


Fig. 3.14. Kinetics of diffraction efficiency of NML $\text{As}_2\text{S}_3\text{Mn}_{2\%}\text{-Se}$ at different state of polarizations of recording beams. Grating frequency 1000 l/mm.

The azopolymers have attracted much attention for the fabrication of sub-micrometer structures in one-step recording, thanks to the mass transport effect under a modulated light irradiation. Many theoretical models have been proposed to explain the mechanism of SRG formation (Ch. 1) on azopolymers. Despite these efforts, the mechanism is still not fully explained.

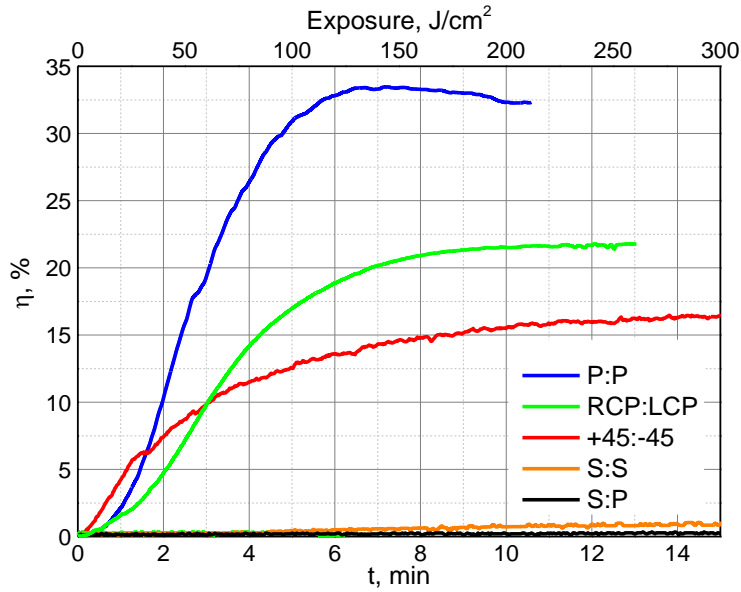


Fig. 3.15. The dependence of diffraction efficiency in transmission mode on recording time and exposure for the all studied polarization configurations using poly(PEPC-co-DO) film with thickness 1600 nm and concentration of azodye 30 wt%.

The dependence of DE of azo-dyed polymer poly(PEPC-co-DO) on recording time and exposure for all of the studied polarization configurations is shown in Fig. 3.15 [175]. Holographic recording was performed on poly(PEPC-co-DO) film with thickness 1600 nm and concentration of azo dye 30 wt%. As it can be seen in the Fig. 3.15, the DE strongly depends on the polarization configuration. The best performance is reached at P:P polarization configuration. For all polarization configurations except S:P, diffraction efficiency versus time has increased and eventually reached a relatively steady state during the exposure.

Since the best polarization configuration was determined, the next step was holographic characterization to find the optimal azo dye concentration in polymer and film thickness. To do it holographic recording using P:P polarization configuration was carried out in poly(PEPC-co-DO) films with different concentration of azo dye DO simultaneously measuring the DE. The dependence of diffraction efficiency on recording time and exposure using P:P polarization configuration during holographic recording in poly(PEPC-co-DO) film with thickness 1600 nm and azo dye concentration from 10 to 60 wt% is shown in Fig. 3.16.

As it can be seen in Fig. 3.16, the optimal concentration of azo dye in the synthesized azopolymer poly(PEPC-co-DO) is about 30% by weight, i.e. 1: 3.5 to the weight of the polymer matrix PEPC. A further increase in the concentration to 60 wt% leads to a decrease in the DE,

which is possibly due to scattering into the film, which is also observed in the transmission spectra in ch. 2.2. This can be caused by a content of undissolved azo dye in the solution and film.

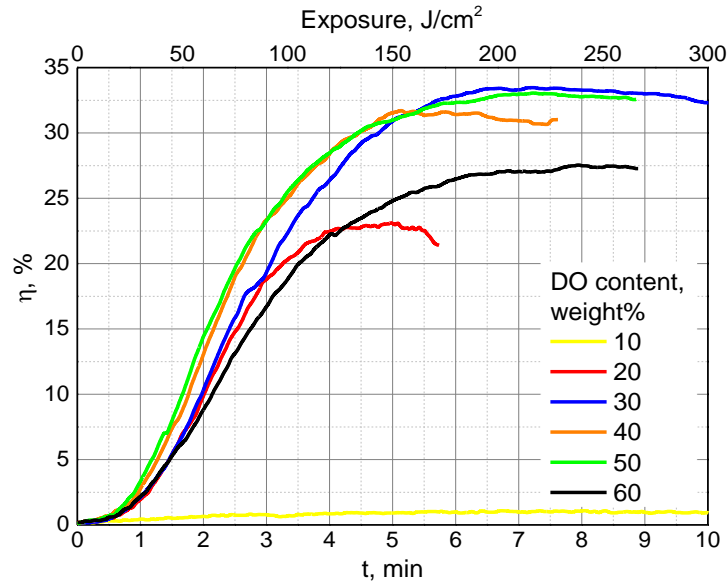


Fig. 3.16. The dependence of diffraction efficiency in transmission mode on recording time and exposure using P:P polarization configuration during recording in poly(PEPC-co-DO) film with thickness 1600 nm and azo dye concentration from 10 to 60 wt%.

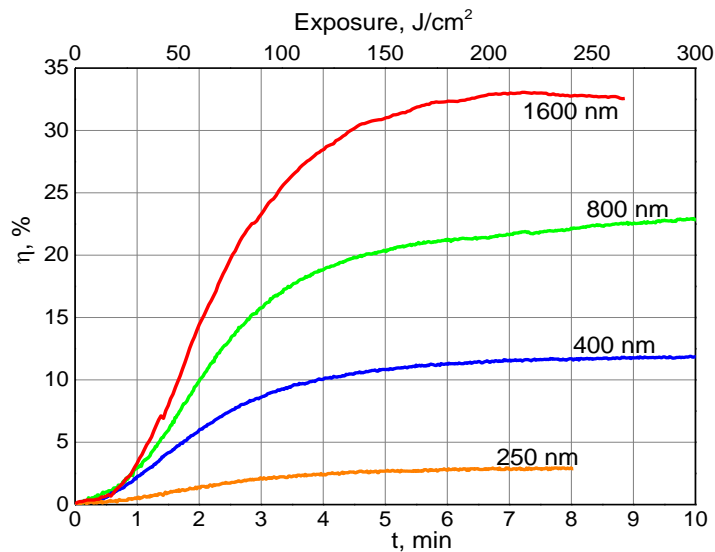


Fig. 3.17. The dependence of diffraction efficiency in transmission mode on recording time and exposure using P:P polarization configuration during holographic recording in poly(PEPC-co-DO) film with film thickness from 250 to 1600 nm.

An experiment was also conducted to study the effect of film thickness on DE. In Fig. 3.17 the growth kinetics of DE during the recording on poly (PEPC-co-DO) films of different thicknesses (concentration of azo dye 30 wt%) using a P: P polarization configuration is shown.

As it can be seen from Fig. 3.18, the optimal thickness of the film exists, which gives the highest value of DE $\eta=33\%$, and which is close to the theoretical maximum DE limit for thin sinusoidal phase gratings equal to 33.8%.

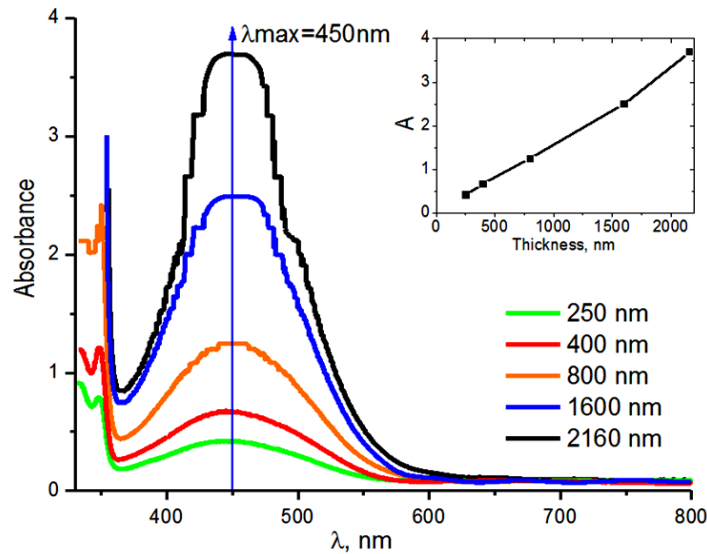


Fig. 3.18. UV-Vis absorption spectra of poly(PEPC-co-DO) films with different film thickness. DO content is 30 wt% and dependence of thickness on the value of absorption.

The maximum of the absorption region for this azopolymer is at wavelength of ~ 450 nm, which is characteristic for DO azo dye classified as pseudo-stilbene [176]. It confirms azo coupling reaction of PEPC with DO.

The films with thickness over 1600 nm show scattering of light due to presence of small bubbles after drying. The origin of the bubbles is vapor of solvent, which presents in film volume. Therefore, samples with thickness over 1600 nm were not measured for estimation of DE.

It is important to notice, that the DE in this readout scheme can result from both the anisotropic grating formed in the volume of the layer, and the surface relief grating induced on the surface of the film. The amplitude grating due to absorption coefficient changes $\Delta\alpha$ is out of readout wavelength $\lambda=650$ nm and hence the DE was not affected by light absorption modulation. Diffraction gratings made by two-beam interference that leads to a sinusoidal profile of intensity/polarization in the film with the modulation direction being parallel to the film surface. This can result in a periodic modulation of the refractive index as well as periodic modulation of film thickness. The phase delay amplitude of such type of grating can be written as $\Delta\varphi = \frac{2\pi}{\lambda \cos\alpha} \cdot (h \cdot (n - 1) + d \cdot \Delta n)$, where λ is the probe wavelength, h — amplitude of surface modulation, n is the average refractive index of azopolymer, d is film thickness, and Δn is the maximum change in the refractive index, α is a angle of diffraction for the probe wavelength. Using a probe beam

at normal incidence, the first-order diffraction efficiency of thin sinusoidal diffraction grating is given by $\eta = J_1^2\left(\frac{\Delta\varphi}{2}\right)$ [8], where J_1 is a Bessel function of the first kind, $\Delta\varphi$ represents the peak-to-peak amplitude of phase delay in grating. According to this equation, the largest possible DE into one of the +1 and -1 diffraction orders is the maximum value of J_1^2 and is equal 33.8%.

The ratio between the diffraction efficiencies due to the volume and the surface relief grating can be determined by measuring not only the intensity, but also the polarization of the first diffracted order [172]. Up to now in our experiment, no evidence of polarization changing of the first diffracted order was observed, but such study will be the subject of our future work.

According to [8], the DE can be rewritten using $\Delta\varphi$:

$$\eta = J_1^2\left(\frac{2\pi}{\lambda \cos\alpha} \cdot (h \cdot (n - 1) + d \cdot \Delta n)\right). \quad (3.1)$$

It is well known that the *cis* molecules are not stable at room temperature and the *cis-trans* isomerization is very rapid [178]. In our experiment the recording gratings were stable and measured value of DE after the grating formation was nearly constant during long storage (at least one month) at room temperature. Moreover, exposure of obtained grating by linear polarization light leads to insignificant DE change. Hence, based on the present experiments, we can presume that the main contribution for the increase of the DE is from surface relief grating.

Let's consider the DE dependence only on surface relief modulation. Thus the Eq. (3.1) could be transformed in

$$\eta = J_1^2\left(\frac{2\pi}{\lambda \cos\alpha} \cdot (h \cdot (n - 1))\right), \quad (3.2)$$

where h is amplitude of surface modulation, n is the refractive index of azopolymer.

In the Fig. 3.19, the kinetics of experimental measured 1st order diffraction efficiency at 650 nm for the poly(PEPC-co-DO) film during P:P polarization recording (blue curve) and kinetics of computed theoretically 1st order DE according to Eq. (3.2) (shown as a red curve) are presented.

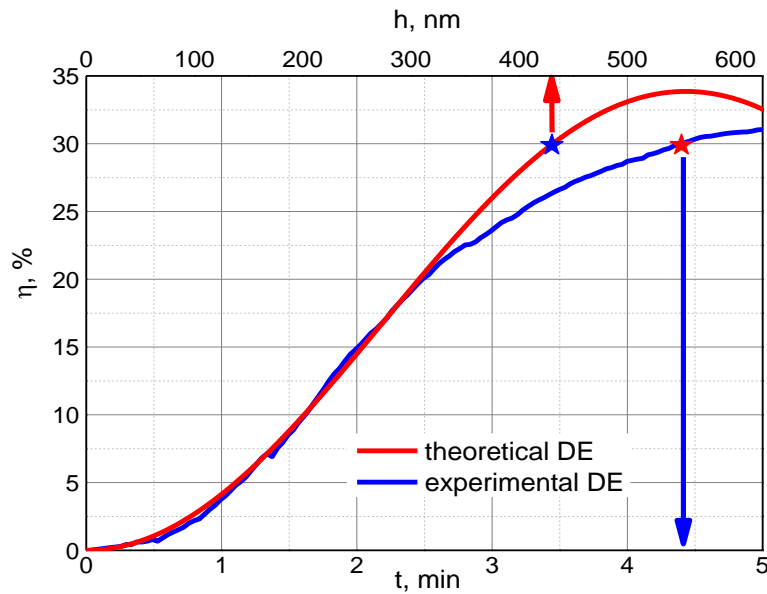


Fig. 3.19. The kinetics of experimental measured 1st order diffraction efficiency at 650 nm for the poly(PEPC-co-DO) film during P:P polarization recording (blue curve) and kinetics of computed theoretically 1st order DE according to Eq. (3.2) (shown as a red curve).

The coincidence of experimental and theoretical curves at the first part of curves is good evidence that SRG occurs in linear mode and after the grating relief depth reaches 300 nm the material feedback for the recording becomes nonlinear. It is therefore possible to estimate h from Eq. (3.2) using the first-order DE. As shown in Fig. 3.19 (red curve, blue star) that at $\eta = 30\%$ we estimate that $h = 430$ nm from Eq. (3.2). The good coincidence of experimental and theoretical estimated value of surface modulation amplitude means that DE analysis of the recorded holographic gratings in poly(PEPC-co-DO) film can be performed by assuming the SRG dominates in DE with slight influence of scalar refractive index gratings.

3.3. Digital holography recording

The science of digital holography rests on the foundations of optical holography and on the development of laser sources in the 1960s, which made his vision a practical reality. Optical holography, however, uses a photosensitive material, both to record a latent image and subsequently to behave as a DOE with which to reconstruct the incident field. In this way display holograms, using silver halide materials for example, can produce life-size images that are virtually indistinguishable from the object itself. Digital holography, in contrast, separates the steps of recording and reconstruction, and the final image is most often in the form of a 3D computer model.

Television cameras have been used from the beginnings of holography to record interferometric images. However, the huge disparity between the resolution of holographic recording materials (more than 3000 l/mm) and television cameras (around 50 l/mm) was raised as a major concern by early researchers. TV holography, as it was sometimes called, generally recorded low NA holograms producing images with characteristically large speckle and was therefore more often referred to as electronic speckle pattern interferometry (ESPI). It is possible, however, to record large NA holograms on a sensor with restricted resolution by using an objective lens or a diverging reference wave. This is generally referred to as DHM since the resolution now places a limit on the size of the object that can be recorded. As holography is a well-defined mathematical process, it can be simulated in the computer, and the results of holographic reconstruction can be displayed graphically.

Modern image sensors are now available with almost 30 million photosensitive elements, which corresponds to a staggering 100-fold increase compared to standard television images. At the same time personal computers have been optimized for imaging and graphics applications and this allows more sophisticated algorithms to be used in the reconstruction process.

Although resolution still falls short of the materials used for optical holography, the ability to process data numerically generally outweighs this drawback and presents us with a host of new opportunities.

It is well known that the fabrication of the DOE with a non-sinusoidal profile significantly improves the performance efficiency and enables the control of the diffraction angles for maximum efficiency. For example, resists with low proximity effect, high sensitivity and linear dependence between the exposed dose and the profile depth are required for the fabrication of the blazed DOE. Owing to the improvement of reconfigurable computer platform to solve any demanding control and monitoring task and the advancement of micro/nano-fabrication techniques in recent years, DOE such as binary optics and computer generated diffractive structures have been actively researched.

The phase of a light beam can be twisted like a corkscrew around its axis of propagation. If the light wave is represented by complex numbers of the form $Ae^{i\Phi}$, where A is the amplitude of the field and Φ is the phase of the wave front, the twisting is described by a helical phase distribution $\Phi = m\theta$ proportional to the azimuthal angle of a cylindrical coordinate system (r, θ, z) , where z is the propagation direction of the wave train.

Because of this twisting, the light wave along the z -axis cancels out because the value of the angular coordinate θ is not well defined at $r = 0$, giving rise to a phase singularity where the

amplitude vanishes. On a flat surface, this light beam will look like a bright ring with a dark hole in its center around which the phase rotates. Due to some analogous phenomena in fluids, this light beam is called an optical vortex (see Fig. 3.20).

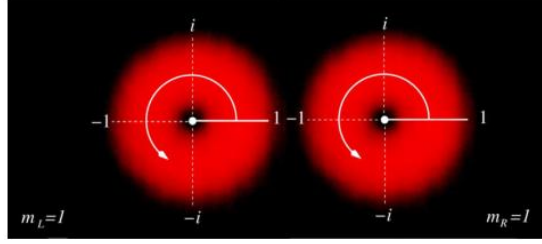


Fig. 3.20. Two beams with the same vortex charge propagating in parallel directions. The origin of the phase is arbitrary with respect to the horizontal axis. In this configuration the left side of the right beam and the right part of the left beam have opposite phases.

To assure the continuity of the field at $\theta = 2\pi$, there exists an integer number m , which indicates the number of phase windings around the dark spot. This number is the topological charge of the vortex, because it is conserved during propagation. The physical meaning of m corresponds to the velocity of the phase rotation around the singularity, which may be positive (for counterclockwise rotation) or negative (for clockwise rotation). The definition of m is given by the z -component of the angular momentum L_z . For light beams the value of L_z per photon is given by

$$L_z = -i\hbar \frac{\partial \Phi}{\partial \theta} = i\hbar m, \quad (3.3)$$

where \hbar is Planck's constant divided by 2π . From Eq. (3.3) it is evident that the continuity condition at $\theta = 2\pi$ implies the quantization of the angular momentum. The value of L_z indicates that there is a rotation of the momentum vector \vec{p} around the dark hole as the beam propagates. This analogy with the velocity fields of fluids suggests that the wave front dislocation observed in light beams should be called an optical vortex.

In recent years several important applications of optical vortices have been developed. For example, the absence of the gradient force in the central hole can be used to make optical tweezers that can trap neutral particulates [179], which receive the angular momentum associated with the rotation of the phase. In nonlinear optics, waveguiding can be achieved inside the central hole [180]. In astronomy the singularity can be used to block the light from a bright star to increase the contrast of astronomical observations using optical vortex coronagraphs [181] which are useful for the search of extrasolar planets. Applications in quantum information employing quantized properties of the angular momentum of vortex light beams have also been proposed [182].

As we show on vortex examples, the agreement between theory and experiment is remarkable for diffraction optics, and thus it provides a well characterized system for the study of such phenomena. The Fig. 3.21 shows the developed interferometer with Spatial Light Modulator (SLM) for recording the vortex diffraction structures.

DOE recorded by laser holographic technique have limit in design of various optical images. On the contrary a variety of DOEs such as Fresnel lenses, gratings with linear and curves lines, variable pitch and special line profile gratings can be sophisticated recorded by e-beam. Of coarse PC program for DOE design and PC-assisted scanning electron microscope for e-beam control must be elaborated.

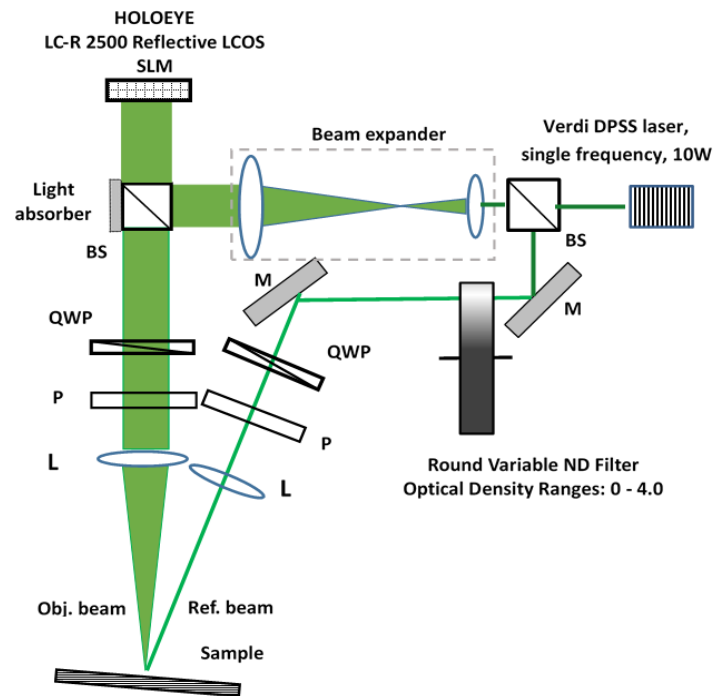


Fig. 3.21. The interferometer setup with SLM for DOE recording.

In the field of diffraction grating recording the e-beam patterning has been developed for exposing the sensitive media to constant electron dose at the desired locations. If a dose variation is implemented during the process of recording, the e-beam sensitive material accumulates different doses under exposure. For common used materials, e-beam resists, the following development process results in different thicknesses of resist, and, correspondingly in the 3D profile of the final structure.

In this chapter, we present the one-step e-beam recording of digital holograms on As_2S_3 thin films, ChG-Se NML, and azopolymers. Some diffraction structures in As_2S_3 thin films de-

signed and recorded by PC-assisted raster electron microscope to demonstrate the software and hardware capabilities. A media used for this purpose should have a high resolution and sensitivity, a linear dependence of the profile depth on the electron dose, and a good repeatability of the profile shape. Irradiation of ChG thin films by e-beam leads to noticeable changes in their properties. These changes are connected with the short-range order modification because of chemical bond transformation in the material. The atomic structure variations modify the electronic structure of the disordered system, leading to changes in the film properties.

The experiments on the surface relief formation were performed using a SEM with the installed computer-assisted system [183]. The system operates a Gaussian beam to write point-by-point in a raster manner. In order to achieve, for example, a solid exposed line, the exposure points should be close enough to each other so that there is no space between them. The point separation (called the beam step-size) is user-defined and totally dependent on the physical size of the chosen beam.

Thin films of As_2S_3 (about 1 μm) were prepared by thermally evaporation in vacuum (10^{-5} mm Hg) on glass substrate covered by semitransparent metal layer. Based on the scanning electron microscope (SEM) BS 300 (Tesla) and 16-bit control adapter NI USB-6216 the system SEM-PC has been developed. In order to design the DOE with numerical methods we have used a specialized software LabWindows/CVI-8.5 compiled in virtual instruments environment. Developed software gives possibility of e-beam positioning both in raster and vector mode of recording of diffraction structures. Square region of recording was determined by SEM magnification and was about 1600 $\mu\text{m} \times 1600 \mu\text{m}$. The diffraction gratings of different configurations were recorded in the vector mode. In this case the minimum distance between pixels was about 0.05 μm . The raster mode of patterning has been applied for recording of the microimages presented in .bmp format. The 8-bit grayscale graphical files have been used for recording of the microimages with the dimensions 256 \times 256 pixels and 512 \times 512 pixels. The black/white levels were obtained by discrete varying the time exposure of e-beam at one-pixel point during the recording process. The minimum exposure time/pixel was 0.1 ms.

MakeHolo software [184] developed in our laboratory was applied for synthesis of digital hologram from an image. These digital holograms were subsequent recorded by e-beam on the thin films of As_2S_3 . In black regions of microimage the e-beam moves significantly quickly than in white ones so no evident influences of electron irradiation on recording media (thin film of As_2S_3) index of refraction occurred. E-beam current determining dose of electron irradiation was ranged from 1 to 2 nA. The e-beam penetrates all the depth of the thin film of As_2S_3 at accelerating voltage 25 kV. Micro-images were recorded by e-beam directly without any addition development.

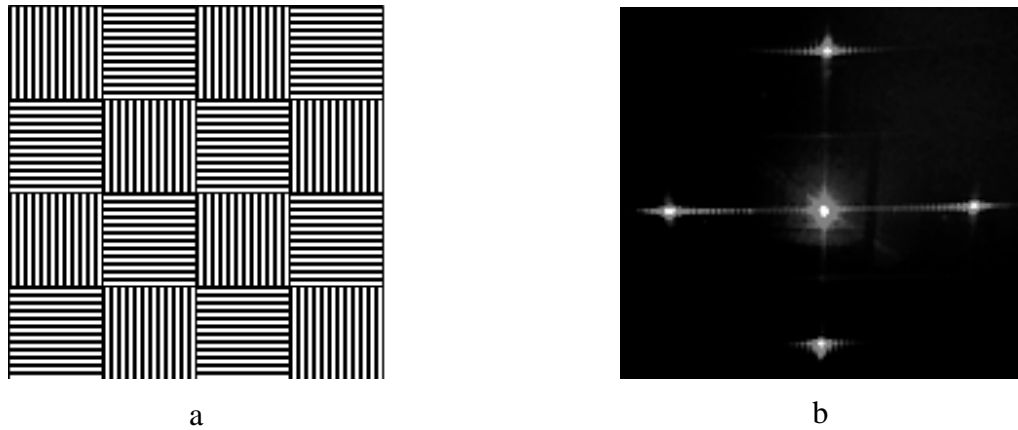


Fig. 3.22. Mosaic chess-board structure composed from diffraction gratings (a) and its diffraction pattern (b).

Important type of DOE is a mosaic of diffraction gratings. It can be consisting of diffraction gratings with different direction of mutual orientation, grating period, including variable period and so on. Diffraction patterns obtained during reconstruction by laser beam illumination in transmission mode depend on how many elements of mosaic are illuminated simultaneously. Multibeam diffraction of light can be obtained if laser beam spot overlaps some diffraction gratings.

The sketch of chess-board structure (Fig. 3.22) composed from two orthogonally oriented diffraction gratings with periods 2.0 and $2.2 \mu\text{m}$ is presented. Mosaic digital hologram and its diffraction grating have dimensions $800 \mu\text{m} \times 800 \mu\text{m}$ and $200 \mu\text{m} \times 200 \mu\text{m}$, consequently.

Laser spot of $400 \mu\text{m}$ diameter illuminates at list two gratings so it can be seen complex diffraction pattern in transmission mode (Fig. 3.22b). Equal intensity diffraction spots can be clear seen from both orthogonal oriented gratings.

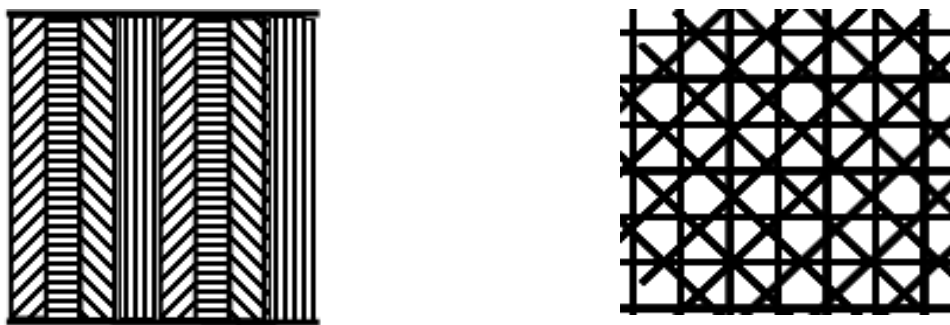


Fig. 3.23. Part of mosaic structure with set of diffraction gratings (a) and the structure of $N=4$ superimposed diffraction gratings (b).

On Fig. 3.23 the sketch of fragment of mosaic composed digitally from gratings in form of strips is presented. Four mutual orientations of gratings lines with 45° steps rotation were chosen to

obtain diffraction pattern with circle symmetry. Period of each grating in form of the strip and size of mosaic are $2\ \mu\text{m}$ and $800\ \mu\text{m} \times 800\ \mu\text{m}$, consequently. Width of each strip is equal to $50\ \mu\text{m}$. Four gratings-strips with total dimension of $200\ \mu\text{m}$ form the mosaic period. Diffraction pattern is presented for case when laser spot diameter is equal to $400\ \mu\text{m}$ (Fig. 3.23a).

Diffraction patterns from mosaic digital gratings Fig. 3.23 (a and b) are shown on Fig. 3.24a and b consequently. The most brightness spots on diffraction patterns are formed by the first order of diffraction beams for both diffraction structures. Additional spots on diffraction pattern are formed when laser illuminates nodes of tangency of diffraction gratings lines (Fig. 3.24b).

Note that in practical application of these digital holograms as optical code the additional diffraction spots appearance in the diffraction pattern are undesirable. So the preferable diffraction pattern contains only first order of diffraction beams (Fig. 3.24a).

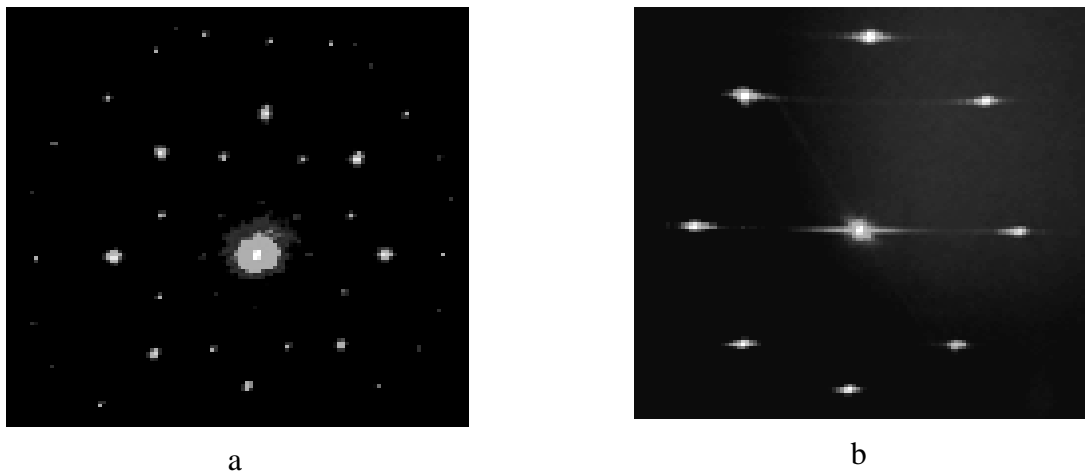


Fig. 3.24. Diffraction patterns generated by structures shown on Fig. 3.23 (a) and (b), consequently.

As to apply the etching development for recorded gratings the quality of single diffraction grating is higher in comparison with the quality of superimposed ones after etching. Drawback of mosaic structures is horizontal stretching of diffraction spots (Fig. 3.24a). We consider this undesirable stretching is defined by small dimensions of strips. Optimization of dimensions of laser spot diameter and strip width can rise the quality of diffraction pattern.

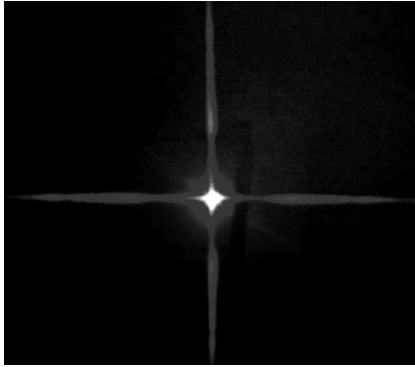


Fig. 3.25. Diffraction pattern formed by crossed superimposed gratings with variable pitch.

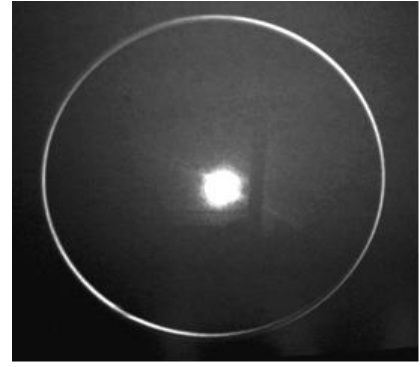
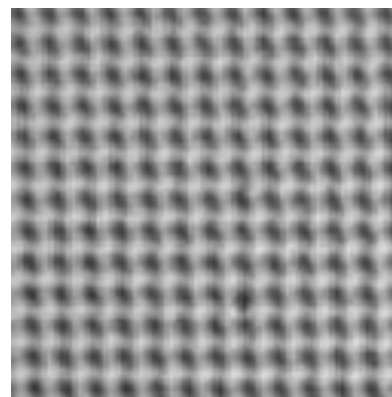


Fig. 3.26. Ring diffraction pattern generated by set of concentric circles

Recording of diffraction gratings with variable pitch is an advantage of PC-assisted raster electron microscope in comparison holographic method of recording. Orthogonally directed diffraction gratings with linearly variable pitch from $2\ \mu\text{m}$ to $1\ \mu\text{m}$ were recorded in superimposed mode. This structure covers surface $400\ \mu\text{m} \times 400\ \mu\text{m}$. Diffraction pattern of this diffraction structure is shown on Fig. 3.25.



a



b

Fig. 3.27. Institute of Applied Physics logo formed by pixels (a) and part of pixels matrix of every line on the logo (b).

Diffraction gratings with linearly variable pitch gives diffraction pattern in form of continuous line compose from \pm first order spots. Obviously orthogonally superimposed diffraction gratings will produce cross of such lines (Fig. 3.25). Set of one hundred of concentric circles with gradation of radii in $2\ \mu\text{m}$ was recorded by PC-assisted scanning electron microscope. Ring diffraction pattern generated by this set is presented on Fig. 3.26.

Microimages were directly recorded by e-beam into square surface of thin film of As_2S_3 with $1.6\text{mm} \times 1.6\ \text{mm}$ dimension. No etching development was applied for microimages. Below

are presented microphotography under compound microscope (Fig. 3.27a) where can be clear seen logo of Institute of Applied Physics in abbreviation on Romanian language.

The logo was composed from wide lines in turn composed a matrix of pixels. Pixel distance is equal to 3 μm . E-beam induced changes of the index of refraction and the absorption coefficient (darkening) give possibility visualization of the logo. Pointed above the matrix of pixels can be clear seen on Fig. 3.27b. A matrix of equal distances pixels works as diffraction grating too with own diffraction pattern.

By using the MakeHolo software for the synthesis of digital hologram from an image of cube with transparent sides was done. Digital hologram in the form of 8-bit grayscale graphical file is shown on Fig. 3.28.

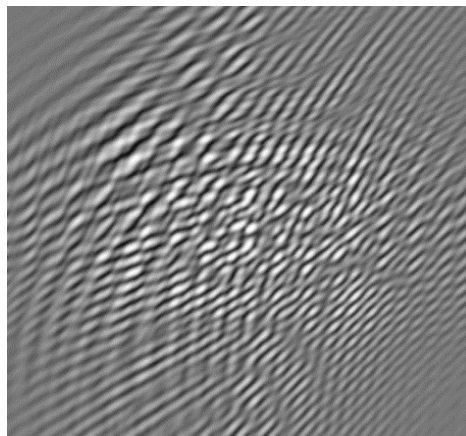


Fig. 3.28. Synthesized digital hologram of cube image, which image has been then recorded on As_2S_3 thin film.

This digital (computer-synthesized) hologram was recorded by e-beam into thin film of As_2S_3 with thickness 1 μm . The surface occupied by hologram on the film was estimated as 600 μm \times 600 μm . Diffraction pattern in the first order of diffraction of cube image has been reconstructed by illumination of red He-Ne laser beam (wavelength is 0.633 μm , Fig. 3.29). This pattern is presented as black/white photography. It is clear seen only two images of cube from the first diffraction orders and zero order of diffraction pattern.

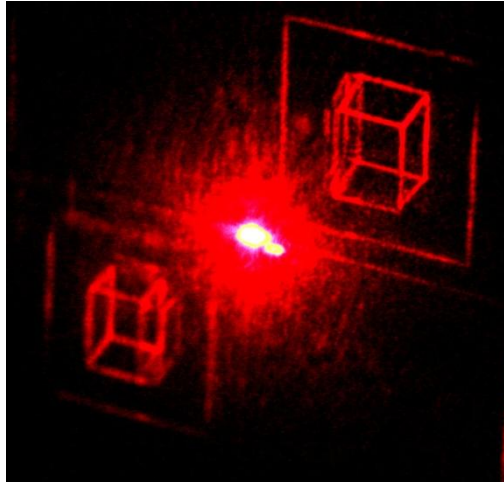


Fig. 3.29. Wire cube image in the first orders reconstructed by red laser beam.

The first objective was to measure the dose dependence of the DE for e-beam recording at currents 1–10 nA for the grating periods of 1 μm , 2 μm and 4 μm . The sample $\text{Ge}_5\text{As}_{37}\text{S}_{58}\text{-Se}$ NML was used [185]. The images of the SRG were obtained on the AFM and are shown in Fig. 3.30 and Fig. 3.31.

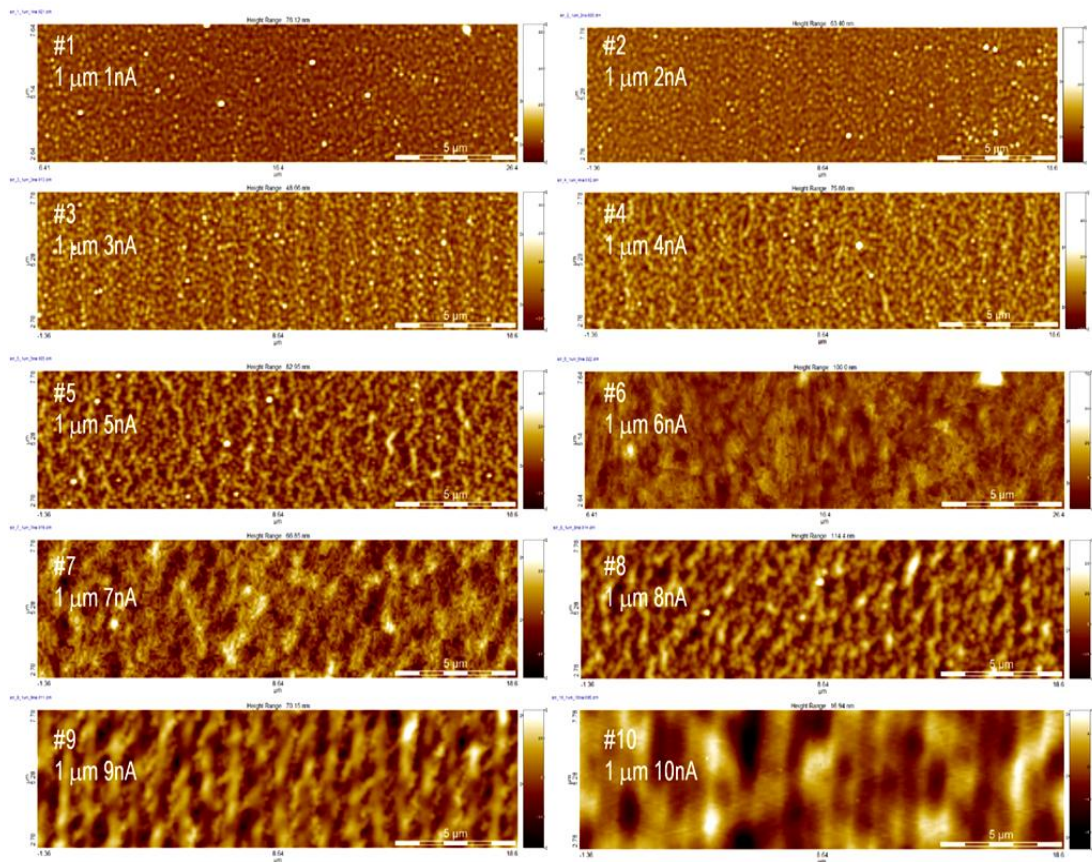


Fig. 3.30. The AFM data of SRG recorded on $\text{Ge}_5\text{As}_{37}\text{S}_{58}\text{-Se}$ NML at different e-beam currents.

It is seen from Fig. 3.30 that period of grating $1\ \mu\text{m}$ is very small to form the grating at the conditions of current beam from $1\ \text{nA}$ to $10\ \text{nA}$ and the diameter of the beam $0.3\ \mu\text{m}$. The Fig. 3.31 shows the AFM data of SRG recorded at different period of gratings.

As it can be seen from the figures, the sharpest image is obtained for grating periods of 2 and $4\ \mu\text{m}$, and also for recording currents $8\text{--}10\ \text{nA}$.

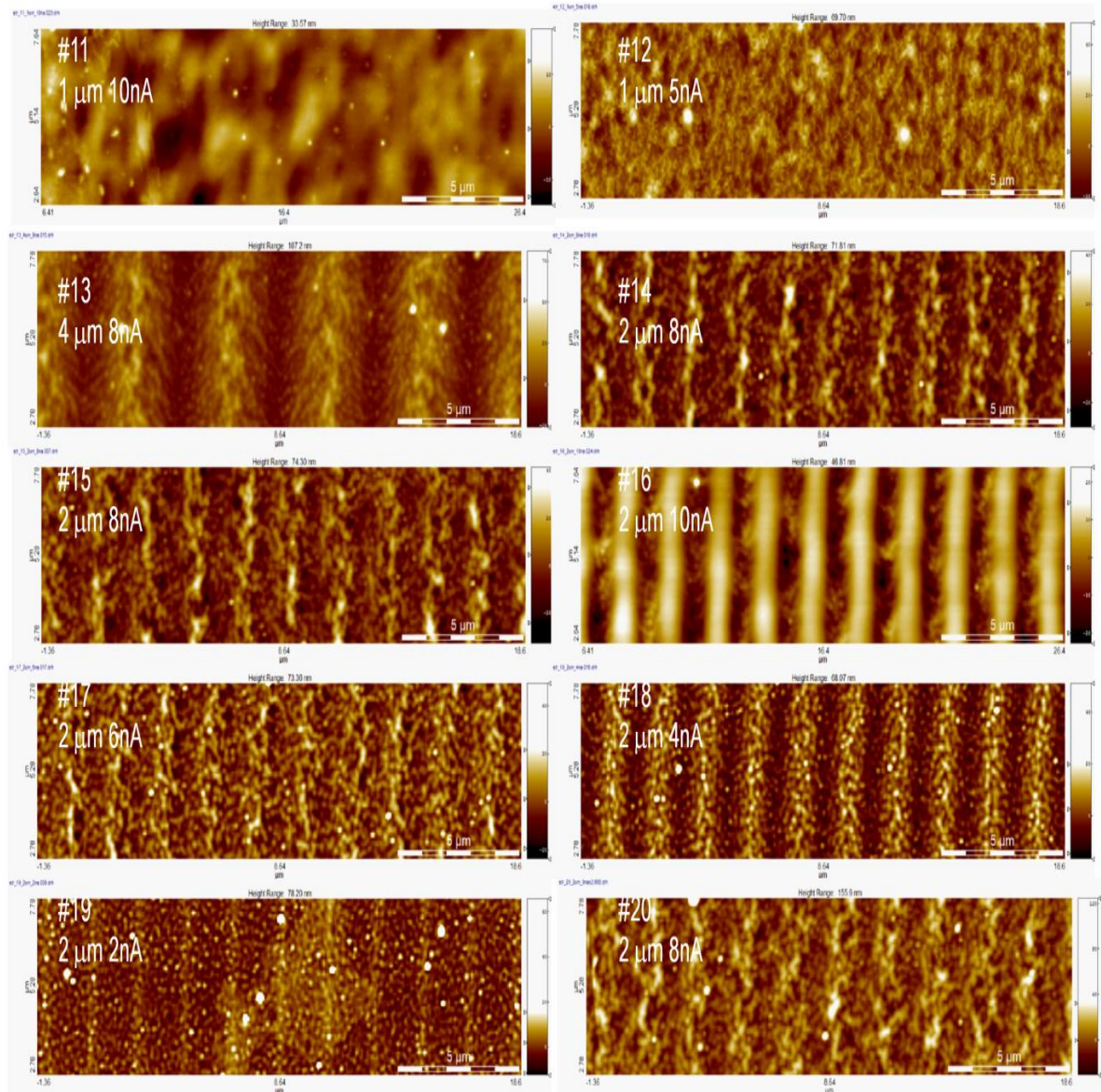


Fig. 3.31. The AFM data of SRG recorded on $\text{Ge}_5\text{As}_{37}\text{S}_{58}\text{-Se}$ NML at different e-beam currents and grating periods.

The results of direct recording (without the selective etching step) of holographic diffraction gratings and images by e-beam exposure using $\text{Ge}_5\text{As}_{37}\text{S}_{58}\text{-Se}$ NML $3\ \mu\text{m}$ thick with the underlying conductive layer ITO as recording media are presented. E-beam recording of diffraction gratings (spatial frequency $500\ \text{mm}^{-1}$) and other elements were carried out using SEM Tesla BS 300

with programmable exposure control unit. Beam current was $\sim 4\text{--}10$ nA. Images were recorded with size 512×512 pixels, pixel size was ~ 2 μm (Fig. 3.32). DE of the recorded gratings were $\sim 1\text{--}2\%$. Also, different figures and letters were recorded with the use of 2 μm pixels. AFM images of the structures obtained by e-beam recording are presented in Fig. 3.33–Fig. 3.35. It can be seen in these figures that different structures like gratings, other optical elements, and figures can be recorded in multilayer nanostructures based on chalcogenide glasses.

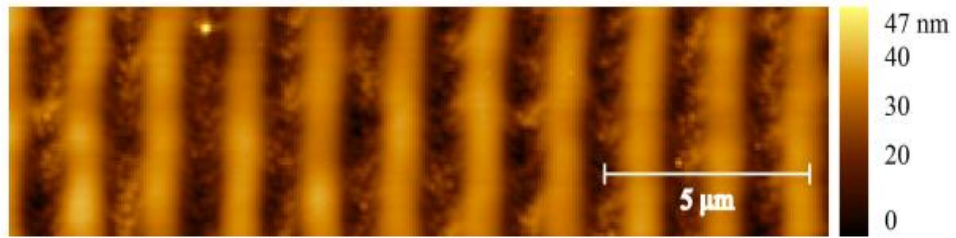


Fig. 3.32. AFM image of the grating with 2 μm period obtained by e-beam recording.

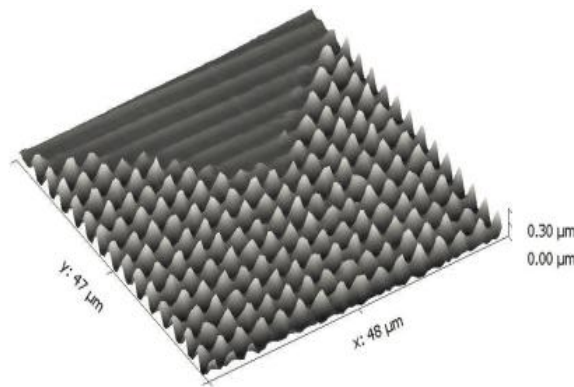


Fig. 3.33. 3D AFM image showing a fragment of the picture recorded by e-beam.

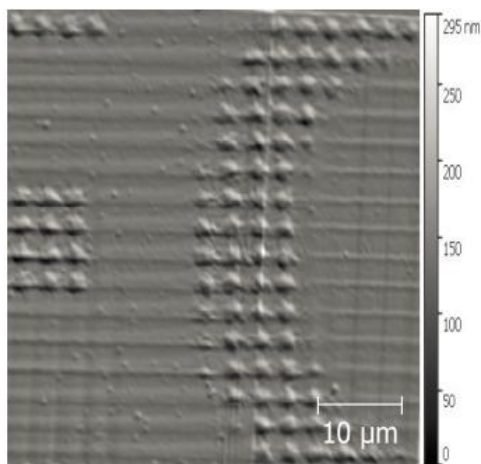


Fig. 3.34. AFM image of the fragment of letter “C”. Pixel size is 2 μm .

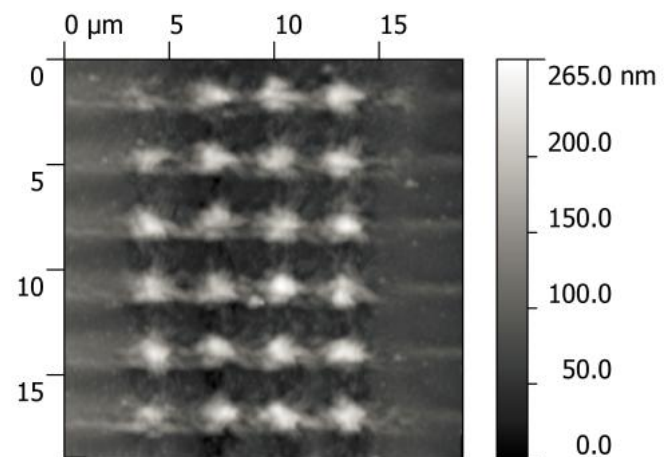


Fig. 3.35. AFM image of the fragment of letter “E”. Note that pixel height is ~ 265 nm.

In Fig. 3.36, AFM images of diffraction gratings recorded by e-beam exposure with 4 μm and 2 μm periods are presented. DE of the gratings was $\sim 1\%$. Further investigations are necessary for the optimization of multilayer nanostructure parameters and conditions of grating recording.

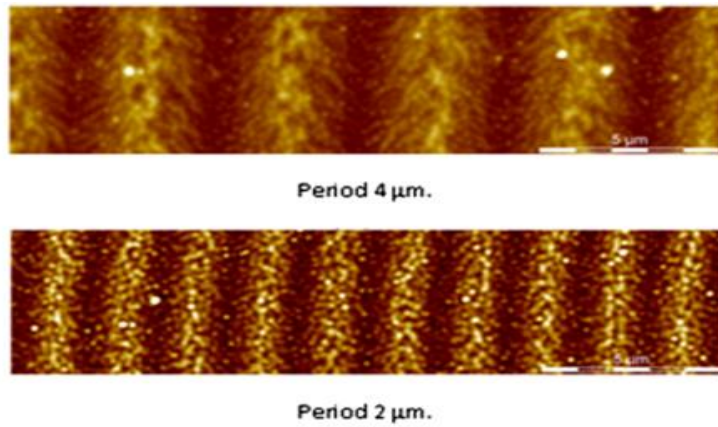


Fig. 3.36. E-beam recorded diffraction gratings with different periods.

As the next image for e-beam recording, a BMP drawing with SECURE text of different sizes was selected. Below it is a pixel-by-pixel representation of the figure produced by the PC-SEM program for the e-beam digital image recording.

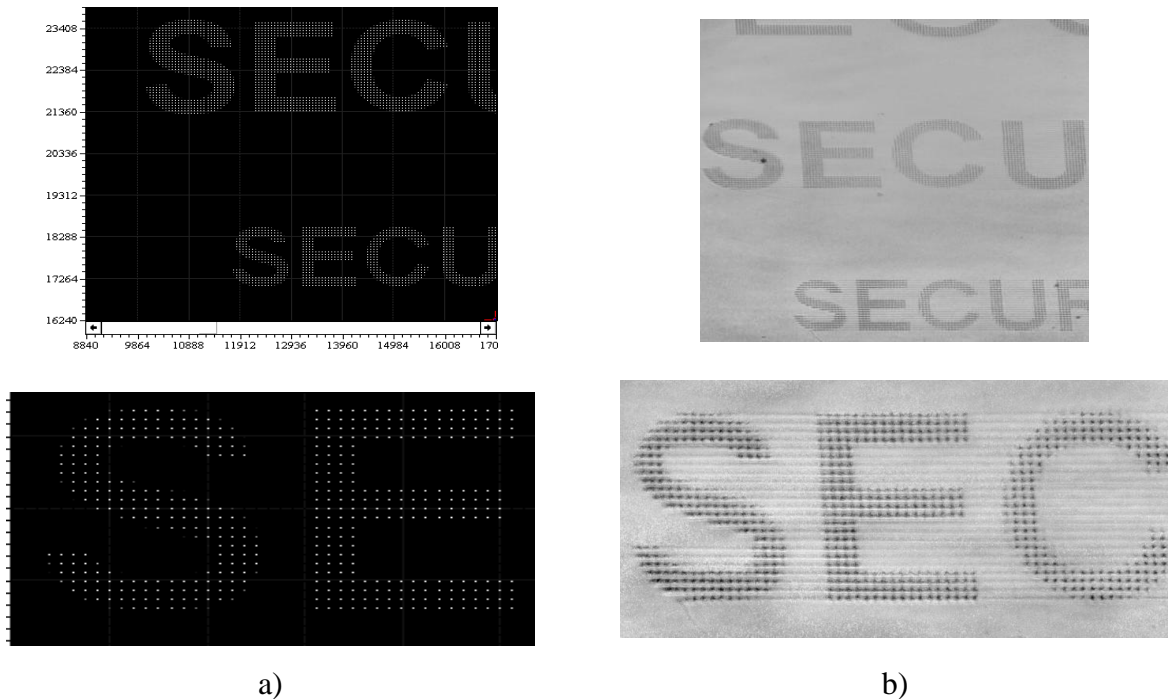


Fig. 3.37. a) The computer simulation of the word “SECURE”; b) The photos of the word “SECURE” patterned on $\text{Ge}_5\text{As}_{37}\text{S}_{58}\text{-Se}$ NML.

Fig. 3.37 presents the computer simulation of the image (Fig. 3.37a) and the photos of the image patterned on $\text{Ge}_5\text{As}_{37}\text{S}_{58}\text{-Se}$ NML and asquired by Web camera mounted on optical microscope БИОЛИАМ-Р12 magnification 90×10^x (Fig. 3.37b).

Fig. 3.38(a, b) presented the AFM data of the word “SECURE” patterned on $\text{Ge}_5\text{As}_{37}\text{S}_{58}\text{-Se}$ NML, the 3D presentation and the periodical profiles.

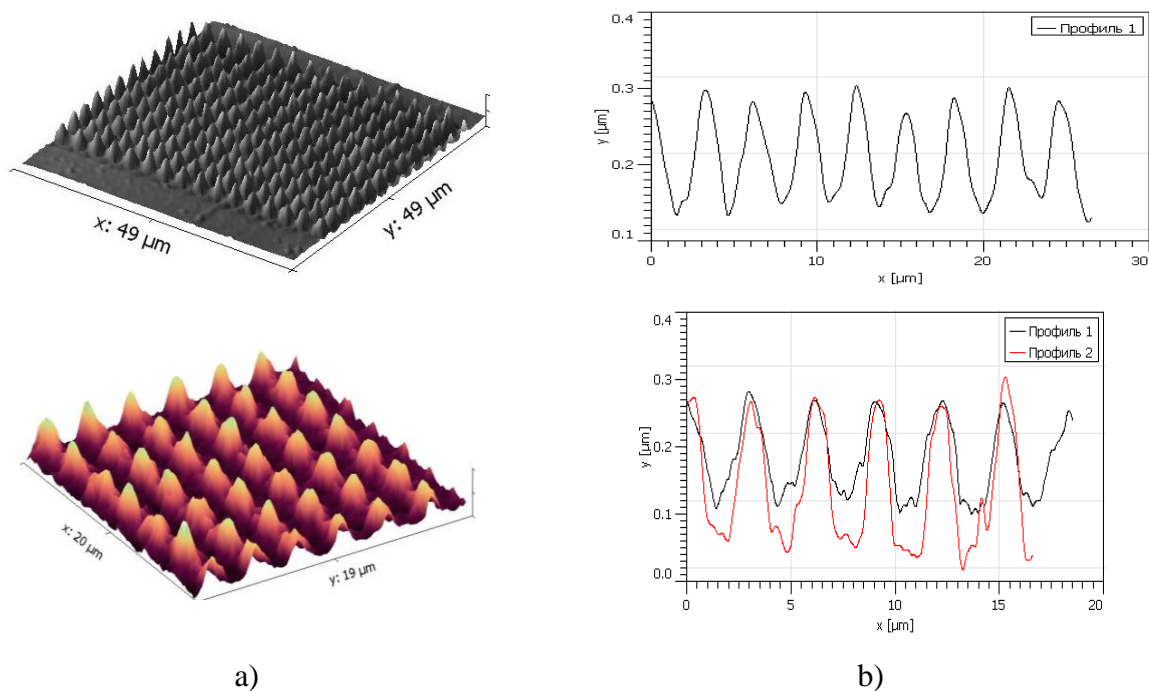


Fig. 3.38. a) 3D presentation of the word “SECURE” patterned on $\text{Ge}_5\text{As}_{37}\text{S}_{58}\text{-Se}$ NML; b) The profiles of the word “SECURE” patterned on $\text{Ge}_5\text{As}_{37}\text{S}_{58}\text{-Se}$ NML.

The State Emblem of Moldova has been chosen for creation of image by computer-assisted SEM microscope. In the Fig. 3.39 one can see the computer simulated image and corresponding image on $\text{Ge}_5\text{As}_{37}\text{S}_{58}\text{-Se}$ NML.

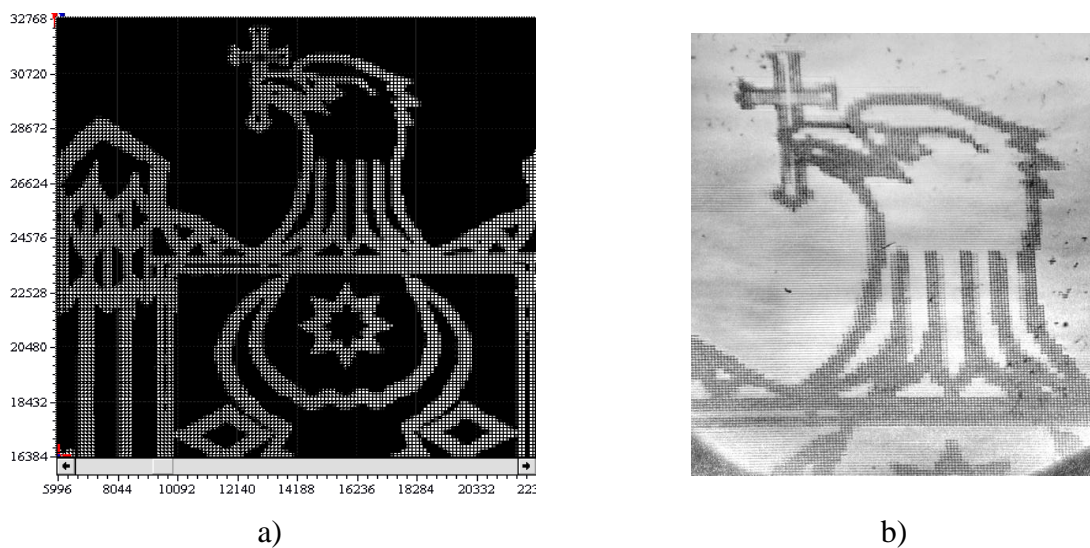


Fig. 3.39. a) The fragment of computer simulated image of The State Emblem of Moldova; b) The image recorded on $\text{Ge}_5\text{As}_{37}\text{S}_{58}\text{-Se}$ NML from Fig. 3.39a.

The AFM data of the image of the State Emblem of Moldova recorded on $\text{Ge}_5\text{As}_{37}\text{S}_{58}\text{-Se}$ NML by PC-SEM system. The maximum depth of profile is 250 nm. The height of the patterns was controlled through changing holding time of e-beam at one point (Fig. 3.40).

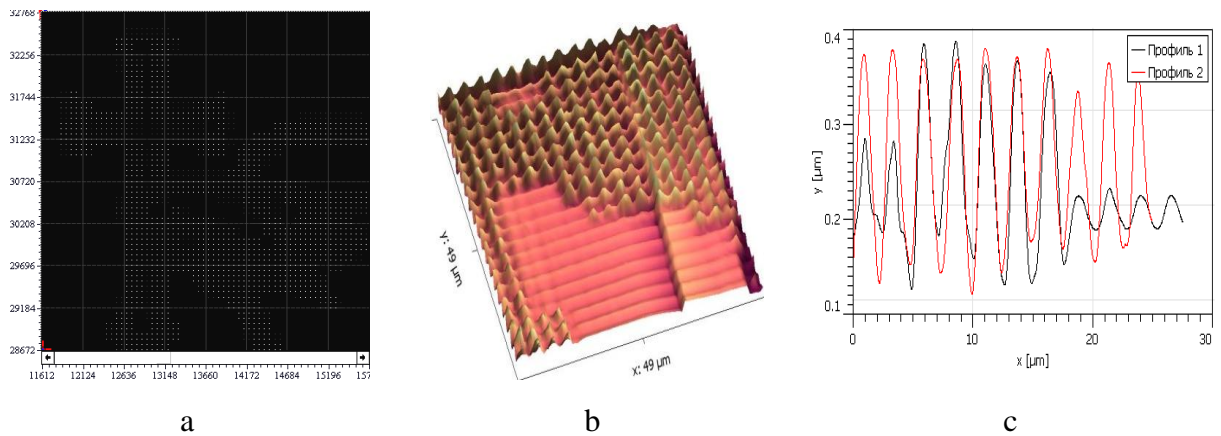


Fig. 3.40. The fragment of computer simulated (a), 3D presentation (d) and profile (c) of the image of The State Emblem of Moldova.

From these results, it is seen that by computer-assisted e-beam not only two-dimensional images, but continuous values of tone raster data are possible to record.

3.4. Conclusions to Chapter 3

1. Scalar and vector holographic methods were exploited for explanation of diffraction efficiencies dependencies. The studying of the diffraction efficiency vs. exposure dose shows the strong dependence of η on the state of polarization of recording beams. Considerable increase of NML diffraction efficiency in comparison with ChG component nanolayers has been demonstrated.
2. Scalar and vector holographic one-step recording properties of three types of nanomultilayers $\text{As}_2\text{S}_3\text{-Se}$, $\text{As}_{37}\text{S}_{58}\text{Ge}_5\text{-Se}$ and $\text{As}_2\text{S}_3\text{Mn}_{2\%}\text{-Se}$ compositions were analyzed.
3. Comparison of the surface relief gratings formation on the NML $\text{As}_2\text{S}_3\text{-Se}$ and As_2S_3 multilayers at different states of the recording beams polarization reveals that circular and $\pm 45^\circ$ polarization create the SRG in NML with higher DE of recording than in As_2S_3 multilayers part of sample with P:P and S:S polarizations. The twofold increase in DE in NML $\text{As}_2\text{S}_3\text{-Se}$ in comparison with As_2S_3 part of film was obtained. The dependence η vs. doses for NML $\text{As}_2\text{S}_3\text{-Se}$ does not reach the saturation of 1000 J/cm^2 and $\eta=25\%$ at 800 J/cm^2 . The contrary behavior has been observed for As_2S_3 multilayers: the dose dependence of η has strong maximum which equals 12% at 40 J/cm^2 .
4. Holographic investigation of the PEPC or CAM: OMA copolymers with iodoform showed their applicability to recording of holographic gratings with the DE $\eta \approx 20\%$ and a resolution of 2000 l/mm achievable only after chemical treatment. The interaction of laser and e-beams with

carbazole-containing photopolymers results of formation the charge transfer complex between carbazole and iodoform the new absorption band arises in the wavelength range of 0.65 μm . The introducing of plastificator minimizes the fracturing of thin films and creates the conditions for hidden gratings. The relief surface gratings forming after etching of hidden gratings have non-sinusoidal profile.

5. The possibility of direct one-step magnetic relief formation using NML $\text{As}_2\text{S}_3\text{Mn}_{2\%}\text{-Se}$ was shown.

6. Holographic recording on the poly(PEPC-co-DO) film at different polarization configurations showed that the P:P polarization of recording beams provides the maximum of DE about 33%. The main contribution in the value of DE of recorded holographic grating brings the surface relief grating.

7. Digital holograms were fabricated in a direct, one-step process of recording by e-beam. Developed programming HoloMake software for digital holograms recording was elaborated.

4. DIFFRACTIVE STRUCTURES INVESTIGATION

Non-contact optical methods become the default tools for quality control of products in laboratory practice and industry as well. Optical non-destructive testing (NDT) have high sensitivity and they allow a full-field analysis of the inspected area without any need for physical contact with the surface. They can sometimes provide more or different information where the other techniques fail or cannot be applied. Experimentally, the SRG formation is usually studied using the diffraction efficiency (DE) method in condition of absence of other reasons.

4.1. Diffraction efficiency method

In this part, we study how the polarization states of recording beams and the period of recorded gratings influence on the diffraction efficiency of the formed structures.

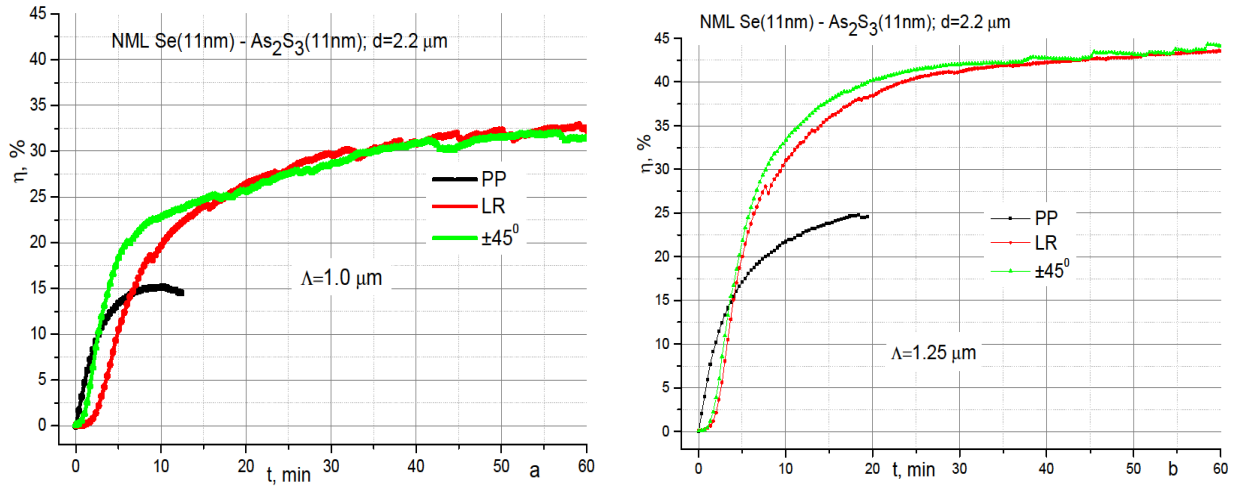


Fig. 4.1. The kinetics of diffraction efficiency for $\Lambda=1.0 \mu\text{m}$ (a) and $\Lambda=1.25 \mu\text{m}$ (b) for different states of polarization.

DE recording kinetics for NML As₂S₃-Se with two grating periods Λ is shown in Fig. 4.1. Recording of grating was continued until saturation level of the DE' value is achieved. The progresses of kinetic curves differ strong for grating periods $1.0 \mu\text{m}$ (Fig. 4.1a) and $1.25 \mu\text{m}$ (Fig. 4.1b), and depend on beams states of polarizations. For intensity gratings the DE' results for S:S and P:P polarizations recording are identical, and we present only P:P. The largest value of DE were obtained for orthogonal linear $\pm 45^\circ$ and circular LCP:RCP polarized beams configuration when SRG is recorded. For these configurations there are components of resultant electric vector of light parallel and perpendicular to the grating vector direction. This indicates that the resultant electric field and its direction variation are essential to the formation of SRG on the ChG.

For polarization gratings i.e. recorded at LCP:RCP and $\pm 45^\circ$ of polarization states the recording process begins in 1–3 min. after turning on the illumination and reach the saturation in 45–50 min. For amplitude gratings (P:P polarization) the recording begins immediately after illumination and have maximum in 7-17 min. and then decline in value. Maximal reached value of DE depends on the recording grating period. In Fig. 4.1 the data corresponding the minimal value of DE for period $\Lambda=1 \mu\text{m}$ and the maximal DE for $\Lambda=1.25 \mu\text{m}$ are shown. Vector recording in NML As_2S_3 -Se is more efficient than scalar one. The best value of $\text{DE}=45\%$ is obtained for vector recorded gratings and $\text{DE}\approx 25\%$ is for scalar one.

Note that in Fig. 4.1 the DE of NML As_2S_3 -Se with thicknesses of nanolayers $d=11 \text{ nm}$ for both As_2S_3 and Se nanolayers is shown. The other nanolayers thickness values as $d_{\text{As}_2\text{S}_3}=9 \mu\text{m}$, $d_{\text{Se}}=5 \mu\text{m}$ gives close to the maximal value of DE for $\pm 45^\circ$ and P:P polarization (see Fig. 4.2).

The grating period dependencies for vector and scalar recordings are compared in Fig. 4.2. Maximal value of DE monotonically increases for scalar HG whereas a maximum around $\Lambda = 1.25 \mu\text{m}$ takes place for vector HG. Moreover, the evolution of DE is constantly rise until saturation for PP polarization whereas for $\pm 45^\circ$ one can see the slope around 10 min at $\Lambda = 1.7 \mu\text{m}$. For periods $\Lambda = 2.0 \mu\text{m}$ and $\Lambda = 2.5 \mu\text{m}$ we observe the N-form of time dependence of DE. It is evidence of the existing more than one process during grating formation.

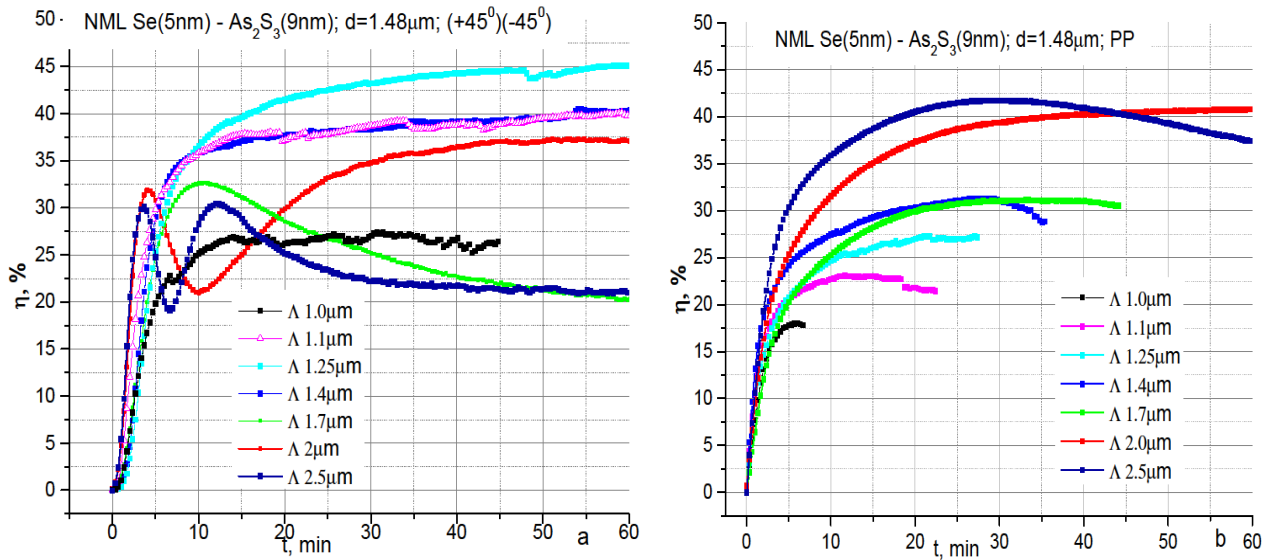


Fig. 4.2. The kinetics of diffraction efficiency of vector (a) and scalar (b) recordings for different periods of diffraction gratings.

Periodic gratings can be categorized as either thick or thin [186]. Thick gratings show Bragg diffraction. Their DE can be approximated analytically using Kogelnik's coupled wave

theory [187], which is valid close to the Bragg angle. Thin gratings show Raman-Nath diffraction. They are classically treated with scalar diffraction theory and their far field diffraction efficiencies are approximated using the Fraunhofer approximation [11].

In order to categorize gratings as either thick or thin for finite values of thickness (d), one may look for a parameter that indicates whether the analytical expressions for Bragg and Raman-Nath diffraction result in reasonable approximations. This is done by comparing the grating thickness d and the wavelength λ with Δn and/or the average index of refraction n and the grating period Λ . Most often, the Klein parameter [188], $Q = \frac{2\pi d\lambda}{n\Lambda^2}$ is used for evaluations and a grating is considered thin when value $Q < 1$ and thick when $Q > 10$.

The estimation of Q parameter for the NML As_2S_3 -Se was shown that we can consider the diffraction grating as a thin grating for period Λ more than $1.4 \mu\text{m}$. The diffraction gratings with period less $1.4 \mu\text{m}$ are intermediate gratings, i.e. neither thick nor thin. In Fig. 4.3 the kinetic of diffraction efficiency are presented for different periods of grating and two combinations of nanolayers thicknesses. It is seen that really the form of curve is changed at period $1.4 \mu\text{m}$. We observe the constant rise of DE up to saturation at Λ from $1.0 \mu\text{m}$ to $1.25 \mu\text{m}$. The maximum value of DE is about 45%, which exceeds the theoretical limit for thin gratings 33.9%. It is indicating that these gratings don't obey the Raman-Nath diffraction. Beginning from periods at $1.4 \mu\text{m}$ to $2.5 \mu\text{m}$ the curves of DE's kinetics have one or even two (for $\Lambda = 1.4 \mu\text{m}$) maximums, whereas the value of DE's maximums is less (30–40%) than for smaller periods. It may be explained by appearance of higher diffraction orders which we observed in experiment.

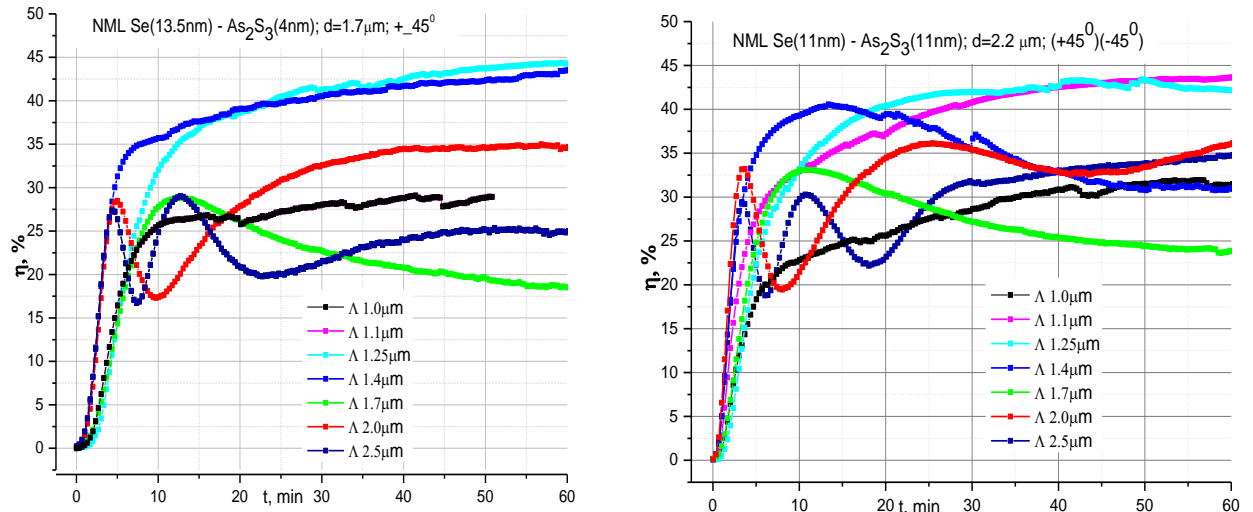


Fig. 4.3. The kinetics of diffraction efficiency in the first order for different thicknesses of nanolayers and $\pm 45^\circ$ of polarization states of recording beams.

Note that this alteration of DE's kinetics exists only for polarization gratings recorded at $\pm 45^\circ$ and LCP:RCP polarizations, not for intensity gratings. For comparison we present the data on 0 showing the kinetics of scalar gratings diffraction efficiency for P:P recording beams polarizations.

From Fig. 4.4 one can see that for all samples under investigation the P:P polarization states of recording beams gives the increase of DE reaching the high value $\sim 45\%$. Only for $\Lambda = 2.5 \mu\text{m}$ the DE after the time interval around 25–35 min begins to decrease. So the intermediate (between Raman-Nath and Bragg) diffraction behaviour presents in NML samples at P:P polarizations states up to $\Lambda = 2.5 \mu\text{m}$.

It is necessary to say that that, from a practical point of view, polarization modulation configurations are inevitably accompanied by intensity modulations, except in the case where S and P polarized laser beams are used for exposure create neither intensity nor polarization interference pattern. Note also that in those cases the scalar effects can play a predominant role if the samples are not photodarkened prior to their exposure to the polarization modulated light [189]. Therefore, it is difficult to separate scalar and vector effects and it confirms that the mechanism of relief modulations, in the case when spatially modulated polarization is used for exposure, is pure polarization driven.

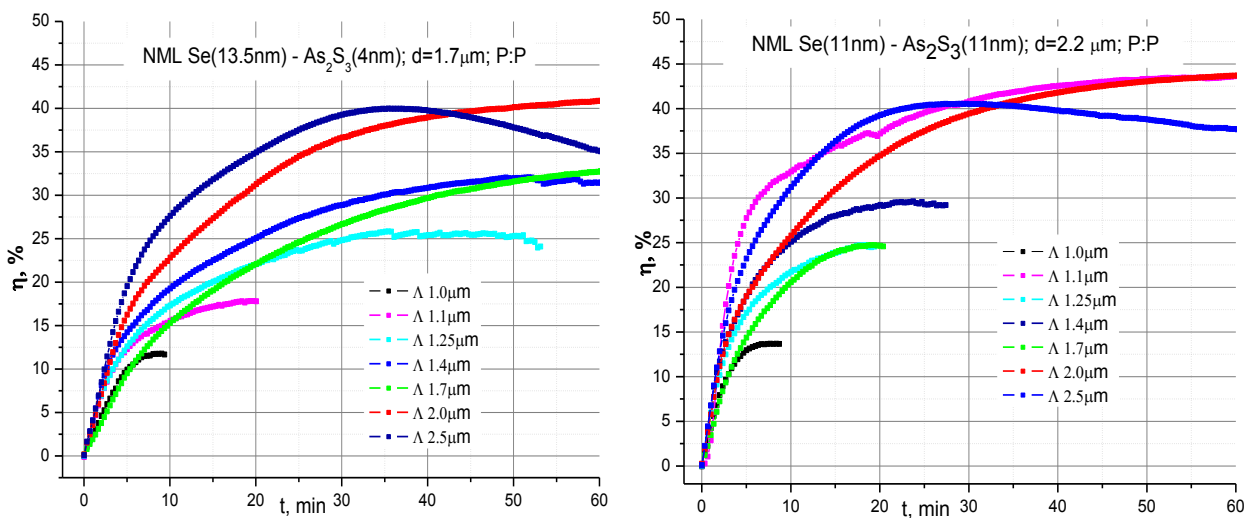


Fig. 4.4. The kinetics of diffraction efficiency for intensity polarization gratings recorded at P:P polarizations states.

There are some concepts to explain the origin of intensity and polarization recording features in ChG. It is known that molecules and nanoparticles can be manipulated in fluidic systems using dielectrophoretic (DEP) forces [190]. A DEP forces generated when a neutral molecule or particle is suspended in a nonuniform electric field. This electric field induces electrical charges

within the particle to establish a dipole. If a nonuniform electric field is applied, the ends of the dipole experience unequal Coulomb forces, which result in a total nonzero imposed force. If the particle is less polarisable than the suspending medium, it is repelled from the regions of higher electric field and the motion is called negative dielectrophoresis while the opposite case is referred to as positive dielectrophoresis.

The authors [190] proposed a photo-induced DEP model to explain the photoinduced mass transport in amorphous films. Model is based on the photoinduced softening of the matrix, formation of defects with enhanced or decreased polarizability, and their drift under the electrical field intensity gradient of the light. An interference pattern from the orthogonal $\pm 45^\circ$ polarizations states can be expressed as a sum of two linearly polarized light components: the electric vector parallel to the grating vector or the P polarization and the electric vector perpendicular to the grating vector or the S polarization. For both components the electric field intensity gradient is parallel to the grating vector. This polarization modulation causes an arrangement of polar photoinduced defects in the film. As a result, their polarizability regarding the direction of electric field intensity gradient has been increased by P electric field component and decreased by S electric field component. Due to the DEP forces material is transferred out of the S polarized light region into the P polarized region. This model is in well agreement with results obtained for homogenous ChG. In case of NML we obtain the regions with different structures and as a consequence different polarizability of nanolayers constituent of total NML.

The other model was proposed by [32]. Note that all models suppose the creation of anisotropy in the material, but the reason for appearance of this anisotropy is different. These optical anisotropies induced by exposure to polarized light are observed not only in annealed glasses but also, and essentially undiminished, in glasses photo darkened by light exposure.

On the molecular scale, the structure of chalcogenide glasses is strongly anisotropic [32]. Even without specifying the larger anisotropic structural units, such as rings, chains, platelets, or pyramids, which may define the local structure or medium range order of a particular glass composition, it is clear that one needs a volume containing a considerable number of atoms to find the optical isotropy of a macroscopic sample. The minimum isotropic volume will grow with the size of the anisotropic structural units. This minimum volume is optically isotropic only because of the spatial averaging over smaller anisotropic volume elements it contains. Optical anisotropies can arise only when one or both of the photocarriers remain in the absorbing microvolume and recombine nonradiatively. The recombination is called geminate when both carriers remain and recombine in the absorbing microvolume. Accept this model, we can explain the different photoinduced behaviour of As_2S_3 films and NML As_2S_3 -Se which we observed in [191].

4.2. Digital holographic interferometry

Digital holographic interferometry (DHI) is widely used as a non-contact optical measurement technique for engineering structures; examples include examining the deformation or vibration of body panels, engines and engine components in the automotive, aircraft industry. An established area of application of DHI concerns the non-destructive examination of technical objects for localized structural abnormalities, e.g. the screening of car and plane tyres for hidden defects.

An essential feature of DHI (as digital counterpart of holographic interferometry) is that it provides simultaneous measurement over an extended area of the target surface. DHI thus offers distinct advantages over point measurement techniques, such as laser velocimetry and interferometric vibrometry, and yields data unavailable from those techniques.

Despite many features of holographic interferometry there are some disadvantages which put limits a wide spread for this technique. The main of them are:

- Complicate optical equipment for obtaining a holographic interferogram with high quality;
- The assessment of quality of individual hologram is carried out mainly visually;
- The necessity of wet developing of holographic carriers.

The similarities between DHI and holography interferometry led to the result of both techniques being fringe pattern where the fringes represent a change in phase between an object and a reference wave. The main advantage of DHI over holographic interferometry is that it enables real-time correlation fringes to be displayed directly upon a computer monitor without any form of photographic processing or plate relocation. This comparative ease of operation allows the technique to be extended to considerably more complex problems in deformation analysis. DHI also allows the displacement in different planes to be measured separately. Furthermore, DHI does not require high-resolution recording media and imposes less stringent conditions on vibration isolation and ambient light.

The DHI offers sub-wavelength sensitivity in deformation measurements, but on the other hand, highly sensitive interferometric methods require perfect protection from environment disturbances such as vibration, air flows, dust, supports and satisfying coherent condition. Usually holographic set-up should be mounted on anti vibration table which gives such conditions at the cost of significant rising of total set-up price. Dimensions and weight of such set-up are inconvenient especially in case of in situ trials. Price of the table is compatible with other parts of DHI set-up.

This work is aimed at the development of an easy to use, cost-reduced approach, full-field and portable DHI system for visualization and monitoring of states of different kind of samples under test.

The principle of DHI is well documented in the literature elsewhere [192, 193], we will describe here only the features of our DHI set-up.

A wide variety of laser types such as continuous wave (CW) as pulsed lasers are being used in DHI. Photochemical and thermal destroying of samples under test is important factor for laser type selection. Using the energy quant of laser wavelength as low as possible is better choice to diminish photochemical influence. A low power CW He-Ne laser is a suitable choice for DHI set-up as from the point of thermal influence on surface of a sample as possibility delivering laser power through optical fibers. Another important factor relies on large coherent length of light therefore we need the monomode laser. Monomode He-Ne red CW 25 mW laser was considered suitable for our purpose. One more item for DHI set-up was a power of laser to distinguish a good S/N ratio on CCD camera.

After studying some variants of DHI set-ups we decided to separate illumination and monitoring parts and to use fibre optic cables for laser beam delivering. According with our aims by splitting the DHI set-up into two separate units for illumination and monitoring linked by the optical fibre cables a very flexible usage of the set-up in different environments can be constructed.

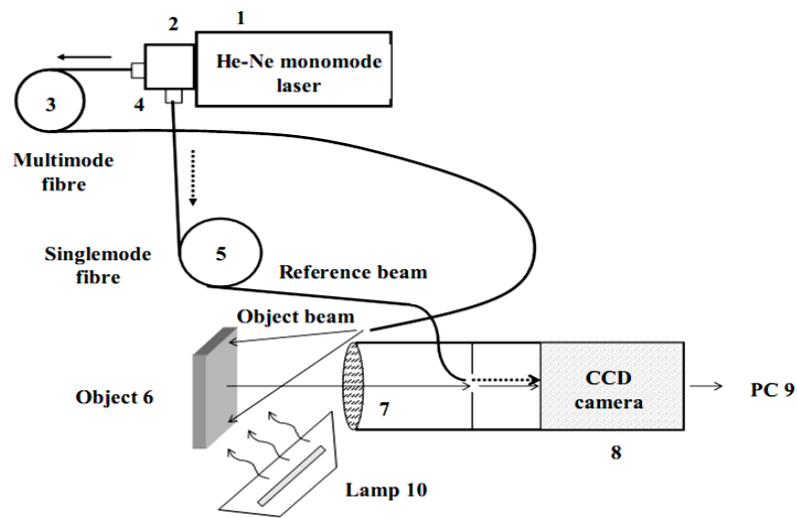


Fig.4.5. Optical scheme of DHI set-up: 1 — monomode 25 mW He-Ne laser Siemens LGK 7626; 2 - variable intensity ratio beam splitter; 3 - multimode optical fibre (fibre core dia 50 μm , NA= 0.6); 4 - two fibre-optic connectors; 5 - polarization maintaining mono mode “Bow-Tie” fibre (mode dia 5 μm); 6 - object with probable internal defects; 7 - objective; 8 - CCD camera; 9 - to PC; 10 - lamp for heating.

The comparison of results obtained by positioning the set-up on the vibration protected table and the tripod has not shown significant difference. In order to testing the different kinds of samples in situ we applied homemade DHI with optical fibers for beam delivering which gives possibility to studying the sample conditions underneath the open surface and inside the sample where

the direct illumination by laser beam is a problem. Delivering laser energy in reference and object arm through the optical fibres gives, on the one hand, good vibration and environment immunity of set-up and, on the other hand, to leave the heaviest laser part on the separated from camera part support. Due to long coherence length of He-Ne laser both optical fibre arms can be designed a dozens of meters long in dependence of distance to the point of measurement. So the compact and lightweight camera part of DHI becomes movable and easy fastening in front of sample region of interest practically independent on laser part position. As a consequence, the portable DHI set-up was designed [194]. The out of plane DHI set-up used in this work is shown on Fig. 4.5.

The light source is Zeeman-stabilized He-Ne laser with wavelength 632.8 nm and TEM₀₀ single mode operation. The coherent laser beam is divided into reference and object beams by beam splitter mounted directly on the laser housing. The object beam is obtained by illuminating the object under investigation with multimode optical fibre and then focusing the light scattered by the object onto black and white digital CCD camera (MARLIN F131B with 1392×1040 pixels, pixel size 4.65 μm × 4.65 μm, fire wire output) using focusing lens. Smaller part of laser light power was coupled into a polarization maintaining single mode “Bow-Tie” fibre and piped directly into CCD head module to serve as the reference arm. No beam splitter was used in front of CCD camera to avoid additional noises, which influence on interference pattern formed on CCD sensor. The spot of reference beam is matched with the size of CCD sensor whose outlet position is at the same distance from the CCD sensor as the lens aperture diaphragm. Hence, the CCD sensor plane is image plane of hologram. The intensities of beams on CCD sensor were equalized by using beamsplitter with variable ratio between reference and object intensities for receiving maximal contrast of interference fringes. The sum of both intensities is constant. It gives possibility to easy adjusting the intensities of both beams in sequence by CCD camera. This feature of set-up exploits all laser energy without significant losses that is very important in strive for the highest efficiency of low level He-Ne laser energy using. Both beams (reference and scattering from the object) are combined onto CCD sensor, so an image plane hologram is formed on the CCD sensor because of the interference between the slightly off-axis reference beams and object beam.

Coherence length of two beams can be adjusted slightly by changing the output position of the object multimode fibre on the CCD camera base. The length of optical fibres in our trials was 3m. Real time optical processor formed by objective lens and diaphragm yields preliminary Fourier processing of images. The photograph on the DHI portable set-up on the tripod is shown in Fig. 4.6.

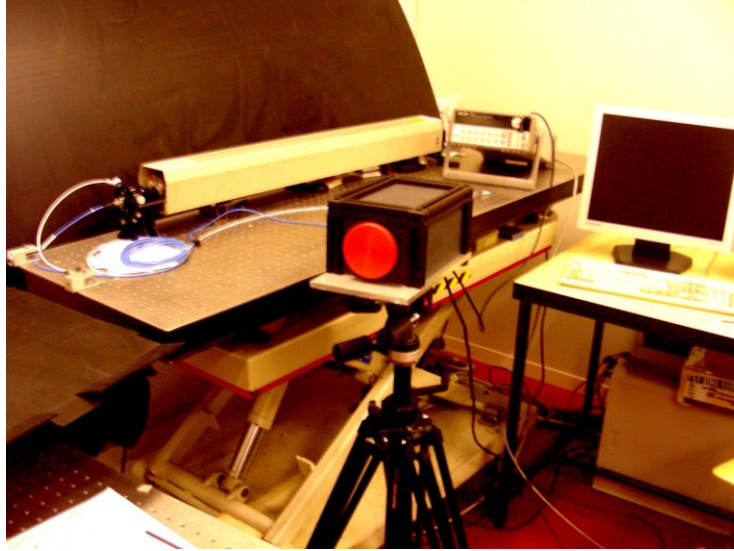


Fig. 4.6. The photo of the DHI portable set-up on the tripod and laser part (on the left).

A brief description of calculation method used is given below, and the main features of our set-up and measuring principles are follows.

A hologram can be seen as a carrier wave whose spatial frequency is modulated by the object information. In order to simplify our description we use a plane wave $r(x, y, z)$ as a reference. The face plate of the camera is located in the image plane of the interferometer (the plane $z = 0$). Under these conditions the output signal from the camera, as obtained with the object in its initial state, is recorded. The object is then displaced (or some other methods deformed) and the live camera signal is subtracted electronically from the stored (no deformed) signal. Those areas of the two images where the speckle pattern remains correlated will give a resultant signal of zero, while uncorrelated areas will give non-zero signals.

We can write by considering the intensities I_1 and I_2 before and after displacement/deformation respectively:

$$I_1 = I_r + I_o + 2\sqrt{I_r I_o} \cos\varphi \quad (4.1)$$

$$I_2 = I_r + I_o + 2\sqrt{I_r I_o} \cos(\varphi + \Delta\varphi) \quad (4.2)$$

If the output camera signals V_1 and V_2 are proportional to the input image intensities, then the subtracted signal is given by

$$V_s = (V_1 - V_2) = I_1 - I_2 = 2\sqrt{I_r I_o} [\cos\varphi - \cos(\varphi + \Delta\varphi)] = 4\sqrt{I_1 I_2} \sin(\varphi + \frac{1}{2} \Delta\varphi) \sin \frac{1}{2} \Delta\varphi \quad (4.3)$$

This signal has negative and positive values. The monitor will, however, display negative-going signals as areas of blackness; to avoid this loss of signal, V_s is rectified before being displayed on the monitor. The brightness on the monitor is then proportional to $|V_s|$, so that we have the brightness B at a given point in the monitor image given by

$$B = 4K [I_r I_o \sin^2(\varphi + \frac{1}{2} \Delta\varphi) \sin^2(\frac{1}{2} \Delta\varphi)]^{1/2} \quad (4.4)$$

where K is a constant.

If the brightness B is averaged along a line of constant $\Delta\varphi$, we see that it varies between maximum and minimum values B_{max} and B_{min} given by

$$B_{max} = 2K \sqrt{I_r I_o}, \Delta\varphi = (2n + 1)\pi, n = 0, 1, 2; \quad (4.5)$$

$$B_{min} = 0, \Delta\varphi = 2n\pi, n = 0, 1, 2. \quad (4.6)$$

High-pass filtering of the signals is found to give improved visibility fringes by removing low frequency noise together with variations in mean speckle intensity and is normally used to enhance the fringe clarity.

Special carrier phase measurement method is based on idea of superposing a carrier fringe pattern onto the interferograms fringes. The two basic approaches to the special carrier technique include the Fourier transform method (FTM), in which the processing is performed in frequency domain, and methods which are equivalent but the processing is performed in special coordinates. We have used FTM.

Let $R(x,y)$ be the smooth reference wave and $U(x,y)$ the object wave. The intensity recorded on the CCD is given by

$$I(x_H, y_H) = |R(x_H, y_H)|^2 + |U(x_H, y_H)|^2 + R(x_H, y_H) U^*(x_H, y_H) + R^*(x_H, y_H) U(x_H, y_H) \quad (4.7)$$

where x_H and y_H are the co-ordinates at the hologram (detector) plane and $*$ denotes the complex conjugate amplitude. The last two terms in Eq. (7) contain information corresponding to the amplitude and phase of the object wave. This information is obtained by special filtering using the Fourier transform method schematically described in Fig. 4.7.

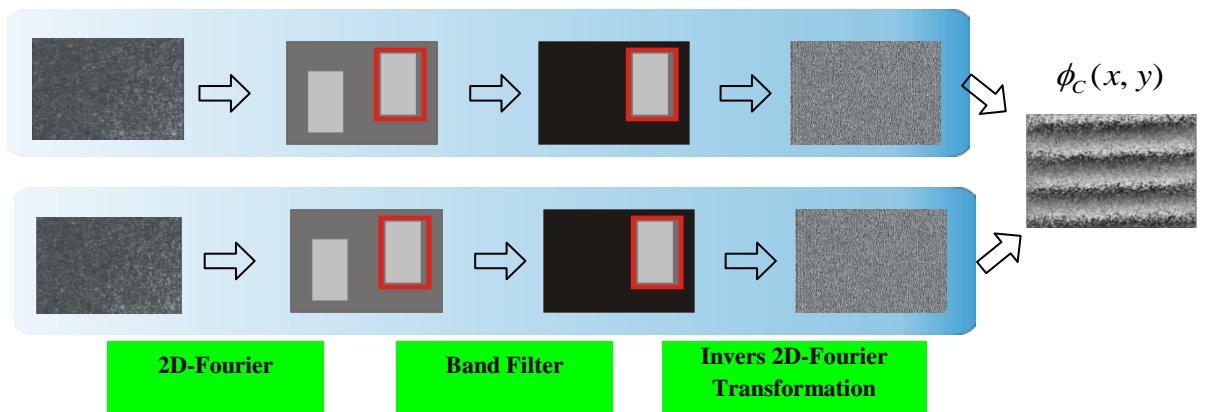


Fig. 4.7. Procedure for calculating the phase map (unwrapped) from two interferograms.

By taking the Fourier transform of the recorded intensity it is possible to filter out of the two last terms in Eq. (4.7). They are separated in the Fourier plane (appear as side-bands) as a result of the slightly off-axis reference beam. After the filtering procedure and inverse Fourier transforma-

tion the complex amplitude of the wave front is obtained. The operation described corresponds to the reconstruction to what in the literature is called quasi Fourier hologram [58, 195].

From the complex digitalized amplitude $U_H(m\Delta x, n\Delta y)$, the phase of the wave front is calculated by the relation

$$\varphi_{Hw} = \arctan [I_m[U_H(m\Delta x, n\Delta y)] / R_e[U_H(m\Delta x, n\Delta y)]] \quad (4.8)$$

where R_e and I_m denote the real and imaginary part, respectively. The phase obtained from the evaluation of the digital holograms is in interval $-\pi$ to π and is indefinite to an additive integer multiple of 2π (the subscript w indicates that this is a wrapped phase). Since we are working in a quasi Fourier hologram, in the reconstructed wave front we have an additional quadratic factor. This does not disturb our investigation as we measure only phase change and we do not need an absolute measurement of phase.

In our research we have chosen LabVIEW™ of National Instruments as language for calculation. LabVIEW is graphical programming environment developed in form of interface with Input/Output (I/O) control acquisition hardware; using the driver to connect with extern data, LabVIEW allows to program based on standard scheme in PC [196].

For software implementation of the calculation phase algorithm, the main algorithm (Fig. 4.8) must be elaborated with following considerations: be flexible and fast, easy control, have the possibility to be implemented in other language due to simple the code conversation.

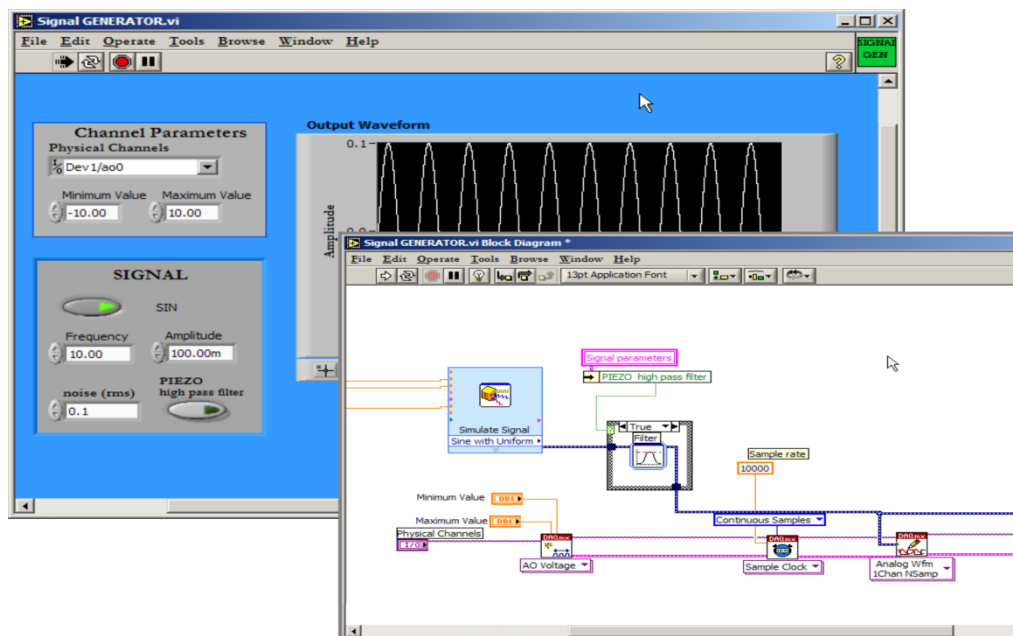


Fig. 4.8. The LabVIEW algorithm for phase map calculation $\Delta\varphi(x,y)$.

In general, by this set-up like ESPI system we can measure the displacements. The method of excitation or produce the displacement may be different. The kind of excitation influences on type of information extracted from displacement obtained.



Fig. 4.9. The scheme of mechanical loading on the object under test.

The measurement of out-of-plane displacements by mechanical loading has admittedly been one of the most wide-spread applications of ESPI technique. The technique owes its popularity to the ease with which fringes corresponding to the out-of-plane displacements are displayed on the examined object surface. The interference fringes are obtained by subtracting images before and after deformation. We acquire two interference patterns before and after mechanical loading. The scheme of the loading is presented on Fig. 4.9. When the object is loaded, the test area undergoes deformation and wave fronts are again scattered, resulting in a change in the speckle pattern. This in turn causes a change in the interference pattern, which is again imaged on the faceplate of the CCD camera and stored in memory.

The DHI software is then used to process the two stored interference patterns so as to display the resulting interferogram of alternate light and dark fringes on video monitor. These fringes represent contours of equal displacement in the Z-direction.

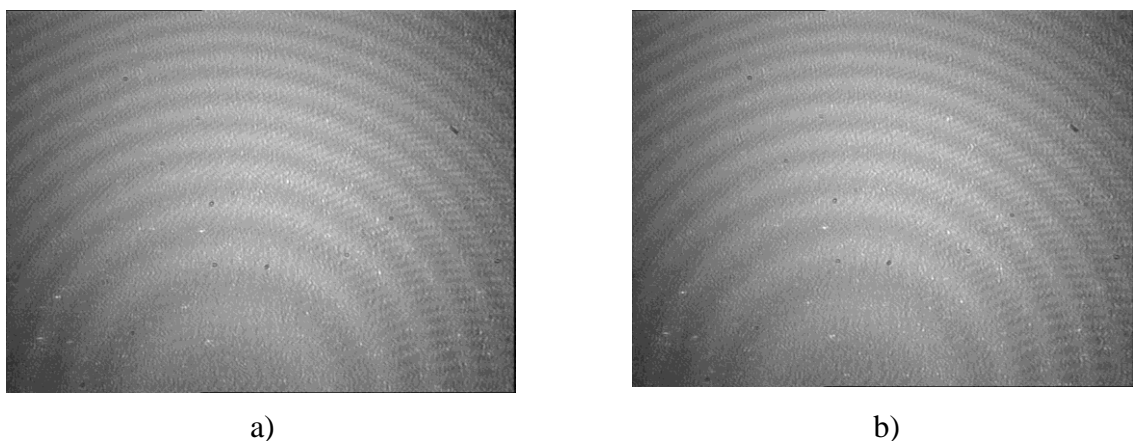


Fig. 4.10. The live images of reference and loaded state of the object.

The Fig. 4.10 presents the live images of two states of the object under test: unloaded (reference) and loaded. As one can see from the comparing of these two images they are speckled interferograms: speckles are delivered by object beam, and Newton's rings belong to reference beam and are evidence that we have a perfect spherical wave into reference fiber. At the naked eye these two interferograms are identical, and their Fourier spectrums are the same.

Then the two interferograms are subtracted. The Fig. 4.11 we present a. interferogram as a result of subtraction the two live images on Fig. 4.10b. wrapped phase map, obtained from first (a) interferogram. The interferogram consists of alternate light and dark fringes, called correlation fringes, as the fringes are produced by correlating the intensities of the resultant speckle patterns recorded before and after displacement.

The fringes represent contours of equal displacement, with each fringe resulting from a displacement of the order of half a wavelength of the laser light source used in the interferometer. Hence the interferogram is a representative of the superficial displacement or deformation of the test object, and the number of fringes indicates the degree or extent of the displacement. The geometry of the fringes also provides an indication of the geometry of deformation. Where the fringes are evenly spaced and of similar shape and size, the underlying surface is uniformly deformed. Where the fringes are distorted or are of uneven size the underlying surface is not uniformly deformed, thereby indicating a surface or subsurface structural abnormality or defect.

The fringe pattern intensity is related to the local phase difference in the object wave. Now we can extract data from phase map instead of fringe map. The difference between these two results is: in second case (phase map) we know how to grow the phase as the plot on Fig. 4.10 is not symmetric while in first case we need any additional measurements.

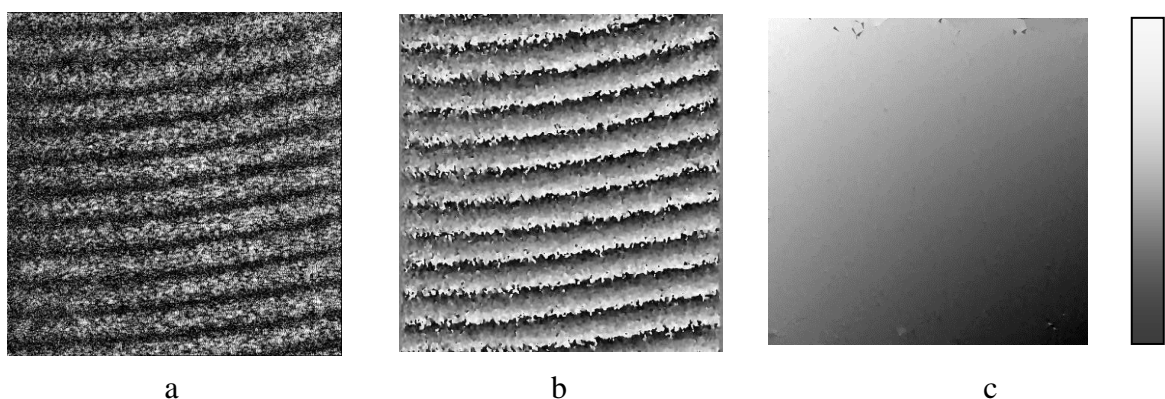


Fig. 4.11. The subtracted interferogram (a), wrapped phase map (b), and unwrapped phase map (c) obtained from the two images subtraction (Fig. 4.10).

Note that the phase obtained from the evaluation of the holograms is in the interval $-\pi$ to π , and is indefinite to an additive integer. However, as we measure only phase change we do not need an absolute measurement of the phase.

On the Fig. 4.12 the pseudo 3D representation plotted in arbitrary units (MathLab) is shown. From this presentation the difference between different values of displacements is seen clearer than from unwrapped phase map shown on Fig. 4.11c.

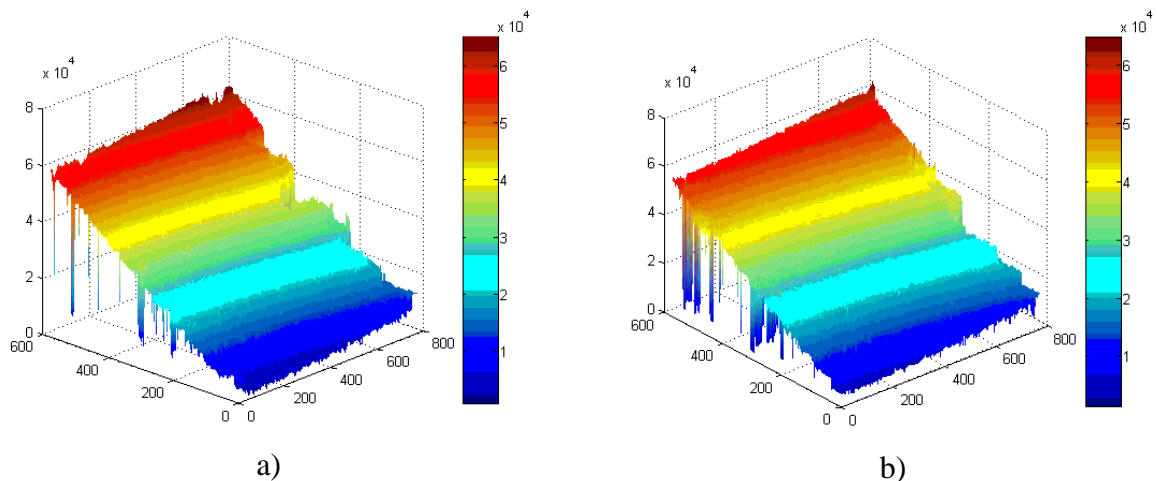


Fig. 4.12. The pseudo 3D representation of different values of displacements: a) $3.83 \mu\text{m}$; b) $3.5 \mu\text{m}$.

The mechanical loading is applied to object by the micrometer screw, and the measurements are conducted by carbide tipped measuring faces. The correlation between applying displacement and real object displacement was set up using the calibration curve (Fig. 4.13).

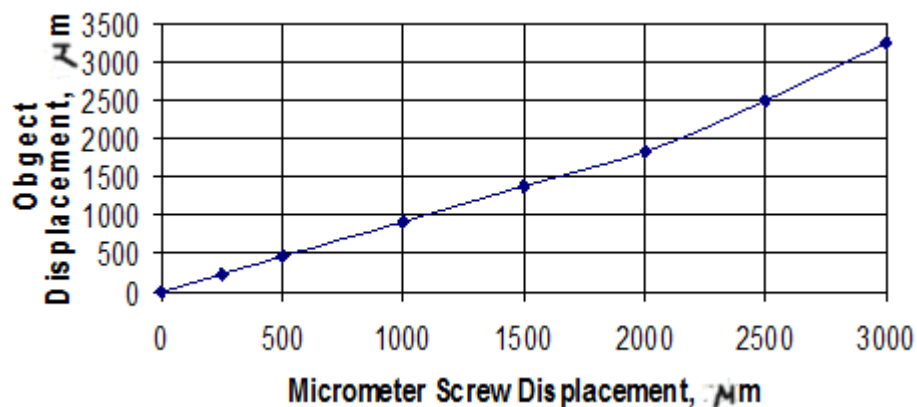


Fig. 4.13. Displacement calibration.

Note that all these results are relevant to displace uniform surfaces without any cracks, flaws, etc. The evidence of this statement is regular form of fringes and even distance between them. By the developed set-up we can test the surface defects or inhomogeneous applying the static loading.

Moreover, in comparison with microscope we see submicron defects on the sufficient larger than in microscope the field and depth of view (field of view $10\text{ mm} \times 12\text{ mm}$, depth of view 2–5 mm).

The DHI is realized with resolved speckle. In that case the mean speckle size approximately equals the pixel size of the CCD- or CMOS-sensor. This is achieved by using a small aperture of the objective which simultaneously reduces the intensity of the object light. If the laser power is limited and large objects are to be illuminated, the aperture must be opened in order to ensure a sufficient exposure of the sensor. Thereby, the speckle becomes smaller and every pixel integrates over number of speckles with random intensity and phase. However, even in this case speckle interferometry is possible, as was shown theoretically by Lehmann [197]. So if we have need to measure large object surface or objects situated on the large distance from the sensor, we can obtain the fringe pattern without changing any optical components, but doing it only by software.

The large variety of possible descriptions of the image quality and representations is available for optical designers. The quality of an optical system must always be measured and described by criteria, which are appropriate to the application and the system type. As a consequence, there is no universal quality metric, which makes sense for all systems.

Understanding optical properties of DHI set-up can help in understanding measuring properties and possibilities of it. There are some guidelines that can help designers and users to construct the DHI system which meet the proper consumer requirements.

It is well known that when an optically rough surface is illuminated by coherent light, speckles can be observed and imaged on a detector. Changes in the speckle pattern due to displacement and deformation of the diffusing surface can be used within a double-exposure metrology approach. Indeed, for objects with optically rough surfaces, DHI is one of the most suitable methods to obtain high-sensitivity measurements of out-of-plane and in-plane displacement components, strain and vibration. Since nowadays the signal can be acquired in a digital form, various image processing techniques could be applied to process DHI interferograms.

The system engineering approach is important in system design and system analysis so as to determine final image quality or to design for a given required image quality. This requires quantitative criteria with which to define image quality. It also requires analytical tools for determining the weak link in the system, the link that has the chief role in limiting the image quality.

Before choosing the criteria for DHI set-up we consider some prerequisites [198].

There is a great difference between the DHI data presentation in form of speckle image and vision system presentation in form of real “pleasuring” image of an object. Direct comparison between real object and its image created by vision system helps us at first, to see, and then to adjust video camera and objective for performing the image with better quality. This possibility

is restricted in case of speckle image acquired by DHI sensor. The limited acceptance of the DHI method image is not only due to speckled image, but because of an unfamiliar representation of data. There is no image of the object that usually helps to focus the objective. It is difficult to define the distance “in focus” or “out of focus”. Image of point light source with dimension of one pixel on camera chip can help to adjust focus position. Sometimes it is needed to fit optical system of DHI with the respect to object dimensions or to make upgrade of the set-up with more powerful components. Necessary to change objective often follows from object field coverage. Design types of objective commonly used define the aperture and field of view combination of set-up. For example, camera and objective can be replaced with different models with little or no changes in the application LabVIEW software but measuring properties of set-up will change.

Every component within optical set-up has an influence on image obtained by PC and, as a result, contributes to the overall accuracy and performance of the system. It is important to determine the key parameters as for set-up in general as for each optical component like objective, stops, aperture, diaphragm, fibres and camera chip. Preliminary geometric model design, optimization and tolerance must be done by optical software before designing and buying components for replacing.

The most important parameter of DHI setup is resolution. Two components of DHI are responsible for that parameter: objective and camera chip. Keeping objective resolution down to the size of camera pixel is especially demanding on the optical design during replacement or upgrading of objective.

A digital imaging device, such as a CCD or a CMOS image sensor, samples an image by means of finite-size image cells. According to sampling theory, perfect image restoration is possible when the incoming image has no spatial frequency component above the Nyquist frequency, which is half the inverse of the sampling period, or pixel size. When the incoming image has frequency components larger than the Nyquist frequency, image distortion originating from aliasing is inevitable. For example, the pixel pitch of B/W ½"Marlin F 145B2 camera chip is $4.65 \mu\text{m} \times 4.65 \mu\text{m}$, giving Nyquist limiting spatial frequency of approximately 108 lp/mm. Camera has 1392×1040 pixels and 8 mm diagonal of the chip. So it is threshold value for objective resolution which will be used with this camera chip. This is relatively poor resolution compared with that available from fine grain holographic film or thermoplastic one (typically up to 1000 l/mm). It is a major limit of speckle image quality of DHI.

When characterizing the resolution of an imaging system, it is extremely useful to refer to the Modulation Transfer Function (MTF). An easy way to interpret MTF results is to think of imaging a target with black and white lines (100% contrast). No lens (even theoretically perfect) at any resolution can fully transfer this contrast to the image because of the diffraction limit. In

fact, as the line spacing is decreased (i.e. the frequency increases) on the target, it becomes increasingly difficult for the lens to efficiently transfer this contrast (see Fig. 4.14). Therefore, as the frequency increases, the contrast of the image decreases. The MTF of an objective is a measurement of its ability to transfer contrast at a particular resolution level from the object to the image. In other words, MTF is a way to incorporate resolution and contrast into a single specification, which will be relevant to the aim of measuring.

Any optical software like ZEMAX, CODEV, TracePro, RayCad etc, can calculate MTF of objective. Our choice is ZEMAX [199]. Vendor in the form of .zm file for optical software can supply optical components datasheets in some cases. In this case, import of components prescription is needed. Optical software ZEMAX provides the most comprehensive import and export features which were used. Even though ZEMAX offers the import design prescriptions, this is hardly helpful in most practical cases as they only support the very basic features (such as thickness, radii, distance, semi-diameter and glasses properties) and advanced features like special apertures, coordinate transformation, glass names, components decentre may be lost. In almost all cases (except simple systems like single lens) it usually requires extensive manipulation of the imported data in order to make the system to work. For obvious reasons, they all lack the provision of decent export to other design package. So the better way is to have the components prescription data file from the same software package.

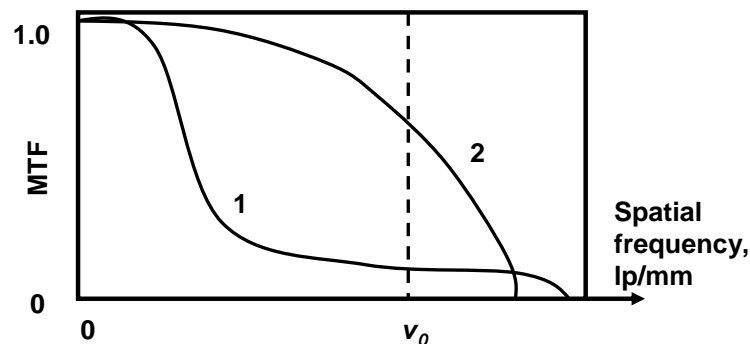


Fig. 4.14. Dependence of MTF for two objectives from spatial frequency.

v_0 — indicates a detector cut-off Nyquist frequency. Dot line shows minimum contrast value necessary for the detection of fringe structure.

By analyzing the system MTF curve, we can predict which combination of camera and objective will yield sufficient performance. In some metrology applications, for example, a certain amount of contrast is required for accurate image edge or dimensions and position of small defects. For example, objective 1 on Fig. 4.14 has lower contrast at v_0 but higher resolution. Dot

line of threshold is specific for every detector and means that the detector can get resultant modulation of an image.

Every component within a system has an associated MTF and, as a result, contributes to the overall MTF of the system. This includes the imaging objective lens, other optics, CCD camera or CMOS sensor, capture boards, etc. The resulting MTF of the system is the product of all the MTF curves of its components. Knowing the MTF curves of components allows an integrator to make the appropriate selection of components to optimize the system for a particular resolution. Resolution may be specified as an average over the entire format, or specific targets may be given at certain field points. The task becomes harder as the field angle increases, the f-number decreases, and resolution requirement increases.

Resolution of the objective and camera must be matched otherwise erroneous results would cause false image details, for example, contrast reversal at high resolutions can be observed. In the case of knowing object the image will be seen with some distortions not presented on the object. In case of ESPI this phenomenon leads the visible speckle image on monitor that you see seems a good quality. Worse the speckle which looks good but information about pixel phase and amplitude are lost and during image processing not can be typically corrected with software. Distortion within an image is not linear, though, nor is always monotonic. Consequently, the last type of optical distortion of object in acquired image plane can become difficult to image processing far as DHI set-up uses He-Ne laser there is absence of chromatic dispersion of objective optical glasses and it is possible to reach up to diffraction quality imagery.

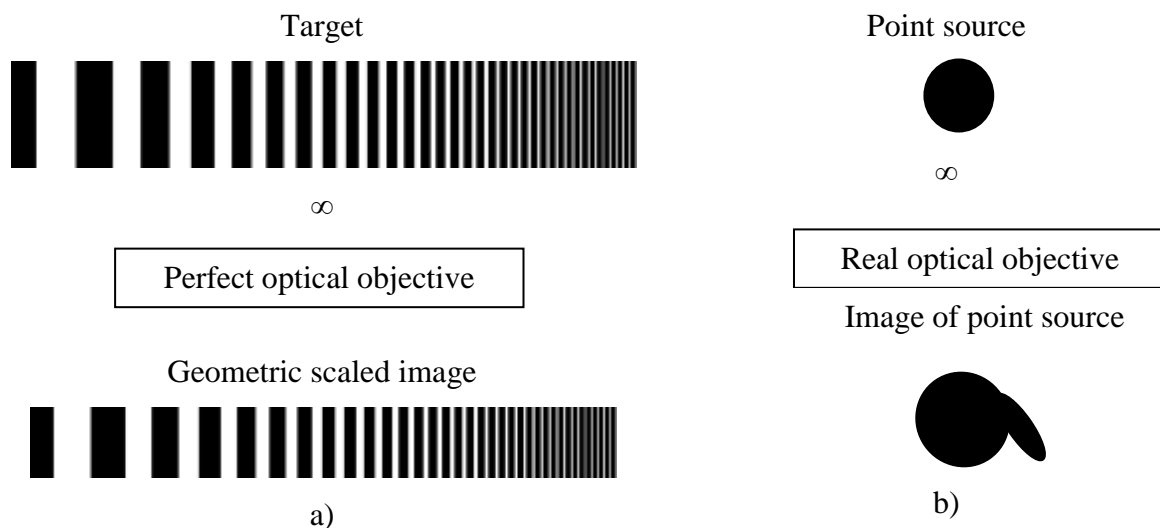


Fig. 4.15 A resolution test target imaged by perfect objective (a); a poorly imaged point source (b).

In practical image quality determination, it is common to use test targets as objects for fast estimation of contrast and resolution of an image. Traceable calibration targets such as USAF, television test pattern and Siemens star targets ensure the optical accuracy, repeatability and give possibility to see the effects of blur because of aberrations over field of view. Important, that pseudo resolution can be analyzed inside image, which in DHI case yields false speckle information. Figures above show how fringe object transform by ideal and real optical objective.

Fig. 4.15a shows a resolution target being imaged by a “perfect” optical system. The image is simply a scaled version of the object. A profile across the image will mimic the object. In Fig. 4.15b we have a point source being imaged by an imperfect optical system. In this case (imperfect system), two things can happen to the pattern: 1) its modulation can decrease; 2) the image can be shifted laterally from its ideal or paraxial location.

For an aberrated system, the image of a point object is a lateral blob of light (Fig. 4.15b). The resulting image is a fuzzy blob instead of a point. This blob is called the point spread function (PSF). If we now combine the two objects so that we image the resolution target with the imperfect system, the image is of poor quality, as illustrated in Fig. 4.16. What has happened is that we have essentially replaced every image point in Fig. 4.15a with the blob image in Fig. 4.15b.

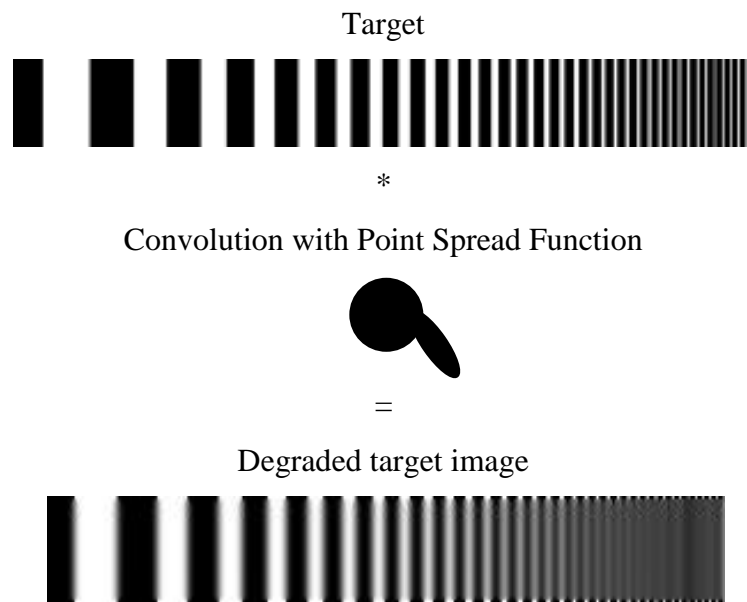


Fig. 4.16. Degradation of the target image due to convolution with blob point image.

Other words, if we are imaging a finite-sized object through the aberrated system, the resulting image can be thought as taking each point in the perfect image and replacing it with the

aberrated PSF (suitably scaled for local irradiance). Mathematically this can be considered as the convolution of the aberrated PSF with the perfect image. The convolution operation becomes a product in frequency space if it is to calculate by the Fourier Transform way. It is often easier to calculate this product rather than the integral. MTF which is the image contrast versus the frequency and responsible for the reduction in image modulation (or contrast) is pertinent expression the transmitting ability of optical system.

Our reasons for choosing telecentric lenses in DHI set-up design emerge from the requirements to cover all field of view (FOV) with the same magnification and permit an object move slightly within the depth of field. Telecentricity defines how the amount of magnification of an object within the FOV changes with object distance. Because telecentric lenses act as if they have an infinite focal length, magnification is independent of object distance. In our case telecentric objective is supplied as object-space. Using He-Ne laser as a light source we are limited in power of illumination. Hence the main application of the DHI set-up is a machine-vision holographic system for precise repeatable measurements of a small object. As to image plane, we can adjust the camera position in accordance with chip size without using image-space telecentric design. Note that object-space telecentric lenses are commonly used in machine-vision applications.

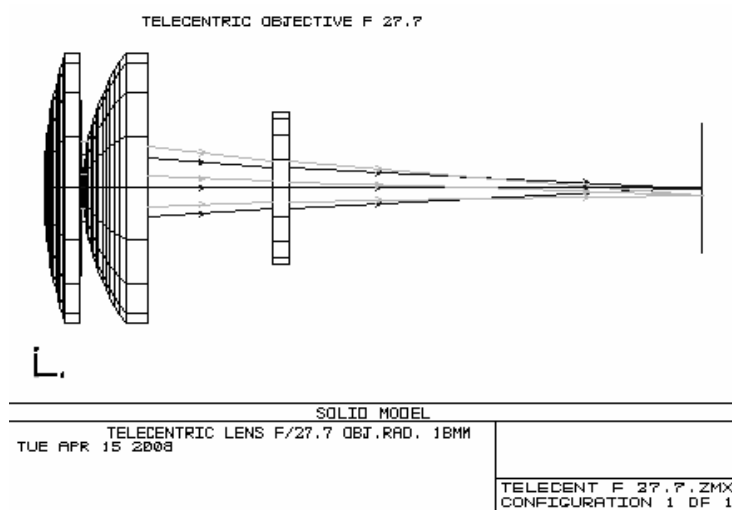


Fig. 4.17. Geometrical wireframe model of three lenses telecentric objective of DHI set-up with f-number =27.7 mm.

The geometrical model of three lenses telecentric objective with f-number =27.7 mm of the DHI set-up was designed by optical software, which is presented on Fig. 4.17. Object position is on the left side, and vertical line points out the camera chip position. Wave front of telecentric objective was calculated for monochromatic light from He-Ne laser with $\lambda=0.63 \mu\text{m}$.

Wavefront of three lenses telecentric objective has shown on Fig. 4.18. The sampling for calculation was put as 32×32 .

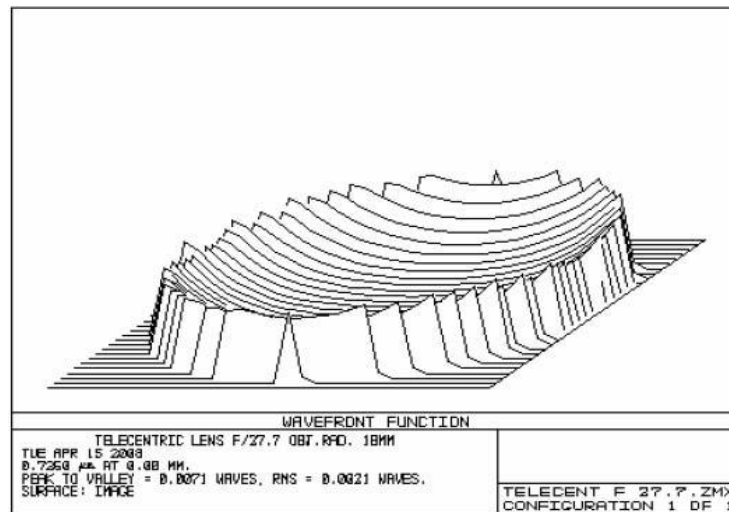


Fig. 4.18. Wavefront of three lenses telecentric objective with f-number =27.7 mm of DHI.

Calculation of MTF was made for X-Y coordinates putting entrance pupil diameter 337 mm, uniform apodization and object high 18 mm. Marlin CCD camera resolution was calculated and presented on Fig. 4.19.

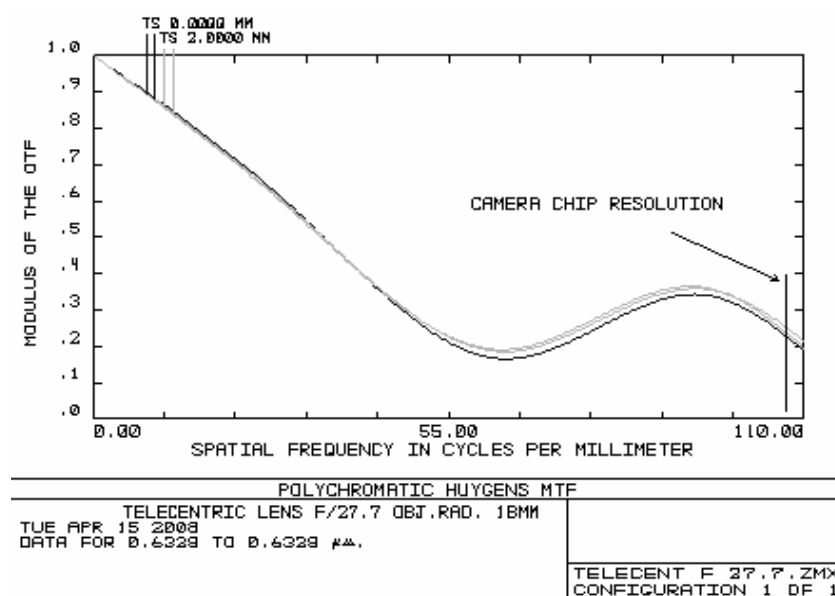


Fig. 4.19. Calculated MTF of the objective with f-number =27.7 mm.

The diffraction MTF data have been calculated using a Huygens direct integration algorithm. Resolution of objective on 30% level is about 40 l/mm. There is fall of contrast of the objective at frequencies 55–66 l/mm.

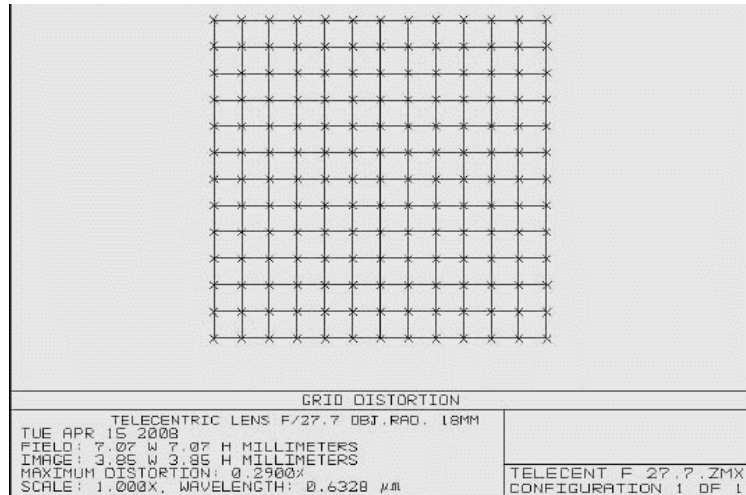


Fig. 4.20. Displays a grid of chief ray intercept points to indicate distortion. Crosses point rays position with respect to image grid.

Notice the information about field and image dimensions. Grid distortion option has shown for the object 7 mm × 7 mm (Fig. 4.20). It is possible to see that maximum distortion over all grid surfaces is equal about to 0.3%.

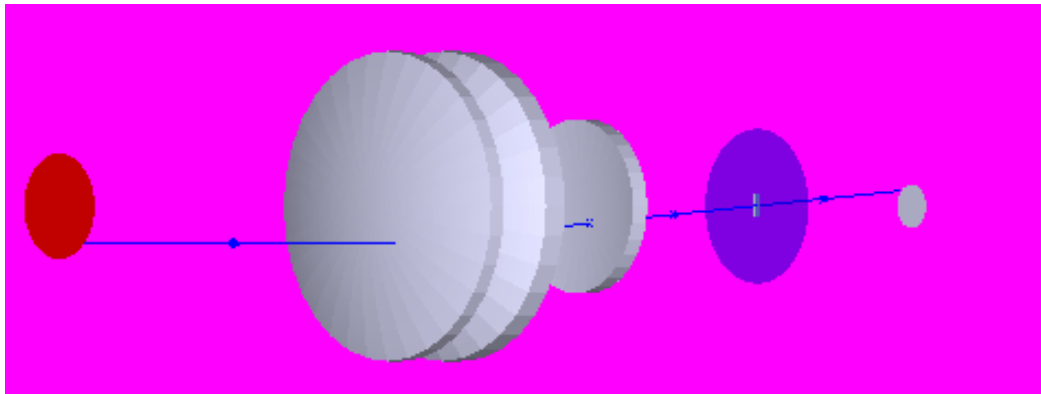


Fig. 4.21. The designed optical part of ESPI setup consists of three lenses telecentric objective and rectangular diaphragm.

After objective parameters calculation the geometric model of objective and rectangular aperture was created. Circle on the left side of Fig. 4.21 is the object. Diameter of the object was put 8.6 mm. Circle on the right side of Fig. 4.21 is the chip of CCD (inscribed diameter 8 mm).

Percentage of the intensity drop with respect to the centre of image intensity often can be seen on DHI monitor. There are some reasons for that:

Non-uniform object illumination is outcome from the Gauss light distribution of camera chip illumination by object that is illuminated by multimode optical fiber coupled with He-Ne

laser and by monomode fiber directed on the chip. It results in light intensity falloff toward the edges of the digital image.

Another source of intensity falloff is shading introduced by the camera objective due to changing transmission properties of lenses AR coating from the centre of the objective lenses to the edges. Optical transmission may have a considerable decrease in illumination near the edge of the image due to AR coating films properties that were calculated for perpendicular incidence.

Diffraction effects on apertures.

All together, the falloffs of the chip illumination lead to decrease S/N ratio near the edges of image sensor. These phenomena can be seen as only central position of interference fringes in the entire image. The distribution of object illumination must be carefully controlled. Illuminated object by laser can be considered like non-uniform radiator of rays and calculation considers vignetting, reflection, transmission in the optical system of objective. The distribution of light on the object surface may be defined to be Lambertian, uniform or etc. Geometric, diffraction image analyses including Optical Transfer Function (OTF) is good at computing detailed image data. Objectives and color camera chips design for application for the human photonic spectral response. As some B/W cameras have significantly wider spectral response, extending from blue to near infrared (1.1 μm). At the invisible 1 μm the sensitivity of B/W silicon camera chip is in its maximum. For more accurate measurements by DHI, it must be to pay attention for absence of these spectral components with the exception of the laser line. The stray light performance is also important. Bright object in the nominal field of view can create veiling glare and spurious images. They become visible by multiple reflections at the lens surfaces and inside lens barrel.

This ghost reflection of the lens focus is formed by a reflection on the outer surface of the camera chip window, on the inner surface of the camera window and on the silicon surface. Bouncing light create multiple points from the one small spot. Dust particles on the all optical surfaces can be visible as centers of scattering. Better way to use for interferometer camera chip without cover glass. All these surfaces illuminated with monochromatic light create not only blur of image but that is worse a Newton's rings. As the result, blurred image can be observed.

In the conclusion we may say, the system engineering approach applied for DHI system design and analysis to determine final image quality has been demonstrated by using ZEMAX optical code. This approach allows us to simulate DHI setup performance for obtaining required image quality before the construction of the setup. The quantitative criteria were elaborated for determining the weak points of the system, their role in limiting the image quality, and ways to overcome them.

4.3. Digital holographic microscopy

Combining microscopy and digital holography offers the unique advantage of simultaneously capturing complete 3D information about the specimen, and under coherent illumination it has been investigated for continuous PC acquisition and identification of different specimens including technical and biological nature. In contrast to conventional microscopy, no depth scanning focusing at various depths of the 3D specimen are necessary in range of some interference fringes. Thus, it is possible to overcome the main limitation of confocal microscope to studying processes that occur on time scales slower than the acquisition time, which is about one second. If a height of an object overcomes distance of several wavelengths of illumination, it is possible to put object on stage with 100 nm steps directed by PC with synchronous acquisition of the images. But the interferometric accuracy of altitude scanning is retained.

DHM is a promising interferometric technique allowing obtaining quantitative phase images of living or technical samples dynamics with interferometric accuracy. There are many interferometry methods which have been developed for microscopy application. Among them, DHI is widely used for deformation studies, and it is the most practical and powerful one [200]. In this work, the DHM was developed based on DHI with modifying illuminating and imaging part to do suitable for hundred nanometers sizes of the samples measurements. As applications of the proposed measurement technique, some experimental results are presented, which are measured with DHM developed.

The topography of SRG is the main feature determining the success of DOE application. The optical quality of the relief surface is very important for designing DOE by recording, printing or master hologram realizing. However, sometimes it is possible to perform direct thermal printing on polymer film from DOE of a large number of copies without master [201]. Finding the methods appropriate for the study of DOE topography is a priority task.

Due to the high resolution required, the profile and surface of SRG are conventionally measured via AFM or SEM [202, 203]. Each of the above methods has advantages and disadvantages. AFM is a precision technology giving detailed images of the sample's surface, but it is to be pointed out that the field of view in AFM is restricted, which allows one to view only a limited part of the surface. In addition, due to the nature of AFM tip, the topography of sinusoid-like surface structure cannot be measured exactly, which leads to the appearance of the artefacts distorting the surface presentation. To create a SEM image, the incident electron beam is scanned line by line in a raster pattern across the sample surface. The SEM method requires an electrode deposited on the surface that would irreversibly change the transmission or damage the surface profile of the lithographically manufactured DOE. In case of e-beam sensitive medium, the elec-

tron irradiation can greatly influence the DOE recording. AFM and SEM are time consuming scanning methods, requiring expensive equipment and complicated software.

DHM is a non-contact full-field technique, which can partially eliminate the negative effects of other methods. DHM is a powerful interference technique having several features that make it an interesting alternative to conventional microscopy. It is worth mentioning that conventional microscopy can easily generate two-dimensional images of a sample surface but cannot measure the vertical dimension (profile) of the sample. The main characteristic of DHM is the capability to retrieve amplitude and phase information of a wavefront reflected/transmitted by a microscopic object. DHM can be used for the measurement of 3D microstructure; moreover, it has also been applied in many fields including topography examination, morphological monitoring of biology objects, particle studying, etc. [91]. The phase information allows one to make the surface topography measurements with nano-meter vertical resolution [204]. Deformations can be measured by evaluating the changes between the phases recorded at two states of the sample [205]. Based on the double exposure principle, phase aberrations, which may emerge in a single off-axis holographic reconstruction, can be compensated, as discussed in [206].

In the work [207] we use DHM together with the noise suppression iterative sparse technique for the 3D high accuracy reconstruction of SRG pattern on a ChG As_2S_3 -Se NML. We are concentrated on the image-plane holography because it better demonstrates the advantages of the sparse modelling of the wavefront than the other holographic methods.

ChG As_2S_3 -Se NML was produced by a computer controlled cyclic thermal vacuum deposition through the mask [134]. The technology enables film deposition control within the whole sample thicknesses in the range from 0.010 μm to 3.0 μm . Thermal depositions occur at rather low temperatures (400–600 $^\circ\text{C}$). The NML sample contains alternating As_2S_3 nanolayers with the thickness of 15 nm and Se nanolayers with the thickness of 10 nm. The total number of the nanolayers was 200, the thickness modulation period of the pair As_2S_3 -Se layers was about 25 nm. The last-mentioned parameter is critical in the recording process for obtaining high quality surface relief.

When laser beams with photon energy equal or above the band gap energy irradiates the ChG thin film, a strong interaction of the light with the material takes place. At relatively low intensity levels (hundreds of mW per cm^2) predominantly photoinduced phenomena, such as photo-polymerization, photo-viscosity, etc. take place [208]. An interferometric procedure for producing a step grating relief the SRG on the As_2S_3 -Se NML has been described [201], where a CW laser with wavelength $\lambda = 532$ nm and average spot power density on the sample from 150 to 350 mW/cm^2 have been used for recording. The holographic surface gratings with a period of

$\Lambda=1 \mu\text{m}$ were recorded by two cross-polarized ($\pm 45^\circ$) laser beams with respect to the fringe of the grating. AFM measurements of the sample surface after recording show that the depth of grooves is about 120 nm.

An off-axis DHM bright-field configuration in transmission mode has been employed for the measurement of the SRG topography. The approach to recover the complex amplitude distribution transmitted by the sample includes: a method to filter the twin image and the zero diffraction order, a numerical reference calculation, and a numerical reconstruction of sample's image [209].

The DHM setup is shown in Fig. 4.22. In order to obtain an environmentally robust and compact setup the laser beam was coupled in a monomode Y-coupler. The spot diameter on the sample was adjusted by the fiber/sample distance. An oil immersion objective with magnification 100x and NA=1.25 has been used. The oil was introduced between the cover slip (0.13 mm thickness) and the first objective lens. The first diffraction order of the SRG (39°) was accepted by the aperture angle (55°) of the objective. The CCD sensor was located at the distance of 195 mm from the objective for minimum aberrations in the image. The light source had a wavelength $\lambda=633 \text{ nm}$ and thus the resolution of DHM was about 506 nm (the smallest resolvable object detail). The camera resolution was 2592 pixel \times 1944 pixel with pixel size $2.2 \mu\text{m} \times 2.2 \mu\text{m}$. The period of the SRG was $\Lambda=1 \mu\text{m}$, it was twice as large as the resolution limit.

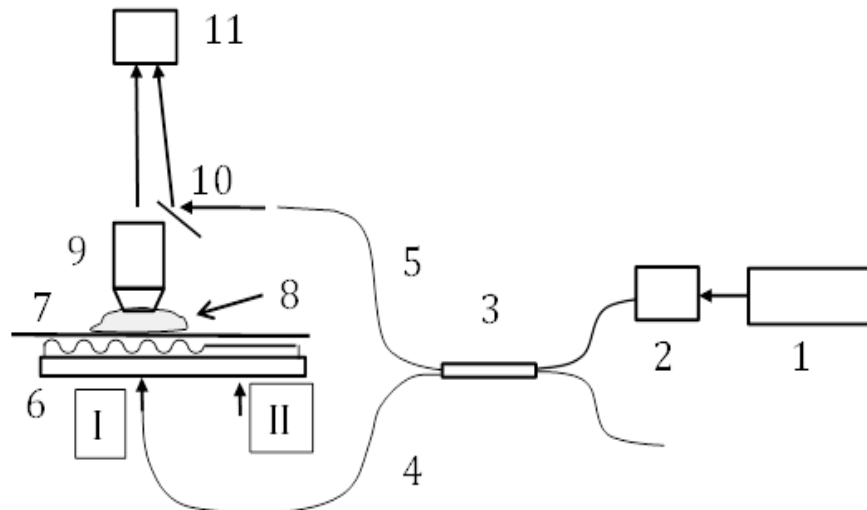


Fig. 4.22. Setup of the DHM: 1 — He-Ne laser ($\lambda=0.633 \mu\text{m}$, power=10 mW), 2 — single-mode fiber launch device, 3 — 2×2 polarization-maintaining single-mode fiber optic coupler, 4, 5 — object and reference beams, 6 — sample with surface diffraction grating, 7 — cover slip ($n=1.51$), 8 — immersion liquid ($n=1.51$), 9 — immersion microscope objective, 10 — mirror and 11 — CCD camera. I, II show two positions of object illuminations beams, namely, I — throughout the grating on NML and II — throughout the NML.

The topography of the SRG was determined by comparing the phases obtained from the reconstructions of the reference object and the sample [207]. In our experiment, the holograms recorded from the unexposed parts of the NML sample and with surface grating, were used as the reference and the object holograms, respectively. The phases of the two reconstructions were subtracted to obtain the phase map $\Delta\varphi(x,y)$ which provided the wavelength λ and the refraction index n are known, can be converted into the topography:

$$T(x, y) = \frac{\Delta\varphi(x, y)}{2\pi(n - 1)} \lambda. \quad (4.9)$$

The considered optical setup is clear from Fig. 4.22. Here the microscope objective (9) projects the object on the CCD plane (11). In this way, we obtain the so-called image-plane holography, where the object image is reconstructed at the CCD camera plane.

The laser light is split into two beams by a beam splitter: the object beam is directed towards the surface of an object under study; the reference beam is directed towards a mirror which turns it to camera. The intensity of the sum of those two beams (hologram) is then acquired by a sensor array. The complex-valued wavefront at the sensor plane is given by

$$u_s = B_o \exp(j\varphi_o) + A_r \exp(j\varphi_r), \quad (4.10)$$

where $u_o=B_o\exp(j\varphi_o)$ and $u_r=A_r\exp(j\varphi_r)$ are the object and reference wavefronts, respectively. For the off-axis configuration and the plane reference wavefront the reference phase φ_r is defined in the form

$$\varphi_r = \frac{2\pi}{\lambda} (x \sin a_x + y \sin a_y) \quad (4.11)$$

where x and y are the angles of the reference beam plane with respect to the optical axis z , $(x; y)$ are the coordinates in the sensor plane and λ is the wavelength. Thus, the reference beam at the sensor plane is a 2D harmonic function of the frequencies $\sin x/\lambda$; $\sin y/\lambda$ on x and y , respectively.

The beam intensity of the above-mentioned beam (hologram) is defined as

$$I = |B_o \exp(j\varphi_o) + A_r \exp(j\varphi_r)|^2 = B_o^2 + A_r^2 + 2B_o A_r \cos(\varphi_o - \varphi_r). \quad (4.12)$$

The measurements are assumed to be noisy in the image processing and below they are given as

$$Y = I + \sigma\varepsilon, \quad (4.13)$$

where σ is the standard deviation of the noise and ε is the standard i.i.d. zero-mean Gaussian noise, $\varepsilon \sim N(0; 1)$.

Two methods have been used for data processing and the shape reconstruction. The first one is conventional and it is based on the Fourier Transform (FT) [210]. In that method the first order item of FT corresponding to $B_o A_r \exp(j(\varphi_o - \varphi_r))$ is extracted. After the inverse FT of the above-mentioned item the phase $(\varphi_o - \varphi_r)$ is calculated and the object phase φ_o is reconstructed

provided the reference phase φ_r is known. The estimate of φ_o is filtered from noise and in this way one arrives to the final estimate.

As alternative technique we use the variational approach originated from [211]. The idea of that approach is to optimize the lost function minimizing the deviation of the estimate from the measurements. The technique is based on the assumption that the variables B_o , φ_o , A_r are invariant in a small neighborhood x_m of each m -th pixel of the observations and the criterion is of the weighted least square form

$$J_m = \sum_{q \in X_m} w(q) [Y(q) - I]^2, \quad (4.14)$$

where $w(q)$, $\sum_{q \in X_m} w(q) = 1$, is a weight function applied to the variables in the neighbourhood of x_m . Here x_m is a small square area centered at the pixel x_m , the weight function $w(q)$ is Gaussian and I stands for the true (noiseless) hologram intensity as defined in equation (4.13).

Contrary to the FT method the above variational approach allows one to use full power of the hologram (in Fourier domain it means the use of all orders of the hologram). That is the principal advantage of the variational approach potentially guaranteeing a better accuracy and a better resolution of imaging. The criterion (4.14) is highly nonlinear with respect to unknown quantities B_o , φ_o , A_r . To make the variational problem manageable a special replacement of the variables is proposed in [212].

Further development of that technique was produced in the paper [129]. The key idea of the new algorithm is the application of the sparse approximation technique for modelling the object amplitude and phase as functions of the coordinates. The sparsity hypothesis assumes the existence of such functions. Moreover, both the phase and amplitude can be approximated by a series of a small number of those functions. This compact approximation enables good noise suppression and the robustness of the estimates with respecting various disturbances.

The details of this iterative algorithm referred as Sparse Phase and Amplitude Reconstruction (SPAR) can be seen in [129]. In this paper a number of modifications have been made in the algorithm in according with features of experiment and sample under investigation. First, a spherical reference wavefront as well as a plane one are incorporated in (4.14) contrary to the linear wavefront (4.11) which is only exploited in [129]. Second, the operating window dimensions x_m are 20-by-20 pixels, and Gaussian standard deviation is 5, which have been produced to improve the reconstruction results.

To discuss new approach let us start with the result obtained by FT technique.

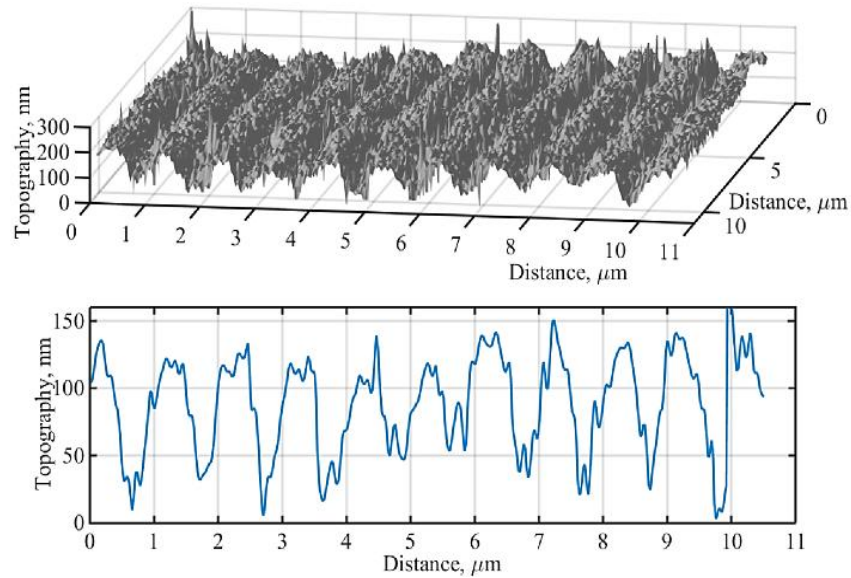


Fig. 4.23. Topography map (top) and cross-section (bottom) of grating at image plane obtained by FT technique.

The conventional DHM imaging technique uses a FT algorithm followed by a filtering and an inverse FT. Topography map and a profile along one-line perpendicular to the grating are shown in 0. A small part of all surface of grating ($12 \mu\text{m} \times 12 \mu\text{m}$) is chosen for a quick estimation of calculation algorithm. The total field of view is $40 \mu\text{m} \times 40 \mu\text{m}$. The profile along a line shows the maximal amplitude of about 120 nm. Due to the high noise the grating period (which is supposed to be $\Lambda=1 \mu\text{m}$) cannot be precisely determined. Nevertheless, the SRG data coincide with the optical measurements of SRG recorded on the $\text{As}_2\text{S}_3\text{-Se}$ NML [201]. Note that DHM approach is the full field express method which can be used without additional sample preparation.

However, it is impossible to see the sinusoidal surface relief definitely. The calculated profile of lines is shown the maximal sweep of amplitudes being about 130 nm. The period of grating is not seen clearly because of the high level of noises. In comparison with the calculated period of grating ($\Lambda=1 \mu\text{m}$) during holographic recording the period of grating is corrupted by noises and is not clearly seen. Thus, the obtained information about the surface relief is not sufficient.

Fig. 4.24 shows the SPAR reconstructions of SRG. The SPAR reconstructions clearly demonstrate the denoised images in comparison with quite noisy reconstructions obtained by standard FT shown in Fig. 4.23. The cross sections show in Fig. 4.24 (bottom) that the SPAR algorithm eliminates the noise and preserves important profile details.

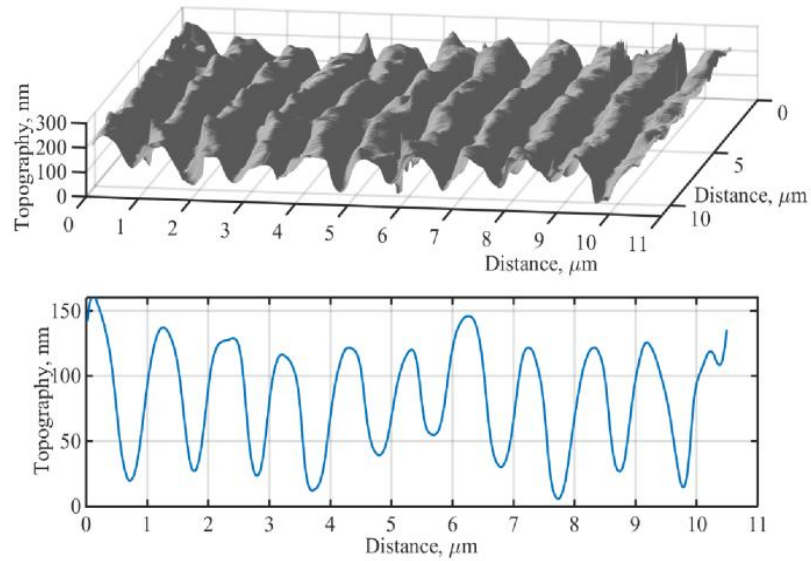


Fig. 4.24. Topography map (top) and cross-section (bottom) of grating at image plane obtained by the SPAR technique.

We may conclude that the high resolution off-axis configuration of the DHM setup is applicable for SRG nanoscale investigation. The novel variational algorithm developed for the digital off-axis holography is able to produce a high-quality imaging for quite noisy data. Moreover, the surface depth and relief of grating are guaranteed in processing.

The other kind of DHM was developed based on DHI with modifying illuminating and imaging part to do suitable for hundred nanometers sizes of the samples measurements [213]. It is well known that when an optically rough surface is illuminated by coherent light, speckle can be observed due to phase difference from surface points imaged on a detector. The rate and uniformity of overall magnification are determined by the camera objective, and their values are sufficient for microscopy application. So it is needed to fit optical system of DHM with the respect to object dimensions.

Entocentric optics is rather unsuitable for the measuring tasks and the inspection of microobjects because it introduces several adverse factors reducing measurement accuracy and repeatability: 1) a variation in magnification leads to coma; 2) the distortion of image due to aberration for parts of object lined away from the optical axis; 3) the perspective errors; 4) the poor resolution.

An illumination system for microscopy must satisfy the following conditions:

1. The object field should be fully and evenly illuminated.
2. The contrast of the images should be high with which is weighty for unstained or darker samples when these are nearly transparent or spoiled by speckle.
3. The NA of the objective should be matching for variable range, from 0.01 to 1.25.

The developed object-space telecentric objective meets well first condition which proves by the wavefront and relative illumination. To satisfy condition 2 and partly condition 3 we choose dark-field epi-illumination that renders the object as bright against a dark background, considerably enhancing the contrast and visibility of small objects. The epi-illumination can be used in most microscopic techniques including bright field, dark field, phase contrast, etc. But careful setting up is required, and some adjustments have to be made in any case.

Our dark-field illumination scheme utilizes the microscope epi-objective in object arm of DHI. The laser light is delivered through a 2000 μm diameter bundle of optical fibers and illuminates the sample under investigation (Fig. 4.25) through the condenser parabolic mirror of microscope epi-objective. The object beam formed by a hollow cone of illumination falls to the object, and only light backscattered by the object gets to camera. This backscattered light passes through the lenses of the epi-objective to be imaged. When passed through the objective, the light reflected from the object is not affected by the light delivered to the sample. In such way more contrast image is produced. An epi-objective does not usually require a cover slip, because it is intended for use with reflected light on a solid sample. In addition, the illumination through the objective lenses produces a very bright glare especially in case of low reflection samples unlike the microscope epi-objective illumination. The light that is reflected by the sample interferes with the reference light on the camera sensor producing interference speckle pattern.

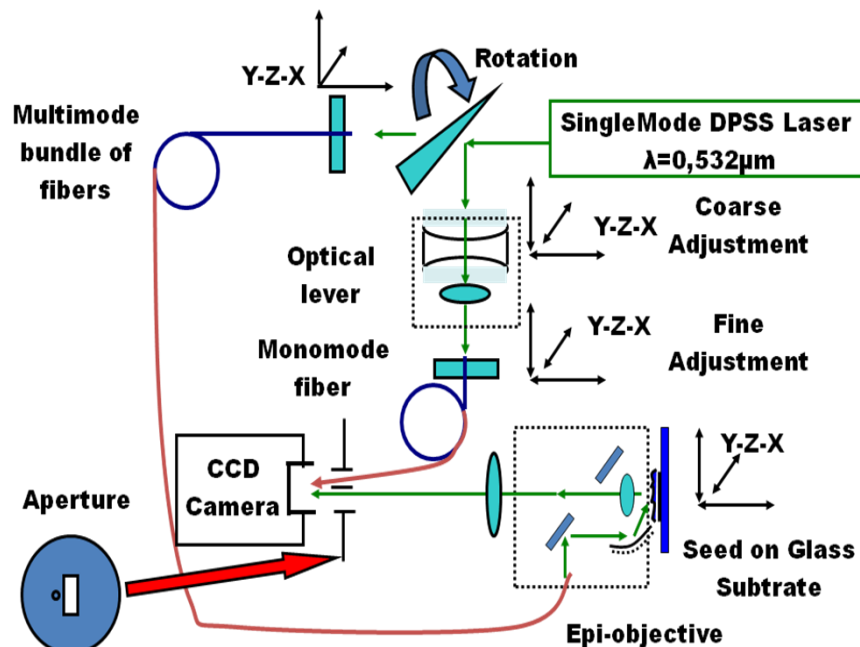


Fig. 4.25. Configuration of the dark-field DHM optical setup.

On the Fig. 4.25 we present the configuration of the developed DHM provided with the microscope epi-objective. There are 100 mW DPSS laser, wedge prism as beamsplitter, bundle of optical fibers as object arm, biological sample (seed glued on dark glass substrate), object arm, camera objective, optical lever composed from negative lens and microobjective ($60\times$ and $NA=1.25$) as positive lens, monomode optical fiber as reference arm, rectangular diaphragm, Smart Camera, PC.

Compared to classical phase shift interferometers, DHM offers similar performance in terms of resolution, precision, repeatability, and FOV but can be considered as an attractive solution as a result of five main features:

The acquisition rate is higher because a complete description of the complex wavefront is obtained from a single hologram.

The sensitivity to external perturbations (vibration and ambient light) is reduced since the capture time can be reduced to a few tens of microseconds.

The accuracy is not intrinsically limited by the precision of the control of moving parts, such as piezoelectric transducers.

DHM instrument can be used without adaptations to investigate a wide variety of micro-optical component shapes and biological samples.

It is easy to use and flexible for implementations in automated processes for quality control because of the robustness of the technique regarding positioning tolerances.

4.4. Imaging ellipsometry and AFM measurements

ChG exhibit a variety of properties applicable to optical devices. The photodarkening refers to a red-shift of the band edge upon illumination, which means an increase in the absorption coefficient in the vicinity of the absorption edge. The photoinduced surface corrugations are connected with viscosity modification. The photoinduced refractive index change refers to an increase in the refractive index upon illumination. The absorptive and dispersive changes are connected with each other [214], and are related to structural rearrangement in the illuminated volume. The As_2S_3 exhibits a majority of the photoinduced phenomena [215–217] and is a model material with stoichiometric composition within the prototypic arsenic-based sulfide glass system.

Since the DE of diffraction gratings are defined by three parameters such as refractive index change (photorefraction), transmittance change (photodarkening) and relief change (photo-expansion), it was necessary to investigate the contribution of each parameter in the diffraction grating formation. For this purpose, optical techniques are suitable and widely used in thin films inspection and applications thanks their inherent nondestructive nature and high accuracy. Each

of them has its merits and drawbacks. The refracted near-field measurement [218] can map out refractive index patterns, but this method is applicable for small variation of index, and the sample must be immersed in an index matching liquid. Spectroscopy has limited accuracy and interdependent determination of refractive index and thickness of thin films.

Among the optical techniques, ellipsometry is one of the most powerful tools. It allows simultaneous independent determination of film thickness and refractive indices with high accuracy [219]. However, as the feature sizes of devices become smaller, the application of ellipsometry in this area is hampered by the large illumination spot size and slow scanning process of conventional ellipsometry. Imaging ellipsometry can be used for an assessment of two-dimensional morphologies of surface. It combines the high vertical resolution of conventional ellipsometry, which is in the sub- μm range with a lateral resolution in the micrometer range of optical microscopy.

In our work, we applied the imaging ellipsometry for study the diffraction grating recorded on As_2S_3 thin films [137]. The processes of patterning the diffraction gratings on As_2S_3 layers depending on the exposure were studied in a number of articles [220, 221]. It was shown that relief diffraction gratings can be obtained with a sinusoidal or cycloid surface profile against the exposure recording conditions. However, to distinguish the gain of different photoinduced processes taking place in As_2S_3 layers is important for recording investigation. In addition, to our knowledge until now the dependence of the profile of phase grating on exposure (where the distribution of light exposure in the layer defines the refractive index profile) remains under consideration.

In this chapter of the work it is determined the full-field imaging of the refractive index profile patterned in As_2S_3 layers at different values of amplitude holographic exposure by imaging ellipsometry [137]. As_2S_3 films were prepared by thermal evaporation in a vacuum chamber at pressure of 10^{-5} Torr. During deposition, the chalcogenide glass temperature was 270°C , yielding a deposition rate about 10 nm/min. Thin As_2S_3 film (about 1.0 μm) was deposited on optical glass substrate at room temperature. The monitoring of As_2S_3 film thickness was carried out during the evaporation by interference technique at wavelength of 940 nm. An interferometric holographic recording was used to expose linear grating on the As_2S_3 film. The period of the grating $\Lambda = \lambda / 2 \sin(\alpha/2)$, where λ is the wavelength of laser beam, α is the angle between the incidence laser beams. DPSS single mode laser operated at 532 nm and power density 122 mW/cm^2 was used for recording. The holographic gratings with a period of $\Lambda = 20 \mu\text{m}$ were recorded by two spatially symmetrical laser beams, the intensity ratio of recording beams was 1:1. The experimental set up is sketched in previous chapters.

The holographic gratings with different profiles were obtained depending on the exposure conditions. DE changes were observing in transmission mode during the recording time. Diffraction efficiency η_{1tr} was measured in real-time at normal incidence of laser diode beam ($\lambda=650$ nm, $P=5$ mW) by monitoring the intensity of the 1st order diffracted beam during the hologram recording. Fig. 4.26 shows the dependence of 1st order diffracted intensity on exposure by laser diode ($\lambda=650$ nm) during the holographic grating recording. It is seen the maximum value of DE takes place at exposure 42 J/cm². The form of curve on Fig. 4.26 coincides with data of [221] for recording process in chalcogenide glasses. After reaching the maximum, the diffraction intensity is diminishing due to overexposure of recording media like in the conventional holographic case. It should be noted that optimum exposure is depend on the recording wavelength and film thickness. To investigate the exposure dependence, three types of diffraction gratings were chosen corresponding to: 1 — underexposed grating (recording time 4 min, exposure dose 28 J/cm²); 2 — proper exposed grating with saturation of the photo-induced effects, when no more increasing of diffraction intensity was observed with further irradiation (recording time 5.9 min, exposure dose 42 J/cm²); 3 — overexposed grating when the diffraction intensity begins to decrease (recording time 7.6 min, exposure dose 55 J/cm²) (Fig. 4.26).

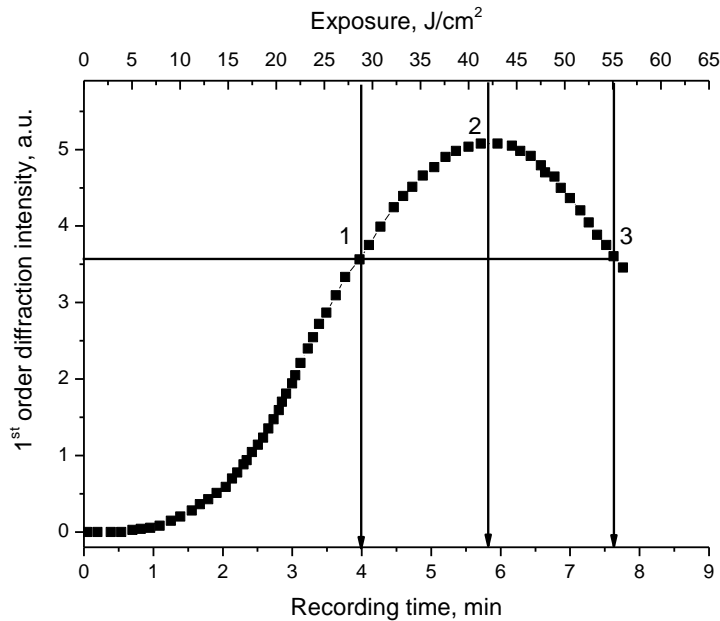


Fig. 4.26. Exposure dependence of diffraction efficiency during holographic recording of gratings by DPSS laser $\lambda=532$ nm; $P=122$ mW/cm². 1 — underexposed; 2 — proper exposed; 3 — overexposed.

It is interesting to compare our results with the exposure dependence of the diffraction efficiency of ordinary holographic gratings, recorded in thin As_2S_3 films with other wavelength. To

the best of our knowledge, for the 442 nm recording wavelength (He-Cd laser) the optimum exposure is 70 mJ/cm^2 [221], for the 488 nm recording wavelength (Argon ion laser) the optimum exposure is 2 J/cm^2 [222], for the 514 nm recording wavelength (Argon ion laser) the optimum exposure is 30 J/cm^2 [220], for the 532 nm recording wavelength (DPSS laser) the optimum exposure is 50 J/cm^2 [221]. Obviously, the optimal exposure decreases with the wavelength increasing for holographic gratings recording process.

The resulting phase gratings were characterized using an Imaging Spectroscopic Ellipsometer Nanofilm-EP³SE with integrated spectroscopic ellipsometry (SE) with wavelength field 600–1000 nm for film thickness determination, Variable angle ellipsometry (VAE) ($\lambda = 658 \text{ nm}$, $53\text{--}57^\circ$) for determination of average refractive index of the patterned area, and Imaging Ellipsometry (IE) for imaging of refractive index profile of the patterned area. Used Imaging Ellipsometer was based on solid state laser (658 nm, 20 mW), separate spectroscopic box with Xenon Arc lamp and 46 interference filters in the range between 360 and 1000 nm; 768×572 pixel CCD camera; patented motorized goniometer and 10^\times objective. For this setup, the absolute error of measurement is about 5 \AA for thickness measurement and 0.0002 for refractive index measurement. Since our aim was to measure the refractive index profile in ChG, we were mainly interested in measuring the peak-to-valley refractive index change due to photomodification and subsequently the maximum change in refractive index over the recorded diffraction grating.

Imaging Ellipsometry overcomes the limits of classical ellipsometry because it determines film thickness and optical properties (refractive index) independently by combining nulling ellipsometry with microscopy. To add imaging to an ellipsometer one mainly needs an objective and a spatially resolving detector, e.g. a sensitive CCD camera. The objective image is the illuminated area of the sample transferred onto the camera. Ellipsometric high contrast images from the surface or/and refractive index map with highest lateral resolution down to $1 \text{ }\mu\text{m}$ could be obtained. With the Imaging Ellipsometer one not only gets immediate qualitative information but it is also possible to restrict ellipsometry analysis to a particular region of interest within the field-of-view. A general problem of Imaging Ellipsometry is the inclined observation angle. Thus, only a limited area of the image appears to be well-focused when using conventional optics. The Imaging Ellipsometer overcomes this limitation by using a motorized focusing mechanism to collect a series of images with different foci within the field-of-view. A digital image processing system then superimposes only the focused parts of an image series, resulting in a digitized image sharp from edge to edge. Since motion of the objects under observation is critical, a variable scanner speed is provided to adapt the system to a wide range of experimental situation. Simultaneously, it is possible to generate maps of ellipsometric data with spatial reso-

lution down to a micrometer, while preserving the sub-nm film thickness resolution of a classical ellipsometer.

For the non-exposed thin As_2S_3 film the thickness and the refractive index were determined by spectroscopic and variable angle ellipsometry respectively. The thickness of As_2S_3 thin film averages $966 \text{ nm} \pm 9 \text{ nm}$, and the refractive index of As_2S_3 film 2.5873 ± 0.0002 ($\lambda=658 \text{ nm}$), which coincides with [221].

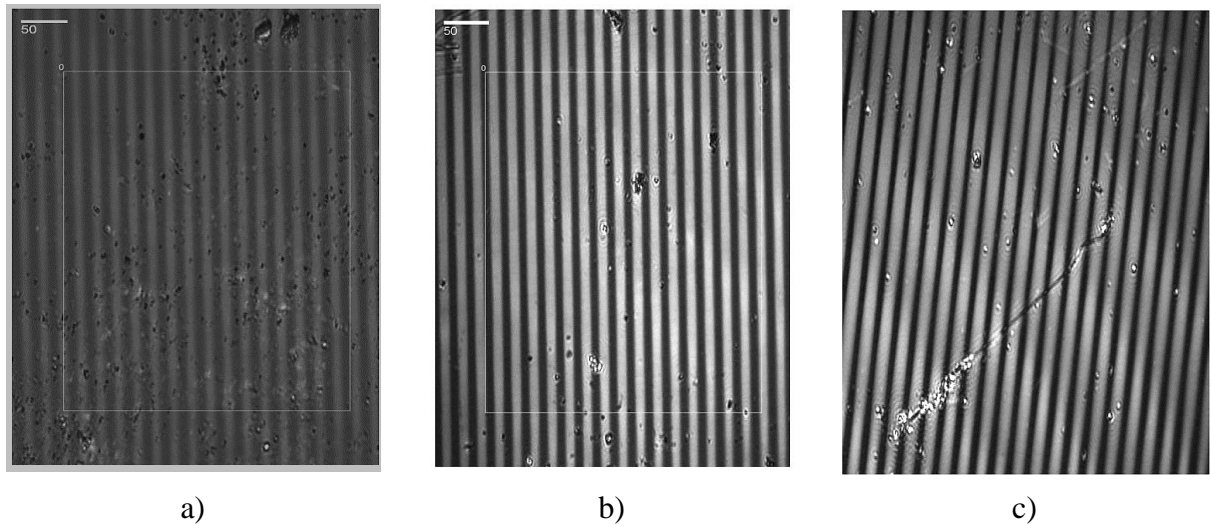


Fig. 4.27. The topography of extinction coefficient k of recorded diffraction gratings: *a* — underexposed; *b* — properly exposed; *c* — overexposed. Scale in left up is 50 nm.

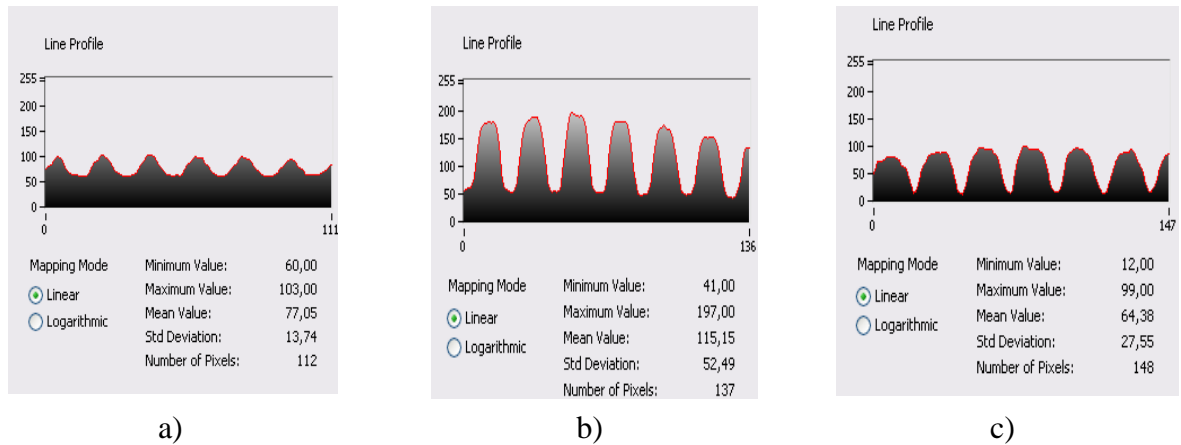


Fig. 4.28. The profile of extinction coefficient k of recorded diffraction gratings: *a* — underexposed; *b* — properly exposed; *c* — overexposed.

Fig. 4.27(a–c) shows the topography of extinction coefficient (k) obtained by imaging ellipsometry for three different areas: underexposed, properly exposed and overexposed gratings. It is seen that with exposure increasing change not only contrast of recording gratings, but also their form: the distance between fringes and width of them.

Fig. 4.30(a–c) shows the topography of refractive index pattern of area with underexposed, proper exposed and overexposed gratings, obtained by imaging ellipsometry. On the Fig. 4.28 the profiles of the ellipsometric enhanced contrast micrographs calculated for three different gratings are presented by using Vision Assistant LabVIEW from National Instruments. The profile of underexposed grating (Fig. 4.28a) repeats the light field distribution which is similar to sinusoidal profile at holographic recording. With increasing exposure (Fig. 4.28b) we observe the increase of the amplitude of profile and modifying its form: flattening the maximums and minimums. The profile of overexposed gratings departs from the sinusoidal form and the valleys becomes narrow. The contrast of the fringes falls down.

Fig. 4.29(a–c) shows the topography of extinction coefficient and Fig. 4.30(a–c) the topography of the refractive index pattern of area with underexposed, proper exposed and overexposed gratings, obtained by imaging ellipsometry.

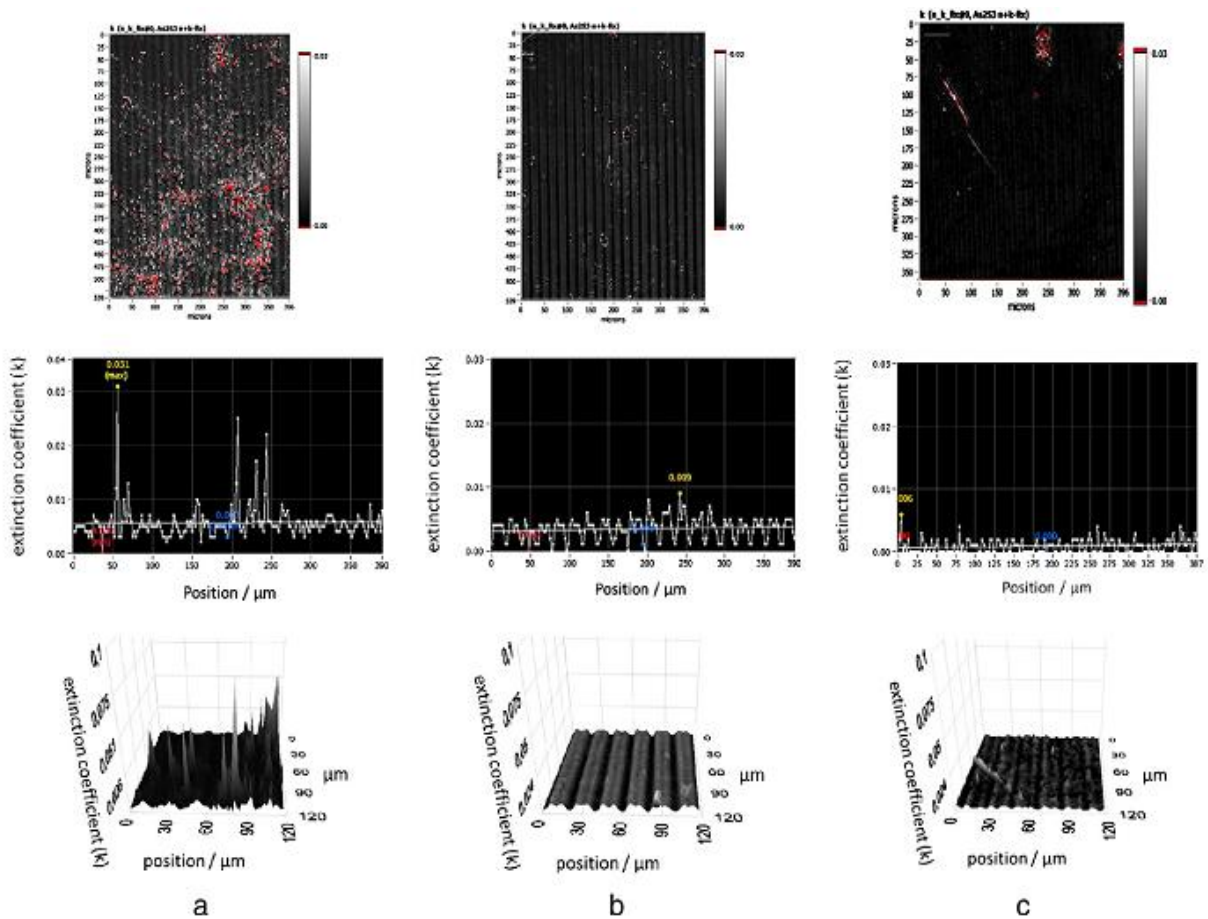


Fig. 4.29. The topography of extinction coefficient k of recorded diffraction gratings: a — underexposed; b — proper exposed; and c — overexposed.

At the lower exposure, the refractive index grooves are relatively shallow, the widths of peaks and valleys differ insignificantly, and the grating profile is close to sinusoidal, but the refrac-

tive index profile depth is relatively small (~ 0.02). Because of this, the grating recorded at this exposure exhibits low diffraction efficiency. It is known that refractive-index change by means of light exposure in As_2S_3 glasses is, in general, about 0.03. At the highest exposure, the grating profile changes to cycloidal. The peaks of refractive index become flat and wide; the valleys, deep and narrow. In case of intermediate exposure — proper exposed grating, the tendency is the same with an increase in the exposure: the peaks flatten and the valleys become narrower and deeper.

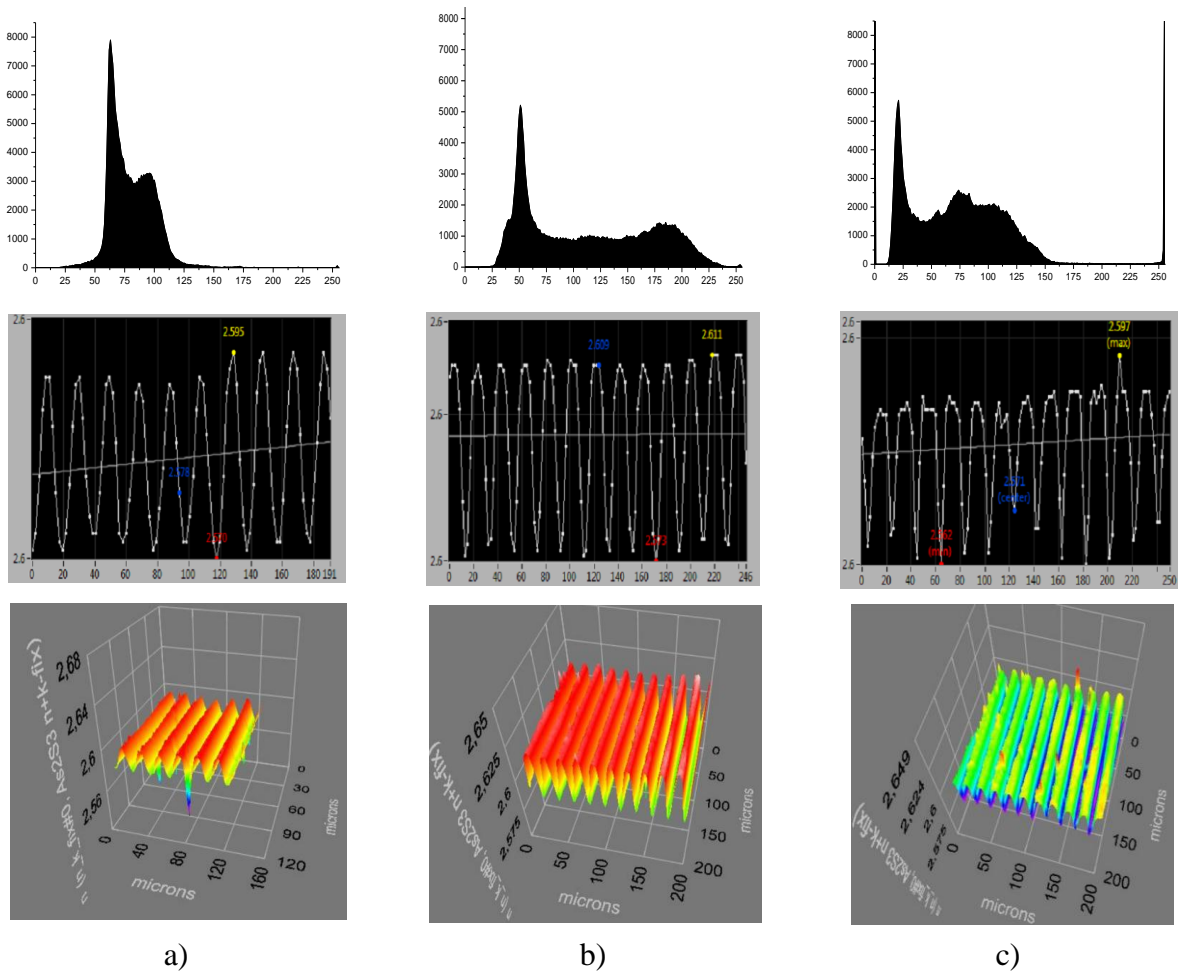


Fig. 4.30. Refractive index profile and real refractive index 3-D image of recorded diffraction gratings: *a* — underexposed; *b* — properly exposed; *c* — overexposed.

For properly exposed grating the refractive index profile depth is about 0.035 for $\lambda=658$ nm. For overexposed grating the decreasing of refractive index modulation (up to 0.03) takes place due to changing the grating profile. Transmission of grating profile from sinusoidal form to cycloidal one decreases the nonexposed area of sample which leads to flattening of refractive index. It can be explained by cumulative action of actinic laser light and photoinduced saturation.

The significant changing of samples thickness under exposure we did not observe. Therefore, it was shown the formation of diffractive gratings conditioning mainly by photoinduced changing of extinction coefficient and refractive index.

AFM measurements.

The surface quality of films is one of the most important characteristic of optical materials defining the recording properties. To study the surface of NML $\text{As}_2\text{S}_3\text{-Se}$ the profile of samples has been measured by AFM before grating recording (Fig. 4.31).

The surface roughness is the vertical variation from the baseline of the surface profile, this ignores the extreme values. Based on these data it is observed that the surface roughness is irregular and has the mean value of heights about 15 nm (see 3 Δ cursors on vertical scale on the right-hand side of Fig. 4.31a).

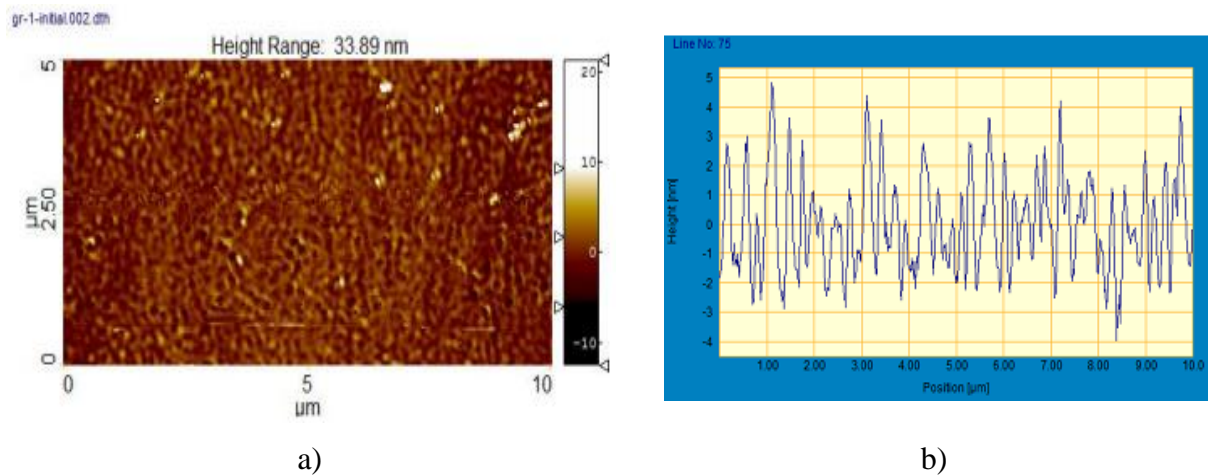


Fig. 4.31. a) Surface of NML $\text{As}_2\text{S}_3\text{-Se}$ investigated by AFM before grating recording; b) Profile of NML $\text{As}_2\text{S}_3\text{-Se}$ surface (from Fig. 4.31a) before grating recording by AFM.

The diffraction gratings with 1 μm period were recorded direct one step on NML $\text{As}_2\text{S}_3\text{-Se}$ by two laser beams with S-S polarization with synchronous DE η measurement by LD light in the first diffraction order. The surface profile of the holographic grating on NML $\text{As}_2\text{S}_3\text{-Se}$ measured by AFM is shown in Fig. 4.32a, b.

It can be observed that grating recording on NML $\text{As}_2\text{S}_3\text{-Se}$ provides high optical quality of the obtained relief with depth of the grating surface about ~ 100 nm at the total NML $\text{As}_2\text{S}_3\text{-Se}$ structure thickness 2500 nm and thickness modulation period of layers $N=25$ nm. The ripples of surface observed before grating recording (Fig. 4.31a) become smooth after recording. In addition, visually bigger signal/noise ratio (smaller halo) in the first diffraction maximum proves high optical properties of the gratings obtained. It is very important to underline that in contrast

to most communications about relief grating formation by laser beam in ChG films in our experiment, no wet etching was applied.

Considering the grating profile presented on Fig. 4.32b, one can see that the surface roughness observed before recording does not distort the profile of grating recorded. One can see that the thickness changes due to surface deformations of NML $\text{As}_2\text{S}_3\text{-Se}$ is $(\Delta d/d)100\% = (0.1 \mu\text{m}/2.5 \mu\text{m}) 100\% \approx 4.0\%$. Changing of $\alpha\text{-Se}$ film structure under exposure shown in [256] can trigger processes of mass transfer in chalcogenide multilayer structure due to arising structural non-uniformity according to intensity distribution during grating recording. In this experiment S:S polarizations of recording beams does not create the conditions for the vectorial mass transfer, for which the polarization along the grating vector is needed. We can assume that 4.0% depth of the grating recorded in NML $\text{As}_2\text{S}_3\text{-Se}$ structure is mainly the result of scalar deformations.

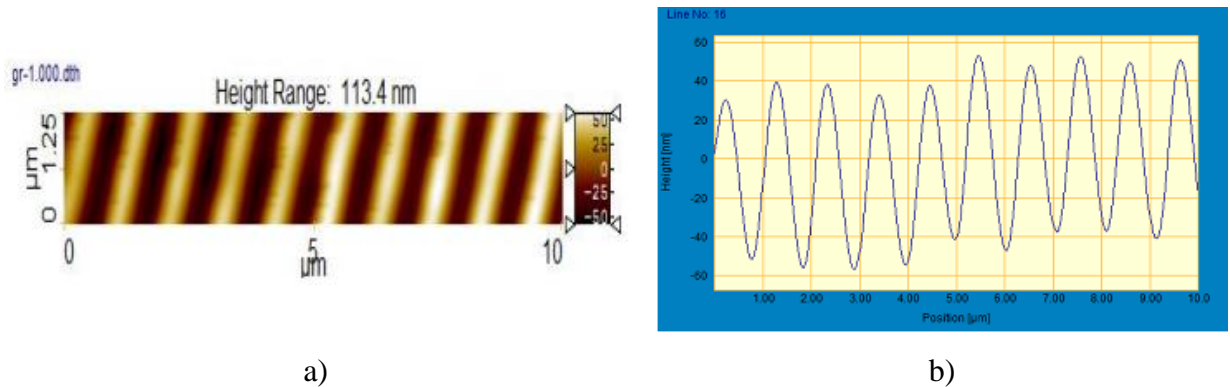


Fig. 4.32. a) Surface of holographic grating recorded on NML $\text{As}_2\text{S}_3\text{-Se}$ investigated by AFM; b) Profile of holographic grating (from Fig. 4.32a) directly recorded by two laser beams with S:S polarization on NML $\text{As}_2\text{S}_3\text{-Se}$ surface.

The surface relief of the gratings optical recorded intensity holographic configuration on the $\text{Ge}_5\text{As}_{37}\text{S}_{58}\text{-Se}$ NML were investigated by AFM. Diffraction gratings with $1 \mu\text{m}$ period were recorded by two laser beams with S:S polarization with synchronous DE η measurement by red laser ($\lambda = 650 \text{ nm}$) in the first diffraction order. Surface of holographic grating recorded on $\text{Ge}_5\text{As}_{37}\text{S}_{58}\text{-Se}$ NML is shown in Fig. 4.33(a and b).

It can be seen that grating recording with the use of NML $\text{As}_{37}\text{S}_{58}\text{Ge}_5\text{-Se}$ provides high optical quality of the obtained relief with depth of the grating surface about $\sim 100 \text{ nm}$ at total structure thickness 1760 nm and thickness modulation period of layers $D=17 \text{ nm}$. Grating profile is shown in Fig. 4.34. It can be seen that the depth of the surface grating is $\sim 100 \text{ nm}$ (see Ch. 3). Profile of the gratings obtained with the use of $\text{As}_{37}\text{S}_{58}\text{Ge}_5\text{-Se}$ multilayers is close to the sinusoidal one.

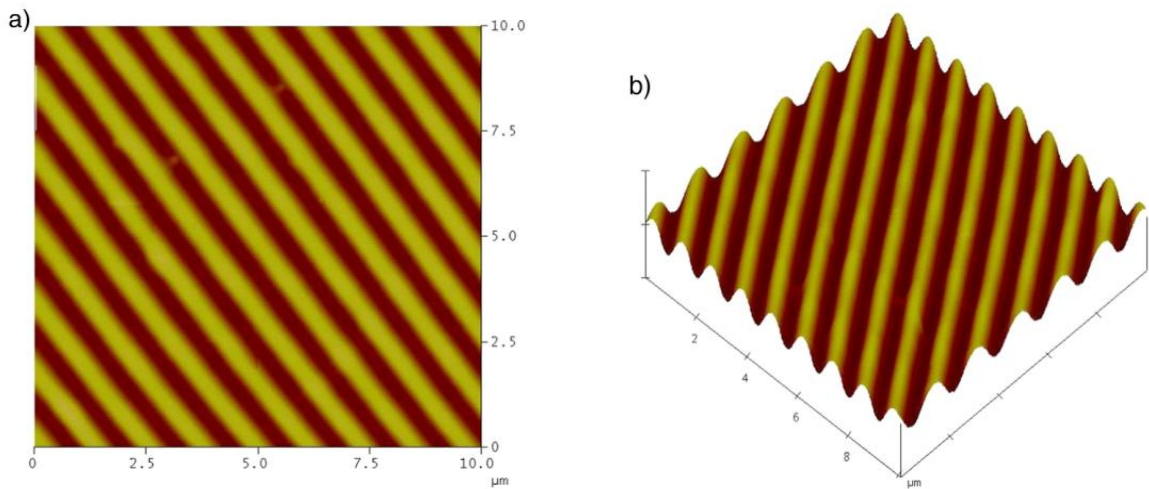


Fig. 4.33. a) Surface of holographic grating recorded on $\text{Ge}_5\text{As}_{37}\text{S}_{58}\text{-Se}$ multilayers; b) 3-D image of holographic grating recorded on $\text{Ge}_5\text{As}_{37}\text{S}_{58}\text{-Se}$ NML.

The application of NML $\text{As}_{37}\text{S}_{58}\text{Ge}_5\text{-Se}$ leads to increase of holographic sensitivity by two times in comparison with NML $\text{As}_2\text{S}_3\text{-Se}$ under similar conditions of holographic recording. The gratings obtained on the base of NML are stable (dependence of diffraction efficiency η on exposure saturates, while for “pure” $\text{As}_{37}\text{S}_{58}\text{Ge}_5$ layers such dependence has maximum with further decrease of η while doze increases).

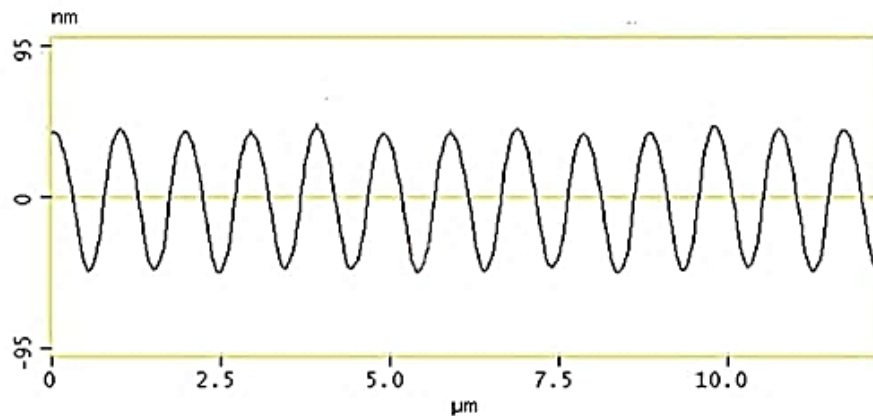


Fig. 4.34. Gratings profile of $\text{Ge}_5\text{As}_{37}\text{S}_{58}\text{-Se}$ NML (cross-section of the grating shown in 0(a) and b) perpendicular to the grooves).

The surface roughness of PEPC thin film measured by AFM and shown in Fig. 4.35 is enough good quality, but it is obtained before structures recording.

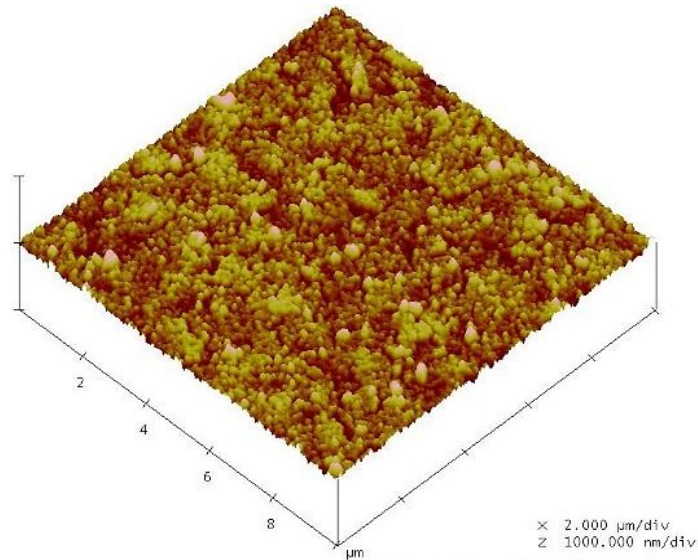


Fig. 4.35. AFM image of the surface of thin films of PEPC.

To prove the estimation of DE for the poly(PEPC-co-DO) film (Ch. 3.2) the holographic grating recorded by P:P polarization with up to 30% of DE was observed with AFM. The AFM analysis revealed the creation of a surface relief modulation with high quality. In the next Fig. 4.36 the 2D image of holographic grating with frequency 750 l/mm recorded by P:P polarizations is shown.

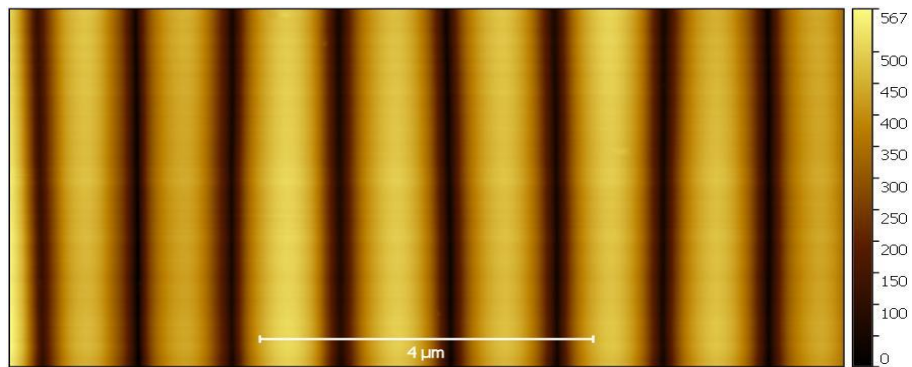


Fig. 4.36. 2D AFM image of holographic grating recorded on the poly(PEPC-co-DO) film.

The h of such modulation (peak-to-peak amplitude) of the obtained grating (see Fig. 4.37) was measured to be about 440 nm. Despite sinusoidal distribution of intensities during holographic recording, the profile of grating is not sinusoidal. Possible reason for that is nonlinear response of polymer on intensities excitation.

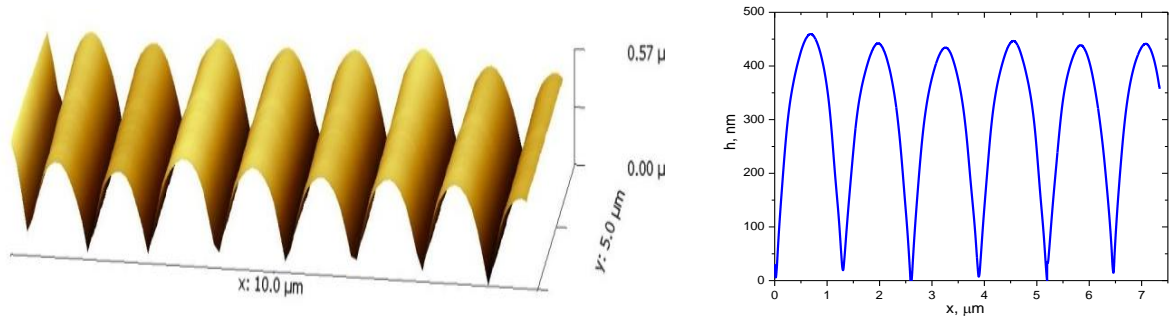


Fig. 4.37. AFM image (a) and cross-section (b) of surface relief grating recorded in poly(PEPC-co-DO) film (thickness 1600 nm, azo dye content 30 mass%) in P:P polarization configuration up to DE 30% measured at 650 nm.

4.5. Conclusion to Chapter 4

1. The recording kinetics of DE of SRG patterned on NML $\text{As}_2\text{S}_3\text{-Se}$ by one-step polarization holographic recording were investigated in dependence of the intensity grating periods. The highest possible efficiency of the one-step surface relief holographic recording can be achieved using LCP:RCP and $\pm 45^\circ$ polarizations ($\sim 45\%$). The light intensity contrast of interferograms is very close to zero and the electric field intensity gradient plays the main role for the direct surface relief patterning. The estimation of the Klein Q parameter for the NML $\text{As}_2\text{S}_3\text{-Se}$ was shown the gratings with period Λ more than $1.4 \mu\text{m}$ can be considered as thin gratings with Raman-Nath diffraction.
2. The behaviour of mass transfer and thus the resulting recording gratings is related to interaction between the photo-induced anisotropy in nanolayer with enhanced or decreased polarizability of molecules and their drift under the electrical field intensity gradient.
3. The optical performance of DHI system has estimated on the base of ZEMAX code. Geometrical model of three lenses telecentric objective and rectangular diaphragm, MTF, wavefront and grid of chief ray were presented and analysed. Resolution of the objective and chip of the camera were considered.
4. We demonstrated that the high resolution off-axis configuration of the DHM setup is applicable for SRG nanoscale investigation. The novel variational SPAR algorithm developed for the digital off-axis holography is able to produce a high-quality imaging for quite noisy data. Moreover, the surface depth and relief of grating are guaranteed in processing. The reconstruction results demonstrated a better effectiveness of our approach in comparison with standard FT.
5. Imaging ellipsometry technique for the characterization of laser-written diffraction gratings in As_2S_3 films was applied. We performed quantitative diagnostics for photodarkening effect and

photoinduced index gratings formed by holographic recording in As_2S_3 thin films. The thickness measurement showed a sensitivity of 5 Å and provided a spatial resolution of approximately 1 µm. An index sensitivity of 0.002 was obtained in the index of refraction measurement with the same spatial resolution. The maximum change in refractive index is 0.035 ± 0.0002 for diffraction gratings recorded in As_2S_3 films. The refractive index profile varies with exposure from sinusoidal ($H= 29 \text{ J/cm}^2$) to near cycloidal ($H= 42 \text{ J/cm}^2$) and to cycloidal ($H= 55 \text{ J/cm}^2$).

6. A very important finding was discovered by AFM measuring: the grating recording on NML As_2S_3 -Se provides high optical quality of the obtained relief with depth of the grating surface about ~ 113 nm at total NML As_2S_3 -Se structure thickness 2500 nm and thickness modulation period of layers 25 nm. In addition, in the recording process visually bigger signal/noise ratio (smaller halo) in the first diffraction maximum proves high optical properties of these gratings.

5. APPLICATIONS OF DIFFRACTIVE OPTICS

In recent years, demand for optical 3D imaging sensors has become increasingly relevant, and has led to the development of instruments that are now commercially available [223]. During the 1970s and 1980s their development was mainly performed in research laboratories, and was aimed at designing new techniques exploiting the use of light beams (both coherent and incoherent) instead of contact probes, in view of their application in the mechanical manufacturing industry, for measurement and quality control applications. Novel measurement principles were proposed, and suitable prototypes were developed and characterized to prove their performances [224–226].

In parallel, we participated in a considerable effort directed towards the miniaturization and integration of optical light sources, detectors and components in the electronic equipment and the mechanical structure of the sensors. In the last decade, the availability of techniques and components has led to the production of a wide spectrum of commercially available devices, with measurement resolution from a few nanometers to fractions of a meter, and ranges from microns to a few kilometers.

In recent times, the trend has been to produce devices at decreased costs and with increased ruggedness and portability.

5.1. Security hologram elements

The DOE is a sophisticated new generation security element which has been developed without the usual restrictions imposed by the substrate, or printing processes. It is a light-diffracting structure embedded into a transparent window of glass or polymer substrate.

Currently, security holograms are one of the most reliable ways to protect products and documents against forgery. Protective holograms are diffractive optical elements with variable diffracting properties. The project “Printing and identification of protective quasiholographic label on precious metals articles” was a development work carried out by the “Recording Media and Photonics” laboratory for the Assay Chamber of Moldova Republic under contract “Development of quasihologram technology to increase the protection level of products made from precious metals”. According to the results of this work it was determined that for the qualitative printing of the labels on the surface of precious metal, which is not flat, it is necessary to focus the laser beam to the point of radius less than 10 microns. In this project, the developed technology was applied to the protective quasihologram printing with a new telecentric objective to improve the focusing of the laser radiation. During the reading out or identifying processes the protective sign is restored which allows to verify its authenticity. The comparison of the protec-

tive holographic sign under test with reference one is conducting in the Fourier domain. The digital Fourier transform of quasihologram is calculated using the computer program for recording of digital holograms also developed in the above mentioned contract.

The aim of the project was the elaboration of laser technology for holographic sign printing and the portable device for identification of authenticity the state protective sign on the products from precious metals.

The main objectives of the research:

- To modify the optical system for focusing the laser beam into the spot diameter about 10 μm . It is necessary for printing the diffraction gratings with high frequency;
- To printing the quasiholographic protective sign in according with partner requirements;
- To construct the portable optoelectronic device for recognizing and identifying the developed protective sign on the surface of the product from precious metals.

In the course of the research have been solved four problems:

1. Development of the optical system for focusing the maximum laser energy to a point less than 10 microns in diameter followed by selecting the telecentric objective from catalogues of known brands.
2. Set the selected telecentric objective into available laser installation.
3. Design and print the protective quasiholographic sign.
4. Development of a portable laser device for optical identification of the protective quasiholographic sign.

For the development of optical systems as a methodology to be used a computer simulation method based on the optical design program ZEMAX (see Ch. 3). The telecentric objective was selected based on calculated parameters, purchased and installed to NAUTILUS. On the basis of the previous contract and opportunities derived from the installation telecentric objective, the protective quasiholographic sign was designed. To recognize this protective label, the portable laser device has been developed.

Currently used the Moldova state protective mark on products made of precious metals does not provide a sufficient level of protection, because there were numerous falsified Moldova state marks of unknown origin. They quite accurately repeat the drawing of the state protective mark. Only visual inspection by optical methods reveals inconsistencies. However, at mass inspection this check is time and money consume. Counterfeits of the state protective mark cause great material damage to Republica Moldova and are estimated by many tens of thousands of lei annually. Control authorities bring to light a large number of smuggling of precious metal products already on sale. All of this allows us to conclude that it is necessary to increase the level of

protection of the state mark and to modify methods for determining falsifications. The presented project given the opportunity to realize the tasks set on the basis of modern testing methods used by the security technology in industry.

Achieving the research's goal allowed to enhance the level of protection of the state marks embossed on articles of precious metals by adapting the holographic technologies and its use for marking.

The results obtained within the framework of the project are used by the Camera de Stat pentru Supravegherea Marcării to improve the level of protection of the state protective marks against counterfeit (Fig. 5.1).

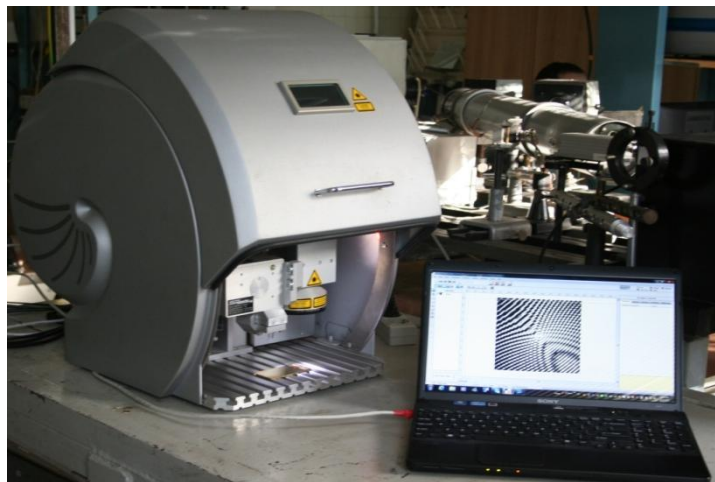


Fig. 5.1. The result of the research - the device for quasi-hologram marking.

We have to enhance the ability of the existing laser device for marking of the protective mark and to develop laser devices for controlling the embossed marks with enhanced control. Note that the acquisition of industrial equipment for the application of holographic protection signs requires an amount of about 100000 Euro, which is currently not available for Camera de Stat pentru Supravegherea Marcării.

In order to increase the level of protection of the state trademark, the following work has been done.

Optical software ZEMAX was used to calculate the optical scheme of the installation, consisting of the laser, the objective and mirrors. The features of optical setup performance such as the minimum diameter of the lens focal spot on the subject, the exact position of the objective in the optical circuit and the simulated image on the product were set by simulating and optimizing the optical circuit parameters. Based on the results of the calculations, the necessary opto-mechanical components were selected, including a focusing lens and other components, which then were purchased to modify the laser installation.

The parameters of the telecentric objective installed in the NAUTILUS laser device (8 W, $\lambda = 1.064 \mu\text{m}$): Focal length = 56 mm; spot of diffraction limit = 10 μm (see Fig. 5.2).



Fig. 5.2. The NAUTILUS laser device with the telecentric objective installed.

With help of video microscopy, the applied drawings of the protective signs made on precious metals with flat and curved surface were monitored. Also, the quality of laser engraving, the depth and distance between the points engraved were controlled which determine the resolution and quality of the mark on the metal. The planned resolution up to $10\ \mu\text{m}$ on metal was get. On the Fig. 5.3 we present the photographic images of the quasi-holograms obtained on the metal surface by microscopic investigation ($400\times$).

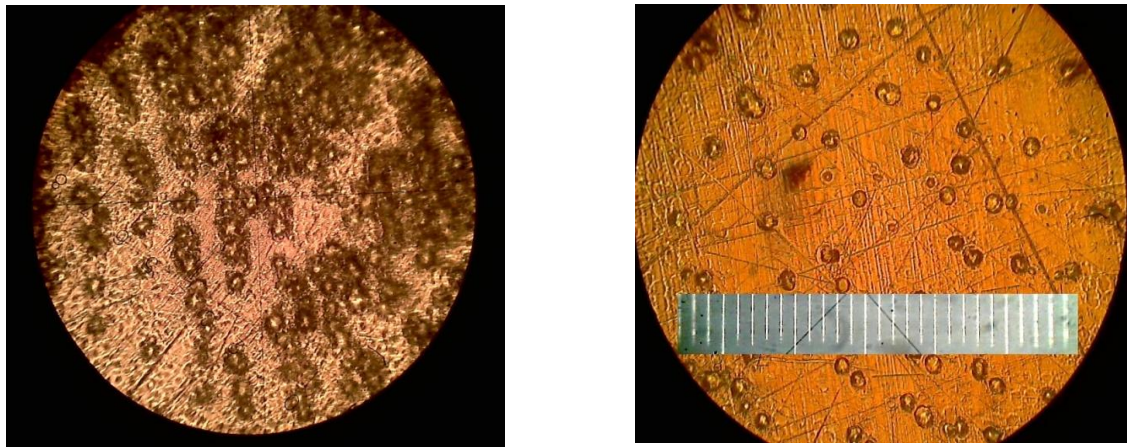


Fig. 5.3. The photographic images of the quasi-holograms obtained on the metal surface ($400\times$).

The next step for implementation of project's tasks was the development of software based on Visual Basic program to create a holographic image of a protective sign according to a customer's drawing.

The image, selected as protective sign, was computer encoded in form of digital hologram via the elaborated software. Then this digital hologram (diffraction optical element) was embossed on the surface of objects under protection by scanning with the NAUTILUS type laser.

The examples of digital holograms calculated by developed software are presented in Fig. 5.4. The “MakeHolog” software that has been developed [184] allows us to encode the marking image in various ways such as the actual image and the Fourier image. This factor allows to further increase the degree of protection of the marking design.

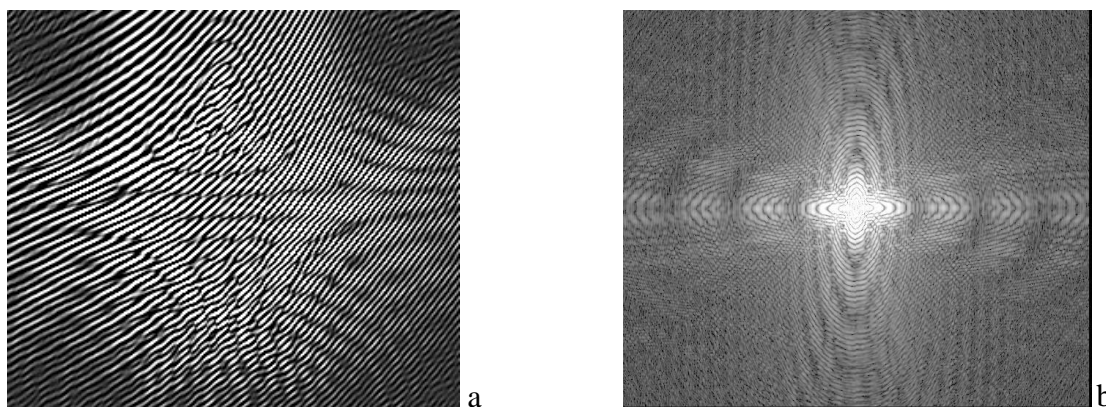


Fig. 5.4. The Fourier — images of digital hologram of one (a) and two (b) ellipses.

Based on the experimental researches of the process of forming lines on the surface of precious metal objects, the parameters of the engraving process were determined to obtain the lines with the required profile (laser power, frequency and duration of impulses). The software was installed on the computer. By applying the software, the laser engraves the quasi hologram to the surface of the metal objects under computer control. The example of a quasihologram, which was designed and applied on the surface of a gold plate using the developed software, is represented in the Fig. 5.5.



Fig. 5.5. The example of a quasihologram applied on the surface of a gold plate at different scales.

Holograms applied to the surface of metal are relief diffraction structures. Using the profile meter, the depth and frequency of the lines formed for different laser operating regimes were studied. Fig. 5.5 shows the profile of the quasihologram obtained for the optimal laser operating regime.

On the other hand, quasiholograms represent reflection diffraction elements. This means that the reconstructed image can be seen at the reflection of light that falls at certain angle on the metal surface with the hologram. This interference image that is observed (the position of the maxims and the distribution of the intensity in these maxims) are determined unambiguously by the character of the formed hologram (Fig. 5.5).

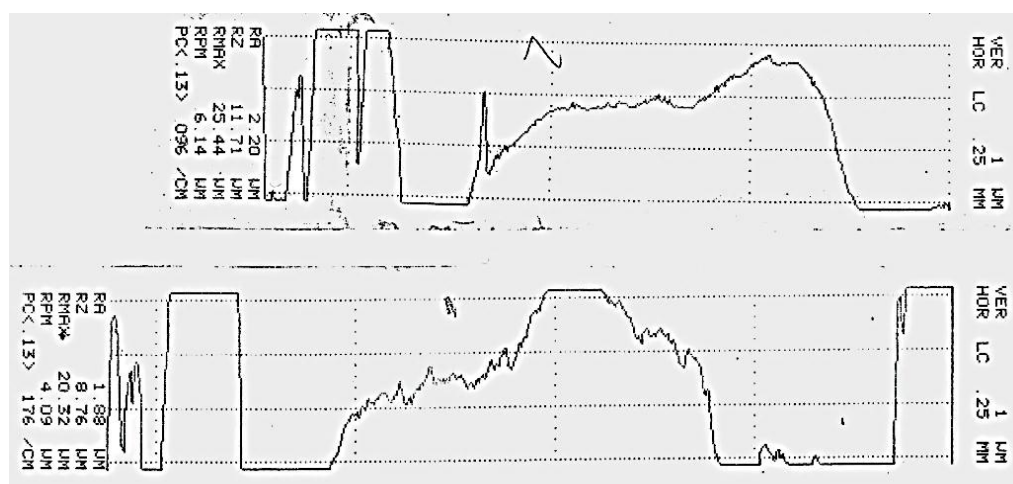


Fig. 5.6. The profilogramm of the relief hologram on the metal surface.

It was studied the surface of the precious metals with diffraction pattern of quasiholograms under the microscope. This investigation was needed to research the surface of precious metals at the action of a laser beam. Fig. 5.7 shows the microscope image of the metal surface on which a microtrees were formed. It is seen that the lines bear a good contrast, they are straight and the surface of the object is not damaged.

The research has shown that in order to increase the degree of protection of objects it is necessary to emboss on the surface of the object such a marking mark which can not be identified in a microscope with subsequent imitation of it. In addition, it has been established that the embossing on the metal surface of only a part of the designed mark, the incomplete or with the lower depth of the mark do not influence the quality of the reconstructed holographic image. So the image has to be obtained by applying of computer technologies. But the image of the original drawing that was used to calculate the quasihologram will be identified in any case. The essential difference of the proposed method is that we used the Fourier image of the drawing. Fig. 5.8 is a photographic image of the metallic object having a quasihologram on its surface. Note that in this case it is impos-

sible to identify the embossed image on the object, even by a powerful microscope. On the other hand, this image can be identified by using the holographic image processing method applied to the object. Besides, the appearance of mechanical defects on the surface of the object does not affect the quality of the holographic image restoration, because the quasihologram can be fully restored even on the basis of only a fragment of the holographic image.

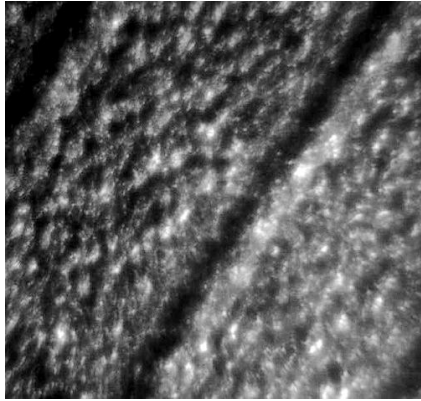


Fig. 5.7. Photographic image of the surface of the metal object on which the grid was formed.

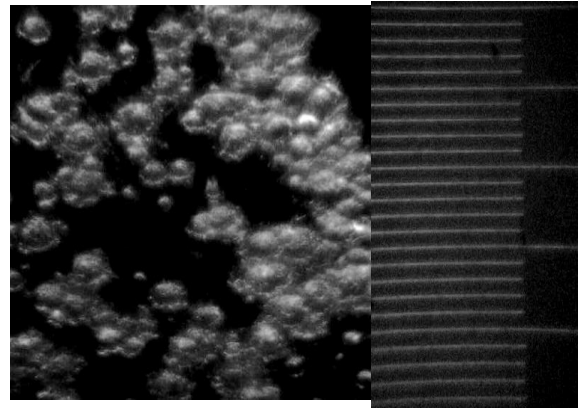


Fig. 5.8. Photographic image of the hologram at the microscope and the scale (10 μm division).

The optical device for control and observation of the original image reconstructed from the hologram embossed on surface of metal was elaborated (Fig. 5.9). The control device includes the following components:

1. The optical system including optical elements for the observation and control of the original image restored from the quasihologram;
2. A semiconductor laser.

A semiconductor industrial laser pointer was used to develop the laboratory model of the device. The use of semiconductor laser gives the possibility of assembling small device, but which meets requirements of the laser sources for holographic reading (Fig. 5.10).

Most people are acquainted with secure holograms like the sparkling holograms found on credit cards as well as bank notes and other kind of documents and stocks. The purpose of these secure holograms is to authenticate the credit cards or the bank notes, and to safeguard against counterfeiting. Secure holograms are simple to verify visually and difficult to copy or counterfeit. This property is caused by the fact that secure hologram contains visible information as well as data readable only with special optical equipment. The latter effect is quite often achieved by the use of DOE embedded in the image-containing hologram. One property that can be affected by the use of sub-micron structures is polarisation.

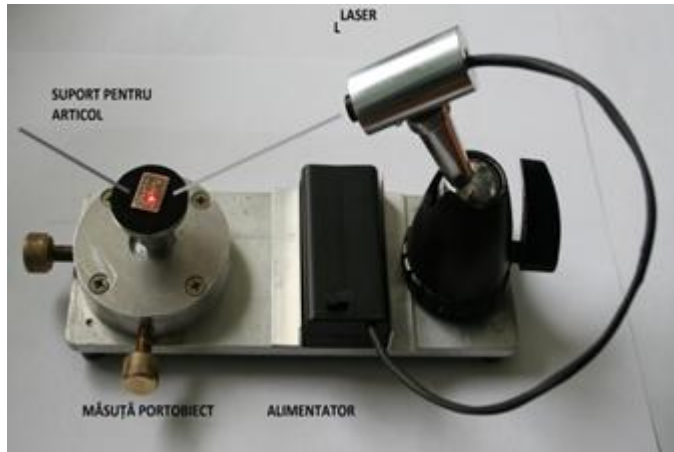


Fig. 5.9. The device for holograms verification.

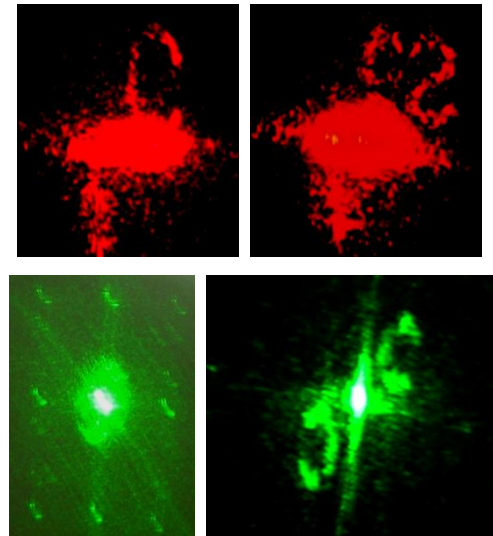


Fig. 5.10. The diffraction patterns of reconstructed holograms.

The practical application of DOE as secure holograms has been demonstrated in FP7 SECURE-R21 Project in frame of Pilot Ukrain-Moldova Project “Implement Security Holograms utilising Diffractive Optical Elements based on Chalcogenide Glasses and Azopolymers”. The main objective of the Pilot project is R&D of DOE based on nanomultilayers structures from ChG and structures from AP as media for recording secure holograms and optical components in various optoelectronic devices. The existing recording methods (laser/e-beam) have been developed for creation DOE on ChG and AP media. DOE design was elaborated on the base of systematic studies of ability NML from CHG and AP thin films to be structured under direct recording either by laser or e-beam exposure.

In Fig. 5.11a, the results of e-beam pixel recording of the Ukraine state emblem with the use of $\text{Ge}_5\text{As}_{37}\text{S}_{58}\text{-Se}$ NML are shown. Image sizes of the Ukraine state emblem consisted of 512×512 pixels (pixel size $\sim 2 \mu\text{m}$). AFM image of the recorded emblem fragment is shown on the right side of Fig. 5.11a. It is necessary to note that at the given recording conditions, pixel height is up to 200–300 nm. 0b shows the results of e-beam pixel recording of the Moldova state emblem with the use of $\text{Ge}_5\text{As}_{37}\text{S}_{58}\text{-Se}$ NML. AFM image of the recorded emblem fragment is shown on the right side of Fig. 5.11b.

Different surface relief patterns were recorded by e-beam irradiation of nanomultilayer structures on the base of ChGs. In the Fig. 5.12 AFM image of diffraction grating, recorded in $\text{Ge}_5\text{As}_{37}\text{S}_{58}\text{-Se}$ nanomultilayer structures by computer-assisted raster e-beam with period $2 \mu\text{m}$ at the e-beam current 7 nA and expose time at pixel — 0.3 ms, are presented. In this case the re-

lie's height reaches 60 nm for 2 μm of period. In Fig. 5.13 AFM image of surface relief structure recorded by e-beam exposure is shown. Pixel size is 2 μm .

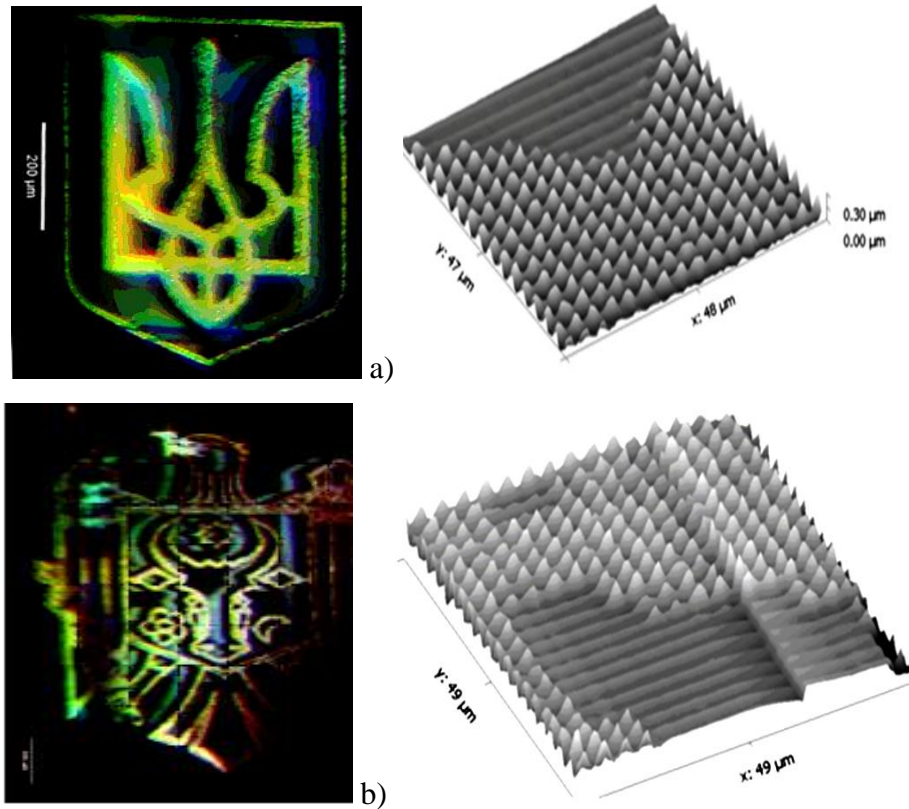


Fig. 5.11. Results of e-beam pixel recording of Ukraine (a) and Moldova (b) State Emblems with the use of $\text{Ge}_5\text{As}_{37}\text{S}_{58}\text{-Se}$ multilayer nanostructure. AFM images of the recorded emblem fragments are shown on the right sides of figures.

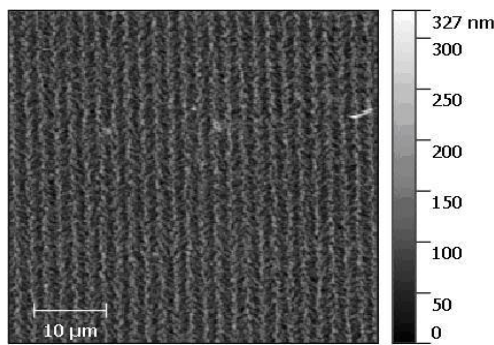


Fig. 5.12. AFM image of the diffraction grating with period 2 μm .

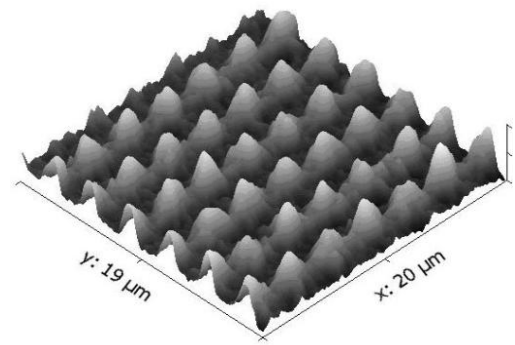


Fig. 5.13. 3D image of the diffraction grating with period 2 μm .

In the 0(a, b) we present the surface relief grating with relatively large amplitude on the epoxypropylcarbazole (EPC) and azodye Disperse Orange (DO) recorded by holographic method without any subsequent processing steps. We also found that the R:L polarization con-

figuration is the best case, which allows to achieve the largest amplitude of SRG about 130 nm (48% of film thickness). On the other hand, the S:S polarization configuration, providing 100% of intensity modulation, doesn't lead to grating formation. The formation of surface relief grating therefore depends strongly on the polarization distribution.

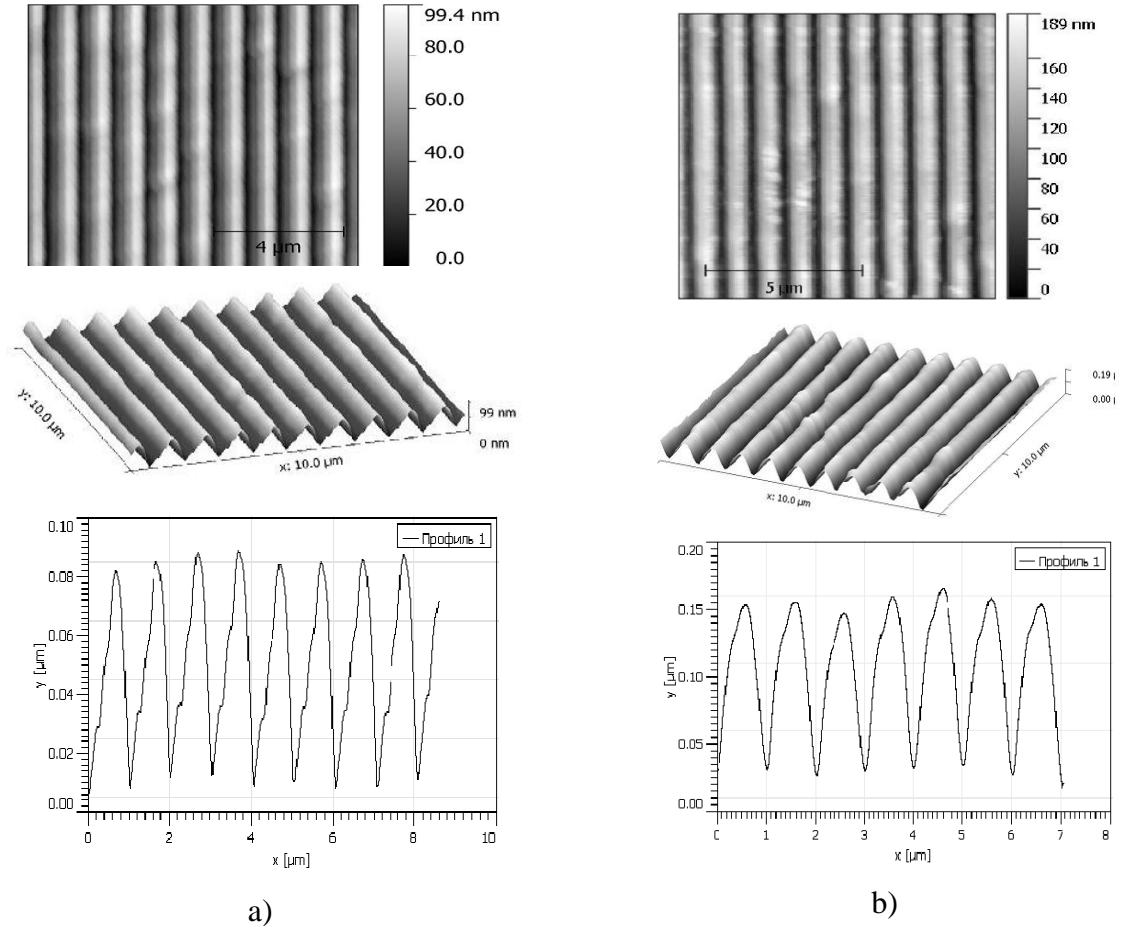


Fig. 5.14. Topography, 3D image and profil of the surface gratings recorded under $\pm 45^\circ$ (a) and LCP:RCP (b) polarization configurations.

From our experiments with AP we concluded that the surface relief grating formation plays a dominant role in diffraction efficiency evolution.

5.2. Diffractive optics elements

The practical application of DOE recorded in AP thin films as solar cell concentrator has been demonstrated in FP7 Project “ener2i INNOVATION VOUCHER COMPETITION”. We hit upon the idea of using a Fresnel concentrator, cheaply made from of transparent polymer film. The holographic technology is very close to thin polymer Fresnel concentrator for enhancing light trapping efficiency of photo voltaic cells (PVC). There are at least two problems which limited PVC implementation: a. cost and b. tracking of panel. Efficiency of PVC is limited by

modern level of semiconductors technology. But power efficiency of PVC can rise by concentrating sunlight. In several times more efficiency of harvesting sunlight with solar concentrator can rise of power efficiency and reduce PVC cost as for the same power needed smaller area and quantity of expensive PVC semiconductors. The reduction in the PVC surface area implies a considerable reduction in cost when compared with conventional PVC. On the other hand, the concentrator can harvest diffused sunlight in a cloudy day when PVC produces less power and power efficiency will be higher. Special optical design of Fresnel concentrator allows omnidirectional harvesting of sunlight. So eliminating/reducing sun tracking needed rise the power efficiency of PVC panel in overall power production. We designed Fresnel concentrator optics and prepared polymer films.

New applications of the developed AP thin layers have appeared in solar energy, where Fresnel lenses are used to concentrate sunlight. It is very important for widespread home applications.

Various methods for Fresnel lenses preparations for sunlight harvest are well known, but in the lab was elaborated know-how innovative laser method for one step direct recording of optical components. Steps of the method are: optical computing of concentrator, thin polymer film deposition on glass substrate, direct recording of concentrator pattern on film by laser beam. This experience was used in Fresnel concentrator design, testing and producing of the samples. AP thin film with Fresnel concentrator put on a cover protection glass which absorbs unwanted infrared part of solar spectrum. PVC output and life degrades by increased temperature. In this way we diminish heating silicon wafer. Solar panel consists of square wafers cut from circular ones. The dicing of silicon wafer results the elimination of 4 part of costly wafer. The innovative issue of the project is application of Fresnel concentrator with circular focus spot on circular wafer not square die.

Our innovative solution consisted in the Fresnel lens design from the AP thin film to improve useful power efficiency. So the holographic Fresnel lens concentrator adapted to producer needs/items has been elaborated by the following way:

1. The innovation is over all technology of Fresnel lenses production by deposition of AP on transparent photosensitive polymer film and its surface modification by direct laser exposition. The innovative design of Fresnel lens concentrator was optimized by optical software ZEMAX with such concentrator optical properties as circle spot focus (contour of cell), short focal distance to put film on PVC cover glass, quasi omnidirectional sunlight harvest;
2. The optical recording on AP thin films the Fresnel lens by using laser beam going through spatial light modulator and sub-micron stages of the Fresnel lens in accordance with the design elaborated;

3. The application of novel one step process of the direct laser surface modifications of films leading to holographic Fresnel lens formation;
4. Polymer recording media is one of the newest materials of the recording photosensitive elements. Compared to standard common used photoresists it doesn't require thermal vacuum evaporation and can be obtained as uniform thin films by spin-coating technique.

It is shown in Fig. 5.15 the surface relief a part of Fresnel lens, directly recorded in AP thin film by the direct polarisation holography method.

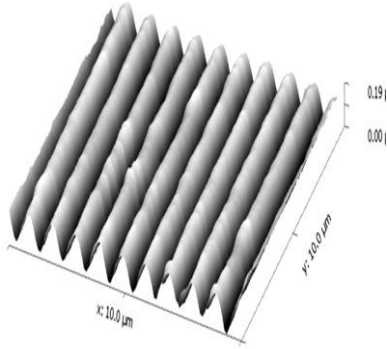


Fig. 5.15. The three-dimensional view surface relief a part of Fresnel lens in AP thin film.

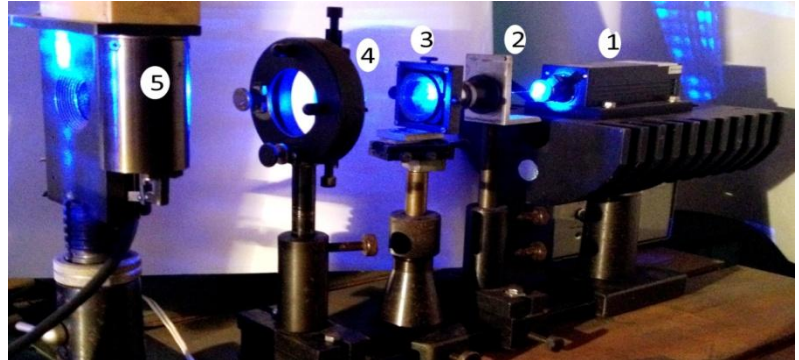


Fig. 5.16. The set-up for Fresnel lens formation: 1 — laser; 2, 3, 4 — lenses; 5 — photosensitive polymer film for Fresnel lens formation.

In the Fig. 5.16 we demonstrate the semiconductor laser set-up for Fresnel lens manufacture by direct surface relief formation.

The development of DOE for application in optoelectronics carried out by our group in frame of the Project Bilateral Moldova- Ukraine “New composite functional materials and structures on the base of chalcogenide glasses and photopolymers for optical and optoelectronic applications”. Method of polarized holographic recording for one step direct surface relief patterning on the azopolymer film was applied. The gratings were recorded at the RCP: LCP polarization, obtained with computerized LC waveplates with HOLOSTEP v1.0 software. Such beams configurations not create amplitude modulation, but only phase one. To obtain pointed above circular polarizations, the waveplates were rotated around the fast axis by computerized motorized system and set at angles of $\pm 45^\circ$, with 0.9° accuracy. Real-time control of DE by photo detector in first order of diffraction was done. Mathematical modelling of 2 superimposing diffraction patterns was performed in MATLAB by summing two perpendicular diffraction gratings for the analysis of the diffraction pattern formation. This simulation allowed the modification of the hologram recording parameters, the angle of incidence of the beams, grating period, the wavelength and the intensity of each beam. Pattern of both grating with the spatial frequen-

cies of 200 l/mm was modelling and recorded. In Fig. 5.17 the simulated in MATLAB the superimposed diffraction pattern and diffraction pattern recorded on an azo-polymer film PVA: MethylRed are presented.



Fig. 5.17. Simulated superimposed diffraction pattern in MATLAB (a), diffraction pattern recorded on an azo-polymer film PVA: MethylRed (b).

The parameters of recorded diffraction gratings were compared to the gratings simulated in MATLAB. It has showed a good correlation, indicating the correctness of the simulation. Superimposed grating analysis with the MII-4 interferometric microscope demonstrated that the pattern relief is 162 nm [227, 228].

5.3. Digital holography

The developed portable DHI has been applied for visualization and monitoring of wood art works, the under surface hidden damages — their position, shape and dimensions — by the heat excitation as the most suitable way of excitation for wood. In our experiments the wood samples have been heated by Rod Halogen Lamp R7S with reflector HLF-500W, so the thermal excitation of wood samples has been done. If a short heat pulse of lamp (2–4 s) hits at the surface of test sample, the wood surface changes the shape by the temperature. These changes depend on different thermal material properties (parallel and perpendicular to the grain of wood) and defects in the sub-surface such as deterioration of wood by insects' attacks, or detachments under veneered layer can be revealed. So observing the phase map changing we detect the existing defects under the surface and evaluate the position, size and the shape on these defects [229].

The samples for measuring were made on the model simulating cabinet wood panels for EU project LASERACT, and they have been kindly placed in our disposal. Similar technique of furniture was used for ebony cabinets from the early 17th century until the 19th century. We have used two sets of sliced veneered samples (150mm×150mm×18 mm) distinguishing presence and absence of damages into support. The illustration of sample structure with and without damages under the veneer can be seen in Fig. 5.18(a–d). Fig. 5.18(a), (b) presents the face side of the

samples, and Fig. 5.18(c), (d) — rear side of them. The sample consists of two layers: pine support (tangential cut) and six layers of plywood with two brasses cutting-off. Visible diagonal cut in Fig. 5.18(a), (b) is a veneer cut only. The grains of wood support are perpendicular to the grains of veneer.

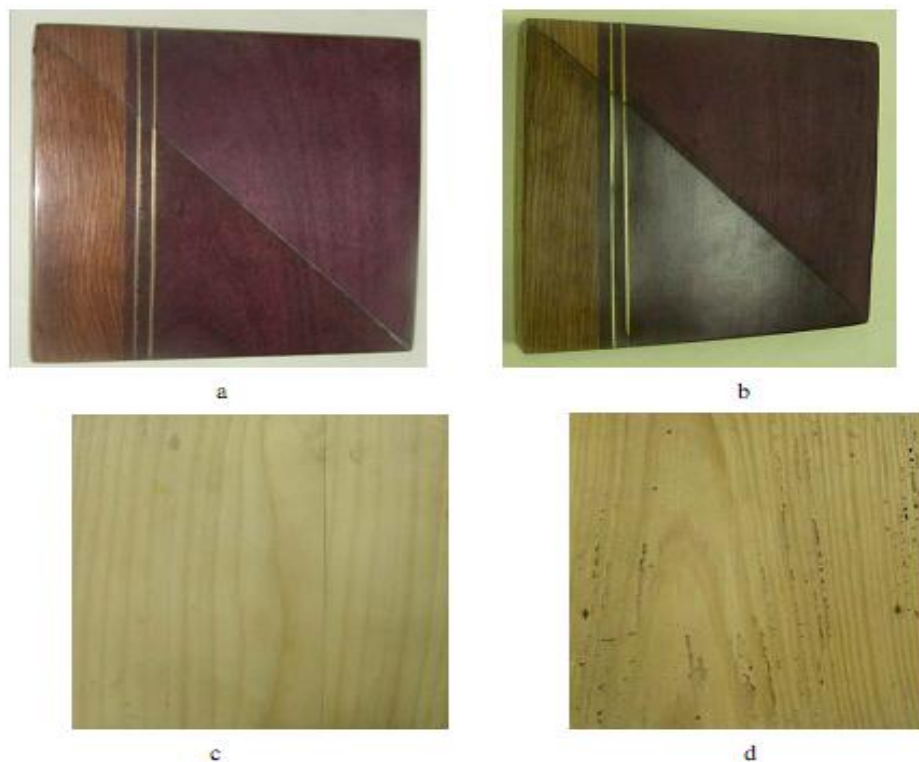


Fig. 5.18. Face and rear surfaces of the veneer samples are presented without damages (a), (c); with insect damages visible on backside only (b), (d).

Our choice of the sample structure is caused by our interest to detect invisible damages. The face veneer covers the support, so make its damages invisibles. In addition, sawed face veneer with brass cutting-off can influence on data interpretation due to its non uniform structure. We didn't test the cut part, only its affected support. The support presents tangential cut two glued pieces of pine wood. Painted veneer sheets with a thickness of six tenth of millimetre were glued to the one face surfaces by the adhesive (MC2) of animal origin. The problem faced by restorers is often related to gluing such as delaminating and “bubble”. Sometimes, little xylophage insects cause damages that are easy to detect but difficult to rate, especially when the support is deeply attacked in its core, but only a few flight holes are visible on the veneer. Indeed, veneer woods are often “siliceous and indigestible”, and insects prefer to go out through ends, joints or some holes dug by more vigorous insects. The damages like delaminating under veneer layer are not visible on both face and rear edge of the samples.

The measuring method is based on visual and instrument observation of the thermal out-of-plane deformation fringes on the surface of the inspected area (objective lens chosen for the field of view is 20mm×16 mm); the temperature of inspected surface is briefly increased by above mentioned way. The heating induces micro-expansions (micro-displacements) of the surface, read by the DHI head (fringe patterns in interferograms), and reveals the possible presence of defects under the surface and invisible to visual inspection.

The veneered wood sample without worm galleries defects visible inside the wood support has been tested. As an example, Fig. 5.19(a–c) shows succession of images which reflects the steps of acquiring and processing of data: (a) intensity interferogram obtained by subtracting images of heated and unheated (named reference) sample; (b) wrapped phase map obtained from the intensity interferogram; and (c) unwrapped phase map. By the application of phase shifting techniques “saw tooth” fringes are generated as the result of DHI deformation measurements.

The Fig. 5.19(a, b) show the possibility of influence or the structure of wood support which is deformed by different way or veneer delaminating. Veneer delaminating yields smooth bending of interferogram fringes, but none linear form of the fringes and mainly the break of them could indicate out the connection of two boards of wood forming the sample support.

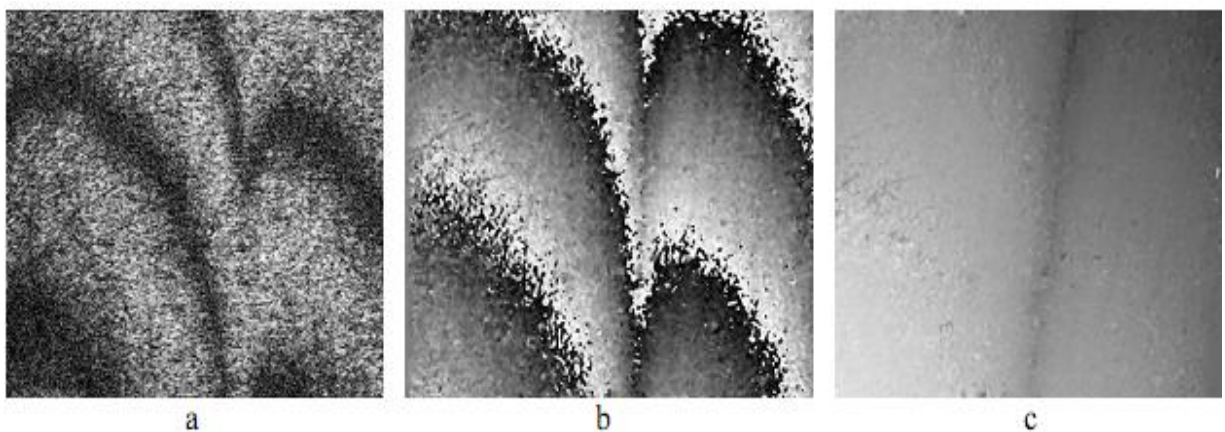


Fig. 5.19. Non-damaged wood sample intensity interferogram (a); wrapped phase map (b); unwrapped phase map (c).

The proof of the support influence can be seen from Fig. 5.20. The Fig. 5.20 are the photos of sample: the face side of inspected region (Fig. 5.20a), and end cross-section of the sample of the sample (Fig. 5.20b). The rectangle and the arrows point out the field of measuring. From the photo it can be clearly seen the presence of two regions inside the wood support with different directions of growth rings (two boards joint in Fig. 5.20b) and the absence of any other defects in

the support (e.g. worm galleries or delaminating). The position of the darker straight line in Fig. 5.19c coincides with the position and orientation of two boards joint on Fig. 5.20a (white line). Parallel delaminating lines of veneer are clear visible on the right down part of the sample surface only (Fig. 5.20, oval).

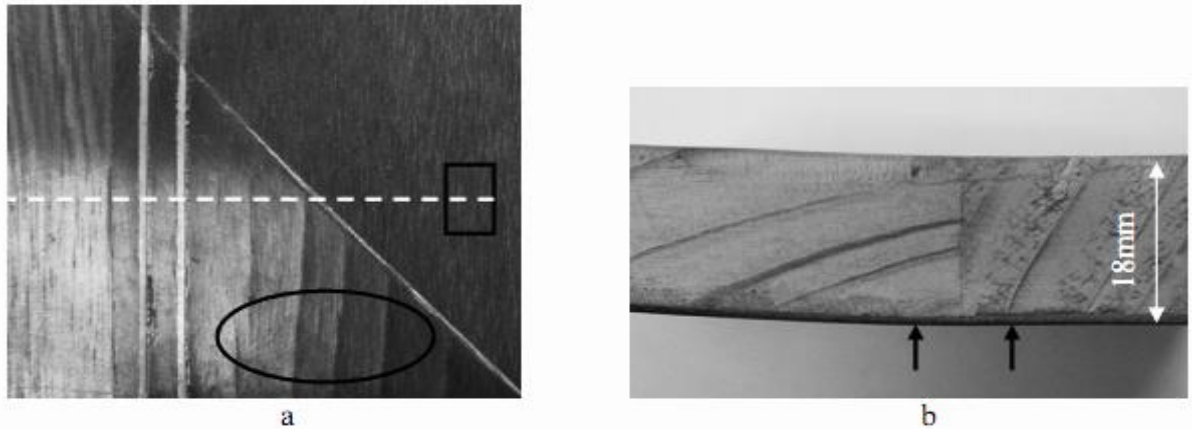


Fig. 5.20. Non-damaged sample with lines of delaminating (a, oval); end cross-section of the sample (b). The rectangle and the arrows point out the field of measuring.

White line indicates glued section of two parts.

The set of pictures presented in Fig. 5.21(a–c) shows the other region (without brass inset or cutting) on the same sample. The sequence of the images reflects the paths of data acquiring and processing similar as presented on Fig. 5.19. From these pictures we can see that the wood surface displaces uniformly by the heating, so delaminating is absent. Likely on the Fig. 5.19 the structure of the veneer layer is seen.

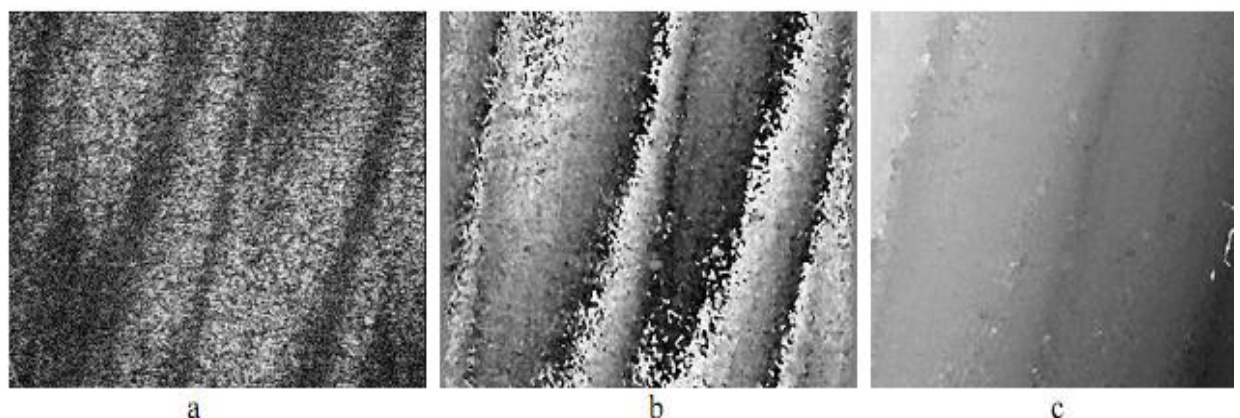


Fig. 5.21. Non-damaged wood sample intensity interferogram (a); wrapped phase map (b); unwrapped phase map (c).

Moving on the surface of the sample (Fig. 5.22) we have found the other form of deformed surface which indicates feature under surface (frequencies and orientation of fringes). Note that as on the face surface of the sample as on the back surface we do not see the features by naked eye, both surfaces look uniformly. We suppose that due to the lack of adhesion, the delaminated region disperses heat at a lower rate than the surrounding regions, and the delaminated region lies between veneered surface layer and support. Therefore, both the local temperature rise and the thermal expansion effects are higher for the delaminated region.

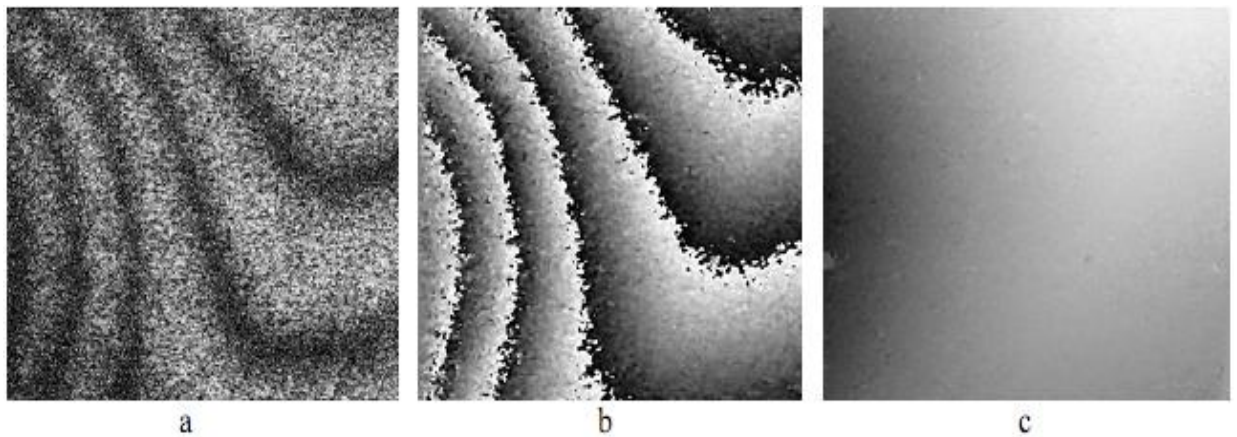


Fig. 5.22. Damaged wood sample intensity interferogram (a); wrapped phase map (b); unwrapped phase map (c).

Set of pictures presented in the Fig. 5.23 shows the intensity interferogram (Fig. 5.23a), wrapped phase map (Fig. 5.23b), and unwrapped phase map (Fig. 5.23c) of damaged sample. It is seen brass cutting like the non-damaged sample (Fig. 5.19) and the other defects, which have not been seen on the surface. The feature of these interferometric fringes is their straight form. This fact indicates that the whole sample included veneered surface layer and support, displaces uniformly by the heat excitation.

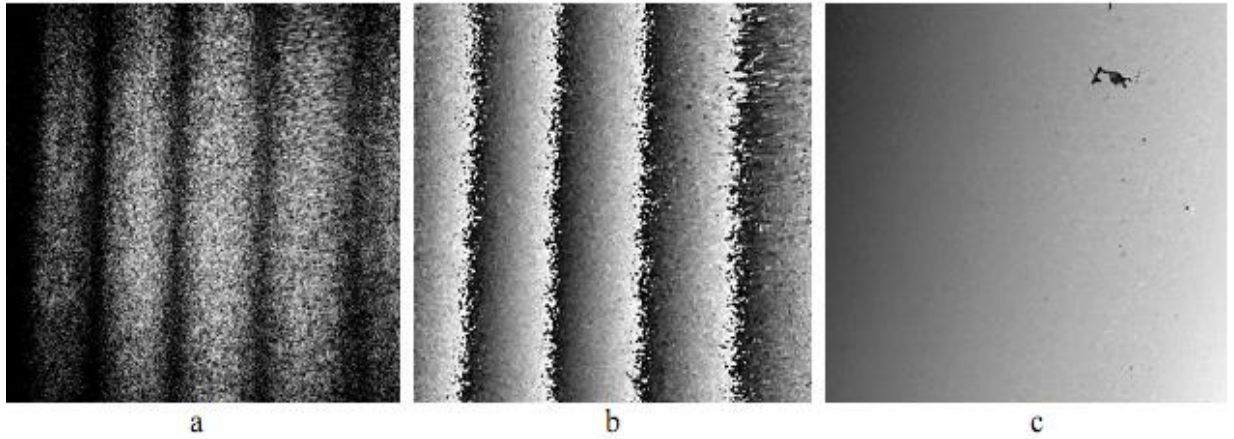


Fig. 5.23. Damaged wood sample (Fig. 5.21c): intensity interferogram (a); wrapped phase map (b); unwrapped phase map (c).

Then the damaged sample has been examined, the structure of the sample is shown in Fig. 5.24. The face surface of the sample is the same as in previous case (Fig. 5.20a), the end crosssection is uniform, but the back side or, in other words, the support of the sample is damaged by worm galleries (Fig. 5.24(c, d)).

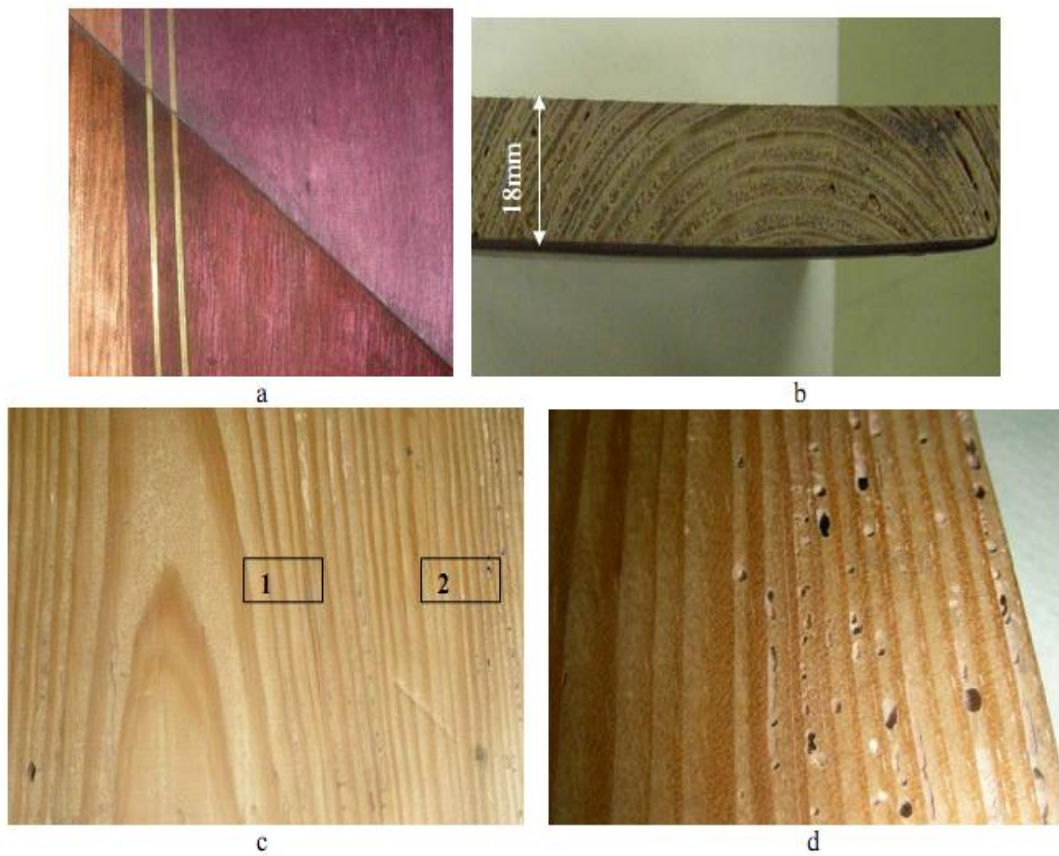


Fig. 5.24. Damaged sample face side (a); the end cross-section of the sample (b); the rear side at different magnification (c — 1^x , d — 5^x).

The field of view in our experiments is 20mm×16 mm. The Fig. 5.24 presents the face (Fig. 5.24a), end cross-section (Fig. 5.24b), and back side with magnification 1, (Fig. 5.24c) and magnification 5) (d) of damaged sample. The face side of non-damaged and damaged samples are identical (Fig. 5.20a and Fig. 5.24a). From the Fig. 5.24(c, d) we see that the support of defected sample is damaged by worms, and numerous galleries penetrate the support. The distribution of these galleries is irregular (Fig. 5.24(c, d)), and we have done the scanning of the sample by DHI system. Interferograms presented on Fig. 5.21 correspond to the face region 1 on Fig. 5.24c.

The set of interferograms in Fig. 5.25 corresponds to the face region 2 on Fig. 5.24c. Note that all measurements carried out on the face side of the samples where the damages are not seen. The intensity fringes (Fig. 5.22a, Fig. 5.23a), wrapped phase map (Fig. 5.22b, Fig. 5.23b) are similar for both regions, but unwrapped phase map with damages are differ (Fig. 5.22c, Fig. 5.23c). So the number of damages and the distribution is seen clear from these figures.

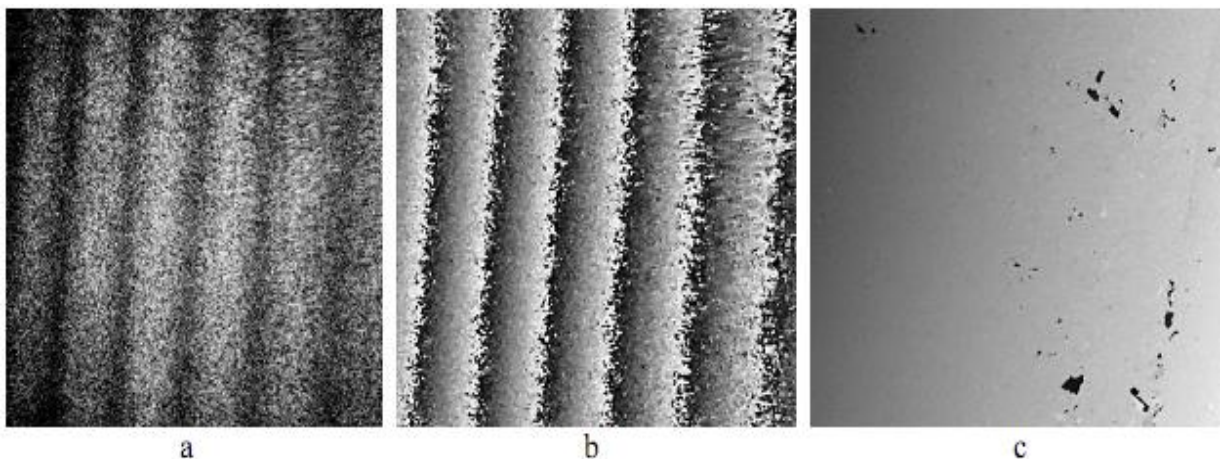


Fig. 5.25. Damaged wood sample (region 2 in Fig. 5.24c): intensity interferogram (a); wrapped phase map (b); unwrapped phase map (c).

The Fig. 5.26 shows the pseudo 3D-presentation of unwrapped phase map of non-damaged (a) and damaged (b) samples under heating. This kind of presentation gives possibility not only to see the existing damages, but to estimate the position, size and depth of them.

Our results indicate that developed variant DHI is well adapted to reveal the under surface damages in veneered wood samples. The set-up may be used in out-of-laboratory conditions and without severe anti vibration preoccupations.

So we have developed the friendly used, low cost, full field and portable DHI set-up. Applying DHI set-up we have determined the presence of different kind of damages located under sur-

face and invisible by naked eye: under surface delaminating and under surface worm galleries. The developed DHI is capable of predicting the position, shape and size of revealed damages. The results presented show that the DHI technique is a promising tool for testing the wood art works.

The control of the composite as a printed circuit boards (PCB) defects by elaborated DHI was implemented. Nowadays a composite has evolved into a major role in many industries as aerospace, automotive, wind energy, electronics etc. Devices and components all demand very high strength but also require low weight. Manufacturing processes is that the material i.e., the fiber composite, is made and molded in a single stage to create the finished composite product. The inner architecture and defects of composite structures determines their mechanical and thermal properties. Sometimes inner defects are invisible by naked eye and optical methods are therefore frequently used in structural characterization.

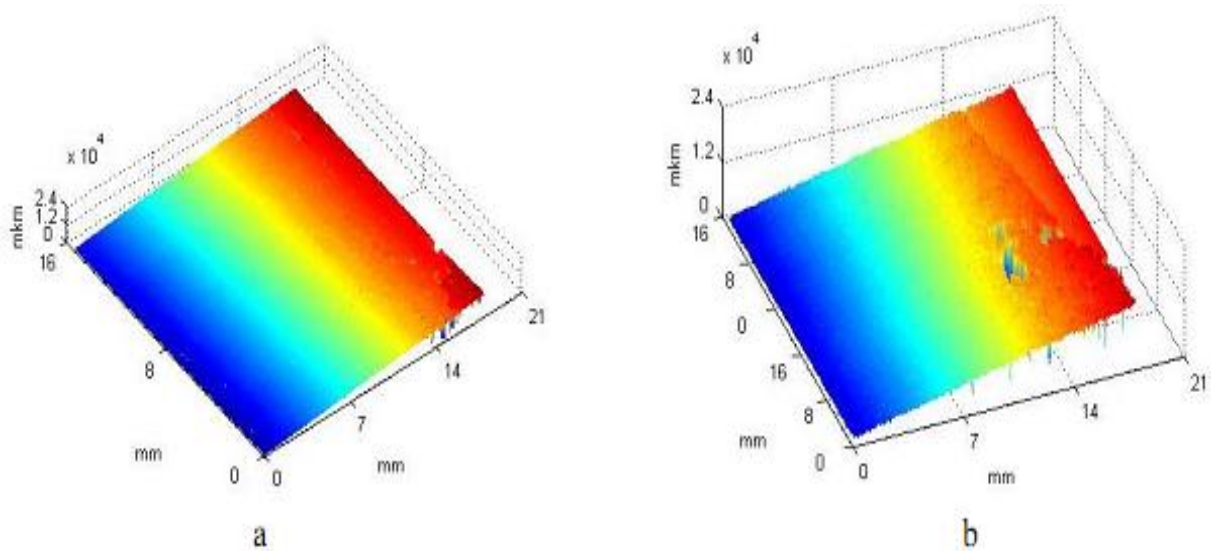


Fig. 5.26. Pseudo 3D-presentation of unwrapped phase map of non-damaged sample (a); damaged sample (b).

PCB structure is laminated structure composed of dielectric layers and copper signal traces with drilled holes. There are any kinds of defects emerging in PCB which can destroy functioning. One of these is micro cracks, swelling in the layers after pressing.

The highly sensitive DHI set-up was design from off-the-shelf components. Here we described performance of a developed system DHI (Fig. 5.27) for the detection damages in composite as PCB. DHI determines the difference after small deformation of the PCB. Optical components of DHI set-up (Fig. 5.27) were mounted on table which is available to isolate passive the table top from floor vibrations. There are 30 mW, $\lambda=532$ nm direct pumping solid state (DPSS) laser (1), (2) - (3)-spatial filter (micro objective (2), diaphragm (3), collimating lens (4)), prism as beamsplitter (5),

object (6), mirrors (7) and (10), camera objective (8), lens (9), beamsplitter (11), USB Camera Philips PCVC690K (maximum 30 fr/s, 640×480 pixels, 1/4" diagonal) (12), PC (13).

We have taken pictures by camera before and after excitation by halogen lamp of the object and subtract them by LabVIEW software. Subtraction is a data analysis process which is usually based on the extraction of the optical phase distributions encoded by the generated correlation fringes.

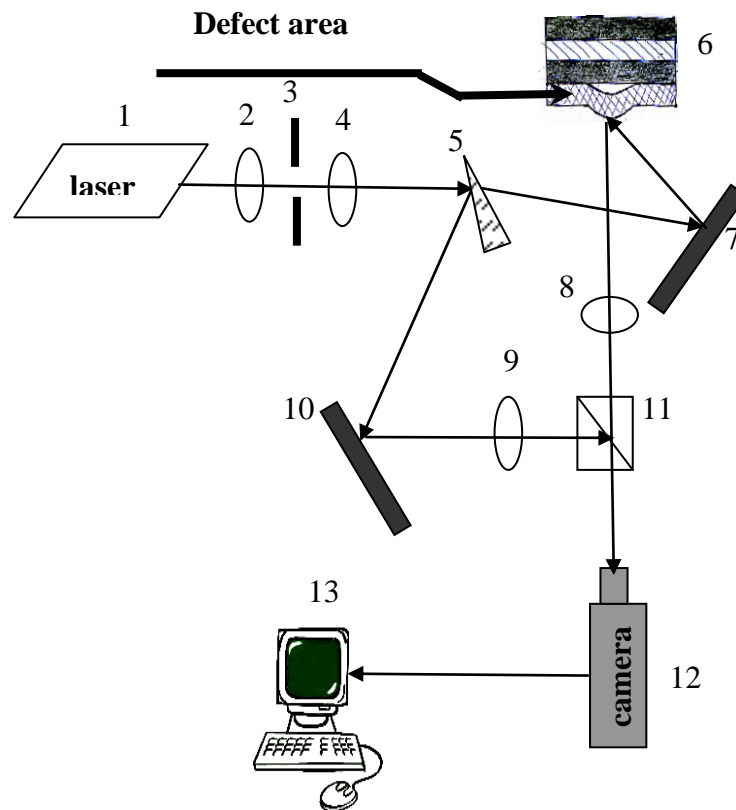


Fig. 5.27. Optical set-up of holographic ESPI.

The result of patterns subtraction shows a fringe pattern (Fig. 5.28), which can be interpreted as a state of deformation and so damages. Due to LabVIEW software application one can calculate the size of the defects, position and shape.

The two frames are then subtracted and correlation live fringes are displayed on a monitor (Fig. 5.28).

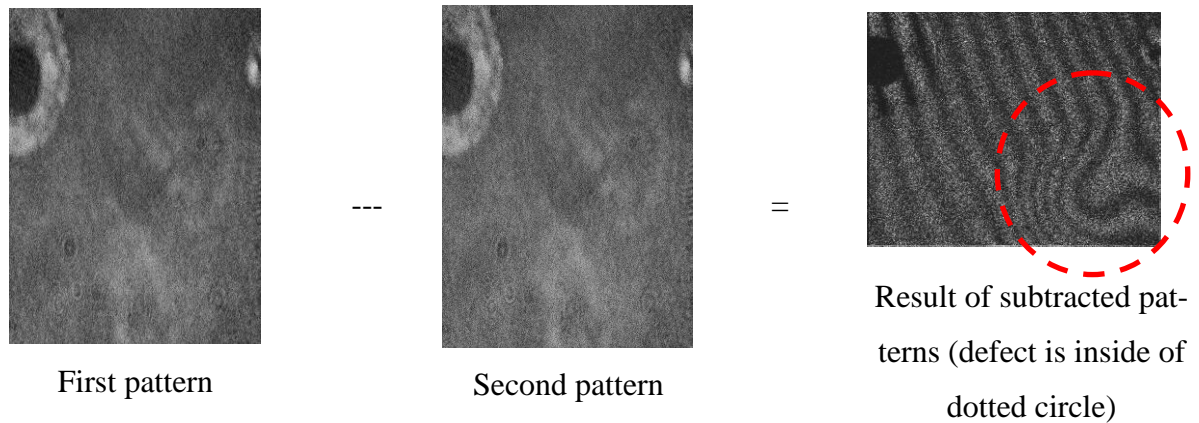


Fig. 5.28. Subtraction of the two speckle images.

The process of measuring by our DHI set-up is reduced to receiving two speckle patterns by using the video camera of unloading and loading PCB. The loading of the PCB was made in a simple way by heating PCB with a halogen lamp. Interlayer defects swelled and so it led to speckles patterns difference. The second step was the image processing of acquired speckle patterns by LabVIEW software for the full-field interferometry map of PCB's defects. Interferogram map of sample clearly highlights defects in PCB such as delaminating and air gap and points they position, size and shape.

The studying of biological samples (seed of *Orobancha cumana*) by using darkfield-microscopy carried out in frame of the Bilateral Germany-Moldova Project "Digital Holographic Microscope for Biological Tissues Investigation with LabVIEW program" (N 13.820.15.10/GA). The samples of *Orobancha cumana* seeds were collected in different regions of the Republic of Moldova (Dondușeni, Sorooca, Bălți, Chișinău, Sîngera, Rezeni, Cimișlia, Ștefan-Vodă, Ciadîr-Lunga, Taraclia), Romania (Fundulea), Ukraine (Izmail) and Spain (Sevilia). Pictures were taken with reflexion and transmission settings (Fig. 5.29). To focus on different surface regions of the seeds, manual adjustments were done varying the distance between lens and sample. In addition, one of the optical pathways was covered to change transmission to reflexion and vice versa.

Comparing the images obtained by using the optical microscope in the UnAŞM (Fig. 5.30a) and those performed in reflection and transmission illumination at the holographic dark field microscope of the ITO of the University of Stuttgart (Fig. 5.29) we distinguished differences significant on the visualization of the morpho-anatomic features of the surface of the seeds subject under the research, which underlie *Orobancha's* systematics.

Biological samples typically have a very complex structure and layers which are barriers to obtaining images with good optical resolution. The most important impediment is the diffraction

of the biological sample structure. In our investigations, a coherent light microscope was applied to remove these obstacles. The installation consists of four off-axis digital microscopes merged into one (Fig. 5.29). It allows us to obtain digital holograms in two lighting modes (dark and bright field with transmission/reflection configurations). Two independent lasers (diode mode) with wavelengths $\lambda = 660 \text{ nm}$ and 405 nm were used to illuminate the biological sample. The optical properties of the biological sample determine the selection of wavelength of illumination. Obtaining dark field images by illumination with $\lambda = 660 \text{ nm}$ in transmission and reflection mode is an appropriate solution for specimens with curved surface. The acquisition of images in the light field at $\lambda = 405 \text{ nm}$ denotes greater resolution and contrast due to high absorption of biological samples at this wavelength.

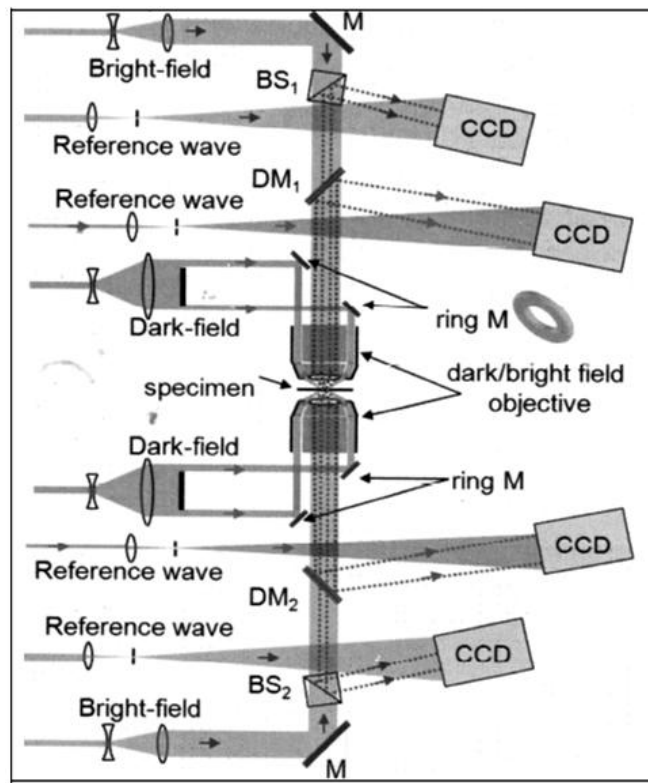


Fig. 5.29. The optical setup of the digital holographic microscope of both dark and bright field configurations.

The analysis of the seed images of 13 geographic populations of the *O. cumana* obtained using holographic microscopy allows to investigate of the surface architecture of the seeds. Thus, the high quality of the images resembles the seed crust, which is cross-linked with polygonal and tangentially elongated cells, sometimes irregular. Also the outer periclinal membrane wall with a very shifting aspect (drilling, granulous, rusty, etc.) was visible. During the experiment the pic-

tures of one seed per category, randomly chosen, were taken using transmission and reflexion adjustments. In samples 1, 2 and 3 more than one seed was taken for testing.

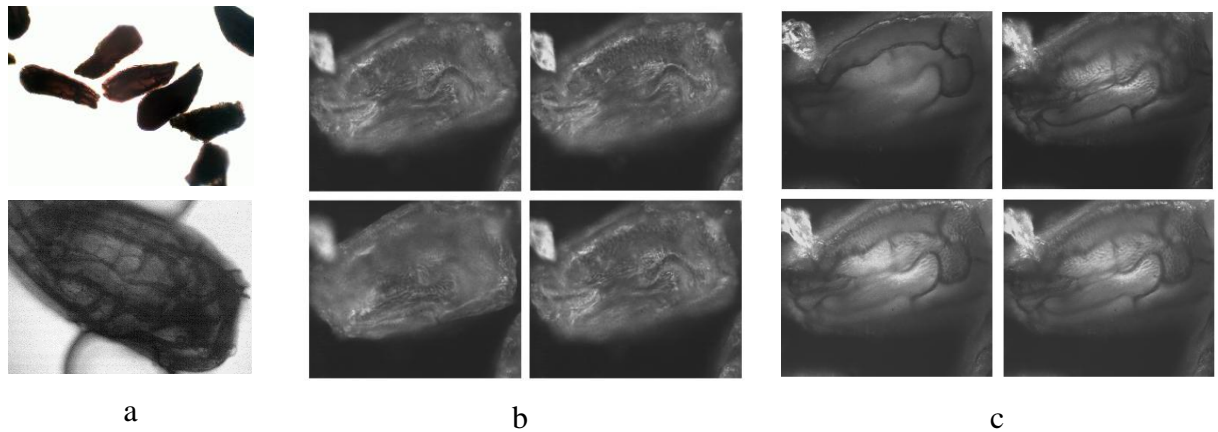


Fig. 5.30. The images of *O. cumana* (Singer, RM): a — at the optical microscope; b — in reflection illumination; c — transmission illumination at the holographic field-dark microscope.

Applying this method provides us information on the type and layout of the seed's outer cell layer, as well as the way of thickening the sides of the tangential cells of the seed layer from the side and inside. The seed coat is dark and opaque, but proper seed illumination allows a clear view of some surface characteristics, especially contours, and highlights the epidermal cells of the seed. The anticlinal walls are very deep and thickened evenly, marking the narrow junctions between the cells, visible to most cells, and the periclinal interior walls are granular or ruddy.

The practical application of a compact digital technique such as DHM in our study has revealed some important features of the method such as the necessity adapting of optical setup and software of the DHM to the sample properties and mode of preparation. Fig. 5.31 is shown the images in the reflection and transmission modes of *O. cumana* seeds from Spain, Sevilla.

The results obtained:

1. LabVIEW-based software for the holographic digital microscope designed to obtain and process images of native biologic preparations was developed.
2. The possibility of applying the DHM in the analysis of biological samples has been demonstrated.

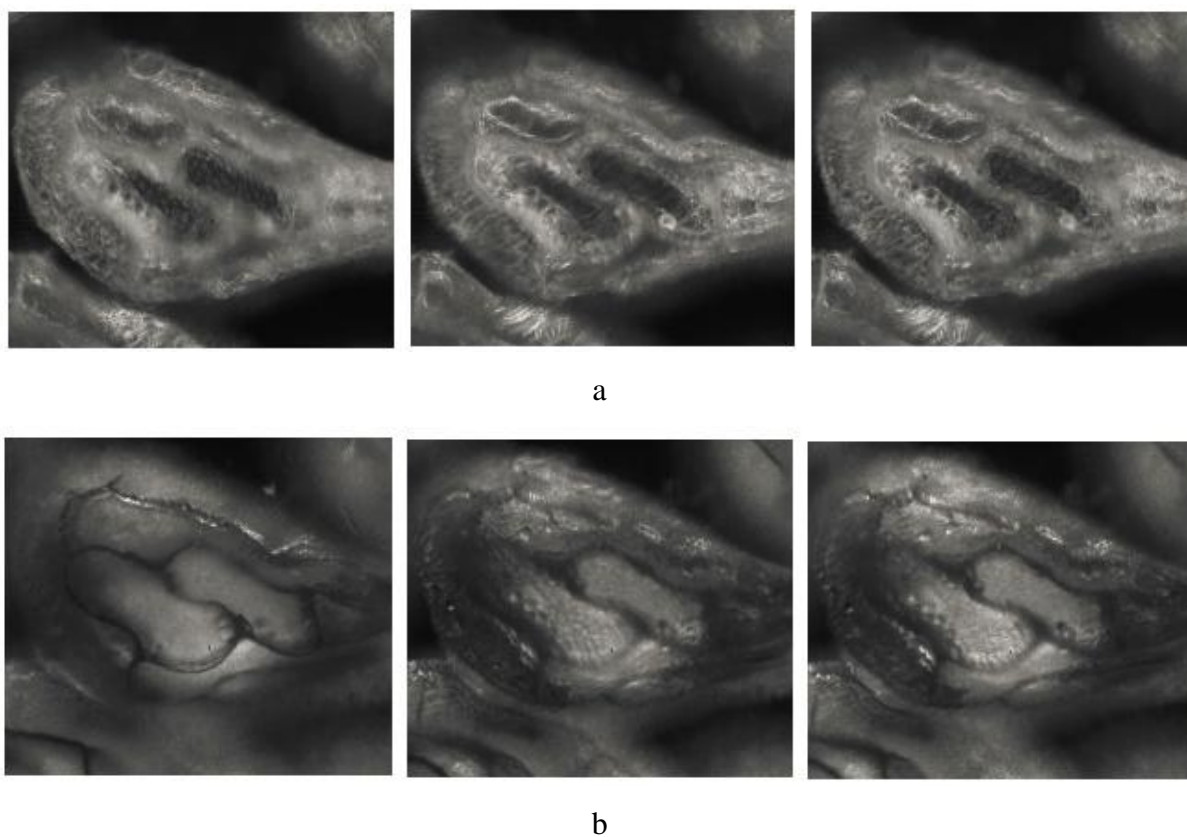


Fig. 5.31. The reflection (a) and transmission (b) modes of *O. cumana* seeds from Spain, Sevilla.

The results demonstrated the DHM technique with software based on LabVIEW is suitable for image processing tasks of biological samples, and for the increasing the amount of object information it is necessary to vary of modes of illumination (wavelength, transmission/reflection, falling angles) of the optical microscopic samples under study.

In order to demonstrate the capabilities of our epi-illumination system in DHM for studying biological sample, we present a preliminary measuring of phase map, which are derived from an interference fringes imaging of two state of the sample. The main procedure of phase map calculation described above (Chapter 4).

In our experiments initial (reference) speckle pattern image of the seed samples glued on black glass substrate has been acquired first. Then the substrate has been heated by quartz Halogen Lamp with reflector, so the thermal excitation of glass substrate has been done. If a short heat pulse of lamp (5–10 s) local hits at the substrate surface. The sample surface out-of-plane displaces the seed position by thermal expansion of glass. The temperature loaded speckle pattern image was done. It displaces sample depend on time of thermal excitation. So observing the phase map changing we detect the existing size and shape of seed surface. We acquire two consequent interference patterns before and after thermal excitation. Then the two speckled inter-

ferograms are subtracted to control interference quality. The image acquisition was accomplished using a Vision Builder Automatic Inspection and consequence speckle patterns processing based on LabVIEW 2011 program. The phase obtained from the evaluation of the interferograms is in the interval $-\pi$ to π , and is indefinite to an additive integer. But as we measure only phase change we do not need an absolute measurement of the phase. Unwrapped phase map extracted by program gives 3D surface morphology.

The seed photo in white light on the Smart Camera trough epi-objective is presented on Fig. 5.32.

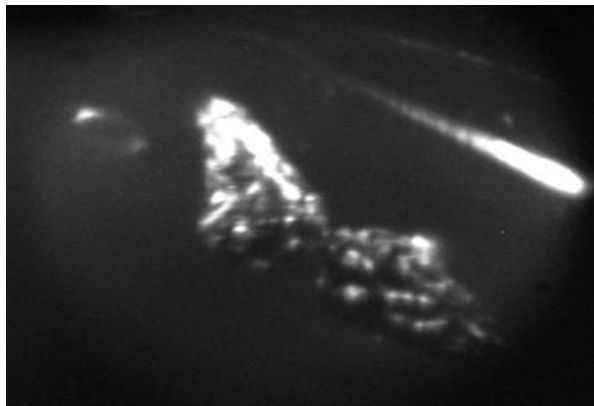


Fig. 5.32. The photo of the seed ($\sim 300 \mu\text{m}$ long) glued on black glass substrate.

To compare the results obtained with and without microscope epi-objective we have measured the phase map of the samples obtained by DSPI with one objective lens and DSPI with microscope epi-objective. Fig. 5.33(a, b) shows succession of images which reflects the steps of acquiring and processing of data: (a) intensity interferogram obtained by subtracting images of heated and unheated (named reference) sample; (b) wrapped phase map obtained from the intensity interferogram. The images presented in Fig. 5.33 were acquired by DSPI.

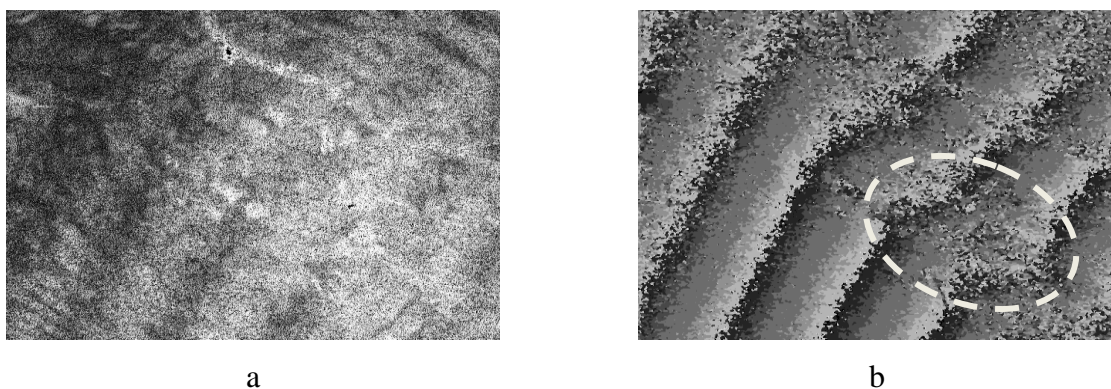


Fig. 5.33. The intensity subtraction interferogram (a), the wrapped phase map (b) recorded by DSPI without epi-microobjective. The seed position is marked by oval.

The surface phase shifts in reflection indicate the differences in height of the seed surface. Unwrapped phase shift map will be the base for extract the 3D form of the seed surface in microscopic mode. It is seen that the magnification of the DSPI (about 7^{\times}) does not allow us seeing the seed surface which introduces some distortion on the correlation fringes. The field of view (FOV) is 1 mm x 1 mm of this optical setup.

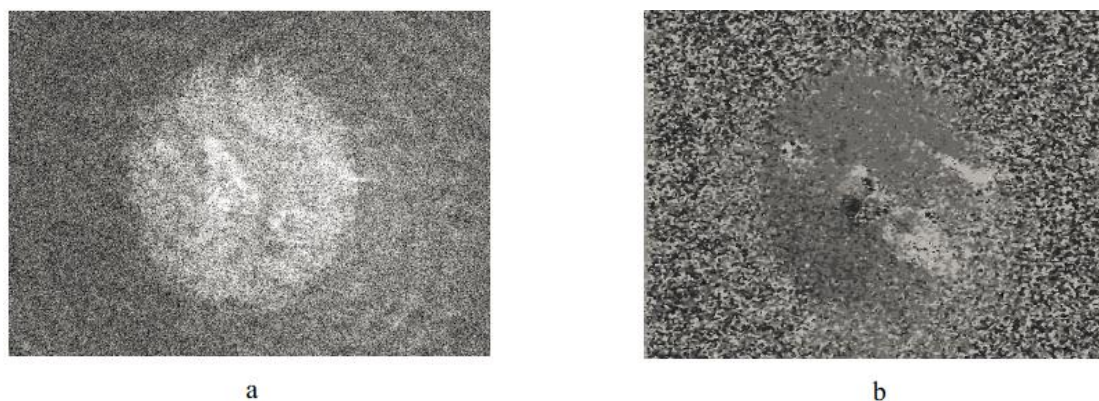


Fig. 5.34. The intensity subtraction interferogram (a) and the wrapped phase map (b) recorded by DHM with epi-microobjective.

On the 0b intensity varieties from the black to the white spots in the oval region pointed out the surface phase shift. The surface phase shifts in reflection indicate the differences in height of the seed surface. The magnification of the DHM is about 70^{\times} , and the FOV is 0.1 mm x 0.1 mm. Unwrapped phase shift map is the base for extract the 3D form of the seed surface in microscopic mode.

5.4. Conclusion to Chapter 5

1. Nanomultilayered, compositionally modulated ChG-Se nanomultilayers and AP thin films are perspective for the recording of different kinds of DOE (security elements, Fresnel lens, optical components). Taking into account that light sensitive and relief formation properties of nano-layered compositionally-modulated structures depend on composition and nano-periodicity further complex research is necessary with the use of direct and indirect structure sensitive methods in order to optimize the composition and structure of multilayers and parameters of the recorded optical elements.
2. The digital holographic method (optical setup, software, device for hologram's reading) was developed for security marks application on the surface of the precious metals that substantially increase the security level of Moldavian state marks protecting of precious metal articles.

3. We have developed the friendly used, low cost, full field and portable DHI set-up. Applying DHI set-up we have determined the presence of different kind of damages located under surface and invisible by naked eye: under surface delaminating and under surface worm galleries. The developed DHI is capable of predicting the position, shape and size of revealed damages. The results presented show that the DHI technique is a promising tool for testing the wood art works.
4. We have demonstrated the ability of the DHM setup to image seeds by laser epi-illumination microscopy in dark-field mode through the imaging telecentric microscope objective. The technique performance with phase analysis of interferograms of the seeds on a glass substrate by its thermal excitation was validated. The results demonstrated the DHM technique with software based on LabVIEW is suitable for image processing tasks of biological samples, and to increase the amount of object information it is necessary to vary of modes of illumination (wavelength, transmission/reflection, falling angles) of the microscopic samples under study.

Main conclusions and recommendations

A feature of diffractive optics is that it is both an object of human consumption (various illumination and communication devices, biomedicine) and tools for further research and development of optical instruments. From this point of view, this work has the twofold goal which is the updating of optical instruments, microscopes and interferometers for acquiring of 3D images, as well as elaborating new diffractive optical components, through which optical devices can be improved.

Optimal design of modern optical components and system is always hybrid of analog (optical) and digital components of the system with appropriately selected functions. The emerging optoelectronic and computer technology — increasing processing speed and memory capacity, new sophisticated softs, CCD video cameras instead of holographic films, SLM — have been used in the work for investigate new possibilities for advanced holographic applications.

To solve the problems of forming and treating of light beams with a given spatial structure and optical processing of information in real time, it was necessary to have media with increased photo and polarization sensitivity, speed of recording and reading information, reliability and fatigue.

The main significance of the work is the demonstration that combining the optical and digital image processing has ability to do progress in modern optical technologies.

The main research results:

- The PC controlled technology of successive vacuum deposition of ChG-Se nanomultilayers was developed and studied. Comparative investigation of the optical and recording features of nanomultilayers and the properties of their constituents nanolayers aimed to widening of DOE applications was done [102, 161, 185, 201, 217, 227].
- The chemical synthesis and spin-coating film deposition of new composition of Disperse Orange doped carbazole-containing polymers (AP) and determination of its recording properties, induced by scalar and vector holography was developed [103-105].
- It was experimentally determined that in the ChG-Se NML and the AP thin films the surface relief gratings are formed by one step direct optical and digital holographic recording methods and are conditioned by vectorial (spatially anisotropic) response of the medium [146, 156, 183, 201].
- The complex variations of optical parameters of the ChG-Se NML and the AP thin films take place responding to the action of both scalar and vector components of electrical field of light [134, 137, 160, 207].

- The surface relief gratings patterned on the ChG-Se NML are governed by photoinduced structuration in nanolayers of ChG and Se that leads to mass transfer in the ChG-Se NML [106, 107, 160, 216, 227].
- The surface relief gratings patterned on the AP thin films are governed by photoinduced *trans-cis-trans* transformation in the AP that leads to mass transfer in this media [116, 228].
- The high optical quality surface relief holograms, obtained by the one step direct method of polarization holography, were patterned on the ChG-Se NML and the AP thin films. Thereby, the etching process which is the most undesirable chemical technological step during the relief holograms manufacturing was excluded [160, 161].
- The phase diffraction gratings on the ChG-Se NML and the AP thin films with diffraction efficiency up to 48% in ± 1 diffraction orders were elaborated and recorded by the polarization holography, and their potentials and limitations for practical applications were studied [166, 175, 215].
- The practical application of developed ChG-Se nanomultilayers and the AP thin films to make use as the diffractive optical components has been demonstrated: the phase masks for optical processing in DHM, the digital security elements with increased protection level, and the protective holographic signs for defence of different kind of products from counterfeit [152, 156, 165, 185, 194, 198, 213, 217, 229, 230].

The following recommendations for further research based on the study findings:

1. The development of the PC controlled technology of ChG-Se NML deposition and carried out technological experiments open the way to choice among the variety of ChG compositions suitable for the required range of spectrum for laser illumination.
2. Elaborated method of digital holograms calculation with subsequent direct laser ablation of them on metal surface can be applied for master holograms production by embossing on plastic films.
3. Studying of diffraction efficiencies — the main performance attribute — of surface relief gratings recorded at different conditions (doze of illuminations, states of polarizations, grating's period) widens the range of practical applications of DOE patterned in ChG-Se NML and AP thin films.
4. Carry out study of photoinduced anisotropy in NMLs as prospective phenomena to discover new ChG and AP properties.
5. Developing digital holographic interferometry/microscopy technologies allows us to widen practicable application of advanced optical non-destructive testing in microelectronics, biomedicine, cultural heritage, and security technologies.

6. The implementation of modern digital hardware (SLM, CCD videocameras, liquid crystal variable retarders) and software (DH, ZEMAX, LabVIEW, DOE) of optical technologies in research and academic processes significant increase the level of national science and industry.

References

1. Gabor D. A new microscopic principle, *Nature*, 1948, v.161, p.777-778.
2. Leith E. N. and Upatnieks J. Reconstructed wavefronts and communication theory, *J. Opt. Soc. Amer.*, 1962, v. 52, p. 1123-1130.
3. Denisyuk Y. N. Photographic reconstruction of the optical properties of an object in its own scattered radiation field, *Sov. Phys. Doklady*, 1962, v. 7, no.6, p. 543-545.
4. Benton S.A. Hologram reconstruction with extended light sources. *J. Opt. Soc. Am.*, 1969, 59, 1545-1551.
5. Brown B. R. and Lohmann A. W. Complex Spatial Filtering with Binary Masks, *Appl. Opt.*, 1966, v. 5, no. 6, p. 967-969.
6. Wu M. C. Micromachining for optical and optoelectronic systems, *Proc. of the IEEE*, 1997, p. 1833-1856.
7. Veldkamp W. and McHugh T. J. Binary Optics, *Scientific American: New York*, 1992, 253 p.
8. Goodman J.W. *Introduction to Fourier Optics*. 2nd ed. New York, NY, USA: McGraw-Hill Inc, 1996. p. 81–83.
9. Weber A.G., Schell M., Fischbeck G., and Bimberg D. Generation of single femtosecond pulses by hybrid model locking of a semiconductor laser. *IEEE J. Quantum Electron*, 1992, vol. 28, p. 2200–2207.
10. Smith H.I. A proposal for maskless, zone-plate-array nanolithography. *J. Vac. Sci. Technol.*, 1996, vol. B14, p. 4318–4322.
11. Kashyap R. *Fiber Bragg grating*. London: Academic Press, 1999, 478 p.
12. Kakicheshvili Sh.D. *Polyarizatsionnaya golografiya*. Nauka. 1989, 143 p.
13. Nikolova L. and Ramanujam P.S. *Polarization holography*. New York: Cambridge University Press, 2009, 266 p.
14. Tanaka K. Chalcogenide Glasses. In: *Encyclopedia of Materials: Science and Technology*, Sec. Edition, Buschow K.H.J. et al., Editors-in-Chief. Amsterdam: Elsevier, 2001, p. 1123–1131.
15. Takats V. Surface patterning on amorphous chalcogenide nanomultilayers. *Optical Materials*, 2010, vol. 32, p. 677–679.
16. Dikova J., Vlaeva I., Babeva Tz., Yovcheva T., Sainov S. *Optics and Lasers in Engineering*, 2012, vol. 50, 838–843.
17. Saito I., Masuzawa T., Kudo Y., Pittner S., Yamada T., Koh A.T.T., Chua D.H.C., Mori Y., Zahn D.R.T., Amaratunga G.A.J., Okano K. J. *Non-Crystall. Solids*, 2013, vol. 378, p. 96–100.

18. Hoegl H. On photoelectric effects in polymers and their sensitization by dopants. *Journal of Physical Chemistry*, 1965, vol. 69, no. 3, p. 755–766.
19. Li Y., Gu P. Free-form surface inspection techniques state of the art review. *Comput. Aided D*, 2004, vol. 36, p. 1395–1417.
20. Bivol V., Andriesh A. New photoresists from carbazol-containing photopolymers. *Proceedings of SPIE “Applications of Photonic Technology”*, 2000, vol. 4087, p. 754–759.
21. Grazulevicius J.V. Photophysics of carbazole-containing systems. 3 Fluorescence of carbazole-containing oligoethers in dilute solution. *Macromolecules*, 1998, vol. 31, no. 15, p. 4820–4827.
22. Kryshenik V.M., Trunov M.L., Ivanitsky V.P. Vectoral response under photo-excitation in amorphous chalcogenides and azobenzene polymer films: a comparison. *J. Optoelectronics and advanced materials*, July 2007, vol. 9, no. 7, p. 1949–1964.
23. Popescu M. *Non-Crystalline Chalcogenides*, Solid State Science Technology Library. Dordrecht: Kluwer Academic Publishers, 2000. vol. 8, 378 p.
24. Kolobov V., Tanaka K. In: *Handbook of Advanced Electronics and Photonic Materials and Devices*. Ed. Nalwa H.S. New-York: Academic Press, 2001, vol. 5, ch. 2, p. 47; Kawaguchi T., Tanaka K., Elliott S.R., ch. 3, p. 91; Tanaka K., ch. 4, p. 119.
25. Fritzsche H. *Insulating and Semiconducting Glasses*, Ed. Boolchand P. World Scientific, 2000. 653 p.
26. Fei Wang, Boolchand P. In: *Non-Crystalline Materials for Optoelectronics*, Eds. Lucovsky G., Popescu M. Bucharest: INOE Publishers, 2004, vol. 1, p. 15.
27. Andriesh A.M., Iovu M.S., Shutov S.D. Chalcogenide non-crystalline semiconductors in optoelectronics. *J. Optoelectronics and Advanced Materials*, September 2002, vol. 4, no. 3, p. 631–647.
28. Aggarwal D., Sanghera J.S. Bulk crystal growth and characterization of semiorganic nonlinear optical materials. *J. Optoelectron. Adv. Mater.*, 2002, vol. 4, p. 665.
29. Tanaka K. and Shimakawa K. *Amorphous Chalcogenide Semiconductors and Related Materials*. New York: Springer, 2011.
30. De Neufville J.P., Moss S.C. and Ovshinsky S.R. Photostructural transformations in amorphous As_2Se_3 and As_2S_3 films. *J. Non-Cryst. Solids*, 1973, vol. 13, p. 191.
31. Elliott S.R. *Physics of Amorphous Materials*. Harlow: Longman Scientific & Technical, 1990.
32. Fritzsche H. Optical anisotropies in chalcogenide glasses induced by band-gap light, *Phys. Rev. B*, 1995, vol. 8, is. 52, p. 15854–15861.
33. Zhdanov V.G., Malinovskii V.K. *Sov. JTF Lett.*, 1977, vol. 3, p. 943.

34. Kolobov A.V., Lyubin V., Yasuda T., Klebanov M., Tanaka K. *Phys. Rev. B*, 1997, vol. 55, p. 8788.
35. Hayashi K. and Mitsuishi N. Thickness effect of the photodarkening in amorphous chalcogenide films. *J. Non-Cryst. Solids*, 2002, vol. 299–302, p. 949–952.
36. Eguchi H., Suzuki Y., and Hirai M. Photo-induced absorption changes in a-As₂Se₃ films at 80 K. *J. Non-Cryst. Solids*, 1987, vol. 95–96, p. 757–764.
37. Indutnyi Z. and Shepeljavi P.E. Reversible photodarkening in As₂Se₃ nanolayers. *J. Non-Cryst. Solids*, 1998, vol. 227–230, p. 700–704.
38. Kokenyesi S. Amorphous chalcogenide nano-multilayers: research and development, *J. Optoelectron. Adv. Mater.*, 2006, vol. 8(6), p. 2093–2096.
39. Takats V., Nemec P., Csik A., Kokenyesi S. *J. Phys. Chem. Solids*, 2007, vol. 68, p. 948.
40. Trunov M.L., Nagy P.M., Takats V., Lytvyn P.M., Kokenyesi S., Kalman E. Surface morphology of as-deposited and illuminated As-Se chalcogenide thin films. *J. NonCryst. Solids*, 2009, vol. 355, p. 1993–1997.
41. Kokenyesi S. Comparison of photo- and deuteron-induced effects in amorphous chalcogenide layers *J. NonCryst. Solids*, 2003, vol. 326&327, p. 209–214.
42. Aleksejeva J., Gerbreders A., Gertners U., Reinfeld M., and Teteris J. Polarization holographic recording in Disperse Red1 doped polyurethane polymer film. *IOP Conf. Series: Materials Science and Engineering*, 2011, vol. 23 p. 012006.
43. Kikineshi A., Palyok V., Szabo I.A., Shipljak M., Ivan I., Beke D.L. Surface deformations and amplitude-phase recording in chalcogenide nanolayered structures. *J. Non-Crystalline Solids*, 2003, vol. 326–327, p. 484–488.
44. Borisova Z.U. *Chalcogenide semiconductor glasses (in Russian)*. Leningrad: University Publications, 1983. 344 p.
45. Rochon P., Batalla E., Natanhson A. Optically Induced Surface Gratings on Azoaromatic Polymer Flms, *Appl. Phys. Lett.*, 1995, vol. 66, p. 136–138.
46. Kim D.Y., Tripathy S.K., Li L., Kumar J., Laser-Induced Holographic Surface Relief Gratings on Nonlinear Optical Polymer Films. *Appl. Phys. Lett.*, 1995, vol. 66, p. 1166–1168.
47. Cai L.Z., Yang X.L. Interference of circularly polarized light: contrast and application in fabrication of three-dimensional periodic microstructures. *Optics & Laser Technology*, 2002, vol. 34, p. 671–674.
48. Lyubin V., Klebanov M. Interaction of polarized light with chalcogenide glasses. *J. Optoelectronics and Advanced Materials*, 2001, vol. 3, no. 2, p. 265 – 277.
49. Ozols A., Reinfeld M. *J. Opt A: Pure Appl. Opt.*, 2004, vol. 6, p. 134.

50. Popescu M., Sava F., Lőrinczi A. *J. Non-Cryst. Solids*, 2006, vol. 352, p. 1506.
51. Ivanov M., Ilieva D., Minchev G., Petrova T., Dragostinova V., Todorov T., Nikolova L., *Appl. Phys. Lett.*, 2005, vol. 86, p. 181902.
52. Lyubin V.M., Tikhomirov V.K. *J. Non-Cryst. Solids*, 1989, vol. 114, p. 133.
53. Pagés S., Lagugné-Labarthe F.F., Buffeteau T., Sourisseau C. *Appl. Phys. B: Lasers Opt.*, 2002, vol. 75, p. 451.
54. Asatryan K.E., Galstian T., Vallée R. *Phys. Rev. Lett.*, 2005, vol. 94, p. 087401.
55. Tanaka K., Asao H. *Jpn. J. Appl. Phys.*, 2006, vol. 45, no. 3A, p. 1668.
56. Asatryan K.E., Frederick S., Galstian T., and Vallee R. Recording of polarization holograms in photodarkened amorphous chalcogenide films. *Applied Physics Letters*, 2004, vol. 84, no. 108, p. 1626–1628.
57. Saliminia A., Galstian T., and Villeneuve A. *Phys. Rev. Lett.*, 2000, vol. 85, p. 4112.
58. Goodman J.W. and Lawrence R.W. Digital image formation from electronically detected holograms. *Appl. Phys. Lett.*, 1967, vol. 11, p. 77–79.
59. Schnars U. and Juptner W. Direct recording of holograms by a CCD target and numerical reconstruction. *Appl. Opt.*, 1994, vol. 33, p. 179–181.
60. Brown G.M., Song M. Overview of three-dimensional shape measurement using optical methods. *Opt. Eng.*, 2000, vol. 39, p. 10–22.
61. Jueptner W. and Schnars U. *Digital Holography: Digital Hologram Recording, Numerical Reconstruction, and Related Techniques*. Berlin: Springer-Verlag, 2005.
62. Kuhn J., Charriere F., Colomb T., Cuhe E., Montfort F., Emery Y., Marquet P., and Depeursinge C. Axial sub-nanometer accuracy in digital holographic microscopy. *Meas. Sci. Technol.*, 2008, vol. 19, p. 074007.
63. Ferraro P., De Nicola S., Finizio A., Coppola G., Grilli S., Magro C., and Pierattini G. Compensation of the inherent wave front curvature in digital holographic coherent microscopy for quantitative phase-contrast imaging. *Appl. Opt.*, 2003, vol. 42, p. 1938–1946.
64. Doval A.F. A systematic approach to TV holography. *Meas. Sci. Technol.*, 2000, vol. 11, p. R1–R36.
65. Schnars U. and Juptner W.P.O. Digital recording and numerical reconstruction of holograms. *Meas. Sci. Technol.*, 2002, vol. 13, p. R85–R101.
66. Javidi A. and Nomura T. Securing information by use of digital holography, *Opt. Lett.*, 2000, vol. 25, p. 28–30.

67. Katz A., Rosen J., Kelner R., and Brooker G. Enhanced resolution and throughput of Fresnel incoherent correlation holography (FINCH) using dual diffractive lenses on a spatial light modulator (SLM). *Opt. Express.*, 2012, vol. 20, p. 9109–9121.
68. Colthup N., Daly L., Wiberley S. *Introduction to Infrared and Raman Spectroscopy*. Academic Press, 3rd Edition. 1990. 547 p.
69. Malyj M., Espinosa G., Griffiths J. Extended defect structures in bulk As_2S_3 glass II. low-frequency Raman spectra and the glass transition. *Solid State Communications*, June 1987, vol. 62, no. 10, p. 671–676.
70. Mott N.F. and Davis E.A. *Electronic Process in Non-Crystalline Materials*. Oxford: Clarendon Press, 1979, 590 p.
71. Gonzalez-Leal J.M. The Wemple-DiDomenico model as a tool to probe the building blocks conforming a glass. *Phys. Status Solidi B*, 2013, vol. 250, p.1044-1051.
72. Shintani H. and Tanaka H. *Nature Phys.*, 2006, vol. 2, no. 200.
73. Kolobov V. *Photo-induced Metastability in Amorphous Semiconductors*. Berlin: Wiley-VCH Verlag, 2003, 436 p.
74. Gonzalez-Leal J.M., Vlcek M., Prieto-Alcon R., Stronski A., Wagner T., and Marquez E. J. *Non-Cryst. Solids*, 2003, vol. 326–327C, p. 146.
75. Stronski A.V., Vlček M., Tolmachov I.D., Pribylova H. Optical characterization of As-Ge-S thin films. *Journal of Optoelectronics and Advanced materials*, 2009, vol. 11, no. 11, p. 1581–1585.
76. Swanepoel R. *J. Phys. E: Sci. Instrum.*, 1983, vol. 16, p. 1214.
77. Wemple S.H. Refractive index behaviour of amorphous semiconductors and glasses, *Phys. Rev. B*, 1973, vol. 7, no. 8, p. 3767–3777.
78. Skordeva R. *J. Optoelectron. Adv. Mater.*, 1999, vol. 1, no. 1, p. 43.
79. Andriesh M., Tsiulyanu D.I. Influence of annealing and temperature on the absorption edge of As_2S_3 -Ge amorphous films. *Phys. Stat. Sol.*, 1973, vol. 19, is. 1, p. 3077–312.
80. Kim M. *Principles and techniques of digital holographic microscopy*. *SPIE Rev.*, 2010, vol. 1, p. 018005.
81. Sharpe J., Ahlgren U., Perry P., Hill B., Ross A., Hecksher-Sørensen J., Baldock R., and Davidson D. Optical projection tomography as a tool for 3D microscopy and gene expression studies. *Science*, 2002, vol. 296, no. 5567, p. 541–545.
82. Ozeki Y., Kitagawa Y., Sumimura K., Nishizawa N., Umemura W., Kajiyama S., Fukui K., and Itoh K. Stimulated Raman scattering microscope with shot noise limited sensitivity using subharmonically synchronized laser pulses. *Opt. Express*, 2010, vol. 18, no. 13, p. 13708–13719.

83. Faridian A., Pedrini G., and Osten W. High-contrast multilayer imaging of biological organisms through dark-field digital refocusing. *J. Biomed. Opt.*, 2013, vol. 18, no. 8, p. 086009.
84. Kemper B., Bauwens A., Vollmer A., Ketelhut S., Langehanenberg P., Müthing J., Karch H., and von Bally G. Label-free quantitative cell division monitoring of endothelial cells by digital holographic microscopy. *J. Biomed. Opt.*, 2010, vol. 15, no. 3, p. 036009.
85. Hahn J., Lim S., Choi K., Horisaki R., and Brady D.J. Video-rate compressive holographic microscopic tomography. *Opt. Express*, 2011, vol. 19, no. 8, p. 7289–7298.
86. Cuche E., Marquet P., and Depeursinge C. Simultaneous amplitude and quantitative phase-contrast microscopy by numerical reconstruction of Fresnel off-axis holograms. *Appl. Opt.*, 1999, vol. 38, p. 6994–7001.
87. Kim M.K. Tomographic three-dimensional imaging of a biological specimen using wavelength-scanning digital interference holography. *Opt. Express*, 2000, vol. 7, p. 305–310.
88. Colomb T., Cuche E., Montfort F., Marquet P., and Depeursinge C. Jones vector imaging by use of digital holography: simulation and experimentation. *Opt. Commun.*, 2004, vol. 231, p. 137–147.
89. Demoli N., Vukicevic D., and Torzynski M. Dynamic digital holographic interferometry with three wavelengths. *Opt. Express*, 2003, vol. 11, p. 767–774.
90. Kreis T. Applications of Digital Holography: From Microscopy to 3D-Television. *J. Europ. Opt. Soc. Rap. Public.* 2012, vol. 7, p. 12006.
91. Kreis T. Handbook of Holographic Interferometry. Weinheim: Wiley-VCH, 2005.
92. Mihaylova E., Naydenova I., Duignan B., Martin S., Toal V., *Opt. Laser. Eng.*, 2006, vol. 44, p. 965.
93. Popescu A., Savastru D., Miclos S. Refractive index anisotropy in non-crystalline As_2S_3 films. *J. Optoelect. Advanced Materials*, 2010, vol. 12, no. 5, p. 1012–1018.
94. Popescu A., Savastru D., Miclos S. Design and realization of low losses chalcogenide As_xS_{1-x} planar waveguides. *J. Optoelect. Advanced Materials*, 2011, vol. 13, no. 3, p. 213–217.
95. Tsiulyanu D.I. Chalcogenide glassy-based photoresists for microelectronics. *10.1109/ICMEL*, 1995, vol. 1, p. 31–35.
96. Marian S., Tsiulyanu D., Liess H.-D. Ge-As-Te-based gas sensor selective to low NO_2 concentrations. *Sensors and Actuators B: Chemical*, 2001, vol. 78, no. 1–3, p. 191–194.
97. Grillet Ch., Freeman D., Luther-Davies B., Madden S., McPhedran R., Moss D.J., Steel M.J., Eggleton B.J. *Opt. Express*, 2006, vol. 14, p. 369.
98. Feigel A., Veinger M., Sfez B., Arsh A., Klebanov M., Lyubin V. *Appl. Phys. Lett.*, 2003, vol. 83, no. 22, p. 44808.

99. Schroeter S., Vlcek M., Poehlmann R., Glaser T., Bartelt H. Proc. of 10th Microoptics Conf., September, Jena, Germany, 2004, p. F44.
100. Bilanich V.S., Onishchak V.B., Makauz I.I., Rizak V.M. Internal friction in glassy semiconductors of the Ge-As-Se system, *Phys. Solid State*, 2010, vol. 52, p. 1820–1829.
101. Stronski A., Paiuk O., Gudymenko A. et al. Effect of doping by transitional elements on properties of chalcogenide glasses, *Ceramics International*, 2015, vol. 41, p.7543–7548.
102. Stronski A., Achimova E., Paiuk O., Meshalkin A., Lytvyn P., Senchenko O., Prisakar A., Triduh G., Abashkin V., Oleksenko P. Nanomultilayer structures on the base of chalcogenide glasses: properties and application in optical elements fabrication, In: Collection of scientific papers "Fullerenes and nanostructures in condensed matter", Minsk 2016, Institute of thermal & mass transfer NAS Belarus, 2016. p. 412–418.
103. Meshalkin A., Robu S., Achimova E., Prisakar A., Shepel D., Abashkin V., Triduh G. Direct photoinduced surface relief formation in carbazole-based azopolymer using polarization holographic recording. *J. Optoelectron. Adv. M.*, 2016, vol. 18, p. 763–768.
104. Meshalkin A., Abashkin V., Prisakar A., Triduh G., Andries I., Bets L., Achimova E. High precision interferometric thickness analysis of sub-micrometers spin-coated polyepoxypropyl-carbazole films. *Sensor Electronics and Microsystem Technologies*, 2012, vol. 3, p. 62–69.
105. Meshalkin A., Andriesh I., Abashkin V., Prisakar A., Triduh G., Achimova E., Enachi M. Digital interferogram processing in nanometer thickness measurement by micro-interferometer MII-4. *Surf. Eng. Appl. Elect.*, 2012, vol. 48, n. 6, p. 114–118.
106. Andriesh A.M., Akimova E.A., Verlan V.I. In: Proc. Conf.: *Stekloobrasnye poluprovodniki*, Leningrad, 1985, p. 383–384.
107. Andriesh A.M., Akimova E.A., Buzdugan A.I., Iovu M.S., Simashkevich A.A., Verlan V.I. Injection sensibilization of photoeffect in two-layer glassy semiconductor heterostructures, *J. Non-Crystalline Solids*, 1987, vol. 90, is. 1–3, p. 339–342.
108. Buzdugan A.I., Zelenina L.I. et al. In: Proc. Conf.: *Stekloobrasnye poluprovodniki*, Leningrad, 1985, p. 56.
109. Mott N., Devis E. *Electron processes in noncrystalline materials*. M. 1982, 858 p.
110. Swanepoel R. Determination of Surface Roughness and Optical Constants of Inhomogeneous Amorphous Silicon Films, *J. Phys. E, Sci. Instrum.*, 1984, vol. 17, p. 896.
111. Holomb R., Mitsa V., Petrachenkov O., Veres M., Stronski A., and M. Vlček. Comparison of structural transformations in bulk and as-evaporated optical media under action of polychromatic or photon-energy dependent monochromatic illumination. *Phys. Status Solidi (c)*, 2011, vol. 9, p. 2705–2708.

112. Poelman D., Smet P.F. Methods for the determination of the optical constants of thin films from single transmission measurements: a critical review, *J. Phys. D Appl. Phys.*, 2003, vol. 36, no. 15, p. 1850–1857.
113. Petkov K. Compositional dependence of the photoinduced phenomena in thin chalcogenide films. *JOAM*, 2002, vol. 4, no. 3, p. 611–629.
114. Lalova A., Todorov R. Sensor properties of asymmetric Bragg stack from chalcogenide glass and PMMA, *Bulgarian Chemical Communications*, 2013, vol. 45, sp. Is. B, p. 59-62.
115. Todorov R. Thickness dependence of the optical properties of amorphous As-Ge-S thin films, *Bulgarian Chemical Communications*, 2013, vol. 45, sp. Is. B, p. 38-42.
116. Kolninov O.V., Kolesnikova V.V., and Milinchuk V.K. *Vysokomol. Soedin., Ser. A*, 1990, vol. 32, no. 3, p. 473.
117. Treushnikov V.M., Zelentsov N.V., and Oleinik A.V. *Zh. Nauchn. Prikl. Fotogr. Kine-matogr.*, 1989, vol. 34, no. 3, p. 165.
118. Yager K.G., Barrett C.J. Novel photo-switching using azobenzene functional materials. *J. Photochem. Photobiol. A*, 2006, vol. 182, p. 250–261.
119. Cembran A., Bernardi F., Garavelli M., Gagliardi L., Orlandi G. On the mechanism of the cis–trans isomerization in the lowest electronic states of azobenzene: S₀, S₁, and T₁. *J. Am. Chem. Soc.*, 2004, vol. 126, p. 3234–3243.
120. Tamai N., Miyasaka H. Ultrafast dynamics of photochromic systems. *Chem. Rev.*, 2000, vol. 100, p. 1875–1890.
121. Kondrat O. Coherent Light Photo-modification, Mass Transport Effect, and Surface Relief Formation in As_xS_{100-x} Nanolayers: Absorption Edge, XPS, and Raman Spectroscopy Combined with Profilometry Study. *Nanoscale Research Letters*, 2017, vol. 12, p. 149-159.
122. Kovalsky A., Vlcek M. *Proc. of SPIE, Conf. Advances in Resist Materials and Processing Technology XXVI.*, 2009, vol. 7273, p. 72734A–1.
123. Naik Ramakanta, Ganesan R., Sangunni K.S. *J. Non-Cryst. Solids.*, 2011, vol. 357, p. 2344–2348.
124. Stronski A.V., Vlček M. Photosensitive properties of chalcogenide vitreous semiconductors in diffractive and holographic technologies applications. *J. Optoelectronics and Advanced materials*, 2002, vol. 4, no. 3, p. 698–704.
125. Tolmachov I.D., Stronski A.V. Linear and nonlinear optical properties of Ge-As-S films, *Photonics, Devices, and Systems IV*, edited by Tománek P., Senderáková D., Hrabovský M., *Proc. SPIE*, 2008, vol. 7138, p. 71381X 1–6.
126. Tolmachov I.D., Stronski A.V. Optical properties of Ge-As-S thin films. *Functional Materials*, 2009, vol. 16, no. 1, p. 32–35.

127. Vateva E., Skordeva E., Nanoscale arrangement in the $\text{Ge}_x\text{As}(\text{Sb})_{40-x}\text{S}_{60}$ systems. *JOAM*, 2002, vol. 4, no. 1, p. 3–12.
128. Popescu G., Mir M., Bhaduri B., Ru Wang, Ruoyu Zhu. Quantitative Phase Imaging. *Progress in Optics*, 2012, vol. 57, p. 134–179.
129. Katkovnik V., Shevkunov I.A., Petrov N.V., and Egiazarian K. Wavefront reconstruction in digital off-axis holography via sparse coding of amplitude and absolute phase. *Opt. Lett.*, 2015, vol. 40, p. 2417–2420.
130. Onural L. and Scott P.D. Digital recording of in-line holograms. *Opt. Eng.*, 1987, vol. 26, p. 1124–1132.
131. Liu G. and Scott P.D. Phase retrieval and twin-image elimination for in-line Fresnel holograms. *J. Opt. Soc. Am. A*, 1987, vol. 4, p. 159–165.
132. Fienup J.R. Phase retrieval algorithms, a comparison. *Appl. Opt.*, 1982, vol. 21, p. 2758–2769.
133. Verrier N. and Atlan M. Off-axis digital hologram reconstruction: some practical considerations. *Appl. Opt.*, 2011, vol. 50, no. 34, p. 136–146.
134. Achimova E., Stronski A., Abaskin V., Meshalkin A., Paiuk A., Prisacar A., Oleksenko P., Triduh G. Direct surface relief formation on As_2S_3 -Se nanomultilayers in dependence on polarization states of recording beams. *Optical Materials*, 2015, vol. 47, p. 566–572.
135. Yang Z. Sub-wavelength imaging of photo-induced refractive index pattern in chalcogenide glass films. *Optics Communications*, 2009, vol. 282, no. 22, p. 4370–4373.
136. Tompkins H.G. *A Handbook of Ellipsometry*. New-York NY: Academic Press, 2005, p. 902.
137. Röling C., Meshalkin A., Achimova A. Imaging ellipsometry mapping of photo-induced refractive index in As_2S_3 films. *Journal of Non-Crystalline Solids*, 2013, vol. 365, p. 93–98.
138. Osten W., Faridian A., Gao P., Körner K., Naik D., Pedrini G., Kumar Singh A., Takeda M., and Wilke M. Recent advances in digital holography. *Applied Optics*, Sept. 2014, vol. 53, no. 27, p. G44–G63.
139. Restrepo J.F. and Garcia-Sucerquia J. Magnified reconstruction of digitally recorded holograms by Fresnel-Bluestein transform. *Appl. Opt.*, 2010, vol. 49, p. 6430–6435.
140. Picart P. Spatial bandwidth extended reconstruction for digital color Fresnel holograms. *Opt. Express*, 2009, vol. 17, p. 9145–9156.
141. Li J., Tankam P., Peng Z., and Picart P. Digital holographic reconstruction of large object using a convolution approach and adjustable magnification. *Opt. Lett.*, 2009, vol. 34, p. 572–574.
142. Krishnaswami K., Bernacki B.E., Hô N., Allen P.J., and Anheier N.C. Lateral shearing interferometer for measuring photoinduced refractive index change in As_2S_3 . *Rev. Sci. Instrum.*, 2008, vol. 79, p. 095101-1–095101-5.

143. Liebling M., Blu T., and Unser M. Complex-wave retrieval from a single off-axis hologram. *J. Opt. Soc. Am. A*, 2004, vol. 21, p. 367.
144. Schedin S., Pedrini G., Tiziani H.J. Pulsed digital holography for deformation measurements on biological tissues. *Appl. Opt.*, 2000, vol. 39, p. 2853–2857.
145. Katkovnik V., Shevkunov I.A., Petrov N.V., and Egiazarian K. Sparse approximations of phase and amplitude for wave field reconstruction from noisy data. *Proc. SPIE*, 2015, vol. 9508, p. 950802.
146. Cazac V., Meshalkin A., Abashkin V., Achimova A., Katkovnik V., Shevkunov I., Claus D., and Pedrini G. Surface relief and refractive index gratings patterned in chalcogenide glasses and studied by off-axis digital holography, *Applied Optics*, **2018**, v. 57, is. 3, p. 507-513.
147. Jones R., Wykes C. *Holographic and Speckle Interferometry*. Second edition, Cambridge (UK): Cambridge University, 1989, 327 p.
148. Andriesh A., Abashkin A. Optical properties of amorphous $(As_2S_{1.5}Se_{1.5})_{0.99}:Sn_{0.01}$. *Moldavian Journal of the Physical Sciences*, 2010, vol. 4, p. 349–355.
149. Sava F., Anghel A., Kaban I., Hoyer W., Popescu M., Atomic scale structure of $Ge_{30}As_4S_{66}$, *JOAM*, 2005, vol. 7, no. 4, p. 1971–1975.
150. Joenathan C. White light lateral shear interferometer with holographic shear lenses and spatial Fourier transform. *Optics Letters*, 2013, vol. 38, is. 22, p. 4896-4899.
151. <http://www.ni.com/> (visited 24.05.2018).
152. Achimova E. PhD thesis “Development of Electron Speckle Interferometry system for diagnostic of structural damages”, Ancona University, Italy, 2006.
153. Ostrovsky Yu., Shchepinov V., Yakovlev V. *Holography interference methods for studying the deformation*. 1988, 248 p.
154. Nagels P. *Physics and Techniques of Semiconductors*, 1998, vol. 32, no. 8, p. 958–963.
155. Trunov M.L., Lytvyn P.M., Yannopoulos S.N., Szabo I.A., Kokenyesi S. Photoinduced mass-transport based holographic recording of surface relief gratings in amorphous selenium films, *Appl. Phys. Lett.*, 2011, vol. 99, no. 5, p. 051906.
156. Stronski A., Achimova E., Paiuk O., Meshalkin A., Abashkin V., Lytvyb O., Sergeev S., Prisacar A., Oleksenko P., Triduh G. Optical and Electron-Beam Recording of Surface Relief's Using $Ge_5As_{37}S_{58}$ -Se Nanomultilayers as Registering Media. *Journal of Nano Research*, 2016, vol. 39, p. 96–104.
157. Iovu M.S., Shutov S.D., Andriesh A.M. Spectroscopic studies of bulk As_2S_3 glasses and amorphous films doped with Dy, Sm and Mn. *J. Optoelectron. Adv. Mater.*, 2001, vol. 3, no. 2, p. 443–454.

158. Tanaka K. Sub-gap excitation effects in As_2S_3 glass, *J. Non-Cryst Solids*, 2000, vol. 266–269, p. 889–893.
159. Sangunni K.S. *J. of the Indian Institute of Science*, 2011, vol. 91, no. 2, p. 295–302.
160. Stronski A., Achimova E., Paiuk O., Meshalkin A., Prisacar A., Triduh G., Oleksenko P. and Lytvyn P. Direct Magnetic Relief Recording Using $\text{As}_4\text{S}_6\text{O}$: Mn–Se Nanocomposite Multilayer Structures, *Nanoscale Research Letters*, 2017, v. 12, p. 286–293.
161. Stronski A., Achimova E., Paiuk A., Abashkin V. et al. Surface relief formation in $\text{Ge}_5\text{As}_{37}\text{S}_{58}$ -Se nanomultilayers. *J. Non-Cryst Solids*, 2015, vol. 409, p. 43–48.
162. Mailhot-Jensen B. et al. Carbazole Containing Copolymers: Synthesis, Characterization, and Applications in Reversible Holographic Recording. *Int. J. Photoenergy Volume*, 2010, Article ID 945242, 11 p.
163. Andriesh A. and Iovu M. Diffraction and luminescent structures based on chalcogenide glasses and polymers, *Phys. Status Solidi B*, 2009, vol. 246, no. 8, p. 1862.
164. Andriesh A., Sergheev S., Triduh G., and Meshalkin A. Diffraction optical structures on the basis of chalcogenide glasses and polymers. *J. Optoelectron. Adv. Mater.*, 2007, vol. 9, no. 10, p. 3007.
165. Andries A., Abaskin V., Achimova E., Meshalkin A., Prisacar A., Sergheev S., Robu S., Vlad L. Application of carbazole-containing polymer materials as recording media, *Physica Status Solidi (a)*, 2011, v. 208(8), p. 1837-1840.
166. Stronski A., Achimova E. Design of new functional materials based on chalcogenide glasses, polymers via modification and nanocomposite techniques, *Sviridov Readings*, Minsk 2015, is. 11, p. 1–9.
167. Bivol V.V., Robu S.V., Prisacari A.M., Meshalkin A.Yu., Vlad L.A., and Karaman M.I., Study of Sensitometric and Holographic Properties of Photoresist Media Based on Carbazole-Containing Polymers Sensitized with Triiodomethane and Pyran Photochromic Materials. *High Energy Chem.*, 2006, vol. 40, no. 3, p. 216.
168. Reinfelde M., Grants R., and Teteris J. Photoinduced mass transport in amorphous As-S-Se films. *Phys. Status Solidi C*, 2012, vol. 9, no. 12, p. 2586–2589.
169. Gertners U. and Teteris J. Photo-induced mass transfer in chalcogenides. *IOP Conference Series: Materials Science and Engineering*, 2011, vol. 23, no. 1, Article ID 012007.
170. Trunov M.L. Surface morphology of as-deposited and illuminated As–Se chalcogenide thin films, *J. Non-Cryst. Solids*, 2009, vol. 355, p.1993–1997.

171. Adarsh K.V., Naik R., Sangunni K.S., Kokenyesi S., Jain H., and Miller A.C. Kinetics and chemical analysis of photoinduced interdiffusion in nanolayered Se/As₂S₃ films. *J. Appl. Phys.*, 2008, vol. 104, p. 053501.
172. Vateva E., Georgieva I. In: *Homage book. Dedicated to Andrei Andriesh*, Bucharest: INOE&INFM Publ. House, 1999, p. 171.
173. Iovu M.S. Spectroscopic studies of bulk As₂S₃ glasses and amorphous films doped with Dy, Sm and Mn, *J. Optoelectron. Adv. Mater.*, 2001, vol. 3, no. 2, p. 443–454.
174. Lucovsky G., Phillips J.C. Length scale discontinuities between non-crystalline and nano-crystalline thin films: Chemical bonding self-organization, broken constraints and reductions of macroscopic strain. *J. Non-Cryst. Solids*, 2008, vol. 354 p. 2702–2705.
175. Losmanschii C., Meshalkin A., Achimova E., Abashkin V., Prisacar A., Kazak V., Pogrebnoi S., Macaev F. Influence of thickness and polarization on diffraction efficiency of direct patterned diffraction gratings in carbazole-based azopolymer films, In Proc. The 9th International Conference “Microelectronics and Computer Science” & The 6th Conference of Physicists of Moldova. 2017, Chisinau, Republic of Moldova, p. 84—87.
176. Yesodha S.K. Stable polymeric materials for nonlinear optics: a review based on azobenzene systems. *Prog Polym Sci.*, 2004, vol. 29(1), p. 45–74.
177. Holme N.C.R., Nikolova L., Ramanujam P.S., Hvilsted S. An analysis of the anisotropic and topographic gratings in a side-chain liquid crystalline azo-benzene polyester. *Appl. Phys. Lett.*, 1997, vol. 70, p. 1518–1520.
178. King N.R. Effect of media polarity on the photoisomerization of substituted stilbene, azobenzene and imine chromophores. *J. Mater. Chem.*, 1997, vol. 7, p. 625–630.
179. Gahagan K.T. and Swartzlander G.A. Jr. Optical vortex trapping of particles. *Opt. Lett.*, 1996, vol. 21, p. 827–829.
180. Salgueiro J.R. et al. Second-harmonic generation in vortex-induced waveguides. *Opt. Lett.*, 2004, vol. 29, p. 593–595.
181. Foo G., Palacios D.M., and Swartzlander G.A. Jr. Optical vortex coronagraph. *Opt. Lett.*, 2005, vol. 30, p. 3308–3310.
182. Mair A. Entanglement of the orbital angular momentum states of photons. *Nature (London)*, 2001, vol. 412, p. 313–316.
183. Abashkin V., Achimova E., Sergeev S., Prisacar A. Computer- assisted electron beam recording of patterns in As₂S₃ films, In Proc 2nd Int. Conf. of Nanotechnologies and Biomedical Engineering. Chisinau, April 18-20, 2013, p.89-92.
184. Certificat de drept de autor PC 2315–2769., Prisacar A. Programa “MakeHolog”, 2010-10-11.

185. Паюк О., Мешалкин А., Стронский А., Акимова Е., Сергеев С., Абашкин В., Литвин О., Олексенко П., Присакар А., Тридох Г., Сенченко Е. Электронно-лучевая и голографическая запись поверхностно-рельефных структур с использованием многослойных наноструктур $\text{Ge}_5\text{As}_{37}\text{S}_{58}\text{-Se}$ как регистрирующих сред, *Optoelectronics and Semiconductor Technique*, 2015, v. 3, p. 33-35.
186. Gaylord T.K. and Moharam M.G. Thin and thick gratings: terminology clarification. *Appl. Opt.*, 1981, vol. 20, p. 3271–3273.
187. Kogelnik H. Coupled wave theory for thick hologram gratings, *Bell Syst. Tech. J.*, 1969, vol. 48, p. 2909–2947.
188. Klein W.R. and Cook B.D. Unified approach to ultrasonic light diffraction, *IEEE Trans. Sonics Ultrason.*, 1967, vol. 14, p. 123–134.
189. Wells G.G. Diffraction grating with suppressed zero order fabricated using dielectric forces. *Optics Letters*, 2011, vol. 36, no. 22, p. 4404–4406.
190. Gertners U. and Teteris J. All-Optical Surface Micropatterning by Electric Field Intensity Gradient. *Advances in OptoElectronics*, 2015, ID 917029, p. 1–9.
191. Malyovanik M., Shiblyak M., Cheresnya V., Remeta T., Ivan S., Kikineshi A. Influence of interdiffusion on the optical and electrical parameters of amorphous chalcogenide multilayers. *J. Optoelectron. Adv. Mater.*, 2003, vol. 5, no. 20, p. 397 – 400.
192. Collier R.J. *Optical Holography*. New York: Academic, 1971, Chap. 5.
193. Rastogi P.K. (ed). *Digital Speckle-Pattern Interferometry and Related Techniques*. New York: Willey, 2001.
194. Abaskin V., Achimova E. Non-destructive testing of wood defected samples by ESPI, In Proc. 7th International Conference on Vibration Measurements by Laser Techniques: Advances and Applications, SPIE 5504–2006, p. 322-329, Ancona, Italy.
195. Yurischeva S., Osintsev A., Shchepinov V. Application of the method of digital speckle interferometry to study contact interactions, 2006, vol. 8, p. 120–121.
196. Clark L. *LabVIEW. Digital signal processing and digital communications*, McGraw-Hill Companies Inc., 2005, 202 p.
197. Lohmann W. and Paris D.P. Binary Fraunhofer holograms, generated by computer. *Appl. Opt.*, 1967, vol. 6, p. 1739–1748.
198. Abaskin V., Achimova E. Rating of electronic speckle pattern interferometer by optical software, In Proc. 8th Int. Conf. on Vibration Measurements by Laser Techniques: Advanced and Applications, 2008, Ancona, Italy, SPIE V.70980, p. 2 - 8.
199. ZEMAX Development Corporation, www.zemax.com.

200. Pedrini G., Alexeenko I. Miniaturized optical system based on digital holography. Proc. of SPIE, WA: Bellingham, 2004, vol. 5503, p. 493–498.
201. Achimova E., Stronski A. Functional structures based on chalcogenide glasses obtained via nanocomposite techniques and their applications, Open Access House of Science and Technology (OAHOST), 2017, v. 3, no. 28, p. 2-24.
202. Bohdan R., Molnar S., Kokenyesi S. Methods comparing peculiarities of surface-relief recording in amorphous chalcogenides. Phys. Status Solidi A, vol. 212, 2015, no. 10, p. 2186–2190.
203. Molnara S., Bohdana R., Csarnovicsa I., Burunkovab I., Kokenyesi S. Amorphous chalcogenide layers and nanocomposites for direct surface patterning. Optical Components and Materials XII, edited by Shubin Jiang, Michel J.F. Digonnet, Proc. of SPIE, 2015, vol. 9359, p. 935908.
204. Abedin K.M., Jesmin S.A., Haider A.F.M.Y. Opt. Laser Technol., 2000, vol. 32 p. 323.
205. E. CuChe, F. Bevilacqua, and C. Depeursinge, “Digital holography for quantitative phase-contrast imaging,” Opt. Lett. 24, 291–293 (1999).
206. D. Claus, J. Watson, J. M. Rodenburg “Analysis and interpretation of the Seidel aberration coefficients in digital holography”, Appl. Optics 50(34), H220-H229 (2011).
207. Achimova E., Abaskin V., Claus D., Pedrini G., Shevkunov I., Katkovnik V. Noise minimised high resolution digital holographic microscopy applied to surface topography, J. Computer Optics, 2018, v. 42(2), p. 267-272.
208. Osten W., Baumbach T., and Juptner W. Comparative digital holography. Opt. Lett., 2002, vol. 27, p. 1764–1766.
209. W. Osten, A. Faridian, P. Gao, K. Körner, D. Naik, G. Pedrini, A. Kumar Singh, M. Takeda, and M. Wilke, “Recent advances in digital holography”, Applied optics, Vol. 53, No. 27, Sept. 2014, pp. G44-G63.
210. Kujawinska, M., and J. Wojciak. "High accuracy Fourier transform fringe pattern analysis." Optics and lasers in engineering, 14(4), 325-339, (1991).
211. Dabov K., Foi A., Katkovnik V., Egiazarian K. IEEE Trans. Image Process., 2007, vol. 16, p. 2080.
212. V. Katkovnik and J. Astola, “High-accuracy wave field reconstruction: decoupled inverse imaging with sparse modeling of phase and amplitude”, J. Opt. Soc. Am. A 29, 44 (2012).
213. Abaskin V., Achimova E. Using the Optical Code for Phase Analyses of the Fiber-Optic ESPI Set-Up, In Proc. AIP –Int. Conf. on Advanced Phase Measurement Methods in Optics and Imaging, Locarno, Switzerland, 17-21 May 2010, pp 320-325.

214. Voynarovych I. Surface corrugating direct laser writing of microstructures in ternary chalcogenide films using a continuous-wave super-bandgap laser. *J. Phys. D: Appl. Phys.*, 2015, vol. 48, p. 265106.
215. Abaskin V., Achimova E., Meshalkin A., Prisacar A., Triduh G., Vlcek M., Loghina L., Voynarovich I. Investigation of Structural Features of As_2S_3 -Se Multilayer Nanostructure by Raman Spectroscopy, *Surface Engineering and Applied Electrochemistry*, 2016, v. 52, no. 4, p. 380–386.
216. Andrieş A., Achimova E., Bivol V., Meşalchin A., Prisacari A., Triduh Gh. Diffraction optical structures on the basis of chalcogenide glasses and polymers, *J. of Optoelectronics and Adv. Materials*, 2007, v. 9, no. 10, p. 3007– 3012.
217. Stronski A., Achimova E., Paiuk O., Meshalkin A., Lytvyn P., Senchenko O., Prisakar A., Triduh G., Abashkin V., Oleksenko P. Nanomultilayer structures on the base of chalcogenide glasses: properties and application in optical elements fabrication, *Collection of scientific papers «Fullerenes and nanostructures in condensed matter» Minsk-2016 Institute of thermal & mass transfer NAS Belarus*, 2016, p. 412-418.
218. Tanaka K. *Solid State Commun.* 1980, vol. 32, p. 201–204.
219. <http://www accurion.com/> (visited 24.05.2018).
220. Kostyukevych S. Fabrication of holographic diffraction gratings based on As_2S_3 layers. *Technical Physics*, 2003, vol. 48, no. 1, p. 115–117.
221. Sainov S., Sainov V., Dikova J. Holographic recording in nano-sized As_2S_3 films. *J. Optoelectronics and Advanced Materials*, 2001, vol. 3, no. 2, p. 395–398.
222. Tanaka K. Photo-induced dynamical changes in refractive index in amorphous As-S films. *Solid State Communications*, 1978, vol. 28, no. 7, p. 541–545.
223. Tiziani H.J. Optical metrology of engineering surfaces-scope and trends. In: *Optical Measurement Techniques and Applications*. Rastogi P.K., Chen F., Ed. Boston, MA: Artech House, 1997, p. 15–50.
224. Galstyan T., Viens J.F., Villeneuve A., Richardson K., Duguay M. *J. Lightwave Technol.*, 1997, vol. 15, p. 1343.
225. Teteris J., Reinfelde M. Holographic recording in amorphous chalcogenide semiconductor thin films. *Journal of Non-Crystalline Solids*, 2003, vol. 326, p. 494–499.
226. Hisakuni H., Tanaka K., *Solid State Comm.*, 1994, vol. 90, p. 483.
227. Paiuk A., Meshalkin A., Triduh G., Prisacar A., Achimova E., Stronski A., Abaskin V., Litvin O., Senchenko O., Gubanova A. Nanomultilayer As_2S_3 :Mn-Se Systems: Properties and Use as the Recording Media, In *IFBME Proc. 3rd Int. Conf. on Nanotechnologies and Bio-*

medical Engineering, V. Sontea, I. Tiginyanu (Eds.) Vol. 55, pp. 72-75, © Springer Science+Business Media Singapore 2016.

228. Loșmanschii, C.; Achimova, E.; Abașkin, V.; Mesalchin, A. PC assisted waveplates application for one step holographic direct surface relief patterning on azopolymer film. În: ICTEI 2018 Proceedings, Chișinău, 2018. The 6th International Conference on Telecommunications, Electronics and Informatics. May 24-27, 2018, Chișinău, Moldova, p. 128—129.
229. Castellini P., Abaskin V., Achimova E. Portable electronic speckle interferometry device for the defect measurements in wood artworks, *Journal of Cultural Heritage*, 2008, v. IX, no 3, p.225-233.

Annex 1

For the determination of film thickness the modified digital MII-4 interference microscope with CCD-camera was applied [104, 105]. True optical resolution (snapshots) is 1920×1080pxs of Logitech HD webcam. A magnification of 490[×] was used. The horizontal field of view, from which a data analysis is performed, was 0.3 mm diameter circle. The optical scheme and photo of MII-4 is shown in Fig. A1.1.

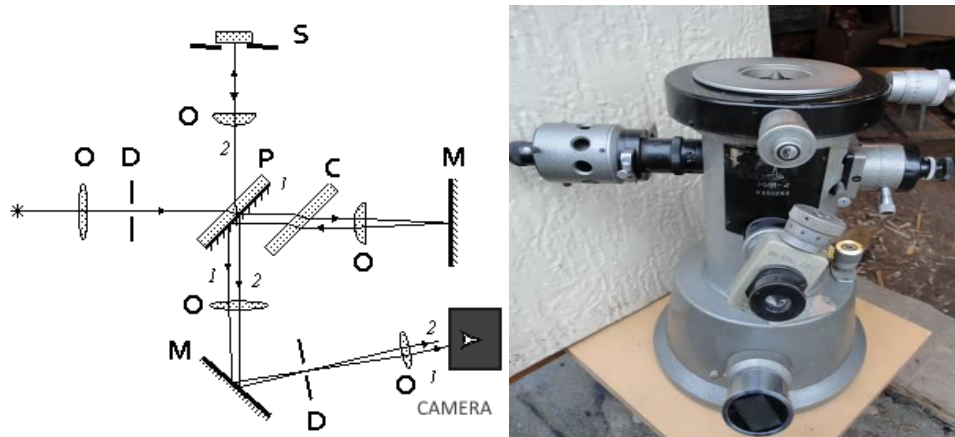


Fig. A1.1. Setup and photo of MII-4 interference microscope. 1 — reference beam, 2 — object beam, O — objectives, D — diaphragms, M — mirrors, P — beam-splitting plate, C — compensating plate, S — sample.

The interference pattern of light reflected from a flat reference surface and the surface of investigated sample was recorded in PC. The software tool OpticMeter has been elaborated for PC processing of interferograms. It permits to fit the interference patterns in an analytical form and precisely calculate the lines shift corresponding to thickness of submicrometer films. This enables a height resolution better than 50 nm. The phase shift in interferogram introduced by different height of layer is shown in Fig. A1.2.

In case of the interferometer microscope MII-4 the value of calculated thickness h of opaque or transparent layer is proportional to shift c of interference fringes (Fig. A1.3a) and inverse proportional to their width b :

$$h = \frac{\lambda}{2} \cdot \frac{c}{b}, \quad h = \frac{\lambda}{2} \cdot \frac{c}{b(n-1)},$$

where λ is the wavelength of light, n — refractive index of the film material. The first expression refers to the opaque films, and the second — to the transparent films. Using the software for interferogram processing in order to determine the parameters b and c allows on the one hand to greatly improve the accuracy of this determination, compared with the visual method,

and on the other hand to facilitate the implementation of the measure. In addition, it is possible to process and store the measurement results in electronic form.

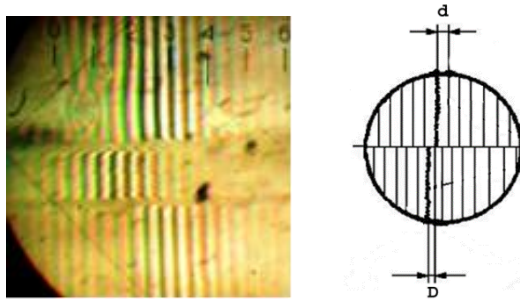


Fig. A1.2. Achromatic interference fringe shift in interferogram introduced by different height of layer. Photo of interferogram obtained by webcam and computerized MII-4.

Using the software for interferogram processing in order to determine the parameters b and c allows on the one hand to greatly improve the accuracy of this determination, compared with the visual method, and on the other hand to facilitate the implementation of the measure. In addition, it is possible to process and store the measurement results in digital form.

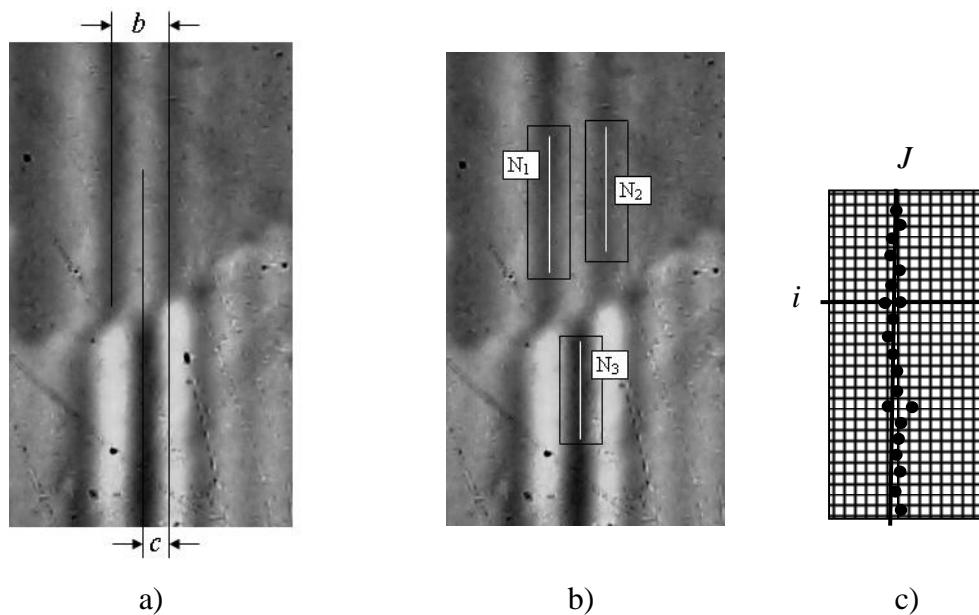


Fig. A1.3. Example of the interferogram processing: a) b — the distance between two adjacent interference fringes; c — shift of the interference fringe; b) Interactive selection of areas N_1 , N_2 and N_3 ; c) Determination of coordinates of extreme points of J lines in the N_i area.

As seen in Fig. A1.3, in order to accurately determine the parameters b and c the extreme lines (minima or maxima) for the biased and unbiased central interferogram bands must be build

up to the appropriate precision. For this purpose, the set of extreme points of a given type (min or max) are defined in the selected in an interactive mode three rectangular areas N1, N2 and N3 (Fig. A1.3b).

It is important that each rectangle covers only one type of extreme lines pre-selected in the interactive mode (regions of the minima in Fig. A1.3). The rectangles are positioned in areas with the best image quality of the central achromatic fringes. To improve the quality of the image pre-processing techniques are provided, especially smoothing and filtering for noise removal.

In the simplest case it is assumed that the interference fringes are strictly parallel to the frame borders (i.e. borders of the pixel's matrix) and, therefore, the lines of extreme points should be parallel to the vertical borders of the frame (Fig. A1.3c). In this approximation the values of the coordinates J for all extreme lines can be carried out as the average values of the extreme points coordinates j (one per horizontal line in the rectangle). Thus, the coordinates J_1 , J_2 and J_3 , representing the average coordinates of extreme points for rectangular areas N₁, N₂ and N₃ respectively, are determined.

Rectangles N₁ and N₂ are arranged in such a way that they covered the sets of adjacent extreme points of the same type and allow to determine the width of the interference fringes b as the difference in absolute coordinates of lines $|J_1 - J_2|$. The rectangle N₃ is positioned so that it covers the shifted set of the extreme points with respect to the N₂ area, so that the difference in absolute value $|J_3 - J_2|$ determines the shift c of the interference fringes. Thus, the desired thickness h is defined by the formula:

$$h = \frac{\lambda}{2} \cdot \frac{c}{b} = \frac{\lambda}{2} \cdot \frac{|J_3 - J_2|}{|J_1 - J_2|}.$$

In the real measuring process, a strict parallelism can not be achieved (Fig. A1.4a) and the set of extreme points (one per line) is located along the slope to the vertical boundary line (Fig. A1.4b). Analytical determination of the slope line position can be carried out using mathematical methods of linear fitting approximation in frame of least-squares method.

For this purpose, for each rectangle the approximation function of extreme line in form $y = ax + b$ is searched, where a and b are the unknown parameters. In this notation, the x -axis is perpendicular to the rows of pixels, and y — parallel (Fig. A1.4b). Following the standard least squares method, we can obtain analytical expressions for the extreme lines in all three rectangles N₁, N₂ and N₃:

$$y_1 = a_1x + b_1,$$

$$y_2 = a_2x + b_2,$$

$$y_3 = a_3x + b_3.$$

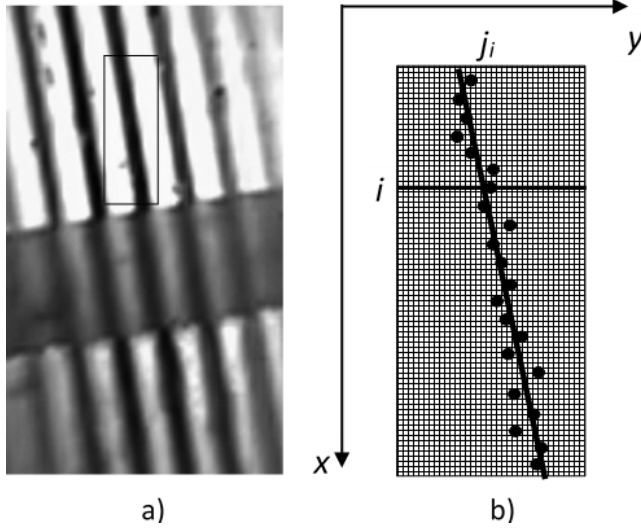


Fig. A1.4. Example of fringes nonparallel to the boundaries of frame, b) slope line of extreme points.

These lines should be parallel to each other in compliance with the physical condition, so the distance δ between them in a common coordinate system is defined by the formula (4):

$$\delta = \frac{|b_1 - b_2|}{\sqrt{a_1^2 + 1}}.$$

The final expression for the desired thickness h has the following form:

$$h = \frac{\lambda}{2} \cdot \frac{c}{b} = \frac{\lambda}{2} \cdot \frac{|b_3 + Y_3 - b_2 - Y_2|}{|b_1 + Y_1 - b_2 - Y_2|}$$

Here, the distances Y_1 , Y_2 and Y_3 are introduced, for which the corresponding rectangles are separated from the left vertical frame borders.

Optical grade of surface quality and uniformity of the films was confirmed by the smooth interference fringes in the interferogram obtained by MII-4. Several samples were prepared out of the same solution. To check the reproducibility of observed structures, the several samples were prepared in the same conditions and examined. In sample series A, PEPC concentration of the solution was kept fixed (10 wt% solutions of the PEPC polymer in chloroform CHCl_3 , boiling point is 62°C) and set of angular velocities was chosen in range pointed above. In sample series B, the PEPC concentration was varied (2.5, 5, 7.5, 10, 12.5 wt% solutions in chloroform) and deposition carried out at fixed angular velocity.

In this experiment a very accurate surface cleaning was carried out, and it was confirmed by many repetitions of the preparation that manifest the same morphology. Though each individual sample shows a different surface features the statistical features of the film morphology remain the same.

The interferograms of the polymer films spin-coated from solutions with different polymer concentrations taken by webcam are shown in Fig. A1.5.

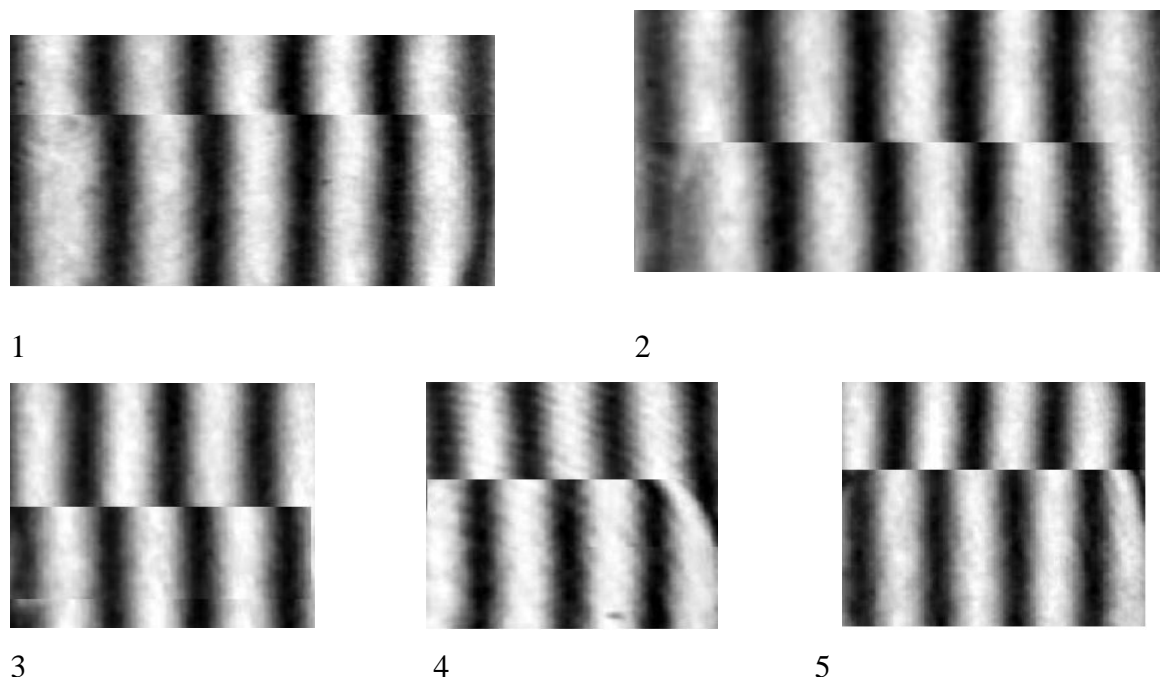


Fig. A1.5. Interference fringe shifts in interferograms MII-4 introduced by step of different thickness of series B layers obtained from following concentrations of PEPC solution: 1 — 2.5 wt%; 2 — 5.0 wt%; 3 — 7.5 wt%; 4 — 10.0 wt%; 5 — 12.5 wt%.

The thickness of series B films determined from the fringe pattern in the interferogram was found to be increased with the increase of polymer concentration in solution. It was shown that by raising the polymer concentration from 2.5 to 15.0 wt%, the final film thickness increase from 160 to 960 nm at a spin speed of 3000 rpm during 20 s. Applied method of thickness measurements has shown a quasi-linear thickness dependence on polymer concentration.

Working with computerized MII-4 interference microscope and elaborated software has shown that precise determination of layer thickness of thin films can be user-friendly. Software can process the interferograms in the case of interference fringe tilt respect to pixels row angles deviation.

In contrast to conventional layer thickness measuring devices such as profilometers or atomic force microscopes (AFM), this technique provides the full field analyzing specimens, is more rapid, noncontact, and does not require complicated specimen preparation. Thanks to these advantages, the modernized MII-4 interference microscope has great potential as a combined

analysis system (optical microscope and layer thickness measurement device), particularly in thin-film engineering. Moreover, the cheaper USB webcam with more than 2mln pxs is a good alternative to CCD camera and framegrabber. Webcam uses the low power USB interface for data transfer and provides the plug-and-play functionality.

Annex 2

LabVIEW is a graphical programming language elaborated by National Instruments Company [151]. LabVIEW programs are called virtual instruments (VIs), because their operation imitates works of physical instruments made by user. Specifically, LabVIEW is used to interface the computer with programmable measuring instruments. LabVIEW contains a comprehensive set of tools for acquiring, processing, analyzing, displaying, and storing data. Because LabVIEW graphical code is easy to comprehend, common programming tasks, like debugging, become more intuitive as well. LabVIEW provides unique debugging tools that can use to watch as data interactively moves through the wires of LabVIEW program and see the data values as they pass from on function to another along the wires between VI or sub VI. Each VI consists of a front panel and a block diagram. The front panel specifies the inputs and outputs which make up the user interface. The block diagram consists of icons which represent subroutines and program control structures [152].

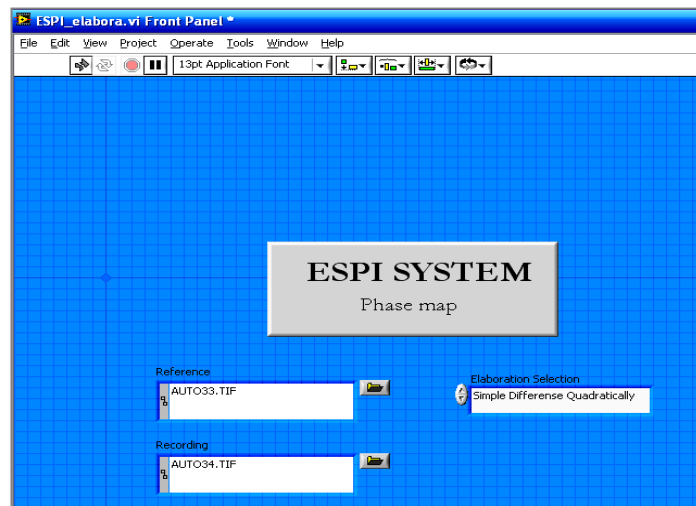


Fig. A.2.1. The screenshot of a LabVIEW user front panel.

LabVIEW is a program development application, much like various commercial C or BASIC development systems, or National Instruments LabWindows. However, LabVIEW is different from those applications in the one important respect. Other programming systems use

text-based languages to create lines of code, while LabVIEW uses a graphical programming language to create programs in block diagram form. Moreover, anybody can use LabVIEW with less programming experience. However, they are analogous to functions from conventional language programs. VIs has both an interactive user interface and a source code equivalent, and accepts parameters from higher-level VI's.

LabVIEW has extensive libraries of functions and subroutines for most programming tasks. LabVIEW contains application specific libraries for data acquisition and instrument control, data analysis, data presentation, and data storage.

The primary step of our program in LabVIEW is images acquisition and storage. Acquired images are stored in memory of CCD Smart Camera or in PC ready for processing. The front panel of our program is shown on Fig. A.2.1. In left side of screenshot one inserts names of two images.

Image acquisition window used for image processing respect options presented on Fig.A.2.2–A.2.4:

- Simple squared difference — Fig. A.2.2;
- Phase map — Fig. A.2.3;
- Rectangular determination for following unwrapped phase map extraction — Fig. A.2.4.

The operator starts the primary task, the data acquisition program, namely the first step is reading a reference image file and a recording image file. Program recognizes image file configurations such as BMP, TIFF, PNG and JPEG. This type definition edits automatically. The reference image in our case is unloaded object image. The recording image represents loaded object. Object loading process can be made by suitable way for object under investigation, for example heating, vibration, etc. The LabVIEW execution engine then distributes data the three our tasks in dependence of the problem needed and chosen by operator on front panel. These tasks are a pointed above.

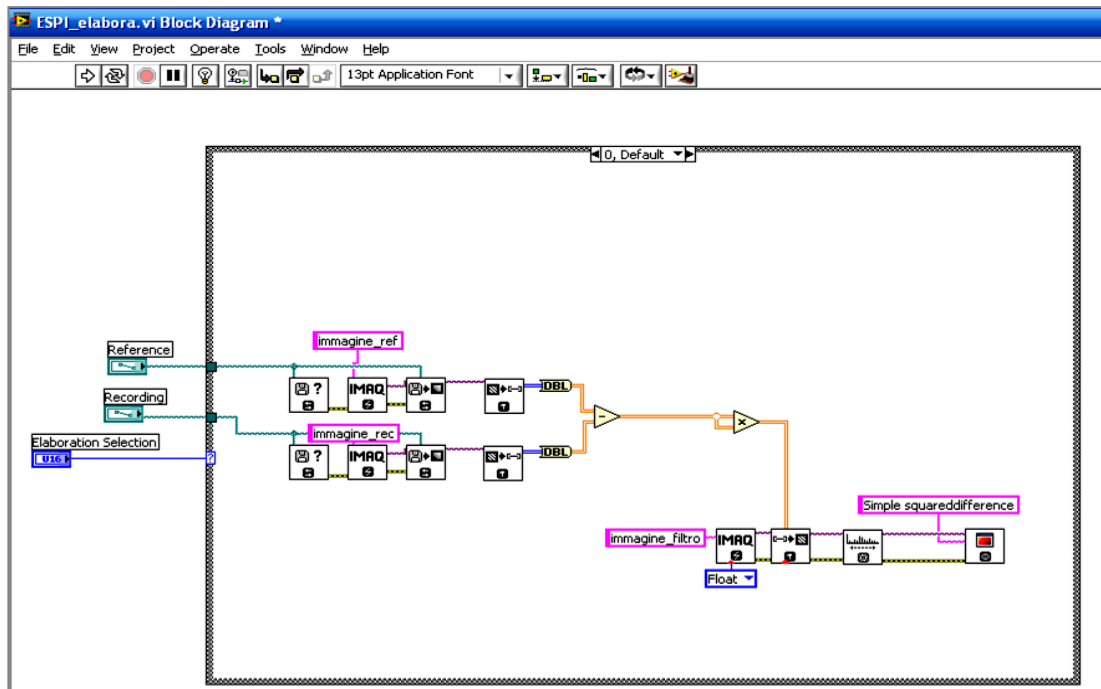


Fig. A.2.2. The screenshot of a LabVIEW user block diagram of VI's for simple squared difference processing.

The simple difference task VI's serve for squared image to increase S/N ratio. This block diagram also produces a histogram equalization of the squared image.

Block diagram for rectangular determinations serves for elimination from complex image low frequencies which are haven't useful information about the object. After that step VI Mask recopies image source into new image for processing.

Inside phase map block diagram VI computes optical FFT of both images and creates complex images in which high frequencies are grouped in the center while low frequencies are located at the edges. Inverse FFT of complex image after VI Mask calculation must be doing for final step as phase map calculation. So this block diagram first produces wrapped phase map and then unwrapped phase map. After final processing surface changes in-plane or out-of-plane will be presented.

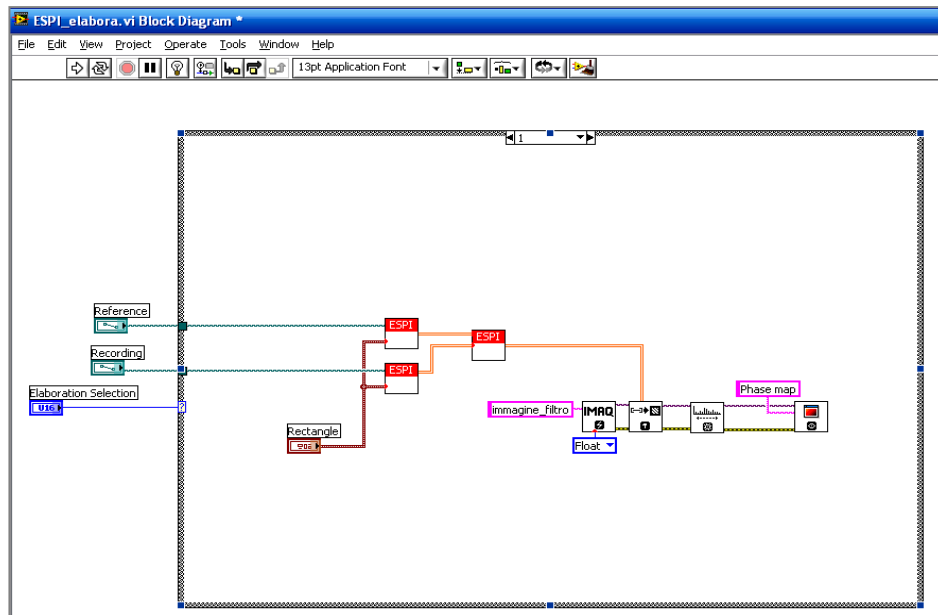


Fig. A.2.3. The screenshot of a LabVIEW user block diagram of VI's for a phase map mode.

Our work consists of two main objectives: the optical set-up design of fiber-optic ESPI and elaboration of satisfied LabVIEW program for refractive index measurement of thin firm samples. The process of measuring by our installation is reduced to receiving two speckle snapshots of unloading and loading object, and type of loading may be various.

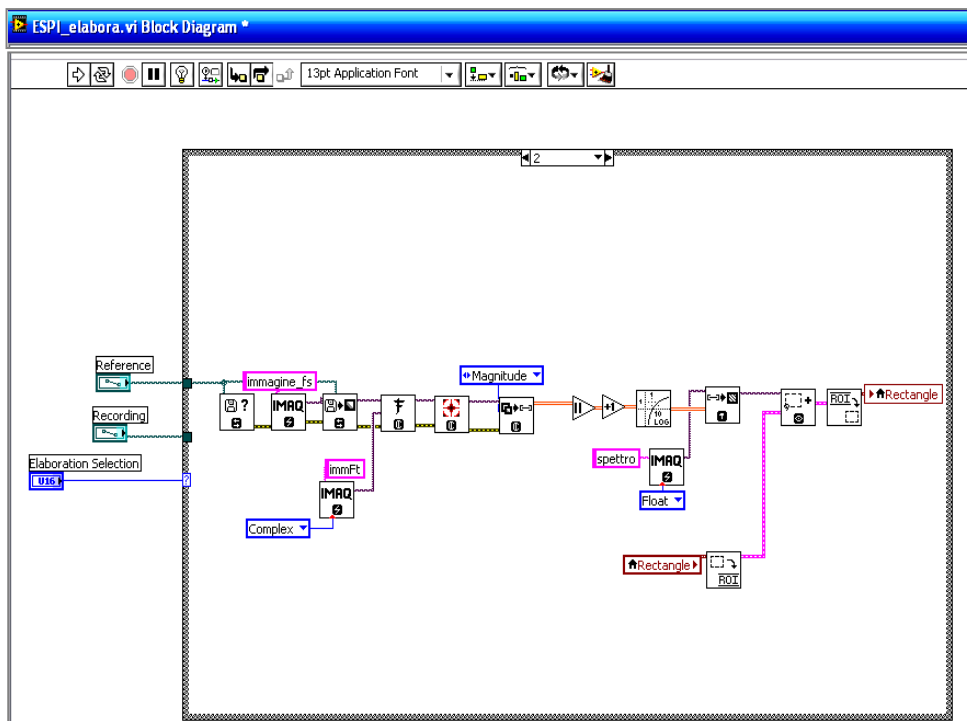


Fig. A.2.4. The screenshot of a LabVIEW user block diagram of VI's for a rectangular determination.

These snapshots will be recorded by using the CCD image sensor. Farther with image processing of speckle patterns and data processing with LabVIEW we can extract phase map, and finally calculate the required optical parameters by elaborated method. Important feature of this method are the full-field measuring of object properties which is important for investigations of optically recorded diffraction elements with very small location of refraction index changes.

In our work the following methods were used:

- Speckle-interferometric measurement of speckle-interferogram with Fourier optical processing in objective plane;
- Digital holographic method of acquiring of images on Smart Camera CCD image sensor;
- Method of forward and inverse Fast Fourier Transformations;
- Methods of processing by using LabVIEW such as optical type of FFT, histogram, phase extraction, S/N of image enhances.